

**IntechOpen**

# Smart Mobility

Recent Advances, New Perspectives  
and Applications

*Edited by Arif I. Sarwat, Asadullah Khalid  
and Ahmed Hasnain Jalal*





---

Smart Mobility -  
Recent Advances,  
New Perspectives and  
Applications

*Edited by Arif I. Sarwat,  
Asadullah Khalid  
and Ahmed Hasnain Jalal*

Published in London, United Kingdom

---

Smart Mobility – Recent Advances, New Perspectives and Applications

<http://dx.doi.org/10.5772/intechopen.97980>

Edited by Arif I. Sarwat, Asadullah Khalid and Ahmed Hasnain Jalal

#### Contributors

Asadullah Khalid, Arif I. Sarwat, Ahmed Hasnain Jalal, Shekhar Bhansali, Nicolae Tudoroiu, Roxana-Elena Tudoroiu, Mohamed Zaheeruddin, Sorin Mihai Radu, Micael Nascimento, Carlos Marques, João Pinto, Jay ZHAO, Scott Gayzik, Allegra Ayala, Yi-Ching Lee, Jong-Gyu Hwang, Tae-Ki An, Kyeong-Hee Kim, Chung-Gi Yu, Yunfei Hou, Montgomery Van Wart, Kimberly Collins, Ziren Zhou, Jin Xie, Yu Hou

© The Editor(s) and the Author(s) 2023

The rights of the editor(s) and the author(s) have been asserted in accordance with the Copyright, Designs and Patents Act 1988. All rights to the book as a whole are reserved by INTECHOPEN LIMITED. The book as a whole (compilation) cannot be reproduced, distributed or used for commercial or non-commercial purposes without INTECHOPEN LIMITED's written permission. Enquiries concerning the use of the book should be directed to INTECHOPEN LIMITED rights and permissions department ([permissions@intechopen.com](mailto:permissions@intechopen.com)).

Violations are liable to prosecution under the governing Copyright Law.



Individual chapters of this publication are distributed under the terms of the Creative Commons Attribution 3.0 Unported License which permits commercial use, distribution and reproduction of the individual chapters, provided the original author(s) and source publication are appropriately acknowledged. If so indicated, certain images may not be included under the Creative Commons license. In such cases users will need to obtain permission from the license holder to reproduce the material. More details and guidelines concerning content reuse and adaptation can be found at <http://www.intechopen.com/copyright-policy.html>.

#### Notice

Statements and opinions expressed in the chapters are those of the individual contributors and not necessarily those of the editors or publisher. No responsibility is accepted for the accuracy of information contained in the published chapters. The publisher assumes no responsibility for any damage or injury to persons or property arising out of the use of any materials, instructions, methods or ideas contained in the book.

First published in London, United Kingdom, 2023 by IntechOpen

IntechOpen is the global imprint of INTECHOPEN LIMITED, registered in England and Wales, registration number: 11086078, 5 Princes Gate Court, London, SW7 2QJ, United Kingdom

British Library Cataloguing-in-Publication Data

A catalogue record for this book is available from the British Library

Additional hard and PDF copies can be obtained from [orders@intechopen.com](mailto:orders@intechopen.com)

Smart Mobility – Recent Advances, New Perspectives and Applications

Edited by Arif I. Sarwat, Asadullah Khalid and Ahmed Hasnain Jalal

p. cm.

Print ISBN 978-1-80355-711-3

Online ISBN 978-1-80355-712-0

eBook (PDF) ISBN 978-1-80355-713-7

# We are IntechOpen, the world's leading publisher of Open Access books Built by scientists, for scientists

**6,400+**

Open access books available

**173,000+**

International authors and editors

**190M+**

Downloads

**156**

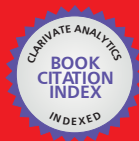
Countries delivered to

Our authors are among the  
**Top 1%**

most cited scientists

**12.2%**

Contributors from top 500 universities



**WEB OF SCIENCE™**

Selection of our books indexed in the Book Citation Index  
in Web of Science™ Core Collection (BKCI)

Interested in publishing with us?  
Contact [book.department@intechopen.com](mailto:book.department@intechopen.com)

Numbers displayed above are based on latest data collected.  
For more information visit [www.intechopen.com](http://www.intechopen.com)





# Meet the editors



Dr. Arif Sarwat has more than 20 years of experience in industry and academia. He is an Eminent Scholar Chaired Professor in the Department of Electrical and Computer Engineering, Florida International University (FIU), USA, and the director of FIU's Florida Power & Light Company Solar Research Facility. His research interests include smart grids, electric vehicles, high-penetration renewable systems, storage, and battery management systems, grid resiliency, large-scale data analysis, artificial intelligence, advanced metering infrastructure, smart city infrastructure, and cybersecurity. He has published more than 200 peer-reviewed articles and multiple patents. He is currently involved in multiple projects funded by the National Science Foundation (NSF) and the Department of Energy (DOE). This list of funded project awards includes the NSF CAREER Award. He is the co-lead of the Masters in Energy & Cybersecurity education program at Florida International University (FIU). Previously, Dr. Sarwat worked at Siemens for more than nine years, winning three recognition awards. He is the author/co-author of a publication that won the best paper award at the Resilience Week in 2017 and a technical article that won both the best paper award in 2016 as well as the most cited paper award in 2018 from the *Journal of Modern Power Systems and Clean Energy* (MPCE). His team won the second-best paper award at the 2020 Institute of Electrical and Electronics Engineers (IEEE) North American Power Symposium conference. Dr. Sarwat received the Faculty Award for Excellence in Research & Creative Activities in 2016, College of Engineering & Computing Worlds Ahead Performance in 2016, and FIU TOP Scholar Award in 2015 and 2019. He has been the chair of the IEEE Miami Section VT and Communication since 2012. He is an associate editor of the journal *ACM Computing Surveys*.



Dr. Asadullah Khalid received his BTech and MS in Electrical Engineering from the Aligarh Muslim University, India, and the Illinois Institute of Technology, USA, respectively. He obtained a Ph.D. in Electrical and Computer Engineering from Florida International University, USA. Dr. Khalid has been working in the consumer electronics and automotive industries for more than five years in different capacities. His research interests include battery management systems, microgrids, applied machine learning, and energy storage cybersecurity.



Dr. Ahmed Hasnain Jalal is an Assistant Professor in the Department of Computer Science, Utah Valley University, USA. He earned his Ph.D. and MS from Florida International University, USA, and Purdue University Northwest, USA, in 2018 and 2010, respectively. His research interests are focused on fuel cells, electrochemistry, the Internet of Things (IoT), biosensors, sensors' data analytics, and thin film fabrication. He holds multiple US patents and published over 35 articles and book chapters.



# Contents

<b>Preface</b>	<b>XI</b>
<b>Section 1</b> Sizing, Sensing and Simulation	<b>1</b>
<b>Chapter 1</b> Sizing and Lifecycle Assessment of Electrochemical Batteries for Electric Vehicles and Renewable Energy Storage Systems <i>by Arif I. Sarwat, Asadullah Khalid, Ahmed Hasnain Jalal and Shekhar Bhansali</i>	<b>3</b>
<b>Chapter 2</b> Tracking Li-Ion Batteries Using Fiber Optic Sensors <i>by Micael Nascimento, Carlos Marques and João Pinto</i>	<b>37</b>
<b>Chapter 3</b> Investigations of Using an Intelligent ANFIS Modeling Approach for a Li-Ion Battery in MATLAB Implementation: Case Study <i>by Roxana-Elena Tudoroiu, Mohammed Zaheeruddin, Nicolae Tudoroiu and Sorin Mihai Radu</i>	<b>65</b>
<b>Section 2</b> Safety and Perspectives	<b>97</b>
<b>Chapter 4</b> Halide Perovskites as Emerging Anti-Counterfeiting Materials Contribute to Smart Flow of Goods <i>by Ziren Zhou, Jin Xie and Yu Hou</i>	<b>99</b>
<b>Chapter 5</b> Accidental Injury Analysis and Protection for Automated Vehicles <i>by Jay Zhao and Francis Scott Gayzik</i>	<b>123</b>
<b>Chapter 6</b> Parent Opinions of Automated Vehicles and Young Driver Mobility <i>by Allegra Ayala and Yi-Ching Lee</i>	<b>153</b>

<b>Section 3</b>	
Mobility Needs and Cybersecurity Applications	171
<b>Chapter 7</b>	173
IoT-Based Route Guidance Technology for the Visually Impaired in Indoor Area	
<i>by Jong-Gyu Hwang, Tae-Ki An, Kyeong-Hee Kim and Chung-Gi Yu</i>	
<b>Chapter 8</b>	195
Intersection Management, Cybersecurity, and Local Government: ITS Applications, Critical Issues, and Regulatory Schemes	
<i>by Yunfei Hou, Kimberly Collins and Montgomery Van Wart</i>	

# Preface

The rapid advancement of technology has completely transformed the way we live, work, and move around. In this era of digital transformation, smart mobility has emerged as one of the most exciting and dynamic fields of study. With the increasing demand for sustainable and efficient mobility solutions, there has been a surge in research and development of various technological innovations that have the potential to revolutionize the transportation sector.

*Smart Mobility - Recent Advances, New Perspectives and Applications* focuses on the latest developments in this field and provides a comprehensive overview of the various components of smart mobility such as sizing, sensing, simulations, safety, perspectives, mobility needs, and cybersecurity applications. This book offers an in-depth analysis of these components and how they are interrelated to create innovative solutions for the future of transportation.

The book covers a wide range of topics, from the latest advances in vehicle sizing, sensing technologies, and simulations to the challenges of ensuring safety and security in smart mobility systems. The authors provide insightful perspectives on the mobility needs of the future and the role of cybersecurity in ensuring the safety and security of these systems.

This book is intended for a wide audience, including researchers, engineers, policy-makers, and students who are interested in understanding the recent advances, new perspectives, and applications of smart mobility. The authors have drawn upon their extensive experience and knowledge to provide a comprehensive overview of this rapidly evolving field and to offer practical insights and recommendations for those working in this area.

In conclusion, this book provides a comprehensive and up-to-date overview of smart mobility and its various components as well as offers new perspectives and applications that have the potential to shape the future of transportation. We hope that it will serve as a valuable resource for anyone interested in this exciting and rapidly evolving field.

**Dr. Arif I. Sarwat**  
Eminent Scholar Chaired Professor,  
Director of FPL-FIU Solar Facility and Energy, Power, Sustainability  
and Intelligence (EPSi),  
Department of Electrical and Computer Engineering,  
Florida International University,  
Miami, Florida, USA

**Dr. Asadullah Khalid**  
Postdoctoral Associate,  
Department of Electrical and Computer Engineering,  
Florida International University,  
Miami, Florida, USA

**Dr. Ahmed Hasnain Jalal**  
Assistant Professor,  
Department of Computer Science,  
Utah Valley University,  
Orem, Utah, USA

---

Section 1

# Sizing, Sensing and Simulation



## Chapter 1

# Sizing and Lifecycle Assessment of Electrochemical Batteries for Electric Vehicles and Renewable Energy Storage Systems

*Arif I. Sarwat, Asadullah Khalid, Ahmed Hasnain Jalal  
and Shekhar Bhansali*

## Abstract

Electrochemical batteries have demonstrated quality performances in reducing emissions in Electric Vehicles (EV) and Renewable Energy Storage (RES) systems. These chemistries, although most of them commercialized, contribute to ecological toxicity and global warming in their lifecycle phases. With the addition of new energy storage chemistries, sizing uncertainty and resulting environmental damage are increasing. This chapter presents a comprehensive comparative exploration of 14 electrochemical batteries, including chemistries in the research and development phase. To identify the appropriate chemistry, the capacity range sizing criteria, and formulations are presented with case studies of Environmental Protection Agency (EPA) approved driving profiles for EVs, and consumption load profiles for RES systems, dependent on a given set of operational constraints. Furthermore, a lifecycle impact assessment (LCA) metric, the Cradle-to-Gate technique, is computed to evaluate the sized storage chemistries' environmental impact supported by five case studies considering short-, medium-, and long-term duration operations and storage services.

**Keywords:** electric vehicles, renewable energy storage systems, electrochemistry, lifecycle assessment, cradle-to-gate, battery sizing

## 1. Introduction

Solar photovoltaics and wind turbines have been the least expensive ways to generate electricity, however, with the increased maintenance requirements in these systems, the demand is shifting and growing towards maintenance-free electrochemical batteries [1]. This has resulted in the development of a wide variety of secondary storage battery chemistries and this demand increase is further supported by the decrease in their prices. For instance, the Lithium-ion (Li-ion) battery, which was once one of the most expensive chemistries with prices over \$450/kWh has seen a

reduction in per-kWh prices to as low as \$200. Berckmans et al. [2] predicts the price to drop down further to less than \$150/kWh (by 2030). In order to reduce greenhouse emissions from vehicles as well as firm renewables for smart city development, a cut above storage chemistry is needed [3]. Lifecycle (impact) assessment (LCA) is a metric to evaluate the equivalent emissions and the damage an energy storage system does to the environment. As defined in ISO 14040 and 14,044, the parameters required for LCA analysis include functional unit, system boundary, impact category, and a data source. Commonly used data sources include E.U. Ecoinvent database, and U.S. GREET. Using Argonne National Laboratory's BatPaC (Battery Performance and Cost) Model. Greenhouse gas emission (GHG), Human health (HH), Ecosystem quality (EQ), Resources depletion (RD), Cumulative water use (CWU), Global warming potential (GWP), Ecotoxicity (ET), Acidification (AD), Ozone depletion (OD), Photochemical smog (PS), Eutrophication (EP), and Cumulative energy demand (CED) are the commonly used impact categories for LCA analysis in literature.

Cradle-to-gate is a standard development period that is taken as the assessment term in this study. Cradle-to-gate along with use impact is also associated and sometimes proportional to the greenhouse gas emissions, which makes it an important evaluation factor for the application-specific storage chemistry assessment [4–9]. CED is a metric to identify the environmental burden (or the lifecycle impact) imposed by a commodity's production and/or its use. This metric, in MJ/kWh, would be used to evaluate the Cradle-to-gate with use impact of selected chemistries.

A technology readiness level chart of all 14 EV and RES (galvanic) electrochemical batteries discussed in this paper is shown in **Figure 1**. This gives an idea of the chemistries which had the potential of going through numerous research and development iterations. For instance, the Lead Acid (Pb-Acid) chemistry has had over 160 years since its discovery in 1859 to go through ameliorations. Charge holding capacity, time duration, and degradation abridging potential are the crucial appraising factors that have been improved upon for every other storage chemistry that is currently commercialized [10, 11]. Further study on improvement and discussions of these key topics are presented in the following sections. Section 2 discusses the electrochemical redox performance of these 14 chemistries and suggests the applicable upside and downside to their designs and developments. Section 3 provides mathematical formulations and results for sizing a battery, taking into consideration a case study of a 2000Kg EV as well as another case study of a hospital and a primary school's loads in Miami, Florida. Section 4 presents the Cradle-to-gate model for LCA of the sized battery chemistries for the EV, hospital, and primary school taking into consideration their electrochemical performance values as well. Section 5 concludes the paper with a scope for future work.

The key contributions of the paper are that it: (1) Provides a comprehensive technical categorization of batteries based on their electro-chemistry; (2) Provides energy storage sizing criteria and formulations for EV and RES systems; (3) Evaluates chemistry- and application-specific lifecycle performance of EV and RES batteries using cradle-to-gate method based formulations.

## **2. Battery electrochemistry performances evaluation**

Specifications comparison is a major preliminary requirement for a battery to be implemented for any defined application [12]. This section discusses the performance,

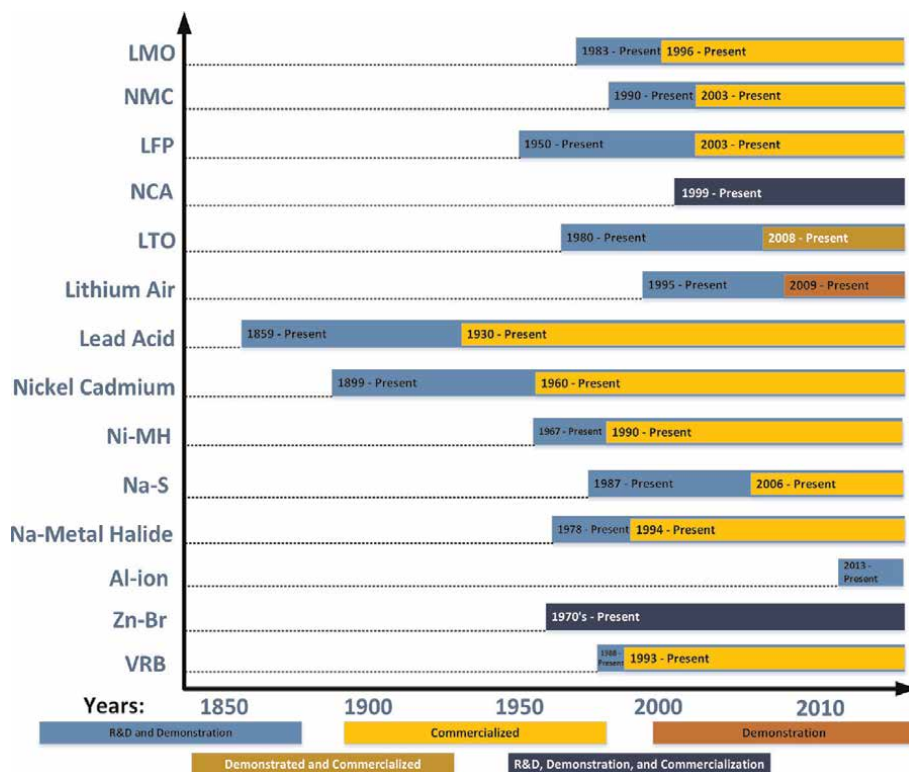


**Figure 1.**  
 Technology readiness levels of EV and RES electrochemical batteries.

internal electrochemical phenomenon details, and redox reactions of the 14 EV and RES chemistries analyzed in **Figure 1**. The effect of Depth-of-Discharge (DOD%) on separate chemistries is also studied in this section, which is an important factor for the case studies discussed in Section 4.

## 2.1 Lithium based batteries

Lithium is a highly researched cell chemistry because of its high specific energy, high cycle life, low self-discharge, and high nominal voltage [13–20]. It supersedes other chemistries such as Lead-acid, Nickel Cadmium (Ni-Cd), and Nickel Metal Hydride (Ni-MH) in almost every category except in over charge and over discharge situations [21]. This sub-section compares and evaluates various commercially available and under development Li-ion chemistries used in EVs and RES systems. Common Lithium chemistries categorized by their properties, composition, along with their possible uses are listed in **Table 1**.

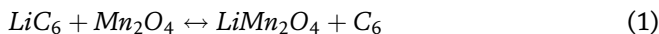
Lithium Manganese Oxide (LMO or  $LiMn_2O_4$ ) has a spinel structure with a nominal voltage of 3.8 V (Eq. 1) [43, 44]. Its low cost and high thermal stability are attributable to the addition of Manganese. Manganese is cheap and low in toxicity, but does not have a high specific energy. This has led to the development of the Lithium Nickel Manganese Cobalt Oxide (NMC or  $LiNiMnCoO_2$ ) chemistry. NMC type lithium cells are created through the addition of Nickel [43, 44]. Nickel, on its own,

	Lithium Manganese Oxide (LMO) [22–28]	Lithium Nickel Manganese Cobalt Oxide (NMC) [22, 23, 25, 27, 29–31]	Lithium Iron Phosphate (LFP) [22, 23, 25, 27, 30, 32, 33]	Lithium Nickel Cobalt Aluminum Oxide (NCA) [22, 23, 25, 27, 30, 34]	Lithium Titanate (LTO) [22, 23, 25, 26, 31, 35, 36]	Lithium Air ( $LiO_2$ ) [37–40]
Anode	Graphite	Graphite	Graphite	Graphite	LTO	Lithium
Cathode	Lithium Nickel Manganese Spinel	NMC	LFP	NCA	LMO or NMC	Porous Air
Electrolyte	$LiPF_6$ in organic solution <sup>†</sup>	$LiPF_6$ in organic solution <sup>†</sup>	$LiPF_6$ in organic solution <sup>†</sup>	$LiPF_6$ in organic solution <sup>†</sup>	$LiPF_6$ in organic solution <sup>†</sup>	Hybrid*
Specific Energy (Wh/Kg)	100–150	150–220	90–120	~ 280	50–80	5200*
Specific Power (W/Kg)	110–340	110–340	200–1200	110–340	3000–5100	0.46*
Safety (Thermal Stability)	++	+	+++	—	+++	++
Nominal voltage	3.8 V	3.6 V	3.3 V	3.6 V	2.2 V	2.9 V
Charging voltage	4.2 V	4.2 V	3.6 V	4.2 V	2.8 V	3.3 V
Cycle Life	300–700	2000–6000	2000–2010,000	500–1000	3000–7000	~ 2000*
Discharge curve	Flat	Sloping	Flat	Sloping	Sloping	Flat
Cost (\$/kWh)	Low	Medium	Low	High	Very High	N/A*
Applications	EV, HEV, PHEV, RES	EV, HEV, PHEV, RES		EV, HEV, PHEV, UPS, RES	HEV, RES	Aviation*, EV*
Form Factor	Coin, Cylindrical, Prismatic, Pouch	Cylindrical, Prismatic, Pouch	Cylindrical, Prismatic, Pouch	Cylindrical, Prismatic, Pouch	Cylindrical, Prismatic, Pouch	N/A*
Technology Readiness Level	R&D, Dem., Com.	R&D, Dem., Com.	R&D, Dem., Com.	R&D, Dem., Com.	R&D, Dem., Com.	R&D

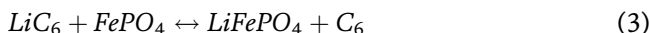
Labels: Poor (–), Good (+), Very Good (++), Excellent (+++).  
 RES: Renewable Energy Storage; EV: Electric Vehicles; HEV: Hybrid Electric Vehicles; R&D: Research and Development; Dem.: Demonstration Stage; Com.: Commercialized.  
 \*as per [41, 42], still undergoing R&D.  
<sup>†</sup>Manufacturer dependent. Standard organic solution is ethylene carbonate (EC)–dimethyl carbonate (DMC) mixture.

**Table 1.** Lithium based batteries comparison based on their electro-chemistries.

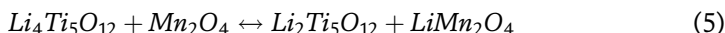
provides high energy density but lower thermal stability, therefore Manganese is added to create a more stable chemistry (in NMC) that increases cycle life and stability (Eq. 2) [45].



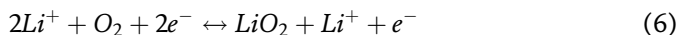
Lithium Iron Phosphate (LFP or  $LiFePO_4$ ) batteries, on the other hand, have improved safety and thermal stability due to the addition of Iron that creates the olivine structure (Eq. 3) [43, 44]. Subsequently, these cells can operate at higher temperatures effectively, however, their specific energy tends to be lower than that of other lithium chemistries, especially Nickel Cobalt Aluminum Oxide (NCA or  $LiNiCoAlO_2$ ) [45, 46]. NCA has a high specific energy and lower thermal stability, both owing to the addition of Nickel [45, 47]. Aluminum present in NCA creates a similar layered crystal structure like in NMC (Eq. 4) [43, 44]. Comparison between LFP, NMC, and NCA in [48] showed that an increasing SOC % increases the temperature of LFP by around 0.8°C per SOC value. The corresponding values for NMC and NCA increase by 1.02°C, and 1.74°C per SOC % respectively. The NCA lithium battery has twice the potential to catch fire if overcharged, when compared to LFP. This further emphasizes the importance in selection of correct lithium chemistries and in general, an effective battery management system for EV and RES applications.



Lithium Titanate (LTO or  $Li_4Ti_5O_{12}$ ) has a low specific energy and high cost (Eq. 5) [43]. In addition, its nominal voltage is very low. An EV or RES manufacturer would need to practically double the number of cells in series to reach the same voltage as the NMC/NCA/LMO chemistries. This will greatly increase the cost and weight of the vehicle and decrease the amount of usable space. These batteries also contain a unique anode composed of LTO which drastically increases its thermal stability and cycle life when compared to other Lithium chemistries. The improved safety/lifespan of LTO can be attributed to the limited expansion of the anode (only 0.2% of volume changes) during charge/discharge operation [45].



Combination of phenomena of Lithium oxidation at the anode, and oxygen reduction at the cathode, using electrolytes ranging from solid state, to aqueous, non-aqueous, or aprotic solvent variants, results in the formation of the Lithium Air ( $LiO_2$ ) battery. This anode and cathode pair creates a practical specific energy of 18.7 MJ/Kg, which is about 10–15 times higher than that of a commercially available Li-ion battery [49]. Oxygen molecules entering cathode through the porous cathode react with  $Li^+$  ions moving from the anode via an electrolyte, to form Lithium Peroxide ( $Li_2O_2$ ) while the electrons flow through the external load during a discharge operation, constituting the redox reaction shown in Eq. (6).



$LiO_2$  batteries can operate effectively at temperatures up to 140°C [50]. They are still under development mainly due to their varying performances with changing electrolytes.  $LiO_2$  started off as an accidental discovery by K. M. Abraham in 1995 while using a non-aqueous electrolyte [51] however deposition of  $Li_2O_2$  on the cathode

electrode with time called for more exploratory research. Liu et al. [52] in 2015 proposed the addition of lithium iodide and water to make the electrodes spongy along with a hybrid (combination of solid state and aqueous) electrolyte, thereby resulting in Lithium Hydroxide crystals which do not coat the surface and impede the flow of electrons, allowing continuous voltage supply. Although this research improves the operational lifetime of the battery, it reduces the overall specific energy due to the inclusion of water.

NCA, LTO, and NMC have sloping discharge curves while LMO, LFP, and  $LiO_2$  have flat discharge curves (**Table 1**). Understanding charge/discharge characteristics of each chemistry is important when selecting a cell to be tested for an application. Generally, the sloping discharge curve reduces the complexity in model selection since the voltage level decreases almost proportionally with SOC%.

The ease with which the electrochemical reaction will occur depends on the ionic/electrical conductivities. Lower conductivities will result in greater resistance and lower efficiency in the conversion from chemical to electrical energy. These values heavily depend on the central testing conditions [17]. Furthermore, for the electrolyte, the ionic conductivity is an important consideration with high conductivity being ideal. During charge and discharge cycles, Lithium ions are shuttled across the electrolyte to the anode and cathode, respectively. Decreased resistance from Lithium ions traversing from anode to cathode and vice versa will mean less heat generation and increased efficiency of the cell [53–56].

Every Lithium chemistry eventually degrades over time from a variety of factors. Solid electrolyte interphase (SEI) development is one of the main contributing factors to degradation. The formation of this layer is important because it allows Li-ion transportation but prevents electrons from moving through resulting in further decomposition of the electrolyte [57].

In addition to charging or discharging operations, factors like storage and thermal conditions also play a major role in SEI formation. The authors in [58] show that the capacity of batteries being stored drastically declines with the increase in temperature. Lithium batteries have a good shelf life but are still prone to losing capacity if stored for an extended period. Increased depth of discharge (DOD) also decreases the cycle life of the cell. Data from [59] shows that discharging the cell too deeply will greatly impact its capacity after many cycles. After 25,000 cycles, a cell discharged at a consistent 30% DOD lost 53% of its capacity, while a cell discharged at 20% DOD lost 40% percent of its capacity with both being at 20°C. Based on these findings, it can be concluded that DOD has a substantial effect on the cycle life of a Lithium-ion battery. Moreover, a decrease in the cell's capacity over many cycles caused by the aforementioned conditions leads to internal issues that are reflected in the cell's available capacity. Some examples are Lithium plating at the anode from high charge current, SEI formation on the anode from electrolyte decomposition due to high temperature/DoD, and volume changes on the anode and cathode due to all of the above stated conditions [60]. Other additional comparative features of the discussed Lithium based chemistries are tabulated in **Table 1**.

## 2.2 Pb-acid based batteries

Physicist Gaston Plante invented the Pb-acid based battery, which is comprised of lead dioxide ( $PbO_2$ ) as the anode, lead (Pb) plate as the cathode, and aqueous sulfuric acid ( $H_2SO_4$ ) as the electrolyte. The reaction mechanism of these batteries relies on

oxidation (on the anode) and reduction (on cathode) reactions and follows the redox reaction shown in Eq. (7):



The electrical turnaround efficiency of these batteries is 75–80% with specific energy ranging between 30 and 50 Wh/kg [61], which is much lower than other EV or RES battery chemistries. Also, the cycle life of these batteries is comparatively short (< 2000 cycles) [62]. Sulfation is one of the major causes of this lower cycle life, which impedes recharging and causes cracking into the electrode plate [63]. This incident causes inadequate charging during regular operation due to amorphous lead sulfate deposits on the negative electrode, which turns into a crystalline structure in a progression. Consequently, the active materials of the negative electrode are covered with this additional layer. This issue can be resolved by integrating the high content of carbon into the lead electrode, which promotes the self-recharging rate and cycle life [63]. The formation of the carbon-Pb alloy accelerates water loss and inner pressure due to the hydrogen evolution reaction [64, 65]. This reaction mechanism involves either absorption or desorption of the intermediate hydrogen by the electrode surface in two separate routes termed as the Volmer-Tafel and Volmer-Heyrovsky mechanisms [66, 67]. The activated carbon doped with heteroatoms (e.g., N, P, B, or S) in the graphene ring improve the charge acceptance and charge retention ability of the Pb-acid based battery and inhibits the hydrogen evolution reaction. Also, Pb-acid requires an additional mandatory thermal management system for reliable temperature efficiency. Moreover, they are bulky in weight, require prolonged charging time and cyclic water maintenance, and suffer from premature failure and degradation at high power operation. However, on the upside, these batteries are cost-effective (in manufacturing and maintenance) and easily recyclable ( $\geq 97\%$  recycling efficiency) [68]. Additionally, their charge retention capability is compatible with both grid and automotive applications. For obtaining the required power/energy ratings, an array of Pb-acid battery cells are connected in such a way that each cell voltage and range of charging rate are 2.15 V and 0.25–4, respectively [69]. Pb-acid batteries are mostly employed as a backup power supply in the range of kW to tens of MWs for grid utilities and hybrid electric vehicles. All the comparative features of this chemistry are tabulated in **Table 2**.

### 2.3 Ni-based batteries

Ni-based batteries are classified into two broad categories: Ni-Cd based batteries, and Ni-MH based batteries. Generally, nickel oxyhydroxide is used as the anode, and Cd or MH, are employed as the cathode. The electrolyte is an aqueous alkaline solution, such as aqueous potassium hydroxide (KOH), used for both Ni-MH and Ni-Cd based batteries. Zn, Fe, or  $H_2$ -based Ni batteries are also used in the applications tabulated in **Table 2**.

Compared with Ni-Cd or Ni-MH based batteries, these Ni-based chemistries have limitations in terms of energy density (low), efficiency (low), maintenance cost (high), lifecycle (low), and self-discharging issues [92]. Contrarily, Ni-Cd performs with 70–90% efficiency, has moderate energy density (50–75 Wh/kg), higher lifecycles (2000–2500), a 10%/month self-discharging rate, and better temperature tolerances [69, 93, 94]. However, both the Cd and Ni chemistries are considered as hazardous substances, and the manufacturing costs of Ni-Cd batteries are also

	Pb-Acid [12, 64, 70, 71]	Ni-Cd [12, 70, 71]	Ni-MH [12, 70, 71]	Na-S [71-75]	Na Metal Halide [76-80]	Al-ion [81-85]	Zn-Br [12, 86-90]	VRB [12, 91]
Anode	PbO <sub>2</sub>	Ni(OH) <sub>2</sub>	Ni(OH) <sub>2</sub>	Na	Na	Al	Carbon Polymer Composites	Carbon Polymer Composites
Cathode	Pb-plate	Cd	Metal Hydrides	S	Porous Transition Metal	Graphite	Carbon Polymer Composites	Carbon Polymer Composites
Electrolyte	Aqueous H <sub>2</sub> SO <sub>4</sub>	KOH	KOH	$\beta$ - Al <sub>2</sub> O <sub>3</sub>	$\beta$ - Al <sub>2</sub> O <sub>3</sub>	1-ethyl-3methylimidazolium chloride*	Zinc Bromide	Vanadium Pentoxide + Sulfuric Acid
Specific Energy (Wh/Kg)	30-50	50-75	40-110	150-240	120-240	40*	75-85	35
Specific Power (W/Kg)	180	150-300	250-1000	90-230	150-230	3000*	90-110	805
Safety (Thermal Stability)	+	+	+	-	+	++	++	++
Nominal voltage / OCP	2 V	1.2 V	1.2 V	2-2.5 V	2.58 V (Ni), 2.33 V (Fe)	2 V*	1.8-1.85 V	1.15 V
Charging voltage	2.15 V	1.55 V	1.6 V	2.67 V	2.67-2.85 V	0.5-2.45 V*	2 V*	1.6 V
Cycle Life	< 2000	2000 to 5000	~ 3000	2500-4500	300-500	7500*	> 2000	12,000-20,000
Discharge curve	Flat	Flat	Flat	Sloping	Flat	Variable*	Flat	Sloping
Cost (\$/kWh)	Low	Medium	Very High	Medium	High	N/A*	Medium	Low
Applications	RES, EV, Industrial	Military, Aviation, EV, RES	RES, EV	RES	RES, EV, HEV, Railways	RES	RES, EV*	RES
Form Factor	Coin, Cylindrical, Prismatic, Pouch	Coin, Cylindrical, Prismatic, Pouch	Coin, Cylindrical, Prismatic, Pouch	Cylindrical	Cylindrical, Prismatic	N/A*	Tank Storage	Tank Storage
Technology Readiness Level	R&D, Dem., Com.	R&D, Dem., Com.	R&D, Dem., Com.	R&D, Dem.	R&D, Dem., Com.	R&D	R&D, Dem., Com.	R&D, Dem., Com.

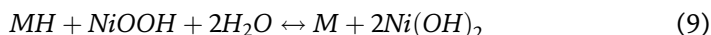
Labels: Poor (-), Good (+), Very Good (++)  
 RES: Renewable Energy Storage; EV: Electric Vehicles; HEV: Hybrid Electric Vehicles; R&D: Research and Development; Dem.: Commercialized.  
 \*Still undergoing R&D.

**Table 2.**  
 Pb, Ni, Na, Al-based and redox batteries comparison based on their electro-chemistries.

relatively high (\$1000/kWh and ten times higher than Pb-acid based batteries). The electrodes, electrolyte, and separator (insulator between anode and cathode) are placed in a low cost and flame-retardant polymer (e.g., polypropylene, polystyrene) container for these batteries. The redox reaction for Ni-Cd based batteries is shown by Eq. (8).



Ni-MH batteries are the other category which is commercially established for the uninterrupted power supply in different applications, such as grid systems, hybrid electric vehicles, and communication systems. Different metal hydrides and Nickel hydroxide (NiOOH) are employed as the anode and cathode, respectively [73]. The overall charging and discharging reaction mechanism in Ni-MH based batteries follows Eq. (9):



Both the anode and cathode are porous in structure. Therefore, they have a large surface area, which enhances the rate of reaction and internal conductivity. Hence, their energy density (40–110 Wh/kg) is higher than Ni-Cd based batteries. Additionally, this battery system is environmentally benign, has high charging and discharging tolerance, longer shelf, cycle life (~3000 cycles) and can operate in a wide temperature range (30–70°C). However, both above-mentioned Ni-based chemistries suffer from the “memory effect”, which happens due to incomplete discharges in preceding uses. Consequently, the energy capacity and rated output potential abruptly deteriorate leading to another effect termed as the “voltage depression effect” [95]. However, this effect can be mitigated by proper charging-discharging management of the battery systems. All the comparative features of both of these chemistries are also tabulated in **Table 2**.

## 2.4 Na-β based batteries

Following chemical composition and reaction mechanisms, Na-β based batteries are classified into the following two types: Sodium-sulfur (Na-S) and sodium-metal halide. A tubular-shaped beta-alumina ( $\beta Al_2O_3$ ) ceramic is employed as an electrolyte, which acts as a superionic conductor and a separator (between the anode and cathode) simultaneously. All these materials are naturally abundant and inexpensive. In Na-S based batteries, both the cathode (S) and anode (Na) are in molten form. Due to oxidation,  $Na^+$  ions are generated at the cathode, which are carried by the  $\beta$ -alumina based solid electrolyte. Later, these ions recombine at the anode and vice versa for the reduction reaction. The overall redox reaction for this chemistry is shown in Eq. (10).



Their energy density and self-discharging rate fall in the range of 140–240 Wh/kg and 1% respectively [96, 97]. Additionally, these batteries have a short response time (1 ms), higher energy efficiency (75–90%), and good recyclability (99%) [69]. At 100% DOD, their lifecycle is around 2500, whereas it increases to 4500 by dropping DOD to 80% [97]. Moreover, this battery system has shown efficient results and is capable of voltage stability (short duration), peak shaving (medium duration), and

load leveling (long duration) grid service requests. These batteries operate at 300–350°C in a thermal enclosure and have a significant tolerance for running in both cold and hot temperatures. However, the operation in a high temperature promotes corrosion and explosion. Hence, this battery system requires a mandatory thermal management system. In September 2011, a 2000 kW – NaS-based battery system from NGK, consisting of 40 battery modules, exploded at Tsukuba in Japan [98]. Another fire incident occurred in a 30-megawatt Kahuku wind farm in Hawaii [99]. Apart from reasons related to other interconnected components, the main reason on the battery side was that one of the faulty cells was ignited by inundating the molten materials over the filler portion of the blocks and was causing a short between the cells.

The other sodium-based chemistry, Sodium metal halide ( $Na - MeCl_2$ ) is another alternative and promising battery for the next generation stationary energy storage systems. They have compatible features, which include reliability, resiliency, and higher roundtrip efficiency. The anode and electrolyte of this battery is similar to the Na-S based batteries. However, the cathode is made from a porous transition metal (Ni or Fe) halide matrix infused by an additional secondary electrolyte, sodium tetrachloro-aluminate ( $NaAlCl_4$ ). This inorganic electrolyte provides higher ionic conductivity and superior battery safety [100]. The transport mechanism of the  $Na^+$  ions through  $\beta-Al_2O_3$  and  $NaAlCl_4$  are reversible for the charging-discharging processes. The reaction mechanism between pyrophoric metal (Na) and hygroscopic metal halides is as shown in Eq. (11), where ‘Me’ stands for Ni or Fe metals.



The theoretical specific energies for Ni and Fe are as high as 788 Wh/kg and 729 Wh/kg respectively. However, the energy density of these batteries lies between 120 and 240 Wh/kg [100, 101]. These batteries can operate over 20 kWh which indicates that they are strong candidates for EV and RES applications. There is no self-discharge (that is, a coulombic efficiency of 100%) occurrence in this battery, and their cycle life is over 1000 at 100% DOD. Additionally, these batteries are corrosion-protective and can operate in the lower resistive cell-failure mode with better charging/discharging tolerance, which ensures higher safety than that of the Na-S battery system. However, their high manufacturing cost, intricate cell architecture, high operating temperature (300–350°C), and performance deterioration with cycling are still a constraint [102, 103]. The high operating temperature is the cause of the high corrosion rate. A high-cost hermetic sealing is essential in this system to prevent this corrosion of the materials and degradation of the performances at high temperatures. All of the comparative features of this chemistry are also tabulated in **Table 2**.

## 2.5 Aluminum-ion (Al-ion) batteries

In the past few years, Al-ion batteries are considered as one of the promising categories of rechargeable batteries for electric vehicles, renewable energy, and mobile devices. Aluminum, being an abundant material, makes these batteries reasonably accessible with low price in comparison with Li-ion batteries (Lithium is only 0.0065 wt% of the earth’s crust) [82, 104, 105]. Lin et al. (Dai group) from Stanford University reported the first paper on such kind of batteries, which consist of aluminum as the anode, an aqueous ionic electrolyte from vacuum dried  $AlCl_3/1$ -ethyl-3-methylimidazolium chloride, and graphite as the cathode [83]. The charging and

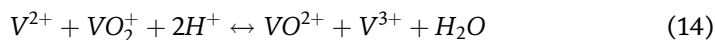
discharging mechanisms of these batteries rely on the electrochemical deposition/dissolution of Al at the anodic electrode and the intercalation/deintercalation of chlor-aluminate ions ( $AlCl_4^-$ ) in the cathodic electrode based on the reactions shown in Eq. (12) and (13).



The nominal voltage obtained from this reaction is around 2 V, and the coulombic efficiency was as high as 98% [105]. These batteries can maintain their lifecycle at around 7500 without compromising significant power density (specific power). Their maximum specific energy and power were obtained to be 3000 Wh/kg and 40 Wh/kg respectively [83]. Moreover, they have a superior recharging ability (1.1 – 60s, with a specific capacity in the range of 60–110 mAh/g) due to their active electrode kinetics and reduced polarization effect. This chemistry is new and still in the research phase. All the comparative features of this chemistry are also tabulated in **Table 2**.

## 2.6 Flow batteries

In Vanadium Redox batteries (VRB), Vanadium-anolyte and –catholyte half cells are stored in electrolyte tanks which allow flow through the adjacent half cells and are separated by an ion exchange membrane. During the charge process, Vanadium ions catholyte half-cell,  $V^{3+}$  are converted into  $V^{2+}$  resulting in an electron attracted by the positive electrode (cathode) and hydronium ( $H^+$ ) which diffuses into the anode half-cell via the membrane. At the anolyte half-cell, the electron from the cathode (via the external load) converts existing  $VO_2^+$  in anode to  $VO^{2+}$  thereby balancing (with  $H^+$  ion) and storing the chemical energy. During discharge process, the stored chemicals start feeding the external load. During this process, the  $VO_2^+$  ion is oxidized to  $VO^{2+}$  releasing the hydronium ion and the process continues until the anode contains  $V^{3+}$  ion and is completely discharged. The applicable redox reaction is shown in Eq. (14) [106].



Although VRB's have long cycle life and high energy efficiency, they constitute only 30% of the energy storage market share [107]. This is mainly because of its limitations which include high form factor, low volumetric energy storage capacity, expensive ion exchange membrane, and low specific energy in comparison to Li-ion, which constitutes 60% of market share [108].

Another redox flow chemistry used in renewable energy storage, Zinc bromine (Zn-Br) batteries, categorized as hybrid redox flow batteries, include carbon-polymer composites as electrodes isolated by microporous polyolefin membrane (separator). One of these electrodes is submerged into the aqueous solution of zinc bromide as the anolyte. The catholyte comprises of two aqueous phases: a solution of Zn-Br at the top layer and dense bromine in the form of a complex organic solution at the bottom [109]. Aqueous zinc bromide is converted into metallic zinc through the electrolyzation process during charging, and the zinc bromide salt is altered back from Zn and bromine during the discharging process. The applicable redox reaction is shown in Eq. (15).



The bromine is expelled during this process and is poisonous, highly oxidative, and less soluble in water. Hence, an additional compound, organic amine, is added to dissolve it in the solution as viscous bromine adduct oil. Additionally, Zn also tends to deposit on the electrode during charging in the form of a dendrite crystal structure with a high current density, which may cause short circuits through the polyolefin membrane [110]. The surface morphology of this electroplated Zn is determined by the current density, temperature of the solution, and the flow velocity [111]. Hence, the overall capacity of energy storage in this battery system relies on the electrolyzation process and the surface area of the electrode, that is, the stacks size and the volume of the electrolyte storage reservoirs. Therefore, the energy ratings of these batteries are not entirely distinct. This battery system requires an obligatory temperature (below 50°C) and oxidation control system for safety, which makes it expensive [112]. The energy density (75–85 Wh/kg), efficiency (65–75%), and cycle life (>2000 cycles) of this battery vary within a moderate range [113]. Some significant advantages of these batteries are their flexibility in ambient-temperature operation, compatible power density in RES and EV applications, fast charging capability, and 100% DOD without any damage to the battery system [11, 89]. All of the comparative features of both of these chemistries are also tabulated in **Table 2**.

### 3. Stationary and In-motion energy storage systems application-specific sizing

#### 3.1 Electric vehicle storage application-specific sizing

Due to widespread use of EVs, standards and regulations have been developed by various regulatory bodies [114]. These regulations include EPA certified driving patterns which permit the minimum permissible operational boundaries for an EV [115]. Four such EPA certified driving patterns are used as the criterion for EV storage sizing in this section. The Federal Test Procedure (FTP) version 75 defined by EPA as a test cycle for emission certification of light duty vehicles is a mandatory test procedure designed to identify the fuel economy performance of new vehicles. It consists of complex driving phases including a cold start phase until 505 seconds, a stabilized phase between 506 and 1375 seconds, and a hot start phase from 1376-1874 seconds. This test represents a transient driving cycle with an average speed of 9.47 meter/second (21.2 miles/hour). The second profile, the Highway Fuel Economy Driving Schedule (HWFET) test cycle, defines certification and performance requirements for driving conditions on a highway. The average speed in this cycle is 21.59 meter/second (48.3 miles per hour). The third profile, the New York City Cycle (NYCC) test cycle, defines stop-and-go traffic driving constraints to assess the vehicle. The average speed in this cycle is 21.62 meter/second (48.37 miles per hour).

For EV certification applications, each of these tests assess vehicle performance, battery state, and energy consumption to simulate the vehicle model prior to production. The velocity versus time plots of each cycle (plotted in **Figure 2** and data for which is obtained from [116]) represent how a vehicle travels under different terrains and conditions, satisfying the minimum EPA requirements.

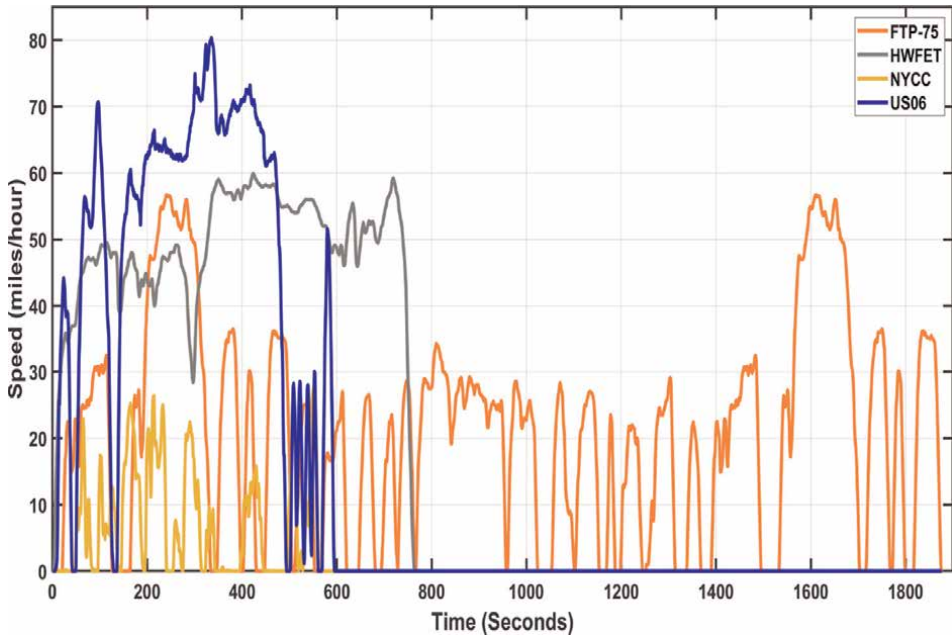


**Figure 2.**  
 Standard EPA driving profile plots.

**Table 3** shows a sizing case study listing applicable values for a 2000 Kg (4409 lbs) EV. The set of equations used for computing the minimum and maximum battery capacity for the EV are shown in Eq. (16).

$$E_{max(or\ min)} = P_b * \delta_{max\ (or\ min)},$$

$$P_b = \frac{\text{Power required by wheels}}{\eta_t * \eta_d} + \frac{P_{acc}}{\eta_a},$$

$$\text{Power required by wheels} = 9.8 * V(r_t + r_w + r_g + 1.1 * r_a),$$

$$r_t = \frac{w}{65} * (1 + 4.68 * 10^{-3} * V + 1.3 * 10^{-4} * V^2), \quad (16)$$

$$r_w = \frac{\rho_a}{g} * \frac{V^2}{2} * (C_d * \lambda),$$

$$r_g = w * \text{Sin}\theta,$$

$$r_a = \frac{w}{g} * \frac{d(V)}{dt},$$

where, gravitational acceleration ( $g$ ) =  $9.8\ m/s^2$ , and air density ( $\rho_a$ ) =  $1.225\ Kg/m^3$ . Weight of the battery is generally  $\leq 30\%$  of vehicle weight. In this case, the velocity averages are identified from the above-mentioned standard driving cycles. The velocity differentials are calculated by building the linear trend-line equations for each of the driving cycles, as shown in Eq. (17). The parameters:  $\theta$ ,  $C_d$ ,  $\lambda$ ,  $\eta_a$ ,  $\eta_d$ ,  $\eta_t$ , and  $P_{acc}$  values are assumed averages from currently commercialized vehicles' testing

$w$	$V$	$\theta$	$C_d$	$\lambda$	$\eta_a$	$\eta_d$	$\eta_t$	$P_c$	$\frac{d(V)}{dt}$	$r_a$	$r_g$	$r_w$	$r_t$	$P_b$	$\delta$ range	$E_{min}$	$E_{max}$
FTP-75 Driving Cycle																	
20	9.47	2	0.2	0.8	0.9	0.9	0.9	6	0.0002	-7.4	1826	1.1	32.4	181.46	0.03-0.5	5.4	91.13
HWFET Driving Cycle																	
20	21.59	2	0.2	0.8	0.9	0.9	0.9	6	0.0166	-7.4	1826	5.7	35.7	415.31	0.03-0.5	12.5	209
NYCC Driving Cycle																	
20	3.17	2	0.2	0.8	0.9	0.9	0.9	6	0.0007	-7.4	1826	0.1	31.2	60.7	0.03-0.5	1.8	30.49
US06 Driving Cycle																	
20	21.62	2	0.2	0.8	0.9	0.9	0.9	6	-0.069	-0.4	1826	5.8	35.7	415.89	0.03-0.5	12.4	207.12

$w$ : EV Gross Weight (in kg);  $V$ : Average Driving Cycle Velocity (in m/s);  $\theta$ : Angle of Inclination of the Terrain;  $C_d$ : Air Drag Coefficient;  $\lambda$ : Frontal Area of Vehicles (in  $m^2$ );  $\eta_a$ : Electrical Efficiency of Accessories;  $\eta_d$ : Electrical Efficiency of Drive-train;  $\eta_t$ : Mechanical Efficiency of Transmissions;  $P_{acc}$ : Power required by accessories (in Watts);  $r_a$ : Acceleration Resistance (in Newtons);  $r_g$ : Gravitational Resistance (in Newtons);  $r_w$ : Wind Resistance (in Newtons);  $r_t$ : Rolling Resistance of tires (in Newtons);  $P_b$ : Battery Power (in kW);  $\delta$  range: Common commercialized batteries;  $E_{min}$ : Minimum Battery Capacity (in kWh);  $E_{max}$ : Maximum Battery Capacity (in kWh).

**Table 3.** Battery storage capacity range identification using driving cycles, for a 2000 kg (4409 lbs) vehicle.

specifications where variations in these values do not create a major change in the resulting battery capacity size. The key parameter is  $w$ , in which a minor change largely varies the battery capacity size range for the respective driving schedules.

$$\begin{aligned} \text{FTP} - 75 : V &= 0.0002t + 20.995, \\ \text{HWFET} : V &= 0.0166t + 42.052, \\ \text{NYCC} : V &= 0.0007t + 7.3611, \\ \text{US06} : V &= -0.0069t + 50.594 \end{aligned} \tag{17}$$

The resulting average energy (battery capacity) is 105 kWh, that is the average of the lowest (1.83 kWh) and the highest (207.12 kWh) values. In terms of current commercially available and EPA certified vehicles, a 2020 Nissan Leaf (3946 lbs., 62 kWh), or a 2012 Tesla Model S (4,323 lbs., 100kWh) fall within this weight - battery capacity range combination.

### 3.2 Renewable energy storage application-specific sizing

The electricity load profile analysis method termed as load summation method is used for computing the RES battery based on average and peak load calculations [117, 118]. In the average load calculation method, the average of the sum of hourly consumptions of the facility is taken into consideration which is mainly performed to define sizes for storage systems used for contingency planning or for operating limited-power (set of) equipment. The peak load calculation uses the peak of hourly consumptions of the facility to design a storage system which is capable of operating all the equipment for a defined period of time. In this case, hourly load profiles of a primary school and a hospital, both located in Miami, Florida for the year 2004 is obtained from [119, 120], corresponding plots for which are shown in **Figures 3** and **4** respectively.

The reason for the selection of the two datasets is the extremity in load profile variations and the frequency of variations. The sizing equations used for the analyses

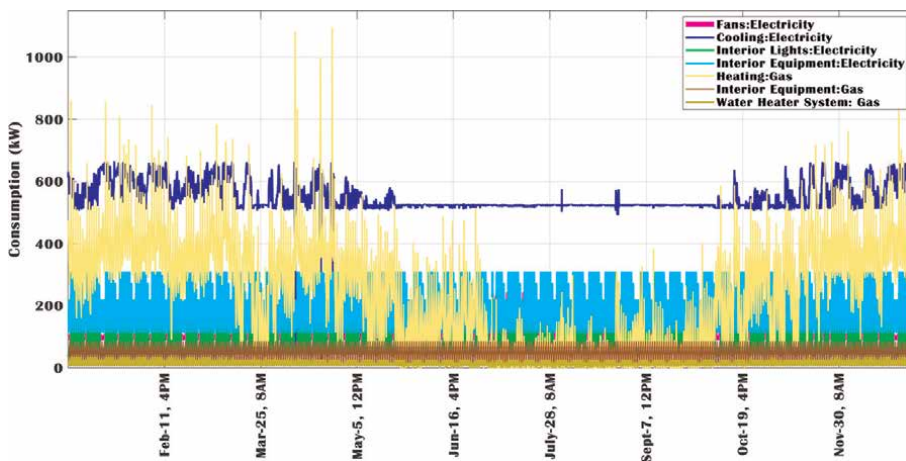


**Figure 3.**  
 Load profile of a Hospital in Miami, Florida for the year 2004.

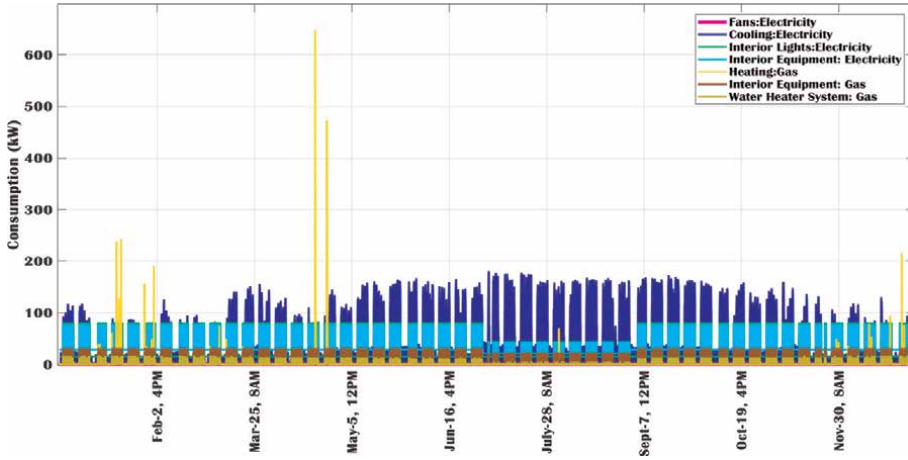


**Figure 4.** Load profile of a primary School in Miami, Florida for the year 2004.

methods are shown in Eq. (18) for  $E_{max(or\ min)}$  (that is, the corresponding capacity range, in MWh) computation. Load factor is an energy consumption characteristic indicator comparing the actual energy used within a defined period with the energy usage if a peak demand occurs during the same period [121]. Here, the load factor is the ratio of the total yearly consumption and the yearly peak demand in the 365 days' time period for 24 hours/day.

The resulting load factor values for the primary school and hospital are 0.213 and 1.18 respectively. The de-rating factor is the expected deviation in battery parameters under defined conditions. There are no defined de-rating guidelines developed for interconnected batteries as the external controller (or a battery management system) provides the operational set points and limits [122]. Hence, it is assumed that the C-rate is fixed for the battery and the de-rating factor is not taken into consideration. Load growth factor is used to take into account the future facility expansion and corresponding growths in electrical loads that can be handled by the existing energy storage system size. Excess load growths beyond the storage system size addressing capability would need to be independent of the battery and be supplied by a separate feeder or a lateral. In this case, this factor is assumed to be 1, which means that the estimated load growth is twice the existing load.

$$E_{max(or\ min)} = P_b * Operating\ Hours, \quad (18)$$

$$\text{where, } P_b = \frac{\text{Average or Peak Demand (kW) of (Motor + Non - Motor Loads)}}{\text{Load Factor} * \text{De - rating Factor} * \text{Load Growth Factor}},$$

$$\text{Load Factor} = \frac{\text{Total Consumption in a selected period (kWh)}}{\text{Peak Demand (kW)} * \text{Days in the selected period} * \text{Hours/Day in the selected period}},$$

$$\text{Load Growth Factor} = \frac{\text{Estimated Consumption (kWh) in the following year} - \text{Current Yearly Consumption (kWh)}}{\text{Current Yearly Consumption (kWh)}}$$

The sizing is performed under the assumption that gas operated equipment is categorized as motor loads and electricity operated equipment are non-motor loads. This categorization eases the addition (or removal) of a load necessary (or redundant) for the required battery backup or an islanded (off-grid) operation. Additionally, no other renewable sources are taken into consideration, and it is assumed that the battery is connected to the load and the grid, for load demand responses and for battery-specific grid services respectively. The short and long duration grid service responses are taken into account for DOD identification in Section 4. The computed stepwise values and resulting  $E_{max}$  and  $E_{min}$  are tabulated in **Table 4**. The *Operating Hours* are chosen as 2 and 10 for the minimum (short duration) and maximum (long duration) capacity value computations, respectively. For the primary school, the resulting average energy is 25.735.

MWh, that is the average of the lowest (1.30 MWh) and the highest (50.17 MWh) values. For the hospital, the resulting average energy is 12.445 MWh, which is also the average of the lowest (2.19 MWh) and the highest (22.70 MWh) values. Although the load consumption peaks and frequency of load operations is higher in case of a hospital, the energy storage size requirement for it is comparatively lower than the primary school mainly because of the load factor. Higher is the load factor, lower is the energy storage size requirement, which also results in reduced average per kWh cost.

Further, comparing the load profiles in **Figures 3** and **4**, it can be seen that the peak consumptions take place at the same times of the year for both facilities. Apart from facility occupancy, the external weather plays a major role in this effect. Studies related to this work are out of scope of this chapter and the interested readers are advised to look into papers authored by Sarwat et al. [123, 124]. If the individual equipment current ratings are available, a duty cycle diagram can be built based on the operating periods of the equipment and the corresponding energy requirements can be evaluated [125]. The interconnection topology of the batteries to meet the required battery module size for both EV and RES applications is dependent on the battery management systems performance and application requirements [126].

#### **4. Application-dependent chemistry-specific battery lifecycle performance assessment**

Development lifecycle of a battery includes the following phases: material extraction, processing, manufacturing, and assembly, use phase, and end-of-life phase. Assessment of this lifecycle is performed by evaluating the battery chemistry for the intended application using Cradle-to-gate and Cradle-to-grave analysis techniques [4, 9]. The Cradle-to-gate technique covers the upstream and production phases, while the Cradle-to-grave technique includes additional downstream phases, as shown in **Figure 5**. In this study, Cradle-to-gate LCA is performed to identify the energy consumption and environmental impact of a battery chemistry from research and development to commercialization for both an EV and a RES battery. Here, the impact in transportation of batteries is not taken into consideration. The evaluated chemistries are limited to Li-based, Pb-Acid, Ni-MH, Na-S, and VRB. Each chemistry is evaluated for five case studies.

Facility	Sizing Criteria	Motor Loads (Hourly)				Non-Motor Loads (Hourly)				P <sub>b</sub>	Corresponding Capacity Range	
		H <sub>g</sub>	IE <sub>g</sub>	WH <sub>g</sub>	F <sub>e</sub>	C <sub>e</sub>	II <sub>e</sub>	IE <sub>e</sub>	Maximum		Minimum	
Primary School	Average	6.79	41.14	39.10	39.01	1.20	7.43	3.44	0.65	1.30	6.48	
	Peak	31.73	180.71	80.53	79.09	647.88	32.06	17.44	5.02	10.03	50.17	
Hospital	Average	112.92	549.86	132.06	207.44	229.23	43.08	14.44	1.10	2.19	10.94	
	Peak	238.63	665.70	243.26	310.11	1094.45	84.97	35.34	2.27	4.54	22.7	

Hourly Average and Peak values for: H<sub>g</sub>: Heating (Gas Operated) (in kW); IE<sub>g</sub>: Interior Equipment (Gas Operated) (in kW); WH<sub>g</sub>: Water Heater System (Gas Operated) (in kW); F<sub>e</sub>: Fans (Electricity Operated) (in kW); C<sub>e</sub>: Cooling (Electricity Operated) (in kW); II<sub>e</sub>: Interior Lights (Electricity Operated) (in kW); IE<sub>e</sub>: Interior Equipment (Electricity Operated) (in kW); P<sub>b</sub>: Battery Power (in MW).

**Table 4.** A primary school and a hospital BES capacity sizing based on load profiles in year 2004.

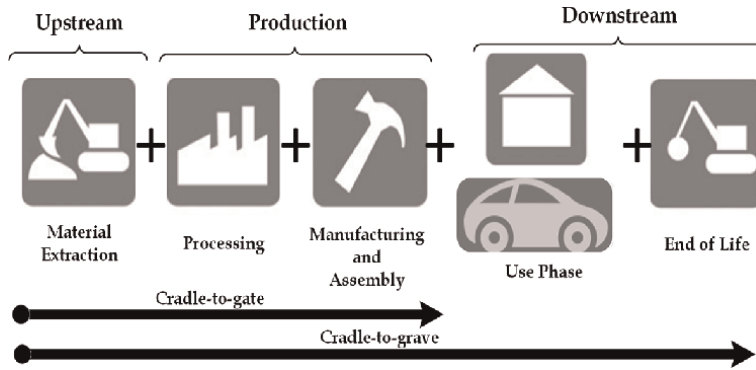


**Figure 5.**  
 RES and EV battery lifecycle phases.

$$C2G/kWh = \frac{C2G/Kg * C_b * m}{E_{life}}, \quad (19)$$

$$\text{where, } C_b = \begin{cases} \frac{10}{\mathcal{L}_{av}}, & \text{if } C_{10} < \mathcal{L}_{10} \\ \frac{C_{10}}{\mathcal{L}_{10}}, & \text{otherwise,} \end{cases}$$

$$m = \frac{E_{res}}{\epsilon_{av}},$$

$$E_{res} = \frac{E_{av}}{\sqrt{\eta_{rt}} * DOD},$$

$$E_{life} = E_{av} * C_{10}$$

Apart from application type categorization, the case studies are majorly divided on the basis of DOD of the battery, which indicate its applicability of operation for the EV or RES application. In RES-based applications, grid services operations are categorized into short (Voltage, Frequency Stability, and Interruption response), medium (Spinning reserve, peak shaving, and contingency reserve), and long duration (load shifting, and energy arbitrage) services [127, 128]. A DOD of 0.2 and 0.8 are selected for short and long duration operations, respectively. For EV storage applications, a medium DOD of 0.5 is selected because of the variation in driving patterns of an EV user, resulting in extreme contrasts (high or low) in consumption from user to user. Case studies use the equations in (19), results for which, along with each parameter's values, are tabulated in **Table 5**. In **Table 5**, the application-specific/–dependent parameters are  $E_{av}$ : Average Application Energy (in kWh),  $C_{10}$ : Number of cycles demanded by the application in 10 years [129, 130], DOD%: Depth of Discharge %, and  $E_{life}$ : Lifetime Energy Delivered (in kWh). The chemistry-specific/–dependent parameters are  $\eta_{rt}$ : Average Round-trip Efficiency [96, 131, 132],  $\epsilon_{av}$ : Average Specific Energy (in kWh/Kg);  $\mathcal{L}_{80}$ : Average Cycle Life of battery at 80% DOD in its lifetime [97, 131, 132],  $\mathcal{L}_{av}$ : Average Calendar Life (in Years) [131], C2G/Kg: Cradle-to-gate impact of battery (in KJ/Kg) [133],  $C_b$ : Number of batteries used in 10 years' time scale,  $E_{res}$ : Resulting System Size (in kWh),  $m$ : Battery Mass (in Kg), and C2G/kWh: Cradle-to-gate impact of battery (in KJ/kWh). The  $E_{av}$ ,  $C_{10}$ , DOD%, and  $E_{life}$  are the application-specific parameters and  $\eta_{rt}$ ,  $\epsilon_{av}$ ,  $\mathcal{L}_{80}$ ,

Case study	Application	$E_{inv}$	$\eta_{er}$	sav	Duration	DOD%	L80	C10	Lav	C2G/Kg	Cb	Eres	m	Elife	C2G/KWh	
I	EV storage	105	Li-based	0.86	0.152	Medium	50	10250	450	10	196	1	226.45	1489.8	47250	6.18
			Pb-Acid	0.72	0.04		1250		3	39.6	3.33	247.49	6187.2	17.28		
			Ni-MH	0.8	0.075		600		5	55	2	234.79	3130.5	7.29		
			Na-S	0.75	0.19		3333		13.5	180.7	0.74	242.49	1276.2	3.62		
			VRB	0.68	0.035		13000		15	37.5	0.67	255.60	7303	3.86		
II	RES-primary school	25731	Li-based	0.86	0.152	Long	80	10250	3300	10	196	1	34683.06	228178.05	84912300	0.53
			Pb-Acid	0.72	0.04		1250		3	39.6	3.33	37905.34	947633.57	1.17		
			Ni-MH	0.8	0.075		600		5	55	2	35960.17	479468.88	1.71		
			Na-S	0.75	0.19		3333		13.5	180.7	0.74	37139.50	195471.05	0.31		
			VRB	0.68	0.035		13000		15	37.5	0.67	39148.47	1118527.7	0.33		
III	RES-primary school	25731	Li-based	0.86	0.152	Short	20	10250	3300	10	196	1	138732.25	912712.2	84912300	2.11
			Pb-Acid	0.72	0.04		1250		3	39.6	3.33	151621.37	3790534.3	4.67		
			Ni-MH	0.8	0.075		600		5	55	2	143840.66	1917875.5	6.83		
			Na-S	0.75	0.19		3333		13.5	180.7	0.74	148557	781884.2	1.23		
			VRB	0.68	0.035		13000		15	37.5	0.67	156593.88	447410.8	1.32		
IV	RES-hospital	12440	Li-based	0.86	0.152	Long	80	10250	3300	10	196	1	16767	110315.8	41052000	0.53
			Pb-Acid	0.72	0.04		1250		3	39.6	3.33	18325.85	458146.3	1.17		
			Ni-MH	0.8	0.075		600		5	55	2	17385.43	231805.7	1.71		
			Na-S	0.75	0.19		3333		13.5	180.7	0.74	17955.59	94503.12	0.31		
			VRB	0.68	0.035		13000		15	37.5	0.67	18926.86	540767.4	0.33		
V	RES-hospital	12440	Li-based	0.86	0.152	Short	20	10250	3300	10	196	1	67071.98	441263.059	41052000	2.11
			Pb-Acid	0.72	0.04		1250		3	39.6	3.33	73303.40	1832585.07	4.67		
			Ni-MH	0.8	0.075		600		5	55	2	69541.71	927222.9	6.83		
			Na-S	0.75	0.19		3333		13.5	180.7	0.74	71822.37	378012.5	1.23		
			VRB	0.68	0.035		13000		15	37.5	0.67	75707.43	2163069.4	1.32		

**Table 5.** Selected chemistry-specific LCA of commercialized battery energy storage systems.

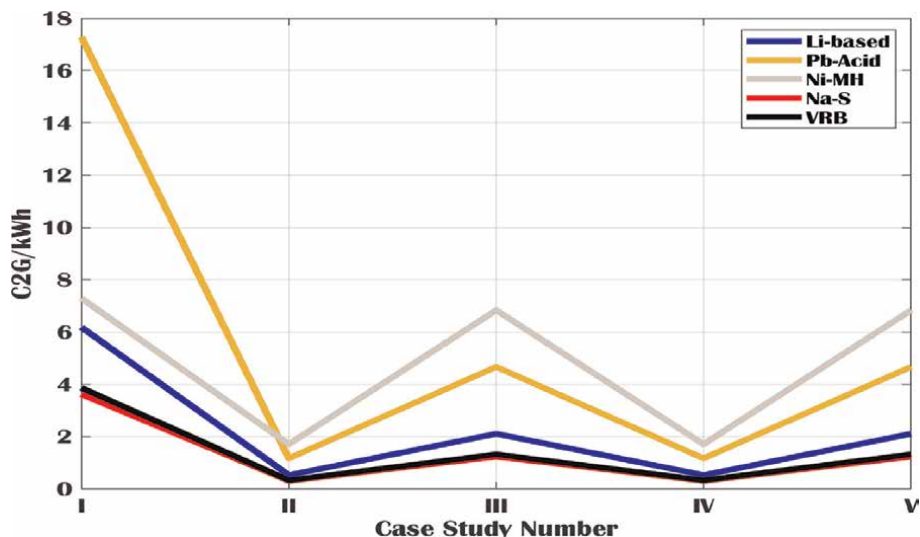


**Figure 6.** Case study versus cradle-to-gate lifecycle phase impact of selected chemistries.

$\mathcal{L}_{av}$ , C2G/Kg,  $C_b$ ,  $E_{res}$ ,  $m$ , and C2G/kWh are chemistry-specific parameters.  $av$  values are obtained from **Tables 1** and **2**, while  $E_{av}$  values are from Sections 3.1 and 3.2. Other parameters are obtained from [97, 129–135].

The resulting Cradle-to-gate lifecycle phase impact of all the chemistries shown in **Figure 6** indicate that the Pb-Acid chemistry has the highest C2G/kWh value for EV applications and Ni-MH has the highest C2G/kWh value for RES applications. Overall, it can also be noticed that the case studies with increased DOD (II and IV) have the lowest impact in the Cradle-to-gate phases.

## 5. Conclusion and future directions of research

For sized EV storage battery, CED order is: Pb-Acid > Ni-MH > Li-based (6.16 MJ/kWh) > VRB  $\approx$  NaS. For sized grid-storage, CED order for: Long duration is: Ni-MH > Pb-Acid > Li-based (0.53 MJ/kWh)  $\approx$  VRB  $\approx$  NaS and Short duration is: Ni-MH > Pb-Acid > Li-based (2.11 MJ/kWh) > VRB  $\approx$  NaS.

Considering the technology readiness level, form factor versatility, other electrochemical factors listed in Section 2.1, and the average C2G impact obtained under all case studies, Li-based chemistries are recommended to be chosen as the favorable chemistry for EV and RES applications. As evident from **Table 6**, the Cradle-to-gate with use system boundary is not commonly analyzed, especially with functional units (as defined by ISO 14040 and 14044) which include both EV and RES applicability. In this figure, Refs. [42, 136–139] have EV's, Refs. [140, 141] have battery chemistry, and Refs. [133, 142–144] have grid storage as respective functional units. Hence, this chapter compensates for this research gap by analyzing both EV and RES functional units, with data obtained from other literatures, in a Cradle-to-gate and use system boundary using CED as the impact category.

The computation approaches discussed in this chapter are simplified for the readers to understand the LCA approach with lucidity. The applicable assumptions

Ref.	Functional Unit*	Data Source(s)		System Boundary		Impact Category*	Conclusion(s)
		E.U. Ecoinvent	U.S. GREET	Other battery suppliers	Cradle-to-gate and use		
[42]	EV with Li-air battery driven for 1 Km	—	—	✓	—	✓	GWP, RD, ET Environmentally benign cell-level recycling is recommended for future battery developments.
[133]	Li-ion, Pb-acid, NaS, and VRB stationary batteries used to deliver 1 MWh of electricity, for a period of 20 years	✓	—	✓	—	✓	GWP, RD, CED, AD, EP, ET, HH CED order: Pb-acid > NaS > Li-ion ≈ VRB.
[136]	Material production involved in 30 kW, 150 kW, and 160 kW LMO batteries modeled for HEV, PHEV, and EV respectively	—	✓	BatPaC	✓	—	GHG Recycling of specific battery materials can result in energy conservation.
[137]	PHEV using 10 kWh LFP driven for 200,000 Km	✓	—	—	✓	—	GWP, RD, OD, PS, EP In addition to production phase, the environmental impact is expected to be significantly dependent on the relation between the weight of the vehicle and vehicle energy consumption, although there is no data available.
[138]	EV and PHEV using NiMH, LFP, and NMC charged with 50 MJ of energy (≈ 100 Km)	✓	—	—	✓	—	GWP, RD, ET, HH, OD, AD LFP eco-friendlier than NMC. Both of them more eco-friendly than NiMH.
[139]	Volkswagen e-Golf equivalent EV using LMO driven for 24,000 Km, with overall 80% efficiency	✓	—	✓	—	✓	GWP, CED, RD CED is 0.91 MJ/kWh. Use phase and the cell production energy demand are the dominant contributor to the environmental burden.
[140]	LFP and NMC modeled for 1 kWh energy release	✓	—	✓	—	✓	GWP, CED, AD, RD CED order: NMC > LFP.
[141]	26.25 kWh/Kg Al-ion battery production	✓	—	✓	✓	—	GWP, RD, OD, AD, EP, ET, HH Suggests that Al-ion is more a sustainable energy storage source than supercapacitors.

Ref.	Functional Unit*	Data Source(s)		System Boundary		Impact Category*	Conclusion(s)
		E.U. Ecoinvent	U.S. GREET	Other battery suppliers	Cradle-to-gate and use		
[142]	Advanced Pb-acid, NaS, Li-ion and NaNiCl <sub>2</sub> used to delivery 1MWh of electricity to the grid	✓	—	✓	—	✓	In terms of environment friendliness, NaNiCl <sub>2</sub> > NaS > Li-ion > Pb-acid.
[143]	LFP, LTO, LMO, NCA, NMC, NaNiCl <sub>2</sub> , Pb-Acid, and VRB connected to PV and E.U. grid. Varying sizes.	✓	—	—	—	✓	Carbon footprint order: Pb-acid > VRB ≈ NaNiCl <sub>2</sub> > LMO > NMC ≈ NCA > LTO ≈ LFP.
[144]	3.04 MWh/8 MW Li-ion battery model with 1 MW capacity reserve run on 9-bus grid for frequency regulation for 1 year.	—	✓	BatPaC	—	✓	GED order: NMC > NCA > LFP > LMO.
This work	2000Kg EV (105.42 average kWh), Two grid-connected ESS (25.7 and 12.4 MWh) operated for 10 years	—	—	✓	—	—	GED For sized EV battery, CED order: Pb-Acid > Ni-MH > Li-based (6.16 MJ/kWh) > VRB ≈ NaS For sized grid-storage, CED order: Long duration: Ni-MH > Pb-Acid > Li-based (0.53 MJ/kWh) ≈ VRB ≈ NaS Short duration: Ni-MH > Pb-Acid > Li-based (2.11 MJ/kWh) > VRB ≈ NaS

GHG: Greenhouse gas emission, HH: Human health, EQ: Ecosystem quality, RD: Resources depletion, CWU: Cumulative water use, GWP: Global warming potential, ET: Ecotoxicity, AD: Acidification, OD: Ozone depletion, PS: Photochemical smog, EP: Eutrophication, CED: Cumulative energy demand, LFP: Lithium iron phosphate, NMC: Lithium nickel manganese cobalt oxide, Li-air: Lithium air, LTO: Lithium-titanium-oxide, LMO: Lithium manganese oxide, NiMH: Nickel metal hydride, Al-ion: Aluminum ion, Pb-Acid: Lead acid, NaS: Sodium sulfur, VRB: Vanadium-redox-flow, NaNiCl<sub>2</sub>: Sodium nickel chloride, EV: Electric vehicle, HEV: Hybrid electric vehicle, PHEV: Plug-in hybrid electric vehicle; 80-DOD: 80% DOD selected; GREET: Greenhouse Gases, Regulated Emissions, and Energy Use in Transportation, BatPaC: Argonne National Laboratory's Battery Performance and Cost Model; \*: Required parameters, as defined by ISO14040 and ISO14044.

**Table 6.**  
Comparison of LCA results.

and constraints in both sizing and LCA are mentioned and discussed in their respective sections. Future works can focus on evaluating and sizing additional chemistries for LCA and possible greenhouse gas emissions evaluation. Authors also intend to perform an additional Cradle-to-grave application-dependent chemistry-specific analysis taking other renewable sources into consideration as a part of the future work.

## **Acknowledgements**

The material published is a result of the research supported by the National Science Foundation under the Award number CNS-1553494.

## **Author details**

Arif I. Sarwat\*, Asadullah Khalid, Ahmed Hasnain Jalal and Shekhar Bhansali  
Department of Electrical and Computer Engineering, Florida International  
University, Miami, FL, United States

\*Address all correspondence to: [asarwat@fiu.edu](mailto:asarwat@fiu.edu)

## **IntechOpen**

---

© 2023 The Author(s). Licensee IntechOpen. This chapter is distributed under the terms of the Creative Commons Attribution License (<http://creativecommons.org/licenses/by/3.0>), which permits unrestricted use, distribution, and reproduction in any medium, provided the original work is properly cited. 

## References

- [1] Islam A, Domijan A. Weather and reliability, in. IEEE Power Engineering Society General Meeting. 2007;2007:1-5
- [2] Berckmans G, Messagie M, Smekens J, Omar N, Vanhaverbeke L, Van Mierlo J. Cost projection of state-of-the-art lithium-ion batteries for electric vehicles up to 2030. *Energies*. 2017;10:1314
- [3] Mohr M, Peters JF, Baumann M, Weil M. Toward a cell-chemistry specific life cycle assessment of lithium-ion battery recycling processes. *Journal of Industrial Ecology*. 2020;24:1310-1322
- [4] Tolomeo R, De Feo G, Adami R, Sesti Osséo L. Application of life cycle assessment to lithium-ion batteries in the automotive sector. *Sustainability*. 2020;12:4628
- [5] Liu L. Life Cycle Assessment of a Lithium-Ion Battery Pack for Energy Storage Systems: -the Environmental Impact of a Grid-Connected Battery Energy Storage System. [Master's Thesis]. Sweden: Uppsala University, Energy Systems Engineering;; 2020. pp. 1-41
- [6] He X, Kim HC, Wallington TJ, Zhang S, Shen W, De Kleine R, et al. Cradle-to-gate greenhouse gas (ghg) burdens for aluminum and steel production and cradle-to-grave ghg benefits of vehicle lightweighting in China. *Resources, Conservation and Recycling*. 2020;152:104497
- [7] Salgado Delgado MA, Usai L, Ellingsen LA-W, Pan Q, Hammer Strømman A. Comparative life cycle assessment of a novel al-ion and a li-ion battery for stationary applications. *Materials*. 2019;12:3270
- [8] Gouveia J, Mendes A, Monteiro R, Mata T, Caetano N, Martins A. Life cycle assessment of a vanadium flow battery. *Energy Reports*. 2020;6:95-101
- [9] Porzio J, Scown CD. Life-cycle assessment considerations for batteries and battery materials. *Advanced Energy Materials*. 2021;11:2100771
- [10] Stan A-I, Świerczyński M, Stroe D-I, Teodorescu R, Andreasen SJ. Lithium ion battery chemistries from renewable energy storage to automotive and back-up power applications—An overview. In: 2014 International Conference on Optimization of Electrical and Electronic Equipment (OPTIM). Cheia, Romania. New Jersey, USA: IEEE; 2014. pp. 713-720
- [11] Khalid A, Sarwat AI, Fast charging li-ion battery capacity fade prognostic modeling using correlated parameters' decomposition and recurrent wavelet neural network, in: 2021 IEEE Transportation Electrification Conference Expo (ITEC), 2021, pp. 27–32. DOI: 10.1109/ITEC51675.2021.9490177
- [12] Nobili F, Marassi R. Fundamental principles of battery electrochemistry. In: *Batteries: Present and Future Energy Storage Challenges*. Vol. 2. New York, USA: John Wiley & Sons; 2020. pp. 13-48
- [13] Sarwat A, Khalid A, Sundararajan A. Systems and Methods for Forecasting Battery State of Charge. Miami, Florida, USA: United States Patents and Trademarks Office; 2021. pp. 1-38. US Patent 10,969,436
- [14] Khalid A, Sundararajan A, Acharya I, Sarwat A. Prediction of li-ion battery state of charge using multilayer perceptron and long short-term memory models. In: 2019 IEEE Transportation Electrification Conference & Expo. Detroit, Michigan in 2019. New Jersey, USA: IEEE; 2019. pp. 1-6

- [15] Khalid A, Sundararajan A, Sarwat AI. A multi-step predictive model to estimate li-ion state of charge for higher c-rates. In: 2019 IEEE International Conference on Environment and Electrical Engineering and 2019 IEEE Industrial and Commercial Power Systems Europe (EEEIC/I&CPS Europe). Genova, Italy. New Jersey, USA: IEEE; 2019. pp. 1-6
- [16] Khalid A, Sundararajan A, Sarwat A. A statistical out-of-sample forecast to estimate lithiumion parameters that determine state of charge. In: Electrochemical Conference on Energy and the Environment (ECEE 2019): Bioelectrochemistry and Energy Storage. 2019. p. 123021
- [17] Khalid A, Hernandez A, Sundararajan A, Sarwat AI. Simulation-based analysis of equalization algorithms on active balancing battery topologies for electric vehicles. In: Advances in Intelligent Systems and Computing. Vol. 1069. Cham: Springer; 2019. pp. 708-728
- [18] Khalid A, Sundararajan A, Sarwat AI. An Arima-narx model to predict li-ion state of charge for unknown charge/discharge rates. In: 2019 IEEE Transportation Electrification Conference (ITECIndia). Vol. 2019. IEEE. pp. 1-4
- [19] Khalid A, Sarwat AI. Unified univariate-neural network models for lithium-ion battery state-ofcharge forecasting using minimized akaike information criterion algorithm. IEEE Access. 2021;9:39154-39170
- [20] Khalid A, Khan M, Stevenson A, Batool S, Sarwat AI. Investigation of cell voltage buffer manipulation attack in a battery management system using unsupervised learning technique. In: 2021 IEEE Design Methodologies Conference (DMC). Detroit, Michigan in 2019. New Jersey, USA: IEEE; 2021. pp. 1-6
- [21] Chen X, Shen W, Vo TT, Cao Z, Kapoor A, An overview of lithium-ion batteries for electric vehicles, In: 2012 10th International Power Energy Conference (IPEC), 2012, Ho Chi Minh City, Vietnam. New Jersey, USA: IEEE; 2012. pp. 230-235. DOI:10.1109/ASSCC.2012.6523269
- [22] Blomgren GE. The development and future of lithium ion batteries. Journal of the Electrochemical Society. 2017;164: A5019-A5025
- [23] Stan A-I, Swierczynski M, Stroe D-I, Teodorescu R, Andreasen S. Lithium ion battery chemistries from renewable energy storage to automotive and back-up power applications — An overview, 2014 international conference on optimization of electrical and electronic equipment. OPTIM. 2014;2014:713-720
- [24] Padmanabh M, Desai MM, Performance and dynamic charge acceptance estimation of different lithium-ion batteries for electric and hybrid electric vehicles, In: 2017 IEEE Transportation Electrification Conference (ITEC-India), Pune, India in 2017. New Jersey, USA: IEEE; 2017. pp. 1-5. DOI: 10.1109/ITEC-India.2017.8333894
- [25] Yoshio M, Brodd RJ, Kozawa A. Lithium-ion Batteries. Vol. 1. New York, USA: Springer-Verlag; 2009
- [26] Yan FJD, Lu L, Ouyang M. Comparing the performances of different energy storage cells for hybrid electric vehicle. In: EVS28 International Electric Vehicle Symposium and Exhibition. Seoul, South Korea: The Korean Society of Automotive Engineers; 2015. pp. 1-13
- [27] Park M, Zhang X, Chung M, Less GB, Sastry AM. A review of conduction

- phenomena in li-ion batteries. *Journal of Power Sources*. 2010;**195**:7904-7929
- [28] Son J, Park K, Kim H, Chung H. Surface-modification of  $\text{LiMn}_2\text{O}_4$  with a silver-metal coating. *Journal of Power Sources*. 2004;**126**:182-185
- [29] Sun X, Luo X, Zhang Z, Meng F, Yang J. Life cycle assessment of lithium nickel cobalt manganese oxide (ncm) batteries for electric passenger vehicles. *Journal of Cleaner Production*. 2020;**273**:123006
- [30] Keil P, Schuster SF, Wilhelm J, Travi J, Hauser A, Karl RC, et al. Calendar aging of lithium-ion batteries: I. impact of the graphite anode on capacity fade. *Journal of the Electrochemical Society*. 2016;**163**:A1872-A1880
- [31] Ma J, Wang C, Wroblewski S. Kinetic characteristics of mixed conductive electrodes for lithium ion batteries. *Journal of Power Sources*. 2007;**164**:849-856
- [32] Forte F, Pietrantonio M, Pucciarmati S, Puzone M, Fontana D. Lithium iron phosphate batteries recycling: An assessment of current status. *Critical Reviews in Environmental Science and Technology*. 2020;**51**:1-28
- [33] Wang C, Hong J. Ionic/electronic conducting characteristics of  $\text{LiFePO}_4$  cathode materials: The determining factors for high rate performance. *Electrochemical and Solid-State Letters*. 2007;**10**:A65-A69
- [34] Bernardi DM, Go J-Y. Analysis of pulse and relaxation behavior in lithium-ion batteries. *Journal of Power Sources*. 2011;**196**:412-427
- [35] Madani SS, Schaltz E, Knudsen Kær S. An electrical equivalent circuit model of a lithium titanate oxide battery. *Batteries*. 2019;**5**:31
- [36] Mei J, Cheng EKW, Fong YC. Lithium-titanate battery (lto): A better choice for high current equipment, in: 2016 International Symposium on Electrical Engineering (ISEE). 2016. pp. 1-4. DOI: 10.1109/EENG.2016.7846362.
- [37] Zhong Y. *Lithium-Air Batteries: An Overview*. Stanford, CA: Stanford University Courses; 2011. Available from: <http://large.stanford.edu/courses/2011/ph240/zhong2/> [Accessed: April 30, 2020]
- [38] Liu T, Vivek JP, Zhao EW, Lei J, Garcia-Araez N, Grey CP. Current challenges and routes forward for nonaqueous lithium-air batteries. *Chemical Reviews*. 2020;**120**:6558-6625
- [39] Imanishi N, Yamamoto O. Perspectives and challenges of rechargeable lithium-air batteries. *Materials Today Advances*. 2019;**4**:100031
- [40] Lai J, Xing Y, Chen N, Li L, Wu F, Chen R. Electrolytes for rechargeable lithium-air batteries. *Angewandte Chemie International Edition*. 2020;**59**:2974-2997
- [41] Tan P, Jiang H, Zhu X, An L, Jung C, Wu M, et al. Advances and challenges in lithium-air batteries. *Applied Energy*. 2017;**204**:780-806
- [42] Zackrisson M, Fransson K, Hildenbrand J, Lampic G, O'Dwyer C. Life cycle assessment of lithiumair battery cells. *Journal of Cleaner Production*. 2016;**135**:299-311
- [43] Falconi A. *Electrochemical Li-Ion Battery Modeling for Electric Vehicles [Doctoral Thesis]*. Communauté Université Grenoble ALPES; France: Université Grenoble Alpes; 2017. pp. 1-214
- [44] Jeon Y, Noh HK, Song H-K. A lithium-ion battery using partially

lithiated graphite anode and amphi-redox  $\text{LiMn}_2\text{O}_4$  cathode. *Scientific Reports*. 2017;7:14879

[45] Nitta WFLJ, Yushin NG. Li-ion battery materials: Present and future. *Materials Today*. 2015;15:252-264

[46] Karthigeyan V, Aswin M, Priyanka L, Sailesh KND, Palanisamy K. A comparative study of lithium ion (lfp) to lead acid (vrla) battery for use in telecom power system, In: 2017 International Conference on Computation of Power, Energy Information and Communication (ICCPEIC). 2017. pp. 742-748. DOI: 10.1109/ICCPEIC.2017.8290462

[47] Kam KC, Doeff MM. Electrode materials for lithium ion batteries. *Material Matters*. 2012;7:56-60

[48] Brand M, Gläser S, Geder J, Menacher S, Obpacher S, Jossen A, et al. Quinger, Electrical safety of commercial li-ion cells based on nmc and nca technology compared to lfp technology, in: 2013 World Electric Vehicle Symposium and Exhibition (EVS27). 2013. pp. 1-9. DOI: 10.1109/EVS.2013.6914893

[49] Daniel C, Besenhard JO. *Handbook of Battery Materials*. New York, USA: John Wiley & Sons; 2012

[50] Pan J, Li H, Sun H, Zhang Y, Wang L, Liao M, et al. A lithium-air battery stably working at high temperature with high rate performance. *Small*. 2018;14:1703454

[51] Abraham KM, Jiang Z. *Solid Polymer Electrolyte-Based Oxygen Batteries*. Norwood, Massachusetts, USA: United States Patents and Trademarks Office; 1996. pp. 1-9. US Patent 5,510,209.

[52] Liu T, Leskes M, Yu W, Moore AJ, Zhou L, Bayley PM, et al. Cycling li-o<sub>2</sub>

batteries via lioh formation and decomposition. *Science*. 2015;350:530-533

[53] Liu C, Neale ZG, Cao G. Understanding electrochemical potentials of cathode materials in rechargeable batteries. *Materials Today*. 2016;19:109-123

[54] Sharova V. *Enhancing the Performance of Lithium Batteries through the Development of Improved Electrolyte Formulation, Formation Protocol and Graphite Surface Modification [Thesis]*. Germany: Karlsruher Institut für Technologie (KIT); 2018. DOI: 10.5445/IR/1000079331

[55] Tuller H. Ionic conduction and applications, In: Kasap S, Capper P. editors. *Springer Handbook of Electronic and Photonic Materials*. Springer, Cham: Springer Handbooks; 2007; p. 213. DOI: 10.1007/978-0-387-29185-7\_11

[56] Li Q, Chen J, Fan L, Kong X, Lu Y. Progress in electrolytes for rechargeable li-based batteries and beyond, green. *Energy & Environment*. 2016;1:18-42

[57] Wang SLHSSQY, Kadam A. Review on modeling of the anode solid electrolyte interphase (sei) for lithium-ion batteries. *npj Computational Materials*. Vol. 4. USA: Nature Publishing Group; 2018. pp. 1-26

[58] Ekström H, Lindbergh G. A model for predicting capacity fade due to sei formation in a commercial graphite/lifepo<sub>4</sub> cell. *Journal of the Electrochemical Society*. 2015;162:A1003-A1007

[59] Ramakrishnan S, Venugopalan S, Jeyakumar AE. Prediction of retained capacity and EODV of li-ion batteries in LEO spacecraft batteries. *arXiv*

- Computing Research Repository. 2010;2: 128-132. Available from: <http://arxiv.org/abs/1004.4480>
- [60] Kellner Q, Hosseinzadeh E, Chouchelamane G, Widanage WD, Marco J. Battery cycle life test development for high-performance electric vehicle applications. *Journal of Energy Storage*. 2018;15:228-244
- [61] Kravchyk KV, Bhauriyal P, Piveteau L, Guntlin CP, Pathak B, Kovalenko MV. High-energy-density dual-ion battery for stationary storage of electricity using concentrated potassium fluorosulfonylimide. *Nature Communications*. 2018;9:1-9
- [62] Will F. Assessment of research needs for advanced battery systems. In: Report of the Committee on Battery Materials Technology. Washington, D.C., USA: National Research Council (U.S.), National Academy Press; 1982. pp. 1-183
- [63] Gandhi KS. Modeling of sulfation in a flooded lead-acid battery and prediction of its cycle life. *Journal of the Electrochemical Society*. 2020;167:013538
- [64] May GJ, Davidson A, Monahov B. Lead batteries for utility energy storage: A review. *Journal of Energy Storage*. 2018;15:145-157
- [65] Hong B, Yu X, Jiang L, Xue H, Liu F, Li J, et al. Hydrogen evolution inhibition with diethylenetriamine modification of activated carbon for a lead-acid battery. *RSC Advances*. 2014;4:33574-33577
- [66] Sugumaran N, Everill P, Swogger SW, Dubey D. Lead acid battery performance and cycle life increased through addition of discrete carbon nanotubes to both electrodes. *Journal of Power Sources*. 2015;279:281-293
- [67] Lee CH, Lee SU. Theoretical basis of electrocatalysis. In: *Electrocatalysts for Fuel Cells and Hydrogen Evolution-Theory to Design*. London, UK: IntechOpen; 2018. p. 13
- [68] Albright G, Edie J, Al-Hallaj S. A Comparison of Lead Acid to Lithium-Ion in Stationary Storage Applications. *Alternative Energy eMagazine Industry*; 2012
- [69] Nadeem F, Hussain SMS, Tiwari PK, Goswami AK, Ustun TS. Comparative review of energy storage systems, their roles, and impacts on future power systems. *IEEE Access*. 2019;7:4555-4585
- [70] Liang Y, Zhao C-Z, Yuan H, Chen Y, Zhang W, Huang J-Q, et al. A review of rechargeable batteries for portable electronic devices. *InfoMat*. 2019;1:6-32
- [71] Vega-Garita V, Hanif A, Narayan N, Ramirez-Elizondo L, Bauer P. Selecting a suitable battery technology for the photovoltaic battery integrated module. *Journal of Power Sources*. 2019;438: 227011
- [72] Xu X, Zhou D, Qin X, Lin K, Kang F, Li B, et al. A room-temperature sodium-sulfur battery with high capacity and stable cycling performance. *Nature Communications*. 2018;9:1-12
- [73] Fan X, Liu B, Liu J, Ding J, Han X, Deng Y, et al. Battery technologies for grid-level large-scale electrical energy storage. *Transactions of Tianjin University*. 2020;26:1-12
- [74] Zahrul F, Lee W, Mohd F, Amir B. Modeling of sodium sulfur battery for power system applications. *Journal of ELEKTRIKA*. 2007;9:66-72
- [75] Capasso C, Veneri O. Laboratory bench to test zebra battery plus super-capacitor based propulsion systems for

- urban electric transportation. *Energy Procedia*. 2015;75:1956-1961
- [76] Revankar ST. Chapter six - chemical energy storage. In: Bindra H, Revankar S, editors. *Storage and Hybridization of Nuclear Energy*. London, UK: Academic Press; 2019. pp. 177-227
- [77] Frutschy K, Chatwin T, Bull R. Cell overcharge testing inside sodium metal halide battery. *Journal of Power Sources*. 2015;291:117-125
- [78] Galloway RC, Haslam S. The zebra electric vehicle battery: Power and energy improvements. *Journal of Power Sources*. 1999;80:164-170
- [79] Sakaebe H. *ZEBRA Batteries*, Springer New York, New York, NY: Springer; 2014. pp. 2165–2169. DOI: 10.1007/978-1-4419-6996-5\_437
- [80] Brady M et al. *Assessment of Battery Technology for Rail Propulsion Application*, Technical Report. United States: Federal Railroad Administration; 2017
- [81] Elia GA, Kravchyk KV, Kovalenko MV, Chacón J, Holland A, Wills RG. An overview and prospective on al and al-ion battery technologies. *Journal of Power Sources*. 2021;481:228870
- [82] Yuan D, Zhao J, Manalastas W, Kumar S, Srinivasan M. Emerging rechargeable aqueous aluminum ion battery: Status, challenges, and outlooks. *Nano Materials Science*. 2019;2:248-263
- [83] Lin M-C, Gong M, Lu B, Wu Y, Wang D-Y, Guan M, et al. An ultrafast rechargeable aluminium-ion battery. *Nature*. 2015;520:324-328
- [84] Li C, Hou C-C, Chen L, Kaskel S, Xu Q. Rechargeable al-ion batteries. *EnergyChem*. 2020;3:100049
- [85] Wang P, Chen Z, Ji Z, Feng Y, Wang J, Liu J, et al. A flexible aqueous al ion rechargeable full battery. *Chemical Engineering Journal*. 2019;373: 580-586
- [86] Kim H-T, Lee J-H, Kim DS, Yang JH. Redox flow–zn–br. In: *Batteries: Present and Future Energy Storage Challenges*. Vol. 2. New York, USA: Wiley; 2020. pp. 230-235, 311
- [87] Biswas S, Senju A, Mohr R, Hodson T, Karthikeyan N, Knehr KW, et al. Minimal architecture zinc–bromine battery for low cost electrochemical energy storage. *Energy & Environmental Science*. 2017;10:114-120
- [88] Lazard L. Lazard’s levelized cost of storage analysis, version 1.0. 2015. Available from: <https://www.lazard.com/media/450774/lazards-levelized-cost-of-storage-version-40-vfinal.pdf>
- [89] Butler PC, Eidler PA, Grimes PG, Klassen SE, Miles RC. Zinc/bromine batteries. In: *Handbook of Batteries*. USA: Mc-Graw-Hill; 2001. pp. 1-22
- [90] Weaver JF. ‘world’s smallest’ zinc bromine residential flow batteries coming for lithium, November 2017. Available from: <https://electrek.co/2017/11/06/zinc-bromine-batteries-coming-for-lithium/>
- [91] Christensen R. Vanadium redox flow battery. In: *Technology Data for Energy Storage*: November 2018. København, Denmark: Danish Energy Agency; 2018. pp. 113-146
- [92] Molina MG. Energy storage and power electronics technologies: A strong combination to empower the transformation to the smart grid. *Proceedings of the IEEE*. 2017;105: 2191-2219

- [93] Council NR et al. Reducing the Fuel Consumption and Greenhouse Gas Emissions of Medium-and Heavy-Duty Vehicles, Phase Two: First Report. National Academies Press; 2014
- [94] Gao D, Jiang D, Liu P, Li Z, Hu S, Xu H. An integrated energy storage system based on hydrogen storage: Process configuration and case studies with wind power. *Energy*. 2014;**66**:332-341
- [95] Sato Y, Takeuchi S, Kobayakawa K. Cause of the memory effect observed in alkaline secondary batteries using nickel electrode. *Journal of Power Sources*. 2001;**93**:20-24
- [96] Letcher TM, editor. Chapter 24 - storing energy in China—An overview. In: *Storing Energy*. Oxford: Elsevier; 2016. pp. 509-527
- [97] Akinyele D, Belikov J, Levron Y. Battery storage technologies for electrical applications: Impact in stand-alone photovoltaic systems. *Energies*. 2017;**10**:1760
- [98] Wesoff E. Exploding sodium sulfur batteries from ngk energy storage. 2011. Available from: <https://www.greentechmedia.com/articles/read/Exploding-Sodium-Sulfur-Batteries-From-NGK-Energy-Storage>
- [99] Wesoff E. Battery room fire at kahuku wind-energy storage farm. 2012. Available from: <https://www.greentechmedia.com/articles/read/Battery-Room-Fire-at-Kahuku-Wind-Energy-Storage-Farm>
- [100] Ha S, Kim J-K, Choi A, Kim Y, Lee KT. Sodium–metal halide and sodium–air batteries. *ChemPhysChem*. 2014;**15**: 1971-1982
- [101] Parkhideh B. Storage technologies for hybrid electric buses, zebra battery. 2006. Available from: [https://www.euromatic.no/ZEBRA\\_Aug17.pdf](https://www.euromatic.no/ZEBRA_Aug17.pdf)
- [102] Yu J, Hu Y-S, Pan F, Zhang Z, Wang Q, Li H, et al. A class of liquid anode for rechargeable batteries with ultralong cycle life. *Nature Communications*. 2017;**8**:1-7
- [103] Li G, Chang H, Lu X, Sprenkle V. Low cost and reliable sodium-metal halide (na-mh) batteries for stationary energy storage application, *TechConnect. Briefs*. 2017;**2**:122-125
- [104] Levy NR, Ein-Eli Y. Aluminum-ion battery technology: A rising star or a devastating fall? *Journal of Solid State Electrochemistry*. 2020;**24**:1-5
- [105] Leisegang T, Meutzner F, Zschornak M, Münchgesang W, Schmid R, Nestler T, et al. The aluminum-ion battery: A sustainable and seminal concept? *Frontiers in Chemistry*. 2019;**7**:268
- [106] Chen R, Kim S, Chang Z. Redox flow batteries: Fundamentals and applications. In: *Redox: Principles and Advance Applications*. 2017. pp. 103-118
- [107] Conca J. Energy's future - battery and storage technologies. New York, USA: Forbes; 2019. Available from: <https://www.forbes.com/sites/jamesconca/2019/08/26/energys-future-battery-and-storage-technologies/#428d111544cf>
- [108] Xie X. Vanadium Redox-Flow Battery. Stanford, CA: Stanford University Courses; 2017
- [109] B.-Z. Magnes, I. B. David, E. Lancry, M. Bergstein-Freiberg, Additives for Zinc-Bromine Membraneless Flow Cells, 2017. US Patent 9,722,272.

- [110] Rajarathnam GP, Vassallo AM. Description of the zn/br rfb system. In: *The Zinc/Bromine Flow Battery: Materials, Challenges, and Practical Solutions for Technology Advancement*. Singapore: Springer; 2016. pp. 11-28
- [111] Gao DEA. Vanadium redox flow batteries. In: *Storing Energy: With Special Reference to Renewable Energy Sources*. Amsterdam, Netherlands: Elsevier; 2016. pp. 227-248
- [112] Leahy MJ, Connolly D, Buckley DN. Wind energy storage technologies. In: *Wind Power Generation and Wind Turbine Design*. WIT Press; 2010. pp. 661-714
- [113] Pang Z, Gong Y, Yuan M, Li X. A newly designed modular znbr2 single cell structure. In: *Batteries*. Vol. 6. Basel, Switzerland: MDPI; 2020. p. 27
- [114] Khalid A, Sundararajan A, Hernandez A, Sarwat A. Facts approach to address cybersecurity issues in electric vehicle battery systems. In: *2019 IEEE Technology & Engineering Management Conference (TEMSCON)*. 2019
- [115] Huzayyin OA, Salem H, Hassan MA. A representative urban driving cycle for passenger vehicles to estimate fuel consumption and emission rates under real-world driving conditions. *Urban Climate*. 2021;**36**:100810
- [116] USEPA. Vehicle and fuel emissions testing: Dynamometer drive schedules. 2017. Available from: [//www.epa.gov/vehicle-and-fuel-emissions-testing/dynamometer-drive-schedules](http://www.epa.gov/vehicle-and-fuel-emissions-testing/dynamometer-drive-schedules)
- [117] Eaton, Technical data td00405018e: Generator sizing guide, 2009.
- [118] Althouse JR, Surbrook TC. *Electrical Tech Note — 600: Standby Power Systems*, 2008
- [119] Wilcox S, Marion W. Users manual for tmy3 data sets, national renewable energy laboratory technical report nrel/tp-581-43156, Golden, Colorado: National Renewable Energy Laboratory; Available from: <https://www.nrel.gov/docs/fy08osti/43156.pdf> [Accessed: July, 2020]
- [120] Office of Energy Efficiency & Renewable Energy (EERE). *Commercial and Residential Hourly Load Profiles for all tmy3 Locations in the United States*. EERE; 2013
- [121] A. Energy, understanding load factor. Available from: <https://austinenergy.com/wcm/connect/8fe76160-0f73-4c44-a735-529e5c7bee61/understandingLoadFactor.pdf?MOD=AJPERES&CVID=kC1aR-I> [Accessed: July 2020]
- [122] Sun Y, Saxena S, Pecht M. Derating guidelines for lithium-ion batteries. *Energies*. 2018;**11**:3295
- [123] Sarwat AI, Domijan A, Amini MH, Damnjanovic A, Moghadasi A. Smart grid reliability assessment utilizing boolean driven markov process and variable weather conditions, in. *North American Power Symposium (NAPS)*. 2015;**2015**:1-6
- [124] Sarwat AI, Amini M, Domijan A, Damnjanovic A, Kaleem F. Weather-based interruption prediction in the smart grid utilizing chronological data, *journal of modern power systems and clean. Energy*. 2016;**4**:308-315
- [125] Webb K. Section 6: Battery bank sizing procedures, ese 471 – energy storage systems. 2019. Available from: [http://web.engr.oregonstate.edu/~webbky/ESE471\\_files/Section%206%20Battery%20Sizing.pdf](http://web.engr.oregonstate.edu/~webbky/ESE471_files/Section%206%20Battery%20Sizing.pdf)
- [126] Khalid A, Sarwat AI. Battery module performance analysis under

- varying interconnection topology for electric vehicles. In: 2019 IEEE Transportation Electrification Conference (ITEC-India). 2019. pp. 1-5
- [127] Leadbetter J. Residential Battery Energy Storage Systems for Renewable Energy Integration and Peak Shaving [Master's Thesis]. Halifax, Canada: Dalhousie University; 2012. pp. 1-148
- [128] Sanfiel JJ, Khalid A, Parvez I, Sarwat AI. Simulation-based sizing and impact study of microgrid on a university campus. In: Southeast con 2021. IEEE; 2021. pp. 1-8
- [129] Yang F, Xie Y, Deng Y, Yuan C. Predictive modeling of battery degradation and greenhouse gas emissions from us state-level electric vehicle operation. Vol 9. London, UK: Nature Communications; 2018. pp. 1-10
- [130] Fqx S. How Does Depth of Discharge Factor into Grid Connected Battery Systems? 2013
- [131] Mongird K, Viswanathan VV, Balducci PJ, Alam MJE, Fotedar V, Koritarov VS, et al. Energy storage technology and cost characterization report. In: Technical Report. Richland, WA (United States): Pacific Northwest National Lab. (PNNL); Richmond, Washington, USA: Pacific Northwest National Lab; 2019
- [132] Rydh CJ, Sandén BA. Energy analysis of batteries in photovoltaic systems. part i: Performance and energy requirements. *Energy Conversion and Management*. 2005;**46**: 1957-1979
- [133] Hiremath M, Derendorf K, Vogt T. Comparative life cycle assessment of battery storage systems for stationary applications. *Environmental Science & Technology*. 2015;**49**:4825-4833
- [134] Bourgeois R. Sodium-metal halide batteries for stationary applications. In: Proc. 2010 Battcon Station. Battery Conf. Orlando. Pompano Beach, FL: Battcon/ Albercorp; 2010. pp. 11-16
- [135] Rantik M et al, Life Cycle Assessment of Five Batteries for Electric Vehicles under Different Charging Regimes, KFB. 1999
- [136] Dunn JB, Gaines L, Sullivan J, Wang MQ. Impact of recycling on cradle-to-gate energy consumption and greenhouse gas emissions of automotive lithium-ion batteries. *Environmental Science & Technology*. 2012;**46**:12704-12710
- [137] Zackrisson M, Avellán L, Orlenius J. Life cycle assessment of lithium-ion batteries for plug-in hybrid electric vehicles—critical issues. *Journal of Cleaner Production*. 2010;**18**:1519-1529
- [138] Majeau-Bettez G, Hawkins TR, Strømman AH. Life cycle environmental assessment of lithiumion and nickel metal hydride batteries for plug-in hybrid and battery electric vehicles. *Environmental Science & Technology*. 2011;**45**:4548-4554
- [139] Notter DA, Gauch M, Widmer R, Wager P, Stamp A, Zah R, et al. Contribution of li-ion batteries to the environmental impact of electric vehicles. *Environ. Sci. Technol*. 2010;**44**: 6550-6556
- [140] Jachura A, Sekret R. Life cycle assessment of the use of phase change material in an evacuated solar tube collector. *Energies*. 2021;**14**:4146
- [141] Melzack N, Wills R, Cruden A, et al. Cleaner energy storage: Cradle-to-gate lifecycle assessment of aluminium-ion batteries with an aqueous electrolyte.

Frontiers in Energy Research. 2021;**9**:  
699919

[142] Oliveira L, Messagie M, Mertens J, Laget H, Coosemans T, Van Mierlo J. Environmental performance of electricity storage systems for grid applications, a life cycle approach. Energy Conversion and Management. 2015;**101**:326-335

[143] Baumann M, Peters J, Weil M, Grunwald A. Co2 footprint and life-cycle costs of electrochemical energy storage for stationary grid applications. Energy Technology. 2017;**5**:1071-1083

[144] Ryan NA, Lin Y, Mitchell-Ward N, Mathieu JL, Johnson JX. Use-phase drives lithium-ion battery life cycle environmental impacts when used for frequency regulation. Environmental Science & Technology. 2018;**52**:10163-10174

## Chapter 2

# Tracking Li-Ion Batteries Using Fiber Optic Sensors

*Micael Nascimento, Carlos Marques and João Pinto*

### Abstract

Batteries are being seen as a key technology for battling CO<sub>2</sub> emissions from the transport, power, and industry sectors. However, to reach the sustainability goals, they must exhibit ultrahigh performance beyond their capabilities today. So, it is becoming crucial to develop advanced diagnostic/prognostic tools injected into the battery that could nonintrusively track in time and space its physical and chemical parameters, for ensuring a greater lifetime and therefore lower its CO<sub>2</sub> footprint. In this context, a smart battery sensing system with high performance and easy implementation is critically needed for the vital importance of safety and reliability in all batteries. Parameters like temperature (heat flow), strain, pressure, electrochemical events from electrode lithiation to gassing production, refractive index, and SoX battery indicators are of high importance to monitor. Recently, optical fiber sensors (OFS) have shown to be a feasible, accurate, and useful tool to perform this sensing, due to their intrinsic advantages and capabilities (lower invasiveness, multipoint and multiparameter detection, capability of multiplexing being embedded in harsh environments, and fast response). This chapter presents and discusses the studies published regarding the different types of OFS, which were developed to track several critical key parameters in Li-ion batteries, since the first study was reported in 2013.

**Keywords:** optical fiber sensors, smart sensing, *in situ* monitoring, Li-ion battery performance, safety

### 1. Introduction

According to recent COP21, COP25, COP26 Conferences, and EU2030 targets, there is a need for significant reductions in CO<sub>2</sub> and greenhouse gas emissions in a short span period, targeting the reduction of climate warming in 1.5–2.0°C up to 2030 [1]. With the worldwide acceptance of electric vehicles together with the new era of connected objects, ensuring battery reliability, lifetime, and sustainability is becoming a necessity [2]. In this way, batteries are currently seen as important technological enablers to drive the transition toward a decarbonized society. They have recently achieved considerable improvements in terms of technical performance and economic affordability [3]. However, for a successful mass introduction of electrified mobility,

renewable and clean energy systems with market competitive performances, fast charging capability, and substantial improvements in battery technologies (autonomy and safety) are required [4, 5].

Currently, to guarantee safe operation, a battery management system (BMS) only measures externally accessible parameters such as voltage, current, and temperature. The scarcity of information regarding the interior of the cell currently hinders the improvement of the accuracy and predicting capabilities of current BMS algorithms and models, while equally limiting attempts to refine the battery thermal design due to the absence of heat-transfer information. This has led to increasing interest in spatiotemporal imaging of the thermal flows within a cell using temperature sensors [6–12]. Typically, they are used in electronic sensing devices, such as thermocouples (TCs) [13, 14], thermistors [15], IR thermography [16], and resistance temperature detector (RTDs) [17]. However, in addition to short resolution and accuracy, huge measurement setup, or higher volume/size preventing them from being inserted in a cell, they cannot be appropriate to be embedded in batteries due to their electro-chemical harsh environment.

Furthermore, batteries are breathing objects that expand and contract upon cycling, with volume changes that can reach up to 10%. These changes, together with the electrode volume expansion associated with the solid electrolyte interface (SEI) growth, lead to important mechanical stress inside the battery materials (like cracks) that are harmful to their performances. Methods, to sense intercalation strain and pressure, are equally critical to control the SEI dynamics affecting their states of charge (SoC) and health (SoH). The methods already used are not acceptable: strain-gauges fall short of providing spatial information and cannot also be embedded to internally sense battery cells [8, 18].

Alternative solutions, due to their full advantages, such as greater precision, multiplexing, immunity to electromagnetic interference, chemical inertness, small size/low invasiveness, and a possibility to be tailored regarding their dimensions and sensitivities, are sensors based on optical fiber technology [2, 19–59]. Since the first study developed by Pinto *et al.* in 2013 [19], OFS starts to be integrated into lithium-ion batteries (LIBs) to monitor critical key parameters, such as temperature and/or thermal gradients, strain, gases, pressure, electrochemical events (chemical changes and lithiation), refractive index, and the states of charge, discharge, health, power, energy, and safety (SoX) battery indicators (**Figure 1**).

Performing a systematic review, we used two databases to retrieve scientific publications: Web of Science ([www.webofknowledge.com](http://www.webofknowledge.com), accessed on 16 November 2021) and Scopus ([www.scopus.com](http://www.scopus.com), accessed on 16 November 2021). A comprehensive search on the use of OFS to monitor LIBs was performed based on a query by topic (title, abstract, and keywords) of the terms: ((optical AND fiber AND sensors\*) AND (lithium AND batteries\*)); spanning over the years 2013 to November 2021. The search query resulted in a total of 60 papers that were subsequently reviewed by the authors, of which 40 were considered eligible for the present work.

**Figure 2A** summarizes the number of studies published by year, since the first paper in 2013, regarding the use of OFSs to track LIBs parameters. From a critical analysis, an increase of publications can be observed from the beginning, however, with a lower number in 2020, probably due to the pandemic world situation. In **Figure 2B**, it is also presented an illustration of the critical parameters tracked in the LIBs. Temperature and strain were the parameters more studied followed by the correlation of the optical fiber signals with the electrochemical events and SoX battery

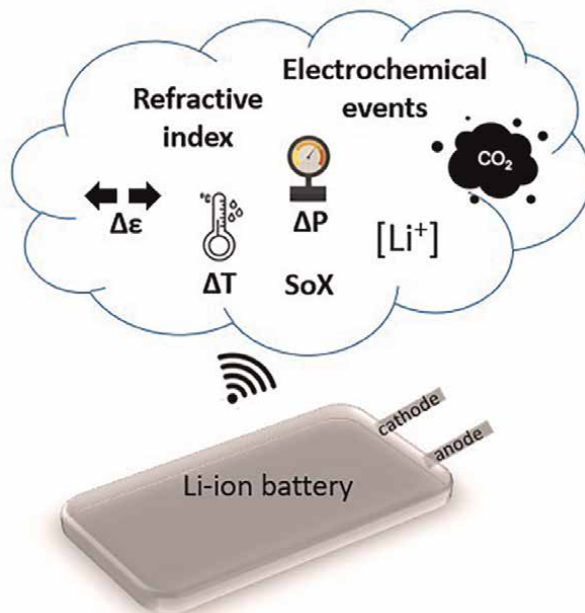


**Figure 1.**  
 Critical key parameters identified to be tracked in LIBs.

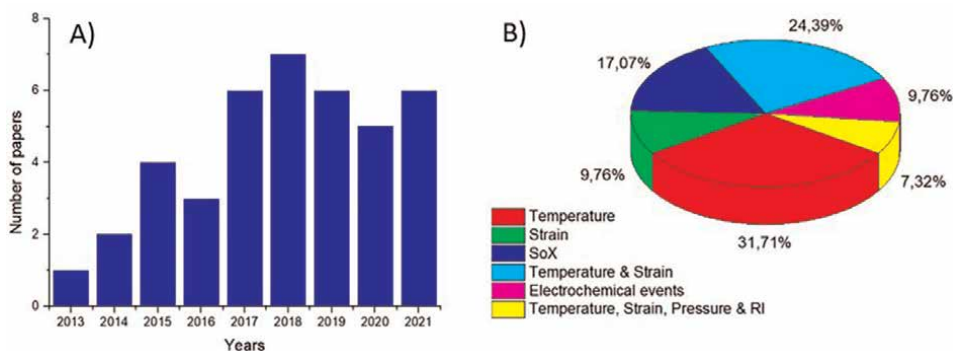


**Figure 2.**  
 (A) Statistical summary of the number of papers by year, published since the first study, regarding the using of OFS in LIBs. (B) Percentual distribution of the critical parameters tracked by the OFS in the LIBs.

indicators. The tracking of gasing, refractive index, and pressure variations are very recent topics of sensing inside the LIBs. However, due to the difficulty and complexity of sensing, the integration of the OFS inside the battery cells being necessary, they were not yet so explored. In this way, this chapter provides a complete overview of all studies published from 2013 to the present on the use of OFS to track critical key parameters in LIBs. Section 2 describes the theoretical approaches of the OFS used (fiber Bragg grating, interferometric, and evanescent wave sensors) to monitor the critical parameters. In section 3, all critical parameters (temperature, strain, SoX battery indicators, and electrochemical events) tracked so far using fiber optic sensing technology are presented and fully described.

## 2. Optical fiber sensors: theoretical approaches

Manfred Börner, a German physicist, developed, in 1965, the first fiber optic patent related to a working fiber-optic data transmission system [60, 61]. Years later, in 1978, the concept of wavelength division multiplexing, where several optical signal channels are multiplexed into a single optical fiber through different wavelengths was firstly published [62]. Since then, the optical fiber community has expanded and the use of optical fibers as sensing elements attracted a lot of attention. **Figure 3** summarizes the different types of fiber optic sensors developed in the last years [63]. Regarding the monitorization of physical and chemical parameters in LIBs, just some of them were already tested. The fiber Bragg grating sensors (FBG) and tilted FBG sensors (TFBGs) were used to track temperature, strain, refractive index, and SoX, inside and outside of batteries, correlating these signals with electrochemical events during their operation. From the interferometric sensors, Fabry-Perot interferometric (FPI) and Mach-Zehnder interferometric (MZI) sensors were tested to monitor and decouple temperature, strain, and SoC signals. Evanescent wave sensors based on surface plasmon resonance and evanescent field fluorescence were also already used to monitor temperature shifts and SoC values in batteries. OFS based on Rayleigh scattering distributed sensing was also already used. However, due to their instrumental complexity, elevated interrogation costs, and low experimental use relative to the other methods, this type of sensor will not be approached in this chapter.

### 2.1 Fiber Bragg grating sensors

The first FBG, fabricated using a visible laser propagating along with the fiber core, was proposed by Ken Hill in 1978 [64]. OFS based on FBGs has been widely applied in the measurement of physical, chemical, biomedical, and electrical parameters, especially for structural health monitoring in civil infrastructures, aerospace, energy, and healthy areas [65].

Classically, an FBG sensor consists of a small segment of a single-mode optical fiber (with a length of a few millimeters) with a photoinduced periodically modulated index of refraction in the fiber core. The FBG resonant wavelength is related to the effective refractive index of the core mode ( $n_{eff}$ ) and the grating period ( $\Lambda$ ). When the grating is illuminated with a broadband optical source, the reflected power spectrum presents a peak (with a full width at half maximum of a few nanometers), which is produced by the interference of light with the planes of the grating and can be described through Eq. (1) [66].

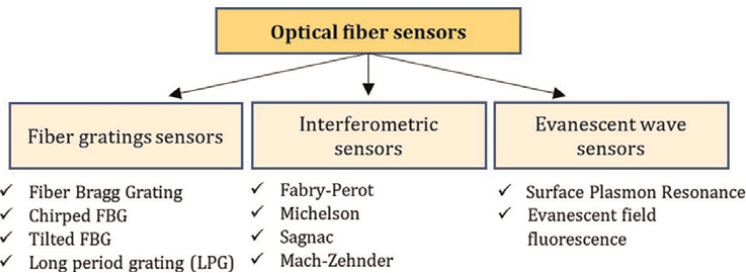


**Figure 3.** Different types of OFS used to track critical parameters in LIBs.

$$\lambda_B = 2n_{eff}\Lambda \quad (1)$$

where  $\lambda_B$  is the so-called Bragg wavelength. When the fiber is exposed to external variations of a given measurand (such as strain, temperature, stress, or pressure, among others), both  $n_{eff}$  and  $\Lambda$  can be changed, causing an alteration in the Bragg wavelength, as shown in **Figure 4** [66]. In addition to the common advantages of fiber sensors, this wavelength interrogation method offers robustness to noise and power oscillations and also enables wavelength division-multiplexing, by recording numerous FBGs with diverse grating periods in the same optical fiber (see **Figure 5**). This permits the monitorization of different spots in one structure/surface with only one sensor line, decreasing in this way, the total interrogation costs. The FBG sensitivity toward a given parameter is obtained simply by subjecting the sensor to pre-determined and controlled variations of such parameters and measuring the Bragg wavelength for each step.

In the case of a linear response, the sensitivity ( $k$ ) is given by the slope of the linear fit obtained from the experimental data. The effects of temperature are accounted for in the Bragg wavelength shift by differentiating Eq. (2),

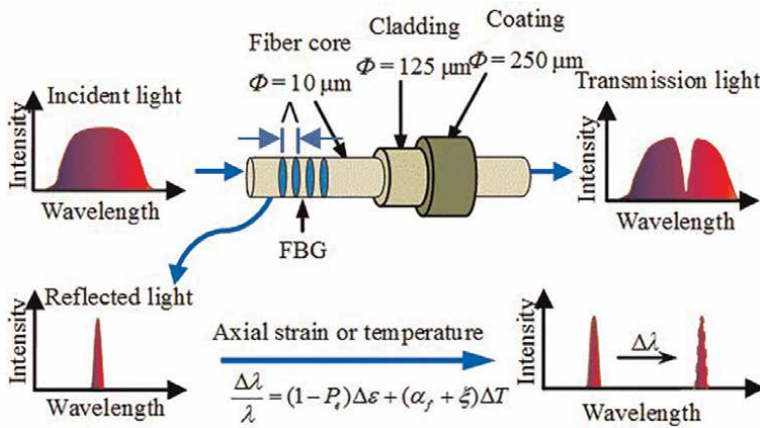


**Figure 4.** Scheme and operation mechanism of an FBG sensor to external strain and temperature perturbations.

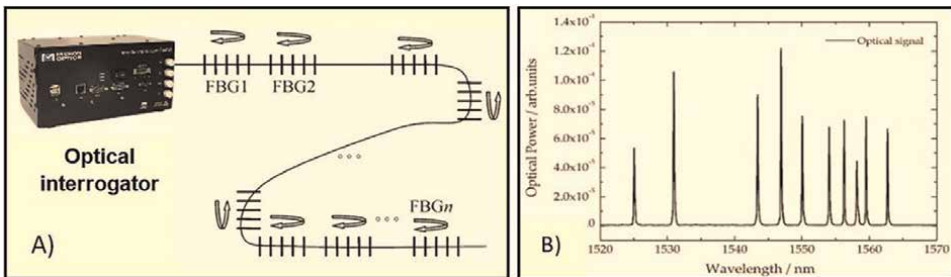


**Figure 5.** A) FBGs network inscribed in the same optical fiber. B) Optical spectrum of a network of 10 FBGs inscribed in the same fiber, where different wavelength peaks can be observed.

$$\Delta\lambda = 2\lambda_B \left( \frac{1}{n_{eff}} \frac{\partial n_{eff}}{\partial T} + \frac{1}{\Lambda} \frac{\partial \Lambda}{\partial T} \right) \Delta T = \lambda_B(\alpha + \xi) \Delta T = k_T \Delta T, \quad (2)$$

where  $\alpha$  and  $\xi$  are the thermal expansion and thermo-optic coefficient of the optical fiber material, respectively. On the other hand, if the fiber is subjected to strain variations, its response can be determined by differentiating Eq. (3),

$$\Delta\lambda = \lambda_B \left( \frac{1}{n_{eff}} \frac{\partial n_{eff}}{\partial \varepsilon} + \frac{1}{\Lambda} \frac{\partial \Lambda}{\partial \varepsilon} \right) \Delta \varepsilon = \lambda_B(1 - p_e) \Delta \varepsilon = k_\varepsilon \Delta \varepsilon, \quad (3)$$

where  $p_e$  is the photoelastic constant of the fiber ( $\sim 0.22$ ) and  $\Delta \varepsilon$  is the applied strain. The strain variations can be determined using the equation  $\Delta \varepsilon = \Delta L/L$  where  $\Delta L$  is the length variation and  $L$  is the fiber length over which strain is applied. On a single measurement of the Bragg wavelength shift, it is not possible to decouple the effect of variations in strain and temperature (for example). Normally, a reference is used for temperature measurement, by using another fiber strain-free or other FBGs and sensing heads that have different strain and temperature sensitivities. Different strategies are being used in the literature, such as FBGs recorded in different fiber thicknesses, FBGs recorded in special microstructured fibers, and FBGs cascaded with other optical fiber sensing configurations (FPI, MZI) [66–68]. The discrimination of both variables is performed, through the matrixial method by using all the sensitivities of both sensors to each variable. In this way, a sensitivity matrix (4) for simultaneous measurement of strain and temperature can be derived as:

$$\begin{bmatrix} \Delta \varepsilon \\ \Delta T \end{bmatrix} = \frac{1}{D} \begin{bmatrix} -k_{FBG1T} & k_{FBG2T} \\ k_{FBG1\varepsilon} & -k_{FBG2\varepsilon} \end{bmatrix} \begin{bmatrix} \Delta \lambda_{FBG1} \\ \Delta \lambda_{FBG2} \end{bmatrix}, \quad (4)$$

where  $D = K_{FBG1\varepsilon} \times K_{FBG2T} - K_{FBG1T} \times K_{FBG2\varepsilon}$  is the determinant of the coefficient matrix, which must be nonzero for possible simultaneous measurement.

The Bragg gratings can be inscribed in an optical fiber core through side exposure; two main types of techniques can be implemented: interferometric and non-interferometric techniques. In the noninterferometric technique, the phase mask method is one of the most commonly used (see **Figure 6A**). Generally, it is associated with longer laser pulses (near the nanoseconds) in the ultraviolet (UV) region. The phase mask consists of a diffraction grating shaped by small depressions in a silica substrate, separated by a predefined period (phase mask pitch,  $\Lambda_{PM}$ ), which will define the modulation pattern linked to the resonant Bragg wavelength of the fabricated FBG (see **Figure 6B**).

Depending on the incident angle of the laser beam on the phase mask surface, different diffraction orders will be predominantly transmitted: the pairs  $+1/0$  or  $+1/-1$ . To attain different wavelength peaks, phase masks with different  $\Lambda_{PM}$  can be used. Typically, when using a UV laser, a better inscription efficiency is expected for doped or hydrogenated optical fibers [67].

## 2.2 Tilted FBG sensors

Compared to the normal FBG sensors, TFBG sensors have a special configuration, which leads to enhanced sensitivity to the surrounding refractive index (SRI). Thus,

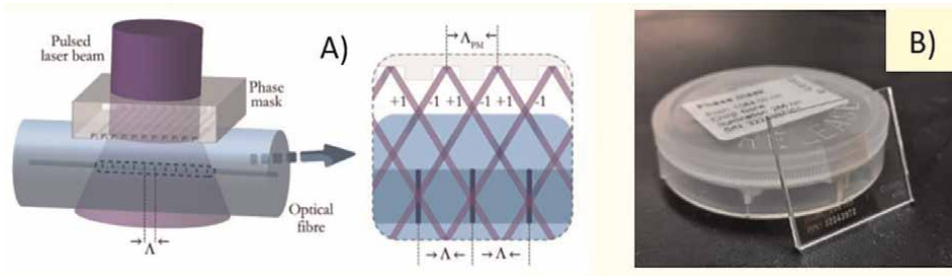


**Figure 6.**  
 A) Schematic representation of the phase mask inscription method using a pulsed laser. +1 and -1 indicate the laser beam diffraction orders used to inscribe the Bragg grating in the optical fiber core. B) Typical phase masks used on FBG sensors recording (from Ibsen®).

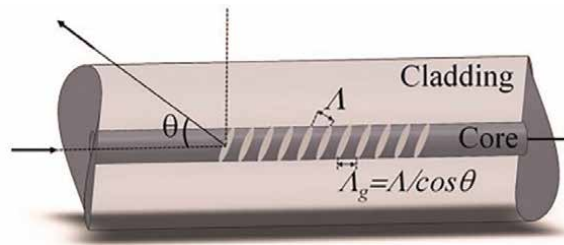


**Figure 7.**  
 Schematic diagram of a TFBG where  $\Lambda_g$  is the grating period and  $\theta$  is the tilt angle (adapted from [68]).

this type of sensor has been employed in many parameters sensing, such as temperature, liquid level, RI, and relative humidity, in biochemical research. TFBGs are short-period gratings in which the modulation of the RI is purposely tilted concerning the longitudinal axis of the fiber, to improve the light coupling between the forward-propagating core mode and the backward-propagating cladding modes (see **Figure 7**) [68].

The wavelength of the coupled  $i$ -th cladding mode  $\lambda_{cl(i)}$  can be expressed as (Eq. 5):

$$\lambda_{cl(i)} = \left( n_{eff}^{core} + n_{eff(i)}^{cla} \right) \Lambda = \frac{\left( n_{eff}^{core} + n_{eff(i)}^{cla} \right) \Lambda_g}{\cos \theta} \quad (5)$$

where  $n_{eff}^{core}$  and  $n_{eff(i)}^{cla}$  are the effective RIs of the fiber core and  $i$ -th cladding mode, respectively.  $\Lambda$  and  $\Lambda_g$  are the grating periods along with the fiber longitudinal axis and perpendicular to the grating plane, respectively. The excited cladding modes are limited in the fiber cladding by total internal reflection on the cladding-surrounding medium interface. Each of the cladding modes propagates with a corresponding effective RI value. When the RI value of the surrounding medium spreads the one of a specific cladding mode, the cladding mode will be coupled out of the fiber cladding, resulting in a variation in the grating transmission spectrum. Therefore, the shifts of the SRI can be quantitatively tracked by detecting the variations in the grating transmission spectrum of the TFBG [69]. These TFBGs can also be fabricated in line with other normal FBGs to simultaneously decouple different parameters, such as RI and temperature, as they have different sensitivities.

### 2.3 Interferometric sensors

Since the first study, published in 1897 by Charles Fabry and Alfred Perot, about the FPI principle [70], the OFS based on this methodology was used in numerous applications, such as biological, chemical, and various physical parameters, including temperature, strain, pressure, and RI [63, 71]. Literature shows that these sensors are used also like candidates to improve the discrimination of strain and temperature in batteries [44]. An FPI sensor is performed by considering two parallel reflecting surfaces divided by a certain physical length of the cavity ( $L$ ). FPI sensors can be classified as extrinsic or intrinsic, as can be seen in **Figure 8a** and **b**, respectively. The intrinsic FPI sensor has reflecting components inside the fiber itself [70]. In the extrinsic FPI, the air cavity is designed by an auxiliary structure. Due to the optical phase difference between two reflected signals, the reflection spectrum of an FPI can be defined as the wavelength-dependent intensity modulation of the incident signal spectrum. The phase difference of the FPI ( $\delta_{FP}$ ) can be given as (Eq. 6):

$$\delta_{FP} = \frac{4\pi nL}{\lambda} \quad (6)$$

where  $n$  is the RI of the cavity material, and  $\lambda$  is the wavelength of the output signal. Consequently, an external perturbation to the FPI sensor (such as strain, temperature, or IR), will promote a length variation of the FPI cavity, resulting in wavelength changes. By tracking the wavelength shift of the spectrum, and after an experimental pre-calibration to each specific parameter, to determine their sensitivities, a linear conversion of the data signals of the measured parameter values can be performed by analyzing the spectrum produced.

Another type of interferometer is the MZI sensor. They are usually applied for sensing parameters such as temperature, strain, curvature, and RI, among others [71], due to their advantages of high RI sensitivity and flexible designs, as shown in **Figure 9**.

An MZI is designed due to the formation of an optical path difference between the fundamental core mode and the higher-order cladding modes in optical fiber. Subsequently, in the interference spectrum, dips or peaks can appear [72]. These peaks or

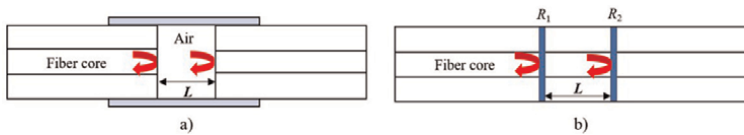


**Figure 8.** a) Extrinsic FP sensor performed by forming an external air cavity, and b) intrinsic FP sensor formed by two reflecting components,  $R_1$  and  $R_2$  (adapted from [70]).

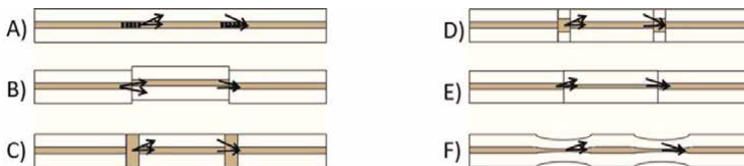


**Figure 9.** Different types of MZIs configurations; using: (A) a pair of LPGs, (B) core misalignment, (C) air-hole collapsing of PCF, (D) MMF section, (E) small SMF core, and (F) tapering fiber regions (adapted from [71]).

dips values are used as tracking signals because they change with external perturbations (such as temperature, strain, pressure, and RI). For simplicity and spectral data analysis, only the core mode ( $I_1$ ) and one cladding mode ( $I_2$ ) are considered. The transmitted interference signal,  $I$ , can be expressed as (Eq. 7) [73]:

$$I = I_1 + I_2 + 2\sqrt{I_1 I_2} \cos(\phi) \quad (7)$$

where  $\phi = \frac{2\pi(n_{eff}^{core} - n_{eff}^{cla})L}{\lambda}$ , is the phase difference, being  $n_{eff}^{core}$  and  $n_{eff}^{cla}$  the effective RIs of the fiber core and cladding mode, respectively. The  $\lambda$  is the input optical wavelength in vacuum,  $L$  is the interferometric MZI length, and  $\phi = 0$  is the initial interference phase. When  $I_1 = I_2$ , the fringe visibility reaches its maximum value.

From Eq. (7), when  $\phi = \frac{2\pi(n_{eff}^{core} - n_{eff}^{cla})L}{\lambda_m} = (2m + 1)\pi$ , the output intensity dips will appear, where  $m$  is an integer. Specifically, the phase difference between two adjacent minimum intensity dips is  $\frac{2\pi\Delta n_{eff}L}{\lambda_{m+1}} - \frac{2\pi\Delta n_{eff}L}{\lambda_m} = 2\pi$ . Therefore, the difference between two adjacent interference wavelengths, as well known as the free spectral range (FSR) can be calculated as  $FSR = \lambda_m - \lambda_{m+1} = \frac{\lambda_m \lambda_{m+1}}{\Delta n_{eff} L}$ , and the theoretical cavity length is  $L = \frac{\lambda_m \lambda_{m+1}}{\Delta n_{eff} (\lambda_m - \lambda_{m+1})}$ . Using these formulas, the theoretical values of MZI length can be compared with experimental results to reduce errors, and also, it can be seen that when the  $L$  increases or the  $\Delta n_{eff}$  increases, the  $FSR$  decreases. Note that when  $\Delta n_{eff}$  changes, it indicates that RI of the external environment changes, promoted by the external parameters, while RI of the optical fiber core is constant. When the external parameters, such as temperature or RI, around the MZI is different, which will lead to the changes of  $\Delta n_{eff}$ , the wavelength of interference dip will also shift. So, the surrounding environment can be analyzed through spectra after a pre-calibration process to each external parameter to which the optical sensor will be submitted.

## 2.4 Evanescent wave sensors

Other types of OFS, which are being used to track specific parameters in Li-ion batteries, were the evanescent wave sensors. This type of sensor is created on the interaction of the evanescent field in the cladding with the fiber surroundings, resulting in fluctuations of the transmitted spectrum. It follows that they hold the capability of translating a discrepancy of the target analyte into optical signals so that they are widely applied to chemical and biosensing [74]. As shown in **Figure 10**, the evanescent field  $E_{ew}(d)$  decays exponentially as (Eq. 8):

$$E_{ew}(d) = E_0 \exp\left(\frac{-d}{d_p}\right) \quad (8)$$

where  $E_0$  is the magnitude of the field at the fiber core-cladding interface,  $d$  is the distance from the core-cladding interface, and  $d_p$  is the distance where the evanescent field decreases to  $E_0/e$  and is described as the penetration depth which is given by (Eq. 9):

$$d_p = \frac{\lambda}{2\pi\sqrt{n_{core}^2 \sin^2\theta - n_{cla}^2}} \quad (9)$$

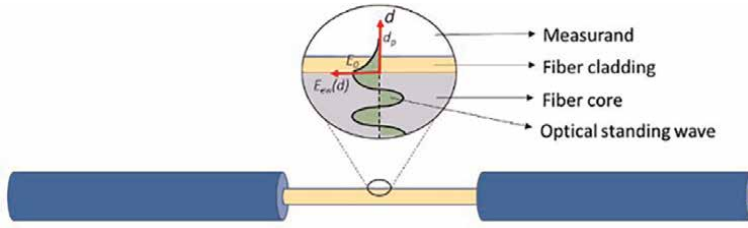


**Figure 10.** Design of a fiber evanescent wave spectroscopy sensor with the standing wave pattern and exponentially decaying evanescent wave.

where  $\lambda$  is the wavelength of the incident light,  $\theta$  is the angle of incidence at the fiber core-cladding interface, and  $n_{core}$  and  $n_{cla}$  are the RIs of the fiber core and cladding, respectively.

This optical fiber methodology of sensing can also be modified by depositing specific film materials (metal-dielectrics) in the fiber cladding surface and interacting between them. In this way, the surface plasmon resonance (SPR) technique can be used. The SPR is a collective oscillation of free electrons excited by light at the metal-dielectric interface. The electromagnetic field decays exponentially into both metal and dielectric, the propagation constant of SPR can be given as (Eq. 10):

$$k_{sp} = \frac{\omega}{c} \sqrt{\frac{\epsilon_m \epsilon_d}{\epsilon_m + \epsilon_d}} \quad (10)$$

where  $\omega$  is the angular frequency of the incident light,  $c$  is the speed of light in space, and  $\epsilon_m$  and  $\epsilon_d$  are the dielectric constants of the metal and dielectric, respectively. The propagation constant of the evanescent wave parallel to the planar metal film surface can be expressed as  $k_{ew} = \frac{\omega}{c} \sqrt{\epsilon_{fiber}} \sin\theta$ , where  $\epsilon_{fiber}$  is the dielectric constant of the fiber. The SPR occurs when both propagation constants are equal, it exhibits high sensitivity to even slight oscillations in the dielectric constant of the dielectric material. Therefore, SPR-based sensors can successfully track diverse variables due to the location of the resonance shifts with the varying the RI of the nearby dielectric.

### 3. Critical parameters tracked in LIBs by OFS

In the almost last 10 years, OFS was introduced and started to be used as a useful and precise tool to monitor critical key parameters inside and outside the LIB. Significant advantages instead of other sensing technologies can be reported comparatively with the electronic technology, in the monitorization of temperature (TCs, RTDs,) and strain (strain-gauges), regarding the low intrusiveness (fibers thickness of  $\sim 125$  microns), higher capacity of multipoint and multiparameter discrimination, and essentially the capability of to be embedded in their harsh electrochemical environment, by tracking in loco and real-time specific parameters with good accuracy and reliability, and without damage the batteries performances. Until now, it was almost impossible to access the internal behavior of these batteries in operation, to know how they behave in terms of physical and chemical performance.

This optical fiber technology presented above has been successfully integrated into battery sensing, allowing their smart sensing of LIB safety aspects, such as temperature and/or thermal gradients, strain, RI, and pressure variations, internal gassing evolution, electrochemical events (chemical reactions, and SEI composition), and their correlation with SoX battery indicators. This section divides and reports all studies presented in the literature since the first paper reported by Yang et al. in 2013, regarding the use of OFS to monitor all these parameters in LIB.

### 3.1 Temperature tracking

Of all safety problems in LIBs, thermal runaway is a vital issue, which is reproduced by the fast increase of temperature. This rise produces heat energy at a rate faster than heat can be dissipated followed by a failure of the LIB internal separator components, resulting in local short circuits and critical situations, to their explosion [75]. Moreover, accumulated heat in the batteries takes worries of performance drops and safety risks. Temperature can affect the LIBs lifetime and energy, and therefore, it should be within an ideal range of temperature, to ensure better performance and long life, both for use and storage [17]. The ability to quantify and evaluate the mechanism of thermal runaway generated during the electrochemical processes which happen will create beneficial information regarding their behavior, as well as an active tool to promote their safety [76–78].

Typically, in the real context of the LIB, this parameter is monitored through external electronic devices, such as TCs and RTDs, by detecting just single points on their surface. Optical fiber sensing technology was used as an alternative method to realize multipoint external and internal temperature measurements on LIBs, during their operation, also performing in different types of LIBs, thermal gradients characterizations, and evolutions. Of the different types of OFS, the FBGs were the mainly used due to their inherent advantage of multipoint monitoring and fast response time.

In 2013, Yang et al. [19], integrated by the first time, FBGs in a coin LIB to measure real-time temperature changes during the battery's operation under normal and abnormal conditions. The FBG sensors exhibited good thermal responses to dynamic loading when compared with the TCs. Novais et al. [26], in 2016, presented the integration of four FBGs in lithium-ion cells for *in situ* and in-operando temperature monitoring during galvanostatic cycling at C-rates ranging from 1 to 8°C (Figure 11A). In the internal FBG locations, the fiber was covered by an exterior silica

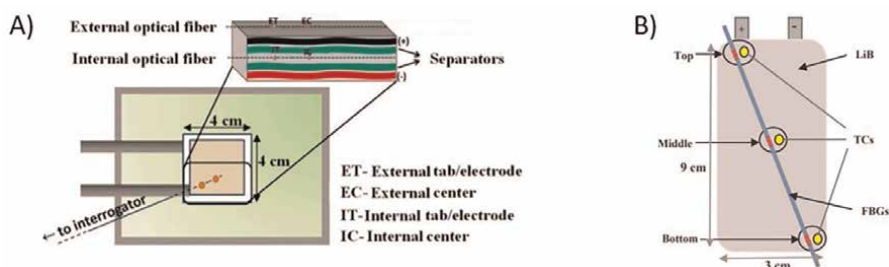


**Figure 11.** A) Schematic diagram of internal and external FBG sensors positions [26]. B) Schematic of a LiB test setup with the location of TCs and FBGs. Copyrights 2016 and 2017.

tube to free the sensors of any external stress promoted by the surrounding materials and, in this way, only detect temperature variations.

The internal sensors registered higher temperature variations at 8°C and in the center of the active area of the one-layer pouch cell. The authors concluded that the low invasiveness and high tolerance to the chemically aggressive environment make them a motivating option for integration into the LIBs. This study also contributes to the detection of a temperature gradient in real-time inside an LIB, thanks to the different locations of the sensors inside the battery. Nascimento et al., one year later [30], attached FBGs, all recorded in the same single fiber and TCs on a commercial LIB surface, to perform a comparative study between their signal responses (**Figure 11B**). The response rates were 4.88°C/min and 4.10°C/min for the FBG and TC, respectively. The results also demonstrate that the FBGs were able to sense temperature fluctuations with a  $\sim 1.2$  times higher response rate than the K-type TCs. The rise time obtained for the FBG was 28.2% lower than the TC, making the FBGs a better choice for the real-time temperature tracking on a LIB.

In 2017 and 2019, Nascimento et al. [29, 43] has developed two studies about the thermal distribution on a surface of a prismatic LIB by a network of five FBGs in a single fiber, to assess in real time and operation, the impact of different environmental conditions, temperature, and relative humidity, on batteries performance. These studies provided a real-time thermal mapping to elucidate which areas of the battery needed to be cooled faster when it was exposed to dry, temperate, and cold climates. Faster variations of voltage usually translated in higher temperature variations at the LiB surface, and this effect is evidenced when the LiB operates under abnormal conditions. After a pre-calibration step, the FBGs were calibrated to convert the wavelength shift peak to the correspondent temperature values based on their calculated sensitivity. These temperature values are tracked by following the FBGs peaks in the spectrum response. Complete temperature values of  $30.0 \pm 0.1^\circ\text{C}$ ,  $53.0 \pm 0.1^\circ\text{C}$ , and  $65.0 \pm 0.1^\circ\text{C}$  were achieved on the top location (near electrodes) during the higher discharge rate, when exposed to the cold, temperate, and dry climates, respectively. The higher temperature shifts detected by the optical sensors in the temperate and dry environments are related to the superior performance of the LiB in terms of discharge capacity and power capabilities. This study demonstrates also which are the best environmental conditions to run the LiBs, in order to extend their lifetime and safety, and is also helpful for the next generation of batteries, showing which areas require faster cooling to reduce accumulated heat.

Bhagat's group, in 2018, performed three studies by embedding FBGs, in cylindrical LIBs, to monitor *in situ* and in-operando temperature variations. The sensors were resistant to the strain imposed during the battery instrumentation procedure and their harsh chemical environment. The results presented a temperature difference between the core and the can temperatures (monitored by K-type TC) of up to 6.0°C during the discharging process, while a temperature difference of 3.0°C was obtained during the charging process. The zones nearer to the anode presented a higher temperature during discharge while the location closer to the cathode performed higher temperature values during charge [38]. The authors demonstrate that FBGs produce reliable core temperature data, while their small mechanical profile allows for a low-impact instrumentation method [41, 42].

Nascimento et al., in 2018, proposed a network of 36 FBGs for real time, *in situ*, and operando multipoint monitoring of the surface temperature distribution on a pack of three prismatic LIBs, performing a spatial and temporal thermal mapping of all

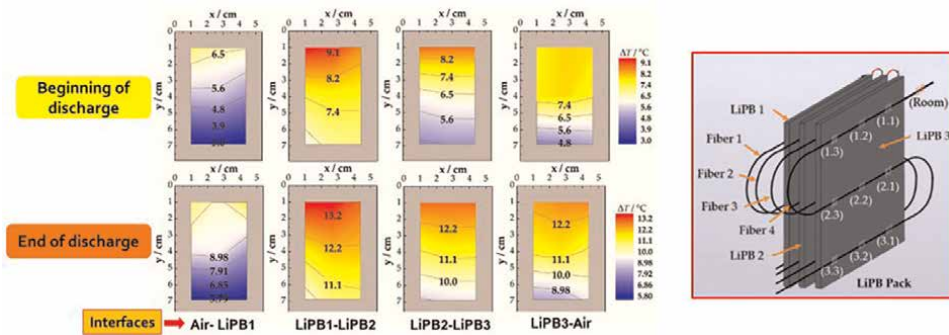


**Figure 12.** Surface LIB pack thermal mapping performed by a network of 36 FBGs, during discharging at 1.4C [36]. Copyright 2018.

pack interfaces (**Figure 12**). In total, four optical fibers were used to monitor all locations of the LIB pack. The results show that in general, a thermal gradient is identified from the top to the bottom surface locations. Due to the higher current density of the  $\text{Li}^+$  ions near the positive tab collector, the presence of hot spots between two of the three batteries was identified [36].

Peng et al., in 2020 [53] and 2021 [55] proposed an OFS to monitor temperature variations in the external LIB electrodes, during cycling tests. The sensor consists of a metal ring and an FBG. The FBGs were gloved on the external electrodes, and PT100 sensors were also attached to the electrodes as a comparison measurement. The FBGs calibration test presents good linearity and high sensitivity. From the results, during all the cycles, the sensors placed on the positive electrodes recorded higher temperature variations instead of those on the negative electrodes. Even this year, Alcock et al. developed an accessible method to attach FBGs on cylindrical LIB surfaces to *in situ* thermal sensing. This study differs from the others by using a “guide-tube” to decouple the temperature and strain variations on the LIB surface [54]. Recently, Li et al. developed an optical fiber temperature sensor for battery temperature monitoring based on fluorescence intensity ratio technology [58]. In this study,  $\beta\text{-NaYF}_4:\text{Er}^{3+}/\text{Yb}^{3+}@\text{NaYF}_4$  nanoparticles were used to design the optical sensor in the fiber tip. After the fiber functionalization, this sensor was preliminary calibrated to temperature in function of their fluorescence intensity response to correctly convert their spectral response in temperature values during battery operation. The maximum relative sensitivity obtained by the optical sensor was  $1.62\% \text{ K}^{-1}$  at 293 K, the temperature detection limit was within  $\pm 0.5 \text{ K}$ , and high-temperature changes were registered under a higher discharge rate.

### 3.2 Strain tracking

Along with the cycling processes of LIBs, strain evolution is also an important parameter to be tracked in order to identify possible cracks in their internal materials or the occurrence of some swelling in case of a wrong operation through a gasification production. In this way, OFS has also been recently used to monitor this parameter. From all studies reported so far, the FBGs were the sensors selected to perform this sensing. Li-ion pouch cell configuration is the most used in tests while coin cell configuration is only employed to demonstrate the preliminary tests.

In 2016, Bae et al. [27] developed two approaches to track strain and stress evolution in the graphite anode of a Li-ion pouch cell using FBGs. In one approach, the optical sensor was attached between the graphite anode and the separator, while in the other implanted approach, the sensor was embedded totally within the anode material. Measurements of strain and stress states of the graphite anode were run over cycling tests. Reproducible peak shifting in both attached and embedded FBGs was observed at different states of charge and discharge. Specifically, an embedded sensor that is completely surrounded by graphite particles simultaneously suffers accumulated longitudinal, as well as transverse strains associated with the expansion or contraction of the negative electrode. Additionally, the embedded FBG showed  $3\times$  higher sensitivity than the attached FBG sensor at 100% SoC. The process to detect and convert the FBG wavelength peaks to strain measurements is the same as used for temperature monitoring, through the strain sensitivities of each sensor and using free FBGs just to decouple temperature variations.

Peng et al., in 2019, have reported two papers regarding an external and novel strain sensor based on FBGs for LIBs [45, 47]. The structure of the strain sensor consisted of two FBGs, a sensitization structure and a protective cover, which contained two symmetrical lever mechanisms and an installation platform, in which the rotating pairs of levers were replaced by flexure hinges. Enhanced strain sensitivity of  $11.55 \text{ pm}/\mu\text{e}$  was obtained, with good linearity and repeatability. From the cycling tests, the drift in strain is analogous to different C-rate charge-discharge cycles. The strain rises evidently close to the end of discharge with an evolution in the C-rate. However, the proposed sensor cannot be embedded inside the LIBs due to their bulky structure, providing higher invasiveness.

Rente et al., in 2021, reported the tracking of strain shifts, also through FBGs, on a surface of cylindrical LIB, under cycling tests [57]. In this study, a simple machine-learning algorithm based on dynamic time warping (DTW) was used to estimate the SoC of representative LIBs. The FBG data obtained were shown to be reliable and sufficiently reproducible to serve as the input for the DTW algorithm used. The use of a model train has proved to be very effective as a proof-of-concept study for future BMS, especially in electrical vehicles.

### **3.3 SoX battery indicators tracking**

The SoX battery indicators are crucial factors reflecting the state of batteries, in which they are commonly estimated under the assistance of the evanescent wave sensors in LIBs. Additionally, the FBGs are combined with them to improve the sensing performance and used as parameters discrimination. In 2015, an integrated OFS technology for monitoring charge steps in LIB cells was studied by Alemohammad et al. [23]. The sensor consists of an optical fiber encapsulated inside a LIB with direct interaction with the cell electrochemical environment. The sensor operates on the basis of the changes in the optical properties of the LIB cell electrodes, that is, variations in optical absorption and reflection at different charge levels, that will change the spectral response in terms of wavelength and also optical power losses, showing the SoC in battery and providing information about aging and stabilization following charge/discharge cycles.

Ghannoum et al., reported in 2016, a reflectance study of commercial graphite anodes in LIB and the optical fiber evanescent wave spectroscopy of electrochemically lithiated graphite [28]. A substantial rise in the reflectance of the lithiated graphite in the near-IR band (750–900 nm) as a function of SoC and similar SoC tendency in the

transmittance when the fiber was embedded in the battery was observed. The same authors, one year later, developed the fabrication and integration of the OFS, by using similar sensing technology, into cylindrical LIBs as well as a Li-ion pouch cell [31]. The sensitivity of the sensor increased along with increasing the contact area of the sensor within the graphite anode and the optical fiber evanescent wave sensor integrated into the graphite anode demonstrated the potential use to track the both SoC and SoH of LIB, by correlating the optical data with the voltage and current signals of the LIBs.

Lao et al., in 2018, designed an innovative method, named TFBG-based SPR sensor, for *in situ* tracking the SoC of supercapacitors, for the first time [39]. This new configuration is based on a 50-nm-thick gold layer of high surface quality deposited on the TFBG. The FBG recording angle was  $18^\circ$  and an additional gold coating was deposited on the fiber end to achieve a single-ended sensor with interrogation in the reflection scheme (**Figure 13A**). The proposed plasmonic TFBG sensor was attached to one of the electrodes of the supercapacitor to monitor the electrochemical activity. The charge density and SoC measurement were demonstrated, and the results showed that the spectral response of the SPR mode of the TFBG was directly related to the charge density and the SoC of the supercapacitor. Basically, the wavelength peak of the TFBG and the SPR mode changes with the SoC level at which the supercapacitor is. Then, the variations of the charge density and the SoC during the cycling steps could be tracked by following the shifts of the place and the intensity of the reflection spectrum.

Modrzynski et al. [46] presented an SoC measurement technique based on an optical fiber sensing system, in 2019. In this system, two optical fibers were etched to increase the interaction between the light propagation inside the fiber core with the surrounding fiber environment, detecting in this way RI changes in real time. The fibers were integrated into both graphite anode and lithium iron phosphate with the addition of indium tin oxide cathode of a Li-ion pouch cell. The SoC was monitored in real time by simultaneously detecting the light transmission through both fibers. The results showed that the SoC correlated transmission behaved equally for both electrodes. However, diverse relaxation and wavelength-dependent behaviors were identified during the charge and discharge cycling steps. The study proved that the OFS process was able to estimate the SoC independent of the electrical measurement methods.

In 2020, Hedman et al. used an OFS based on evanescent waves for monitoring the charge/discharge cycles of lithium iron phosphate batteries in real time [49]. The sensor is fully embedded within the positive electrode in a customized Swagelok cell in both a reflection- and transmission-based OFS configuration. Both constant current cycling and cyclic voltammetry were employed to associate the optical spectrum

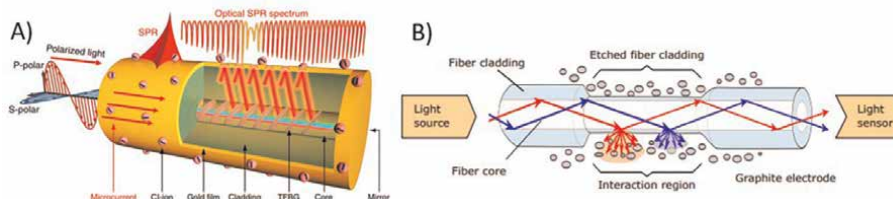


**Figure 13.**  
A) Electrochemical SPR sensing principle and experimental demonstration with a gold-coated TFBG sensor [39].  
B) OFS principle. Multicolored light is guided through an optical fiber embedded in the electrode [59]. Copyright 2018, 2021.

response with the cycling processes of LIBs. From the results, the optical signal correlates well with the SoC in the positive electrode in real time, and it is reproducible over various cycles. Furthermore, the optical signal detected does not rely on other usually estimated parameters in SoC estimation, such as current, voltage, and temperature. Rittweger et al., in 2021, present measurement results based on transmitted light intensities through the optical fiber as an indicator for the SoC (**Figure 13B**) [59]. The work also purposes to present an explanation of how to use the measured transmission intensity to decrease cross effects, such as temperature, pressure, or aging LIBs parameters. For that, a referencing methodology based on transmission intensities from light with different wavelengths is approached. Due to the reduced fiber cladding by a preliminary etching process, the light interacts with electrode material surrounding the fiber. So, transmission losses can be sensed, which depend on the lithium concentration in the electrode. From the results, the calculated transmission ratios are in good agreement with the SoC for various C-rates.

### **3.4 Electrochemical events tracking**

Electrochemical events, such as gassing production, electrode lithiation, and chemical changes of the electrolyte, are fundamental issues that enable the battery manufacturers to identify degradation mechanisms that currently limit the lifetime and capacity of these energy-storage systems.

In 2014, Lochbaum et al. measured the evolution of gaseous CO<sub>2</sub> inside lithium-ion pouch cells during overcharge tests with optical fiber colorimetric sensors (the chemical sensing fiber used comprises a silica core surrounded by a fiber cladding, which is permeable to the chemical to be detected (analyte) and functionalized such that it changes its optical characteristics with analyte concentration) to examine the dynamics of electrolyte decomposition reactions [20]. For the ratiometric read-out principle used, the averaged intensity between 570 nm and 600 nm (CO<sub>2</sub>-sensitive band) was normalized by the averaged intensity between 800 nm and 820 nm (CO<sub>2</sub>-insensitive band). The results indicate a nonreversible gas evolution inside the LIBs during overcharge, in which the beginning of gas evolution is delayed in time relative to the overcharge condition.

Ghannoum et al., in 2017, presented the application of an innovative optical fiber-based sensing system for the lithiation of graphite within a lithium-ion pouch cell in real-time using a narrow-band spectrum concentrated around 850 nm [31]. For that, a polymer optical fiber was used and etched for the fiber core to directly interact with the surrounding materials. The main results show that the sensor signal can be correlated with the lithiation of graphite anode over multiple full and partial cycles.

More recently, in 2020, the same authors show an analysis of the interaction between the optical fiber evanescent wave sensor and the graphite particles within a LIB [50]. The proposed sensor was sensitive to lithium concentration at the surface of graphite particles; then, it was able to monitor the capacity fade of LIBs. In the same year, photonic crystal fibers were used by Miele et al. to monitor chemical changes within LIBs under real working conditions [52]. The technique used was based on optofluidic single-ring hollow-core fibers, which uniquely allow light to be guided at the center of a microfluidic channel. The signal analysis was performed by background-free Raman spectroscopy to identify early signs of battery degradation. From the results, the Raman peaks related to ethylene carbonate and the important

battery additive vinylene carbonate, offer a direct vision in the formation of the SEI, the main buffer layer that largely forms during its first electrochemical cycle, and whose stability is key to the longevity of the LIBs.

### **3.5 Simultaneous tracking of temperature, strain, pressure, and RI**

The main challenge in tracking critical parameters inside the LIB, such as thermal gradients, strain, pressure, and RI changes, is that due to its electrochemical environment, the LIB presents a very dynamic behavior. The temperature variation influences the thermal expansion of the materials that compose the LIB, promoting strain changes. The electrochemical behavior also promotes internal gassing production, which will affect the pressure variation and RI changes on the electrolyte. LIBs primarily employ liquid electrolytes to ensure rapid ion transport for high performance of the variation in the RI of the electrolytes is related to the variations in the conductive salt concentration. Thus, the RI shifts can be treated as an indicator of the degradation evolutions.

As some of the OFS are sensitive to more than one parameter simultaneously, they suffer from large cross sensitivity, such as strain, RI, and temperature. In this way, solutions to decouple these parameters should be considered by the researchers. As the LIBs are very complex systems with dynamic and diverse physical and electrochemical behaviors, in which many parameters are linked and correlated between them, such as temperature, strain, gas formation, and pressure, several studies were already reported by sensing and decoupling simultaneous parameters in LIB since 2013.

Sommer et al. have reported many studies concerning the use of FBGs to simultaneously decouple strain and temperature variations in LIBs [21, 22, 32, 33]. In 2014, the authors start by externally attaching LIB pouch cell FBGs to monitor additional informative cell parameters (strain and temperature) and using other FBGs as a reference to perform this parameters discrimination, as described by Rao et al. [66]. Two FBGs were employed in the experimental setup, one, bonded at two points to the surface of the pouch cell with epoxy, sensing both strain and temperature variations; while the other one, loosely attached to the cell skin with a heat-conducting paste, only detecting temperature variations. Several charge and discharge cycles were performed to examine the repeatability of the measured signals and compared with conventional strain and temperature sensors to verify the accuracy of these sensors. In 2015 [22], the same authors examined the excess volume change at the end of charge and the volume relaxation in the subsequent rest phase by monitoring the strain variations of externally attached FBGs of a lithium-ion pouch cell. The strain was instigated by the alteration of electrode volume, due to the constant  $\text{Li}^+$  oscillation and intercalation from and to the positive electrode, and thermal expansion/contraction during cycling charge/discharge steps. A strain relaxation was observed at higher SoC levels, especially strain signal relaxed by  $\sim 30\%$  at an SoC level of 100%, and the ratio of  $\text{Li}^+$  in the external electrode region to  $\text{Li}^+$  in the internal electrode region was larger at a higher SoC level. The association between them was also explored at various room temperatures. It concluded that the residual strain increased with decreasing temperature for a certain SoC level, and the alteration between the residual strains was higher for superiors SoC levels.

In 2017, two-part papers about embedded fiber optic sensing for accurate internal monitoring of cell state in advanced BMS by monitoring temperature and strain shifts

inside of a pouch cell LIB were developed by Raghavan et al. (part 1) and Ganguli et al. (part 2), belonging to the same research group [32, 33]. Part 1 focuses on the embedding method details and performance of LIBs. The seal integrity, capacity retention, cycle life, compatibility with existing module designs, and mass-volume cost estimates indicate their suitability for electric vehicles and other advanced battery applications. One of the two FBGs was enclosed in a special tubing to make it selectively sensitive to thermal variations alone. The tracked wavelength peak values of the “reference” FBGs in the tubing are subtracted from the total wavelength shift of the adjacent FBG sensor, which is sensitive to strain so that temperature variations are compensated. The second part focuses on the internal strain and temperature signals got under different conditions and their use for high-accuracy cell state estimation algorithms. In particular, the measured strain is used to estimate the battery capacity and predict the capacity up to 10 cycles.

Nascimento et al. have also reported many studies regarding the simultaneous decoupling temperature and strain variations in LIBs through FBGs and interferometric sensors (**Figure 14**). Different type of LIBs was tested on this discrimination. The prismatic and cylindrical configurations were tested externally and pouch cell configurations were tested both internally and externally [25, 37, 40, 44]. In 2015, FBGs were attached to the surface of a cylindrical LIB to track its thermal and strain fluctuations during charge and different discharge C-rates (**Figure 14A**). The tests were repeated twice for each discharge C-rate applied (0.25 C and 1.33 C). The FBG1 and FBG2 only measured temperature variations, while FBG3 was fixed to the battery edges and was subjected to strain and temperature variations. Temperature measurements made by the FBG2 sensor were used to compensate for thermal effects on FBG3, allowing in this way to measure the longitudinal strain variation along the battery length [25]. In 2018, a network of FBGs was attached at a prismatic LiB to sense its temperature and bi-directional (x- and y-directions) strain variations during normal charge and two different discharge C-rates (1.32 C and 5.77 C). The discrimination method used by the OFS was also the reference FBG method [66]. Maximum temperature variations were detected close to the positive electrode side, and higher

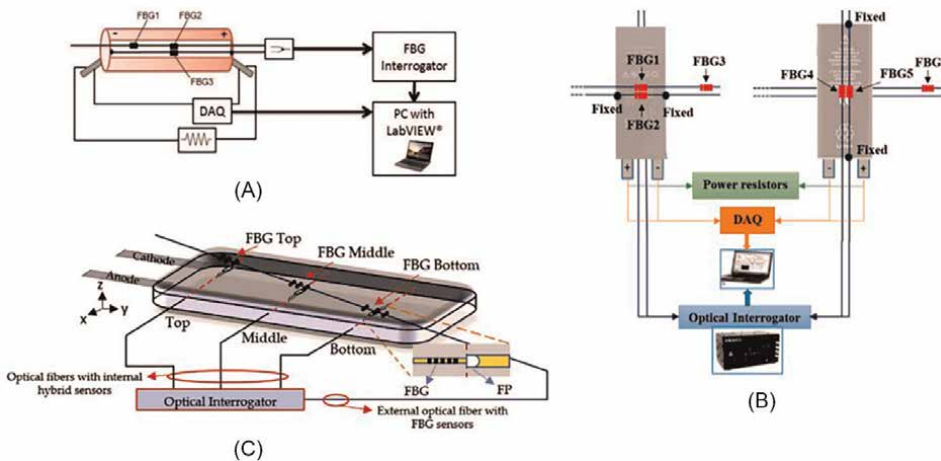


**Figure 14.** Temperature and strain discrimination by OFS in different LIBs configurations. A) Cylindrical B) Prismatic C) Pouch cell [25, 37, 44]. Copyrights 2015, 2018, 2019.

strain values were sensed in the  $y$ -direction (**Figure 14B**). One year later, fiber optic hybrid sensors were embedded in a Li-ion pouch cell to internally monitor and simultaneously discriminate *in situ* and operando strain and temperature shifts in different locations (**Figure 14C**). The hybrid sensing network was constituted by FBGs and FP interferometers. Due to the different strain and temperature sensitivities attained by both types of optical sensors, it was possible to decouple the strain and temperature values by using the matrixial method. Galvanostatic cycles by using different C-rates were applied to correlate the temperature and strain signals with electrochemical processes in the LIB.

In 2017, Fortier et al. also tracked internal strain and temperature variations in the coin cell configuration [35]. However, how this decouple was performed is not explicit in the manuscript. The batteries were evaluated at a cycling C/20 rate, and the FBGs were placed between electrodes and separator layers, near the electrochemically active area. Results show a stable strain behavior within the cell and a near of 10.0°C difference was registered between the interior of the coin cell and room environment temperature over time during cycling steps.

In 2019, a novel-designed OFS, about self-compensating FBGs, to monitor the separator internal status of a LIB by detecting the RI of the battery electrolyte, was proposed by Nedjalkov et al. [48]. The proposed sensor consisted of two FBGs recorded of the same length but in different fiber layers (one on the core and the other near the surface of the cladding, by using a femtosecond laser system). The cladding, near the FBG region, was also softly etched to increase the sensitivity for RI variations. Between the surface FBG, an additional waveguide positioned at half the distance between the fiber core and cladding surfaces in the radial direction was integrated into the inner cladding at the same axial position. Both the influences of the longitudinal strain and temperature could be compensated with this arrangement, so the remaining variable of the measurement was the influence of the effective RI, which was relative to the reflected Bragg wavelength shift. The proposed FBG configuration was embedded centrally between two separator layers of a 5 Ah lithium-ion pouch cell. The results obtained, show that the optical signal was dominantly influenced by the effective RI of the battery electrolyte.

Huang et al., in 2020, published one study, about operando decoding of chemical and thermal events in commercial LIB, by discriminating and sensing temperature and pressure variations through FBGs and microstructured optical fibers (MOF) [51]. The sensing of different parameters was performed, thanks to the different sensitivities of both optical sensors at each parameter (temperature and pressure), in which the matrixial method was applied. These findings allowed to detect chemical events such as the SEI formation and structural evolution in the LIBs. The authors also demonstrate how multiple sensors are used to determine the heat generated by converting the optical data to heat flux values. In the last year, they also demonstrate the feasibility and diversity of TFBGs to operando access the chemistry and states of electrolytes [2]. They show how a single TFBG can simultaneously sense temperature and RI evolutions inside LIB, which is correlated with the chemical electrolyte behavior (see **Figure 15**). From the time-resolved RI signals, the feasibility of monitoring electrolyte deteriorations while accessing their turbidity via particulate-induced optical scattering and absorption was studied as well. These unraveled electrolyte characteristics by TFBG help to determine the electrochemical reaction pathways, being strongly correlated with the batteries' capacity loss.

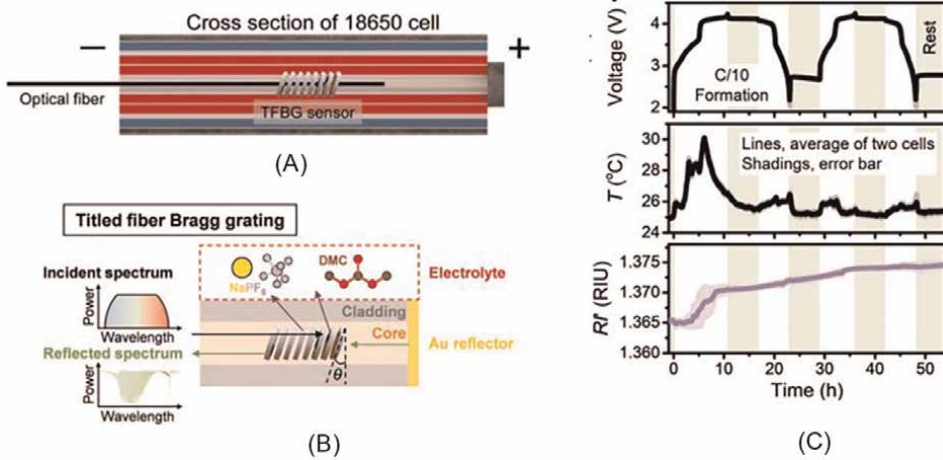


**Figure 15.** Schematics and spectra of the TFBG used by Huang et al. [2]. A) TFBG inserted in the core of a cylindrical LIB. B) A gold layer was deposited on the end of TFBG to obtain the reflection probe. C) The temporal voltage, temperature, and RI of two cells during the first two formation cycles at C/10.

## 4. Conclusions

This chapter fully describes all main optical fiber sensing techniques used and developed for tracking critical key parameters in LIBs since the first study in 2013. According to the operating principles, FBGs, FPIs, optical fiber evanescent waves, and optical fiber photoluminescent sensors are being used so far. Regarding all the studies selected to perform this overview, the principal parameters presented in the literature were temperature (heat flow), strain, pressure, electrochemical events (such as electrode lithiation and gassing production), RI, and SoX battery indicators (such as SoC, SoD, and SoH). In a general overview, the FBGs, FPIs, and photoluminescent sensors are mostly used to track the physical parameters instead of the evanescent wave sensors are most used to detect the electrochemical events in LIBs due to the necessity of measuring RI values from the surrounding materials that interact with the optical fiber surfaces, in this case.

Between all OFS used in the battery sensing applications and with an easier correlation with BMS, the FBGs coupled with other types of sensors (interferometers and/or evanescent wave sensors), seem to be the most advantageous in the future battery applications, due to their intrinsic characteristics, of the possibility of multipoint and multiparameter monitor, and easy interrogation, operating in a reflection system. Those factors detected have a good alliance with the battery SoX, thus can greatly reflect the battery failure condition. However, the development of sensors for battery tracking is still not consistent with the goal of massive processing, low cost, and daily applications. Some problems, such as excessive data treatments, and the high fragility of some optical fibers (reduced thickness) still exist. Generally, the optimal result of *in situ/operando* sensing is to real-time monitor and interpret each shift of wavelength into a concrete chemical reaction, so that the precise battery SoX estimation of BMS can be achieved and corresponding actions can be taken place from the external to sustain the continuing operation of batteries.

Comparatively, with other sensing tools or instruments that were also used to monitor critical parameters in LIBs, such as TCs, RTDs, thermography, and, strain gauges, the OFS presents several advantages. They can be embedded in the electrochemical environment of the cells, detecting with elevated accuracy and simultaneously, in multipoint and multiparameter, which are until now, completely unknown, such as the internal pressure and RI variations, which are directly correlated with electrochemical cells events (SEI layer formation).

This advancement in sensing internal and operational batteries using OFS will allow for the improvement of their performance and safety and will help in understanding and improving the lifetime and behavior of the next generation of LIBs to be developed.

## **Acknowledgements**

The authors gratefully acknowledge the European Project “Innovative physical/virtual sensor platform for battery cell” (INSTABAT) (European Union’s Horizon 2020 research and innovation program under grant agreement No 955930), website: <https://www.instabat.eu/> . Carlos Marques acknowledges the financial support from FCT through the project DigiAqua (PTDC/EEI-EEE/0415/2021) and CEECIND/00034/2018 (iFISH project). The authors also acknowledge the financial support within the scope of the project i3n, UIDB/50025/2020 & UIDP/50025/2020, financed by national funds through the FCT/MEC.

## **Conflict of interest**

The authors declare no conflict of interest.

## **Appendices and nomenclature**

BMS	Battery management system
DTW	Dynamic time warping
FBG	Fiber Bragg grating
FPI	Fabry-Perot interferometer
FSR	Free spectral range
IR	Infrared
LIB	Lithium-ion battery
OFS	Optical fiber sensors
MOF	Microstructured optical fiber
MZI	Mach-Zehnder interferometer
RI	Refractive index
RTD	Resistance temperature detector
SEI	Solid electrolyte interface
SoC	State of charge
SoD	State of discharge
SoH	State of health
SMR	Single-mode fiber

SPR	Surface plasmon resonance
SRI	Surrounding refractive index
TC	Thermocouple
TFB	Tilted fiber Bragg
G UV	grating Ultraviolet

## **Author details**

Micael Nascimento\*, Carlos Marques and João Pinto  
Department of Physics and i3N, University of Aveiro, Campus de Santiago, Portugal

\*Address all correspondence to: micaelnascimento@ua.pt

## **IntechOpen**

---

© 2022 The Author(s). Licensee IntechOpen. This chapter is distributed under the terms of the Creative Commons Attribution License (<http://creativecommons.org/licenses/by/3.0>), which permits unrestricted use, distribution, and reproduction in any medium, provided the original work is properly cited. 

## References

- [1] Rogelj J, den Elzen M, Höhne N, et al. Paris Agreement climate proposals need a boost to keep warming well below 2°C. *Nature*. 2016;**534**:631-639. DOI: 10.1038/nature18307
- [2] Huang J, Han X, Liu F, Gervillie C, Blanquer LA, Guo T, et al. Monitoring battery electrolyte chemistry via in-operando tilted fiber Bragg grating sensors. *Energy & Environmental Science*. 2021;**14**:6464–6475. DOI: 10.1039/d1ee02186a
- [3] Pillot C. *The Rechargeable Battery Market and Main Trends 2016–2025*. Mainz: AABC Europe; 2017
- [4] Schmuch R, Wagner R, Hörpel G, et al. Performance and cost of materials for lithium-based rechargeable automotive batteries. *Nature Energy*. 2018;**3**:267-278. DOI: 10.1038/s41560-018-0107-2
- [5] Zhang G, Wei X, Tang X, et al. Internal short circuit mechanisms, experimental approaches and detection methods of lithium-ion batteries for electric vehicles: A review. *Renewable and Sustainable Energy Reviews*. Elsevier. 2021;**141**:110790. DOI: 10.1016/j.rser.2021.110790
- [6] Leung PK, Moreno C, Masters I, et al. Real-time displacement and strain mappings of lithium-ion batteries using three-dimensional digital image correlation. *Journal of Power Sources*. 2014;**271**:82-86. DOI: 10.1016/j.jpowsour.2014.07.184
- [7] Wang P, Zhang X, Yang L, et al. Real-time monitoring of internal temperature evolution of the lithium-ion coin cell battery during the charge and discharge process. *Extreme Mechanics Letters*. 2016;**9**:1-8. DOI: 10.1016/j.eml.2016.03.013
- [8] Wang X, Sone Y, Segami G, et al. Understanding volume change in lithium-ion cells during charging and discharging using in situ measurements. *Journal of the Electrochemical Society*. 2007;**154**:A14-A21. DOI: 10.1149/1.2386933
- [9] Lee JH, Lee HM, Ahn S. Battery dimensional changes occurring during charge/discharge cycles-thin rectangular lithium ion and polymer cells. *Journal of Power Sources*. 2003;**119–121**:833-837. DOI: 10.1016/S0378-7753(03)00281-7
- [10] Duh YS, Lin KH, Kao CS. Experimental investigation and visualization on thermal runaway of hard prismatic lithium-ion batteries used in smart phones. *Journal of Thermal Analysis and Calorimetry*. 2018;**132**:1677–1692. DOI: 10.1007/s10973-018-7077-2
- [11] Bandhauer TM, Garimella S, Fuller TF. A critical review of thermal issues in lithium-ion batteries. *Journal of the Electrochemical Society*. 2011;**158**:R1-R25. DOI: 10.1149/1.3515880
- [12] Wang Q, Ping P, Zhao X, et al. Thermal runaway caused fire and explosion of lithium ion battery. *Journal of Power Sources*. 2012;**208**:210-224. DOI: 10.1016/j.jpowsour.2012.02.038
- [13] Mutyala S, Zhao J, Li J, et al. In-situ temperature measurement in lithium ion battery by transferable flexible thin film thermocouples. *Journal of Power Sources*. 2014;**260**:43-49. DOI: 10.1016/j.jpowsour.2014.03.004
- [14] Fu Y, Lu S, Li K, et al. An experimental study on burning

- behaviors of 18650 lithium ion batteries using a cone calorimeter. *Journal of Power Sources*. 2015;**273**:216-222. DOI: 10.1016/j.jpowsour.2014.09.039
- [15] Bolsinger C, Birke KP. Effect of different cooling configurations on thermal gradients inside cylindrical battery cells. *Journal of Energy Storage*. 2019;**21**:222-230. DOI: 10.1016/j.est.2018.11.030
- [16] Goutam S, Timmermans JM, Omar N, Van den Bossche P, Van Mierlo J. Comparative study of surface temperature behavior of commercial lithium pouch cells of different chemistries and capacities by infrared thermography. *Energies*. 2015;**8**: 8175-8192. DOI: 10.3390/en8088175
- [17] Wang P, Zhang X, Yang L, Zhang X, Yang M, Chen H, et al. Real-time monitoring of internal temperature evolution of the lithium-ion coin cell battery during the charge and discharge process. *Extreme Mechanics Letters*. 2016;**9**:459-466. DOI: 10.1016/j.eml.2016.03.013
- [18] Leung PK, Moreno C, Masters I, Hazra S, Conde B, Mohamed MR, et al. Real-time displacement and strain mappings of lithium-ion batteries using threedimensional digital image correlation. *Journal of Power Sources*. 2014;**271**:82-86. DOI: 10.1016/j.jpowsour.2014.07.184
- [19] Yang G, Leitão C, Li Y, Pinto J, Jiang X. Real-time temperature measurement with fiber Bragg sensors in lithium batteries for safety usage. *Measurement*. 2013;**46**:3166-3172. DOI: 10.1016/j.measurement.2013.05.027
- [20] Lochbaum A, Kiesel P, Sommer LW, Bae CJ, Staudt T, Saha B, et al. Embedded fiber optic chemical sensing for internal cell side-reaction monitoring in advanced battery management systems. *Materials Research Society Symposium Proceedings*. 2014;**1681**:8-13. DOI: 10.1557/opl.2014.670
- [21] Sommer LW, Raghavan A, Kiesel P, Saha B, Staudt T. Embedded fiber optic sensing for accurate state estimation in advanced battery management systems. *Materials Research Society Symposium Proceedings*. 2014;**1681**:1-7. DOI: 10.1557/opl.2014.560
- [22] Sommer LW, Kiesel P, Ganguli A, Lochbaum A, Saha B, Schwartz J, et al. Fast and slow ion diffusion processes in lithium ion pouch cells during cycling observed with fiber optic strain sensors. *Journal of Power Sources*. 2015;**296**: 46-52. DOI: 10.1016/j.jpowsour.2015.07.025
- [23] Alemohammad H, Ghannoum A, Zdravkova L, Iyer K, Nieva P, Yu A, et al. Embedded fiber optic sensors for battery performance monitoring in lithium ion battery cells. In: *Advanced Manufacturing, Electronics and Microsystems: TechConnect Briefs*. 2015
- [24] Meyer J, Nedjalkov A, Doeringa A, Angelmahr M, Schade W. Fiber optical sensors for enhanced battery safety. *Proceedings of SPIE*. 2015;**9480**:94800Z
- [25] Nascimento M, Novais S, Leitão C, Domingues MF, Alberto N, Antunes P, et al. Lithium batteries temperature and strain fiber monitoring. *Proceedings of SPIE*. 2015;**9634**:96347V. DOI: 10.1117/12.2195218
- [26] Novais S, Nascimento M, Le G, Domingues MF, Antunes P, et al. Internal and external temperature monitoring of a Li-ion battery with fiber Bragg grating sensors. *Sensors*. 2016;**16**: 1-9. DOI: 10.3390/s16091394

- [27] Bae CJ, Manandhar A, Kiesel P, Raghavan A. Monitoring the strain evolution of lithium-ion battery electrodes using an optical fiber Bragg grating sensor. *Energy Technology*. 2016;4:851-855. DOI: 10.1002/ente.201500514
- [28] Ghannoum A, Norris RC, Iyer K, Zdravkova L, Yu A, Nieva P. Optical characterization of commercial lithiated graphite battery electrodes and in situ fiber optic evanescent wave spectroscopy. *ACS Applied Materials & Interfaces*. 2016;8(29):18763-18769. DOI: 10.1021/acsami.6b03638
- [29] Nascimento M, Ferreira MS, Pinto JL. Impact of different environmental conditions on lithium-ion batteries performance through the thermal monitoring with fiber sensors. *Proceedings of SPIE*. 2017;10453:104532S. DOI: 10.1117/12.2276331
- [30] Nascimento M, Ferreira MS, Pinto JL. Real time thermal monitoring of lithium batteries with fiber sensors and thermocouples: A comparative study. *Measurement*. 2017;111:260-263. DOI: 10.1016/j.measurement.2017.07.049
- [31] Ghannoum A, Nieva PM, Yu A, Khajepour A. Development of embedded fiber optic evanescent wave sensors for optical characterization of graphite anodes in lithium-ion batteries. *ACS Applied Materials & Interfaces*. 2017;9(47):41284-41290. DOI: 10.1021/acsami.7b13464
- [32] Raghavan A, Kiesel P, Sommer LW, Schwartz J, et al. Embedded fiber-optic sensing for accurate internal monitoring of cell state in advanced battery management systems part 1: Cell embedding method and performance. *Journal of Power Sources*. 2017;341:466-473. DOI: 10.1016/j.jpowsour.2016.11.104
- [33] Ganguli A, Saha B, Raghavan A, Kiesel P, et al. Embedded fiber-optic sensing for accurate internal monitoring of cell state in advanced battery management systems part 2: Internal cell signals and utility for state estimation. *Journal of Power Sources*. 2017;341:474-482. DOI: 10.1016/j.jpowsour.2016.11.103
- [34] Ghannoum A, Iyer K, Nieva P, Khajepour A. Fiber optic monitoring of lithium-ion batteries: A novel tool to understand the lithiation of batteries. *IEEE Sensors*. 2016;1:1-3. DOI: 10.1109/ICSENS.2016.7808695
- [35] Fortier A, Tsao M, Williard ND, Xing Y, Pecht MG. Preliminary study on integration of fiber optic Bragg grating sensors in Li-ion batteries and in situ strain and temperature monitoring of battery cells. *Energies*. 2017;10(838):1-11. DOI: 10.3390/en10070838
- [36] Nascimento M, Paixão T, Ferreira MS, Pinto JL. Thermal mapping of a lithium polymer batteries pack with FBGs network. *Batteries*. 2018;4(67):1-12. DOI: 10.3390/batteries4040067
- [37] Nascimento M, Ferreira MS, Pinto JL. Simultaneous sensing of temperature and Bi-directional strain in a prismatic Li-ion battery. *Batteries*. 2018;4(23):1-9. DOI: 10.3390/batteries4020023
- [38] Fleming J, Amietszajew T, McTurk E, et al. Development and evaluation of in-situ instrumentation for cylindrical Li-ion cells using fiber optic sensors. *Hardware X*. 2018;3:100-109. DOI: 10.1016/j.ohx.2018.04.001
- [39] Lao J, Sun P, Liu F, Zhang X, Zhao C, et al. In situ plasmonic optical fiber detection of the state of charge of

supercapacitors for renewable energy storage. *Light: Science & Applications*. 2018;7(34):1-11. DOI: 10.1038/s41377-018-0040-y

[40] Nascimento M, Ferreira MS, Pinto JL. Strain and temperature discrimination in operando Li-ion polymer batteries. In: 26th International Conference on Optical Fiber Sensors. 2018

[41] McTurk E, Amietszajew T, Fleming J, Bhagat R. Thermo-electrochemical instrumentation of cylindrical Li-ion cells. *Journal of Power Sources*. 2018;379:309-316. DOI: 10.1016/j.jpowsour.2018.01.060

[42] Amietszajew T, McTurk E, Fleming J, Bhagat R. Understanding the limits of rapid charging using instrumented commercial 18650 high-energy Li-ion cells. *Electrochimica Acta*. 2018;263:346-352. DOI: 10.1016/j.electacta.2018.01.076

[43] Nascimento M, Ferreira MS, Pinto JL. Temperature fiber sensing of Li-ion batteries under different environmental and operating conditions. *Applied Thermal Engineering*. 2019;149:1236-1243. DOI: 10.1016/j.applthermaleng.2018.12.135

[44] Nascimento M, Novais S, Ding MS, Ferreira MS, et al. Internal strain and temperature discrimination with optical fiber hybrid sensors in Li-ion batteries. *Journal of Power Sources*. 2019;410-411:1-9. DOI: 10.1016/j.jpowsour.2018.10.096

[45] Peng J, Zhou X, Jia S, Xu S, Chen J. Design of a sensitivity-enhanced FBG strain sensor and its application in state estimation for lithium-ion battery. *Optical Fiber Sensors and Communication*. 2019. DOI: 10.1117/12.2539787

[46] Modrzyński C, Roscher V, Rittweger F, Ghannoum AR, Nieva P, Riemschneider KR. Integrated optical fibers for simultaneous monitoring of the anode and the cathode in lithium ion batteries. *IEEE Sensors*. 2019;1:1-4. DOI: 10.1109/SENSOR43011.2019.8956755

[47] Peng J, Zhou X, Jia S, Jin Y, Xu S, Chen J. High precision strain monitoring for lithium ion batteries based on fiber Bragg grating sensors. *Journal of Power Sources*. 2019;433:1-7. DOI: 10.1016/j.jpowsour.2019.226692

[48] Nedjalkov A, Meyer J, Gräfenstein A, et al. Refractive index measurement of lithium ion battery electrolyte with etched surface cladding waveguide bragg gratings and cell electrode state monitoring by optical strain sensors. *Batteries*. 2019;5(30):1-20. DOI: 10.3390/batteries5010030

[49] Hedman J, Nilebo D, Langhammer EL, Björefors F. Fiber optic sensor for characterisation of lithium-ion batteries. *ChemSusChem*. 2020;13:5731-5739. DOI: 10.1002/cssc.202001709

[50] Ghannoum A, Nieva P. Graphite lithiation and capacity fade monitoring of lithium ion batteries using optical fibers. *Journal of energy storage*. 2020;28:1-5. DOI: 10.1016/j.est.2020.101233

[51] Huang J, Blanquer LA, Bonefacino J, Logan ER, et al. Operando decoding of chemical and thermal events in commercial Na(Li)-ion cells via optical sensors. *Nature Energy*. 2020;5:674-683. DOI: 10.1038/s41560-020-0665-y

[52] Miele E, Dose WM, Manyakin I, Frosz MH, Grey CP, Baumberg JJ, et al. Optofluidic hollow-core fibers as Raman sensors for Li-ion battery chemistry. In: 22nd International Conference on

Transparent Optical Networks (ICTON). 2020

[53] Peng J, Jin Y, Jia SXS. External electrode temperature monitoring of lithium iron phosphate batteries based on fiber bragg grating sensors. IOP Conference Series: Earth and Environmental Science. 2020;**495**: 012002. DOI: 10.1088/1755-1315/495/1/012002

[54] Alcock KM, Grammel M, González-Vila A, Binetti L, Goh K, Alwis LSM. An accessible method of embedding fiber optic sensors on lithium-ion battery surface for in-situ thermal monitoring. Sensors and Actuators, A: Physical. 2021; **332**:1-9. DOI: 10.1016/j.sna.2021.113061

[55] Peng J, Jia S, Yu H, Kang X, Yang S, Xu S. Design and experiment of FBG sensors for temperature monitoring on external electrode of lithium-ion batteries. IEEE Sensors Journal. 2021; **21**(4):1-8. DOI: 10.1109/JSEN.2020.3034257

[56] Clerici D, Mocer F, Somá A. Experimental characterization of lithium-ion cell strain using laser sensors. Energies. 2021;**14**(19):1-17. DOI: 10.3390/en14196281

[57] Rente B, Fabian M, Vidakovic M, Liu X, Li X, Li K, et al. Lithium-ion battery state-of-charge estimator based on FBG-based strain sensor and employing machine learning. IEEE Sensors Journal. 2021;**21**(2):1-6. DOI: 10.1109/JSEN.2020.3016080

[58] Li H, Wei F, Li Y, Miao Y, Zhang Y, Liu L, et al. Optical fiber sensor based on upconversion nanoparticles for internal temperature monitoring of Li-ion batteries. Journal of Materials Chemistry C. 2021;**9**:14757. DOI: 10.1039/d1tc03701c

[59] Rittweger F, Modrzynski C, Schiepel P, Riemschneider KR. Self-compensation of cross influences using spectral transmission ratios for optical fiber sensors in lithium-ion batteries. IEEE Sensors Applications Symposium (SAS). 2021;**1**:1-6. DOI: 10.1109/SAS51076.2021.9530176

[60] Hecht J. City of Light: The Story of Fiber Optics. New York: Oxford University Press; 1999

[61] Borner M. Electro-optical transmission system utilizing lasers. US Patent 3,845,293. 1974

[62] Minowa J, Ishio H, Nosu K. Review and status of wavelength-division-multiplexing technology and its application. Journal of Lightwave Technology. 1984;448-463. DOI: 10.1109/JLT.1984.1073653

[63] Raffaella DS. Fiber optic sensors for structural health monitoring of aircraft composite structures: Recent advances and applications. Sensors. 2015;**15**: 18666-18713. DOI: 10.3390/s150818666

[64] Johnson C, Hill KO, Fujii Y, Kawasaki BS. Photosensitivity in optical fiber waveguides: Application to reflection filter fabrication. Applied Physics Letters. 2008;**32**:647. DOI: 10.1063/1.89881

[65] Lutang W, Nian F. Applications of fiber-optic interferometry technology in sensor fields. In: Banishev A, Bhowmick M, Wang J, editors. Optical Interferometry. London, UK: IntechOpen; 2017

[66] Rao YJ. Fiber Bragg grating sensors: Principles and applications. Optical Fiber Sensor Technology. 1998;**2**:355-389

[67] Jin W. Simultaneous measurement of strain and temperature: Error analysis.

Optical Engineering. 1997;**36**:598.  
DOI: 10.1117/1.601233

[68] James SW, Dockney ML, Tatam RP. Simultaneous independent temperature and strain measurement using in-fibre Bragg grating sensors. Electronics Letters. 1996;**32**:1133-1334.  
DOI: 10.1049/el:19960732

[69] Guan BO, Tam HY, Tao XM, Dong XY. Simultaneous strain and temperature measurement using a superstructure fiber Bragg grating. IEEE Photonics Technology Letters. 2000;**12**: 675-677. DOI: 10.1109/68.849081

[70] Singh N, Jain SC, Aggarwal AK, Bajpai RP. Fiber Bragg grating writing using phase mask technology. Journal of Scientific and Industrial Research. 2005; **64**:108-115

[71] Erdogan T, Sipe J. Tilted fiber phase gratings. Journal of the Optical Society of America. 1996;**13**:296-313

[72] Alberto NJ, Marques CA, Pinto JL, Nogueira RN. Three-parameter optical fiber sensor based on a tilted fiber Bragg grating. Applied Optics. 2010;**49**: 6085-6091. DOI: 10.1364/AO.49.006085

[73] Fabry C, Perot A. Sur les franges des lames minces argentées et leur application a la mesure de petites épaisseurs d'air. Annales Chimie et de Physique. 1897;**12**:459-501

[74] Lee BH, Kim YH, Park KS, Eom JB, Kim MJ, Rho BS, et al. Interferometric fiber optic sensors. Sensors. 2012;**12**: 2467-2486. DOI: 10.3390/s120302467

[75] Tsai WH, Lin CJ. A novel structure for the intrinsic Fabry-Perot fiber-optic temperature sensor. Journal of Lightwave Technology. 2001;**19**: 682-686. DOI: 10.1109/50.923481

[76] Zhao Y, Zhao H, Lv RQ, Zhao J. Review of optical fiber Mach-Zehnder interferometers with micro-cavity fabricated by femtosecond laser and sensing applications. Optics and Lasers in Engineering. 2019;**117**:7-20.  
DOI: 10.1016/j.optlaseng.2018.12.013

[77] Yin MJ, Gu B, An QF, Yang C, Guan YL, Yong KT. Recent development of fiber optic chemical sensors and biosensors: Mechanisms, materials, micro/nano fabrications and applications. Coordination Chemistry Reviews. 2018;**376**:348-392.  
DOI: 10.1016/j.ccr.2018.08.001

[78] Feng X, Fang M, He X, Ouyang M, Lu L, Wang H, et al. Thermal runaway features of large format prismatic lithium ion battery using extended volume accelerating rate calorimetry. Journal of Power Sources. 2014;**255**: 294-301. DOI: 10.1016/j.jpowsour.2014.01.005

# Investigations of Using an Intelligent ANFIS Modeling Approach for a Li-Ion Battery in MATLAB Implementation: Case Study

*Roxana-Elena Tudoroiu, Mohammed Zaheeruddin,  
Nicolae Tudoroiu and Sorin Mihai Radu*

## Abstract

This research paper will propose an incentive topic to investigate the accuracy of an adaptive neuro-fuzzy modeling approach of lithium-ion (Li-ion) batteries used in hybrid electric vehicles and electric vehicles. Based on this adaptive neuro-fuzzy inference system (ANFIS) modeling approach, we will show its effectiveness and suitability for modeling the nonlinear dynamics of any process or control system. This new ANFIS modeling approach improves the original nonlinear battery model and an alternative linear autoregressive exogenous input (ARX) polynomial model. The alternative ARX is generated using the least square errors estimation method and is preferred for its simplicity and faster implementation since it uses typical functions from the MATLAB system identification toolbox. The ARX and ANFIS models' effectiveness is proved by many simulations conducted on attractive MATLAB R2021b and Simulink environments. The simulation results reveal a high model accuracy in battery state of charge (SOC) and terminal voltage. An accurate battery model has a crucial impact on building a very precise adaptive extended Kalman filter (AEKF) SOC estimator. It is considered an appropriate case study of a third-order resistor-capacitor equivalent circuit model (3RC ECM) SAFT-type 6 Ah 11 V nominal voltage of Li-ion battery for simulation purposes.

**Keywords:** battery management system, Li-ion battery model, battery SOC, SOC UKF estimator, ANFIS model, ARX model, NMSS model, terminal voltage

## 1. Introduction

The most sustainable strategy to accomplish clean and efficient transport is to stimulate the automotive hybrid electric vehicles (HEVs)/electric vehicles (EVs) industry by developing the most advanced battery technologies. There is massive

competition in the markets for selling batteries with different chemistry, especially between the most common nickel-metal hydride (Ni-MH), nickel-cadmium (Ni-Cad) and lithium-ion (Li-ion) batteries. More recently, it seems that the most promising future and great potential of development for HEVs/EVs automotive industry worldwide have the Li-ion batteries due to their advantages compared with other strong competitors on the market. They surpass these competitors by features such as lightweight, high-energy-density, little memory effect, and relatively low self-discharge, as is mentioned in [1, 2]. Furthermore, after substantial improvements and research investments, the Li-ion batteries have become safer and less toxic. The battery state of charge (SOC) represents the available capacity of the battery cell that changes corresponding to the fluctuations in the input charging and discharging current profile during a cycle. It is worth mentioning that the SOC plays a crucial role in keeping the battery safe for various operating conditions and significantly extending battery life [3, 4]. Moreover, the SOC is an essential internal battery parameter of great significance constantly monitored by the battery management system (BMS) [1–6]. In real life, a specialized software package integrated onboard the vehicle estimates the value of the battery SOC due to the lack of an accurate measurement sensor integrated into BMS [1–7]. Let us see why the battery SOC has become a topic of great interest for researchers working in the field, very dedicated for developing the most suitable estimation techniques and strategies supported today by an impressive number of research papers published in the literature. The most used model-based Kalman filter (KF) can estimate the battery SOC with a high accuracy grade [3–7]. The BMS monitors the battery system through sensors and state estimation algorithms to detect any abnormalities during the battery system operation [8, 9]. The performance of the battery SOC estimators' model is highly dependent on the battery model accuracy. If the battery model is accurate, then the different SOC estimation versions will estimate the battery SOC with the same accuracy. Consequently, the battery model is essential for implementing the most suitable SOC estimators. It is always desirable to get a battery model as accurate as the actual battery to reduce the mismatch between the model and the existing battery. Moreover, the battery SOC is “a critical factor in guaranteeing that a battery system operates safely and reliably,” as is mentioned in [10]. Also, “many uncertainties and noises, such as current, sensor measurement accuracy and bias, temperature effects, calibration errors or even sensor failure, etc., pose a challenge to the accurate estimation of SOC in real applications” [10].

Additionally, over time, the effects of battery aging will be more noticeable in degrading its performance, and the mismatch between the battery model and the actual battery will also increase. In the “real-life” applications subjected to the plant/process identification, fixing the possible mismatches between the plant/process and their corresponding models with repeated effective re-identification procedures is almost inapplicable and time-consuming, as is revealed in [10–12]. Therefore, mismatch detection is essential for different plants/processes modeling and identification strategies to isolate defective submodules to avoid complete re-identification, as mentioned in [11].

### **1.1 State-of-the-art Li-ion battery models and SOC estimators**

A suitable identification plant/process strategy is developed in [10–12] that is a polynomial discrete state-space representation of the plant/process models based on a

plant/process input-output measurement data set collected in an open loop. The plant/process input-output measurement data set is used to develop and implement two attractive statistical models.

The first model is a linear discrete state-space autoregressive exogenous input (ARX) polynomial representation, beneficial to model a 60 Ah LiFePO<sub>4</sub> battery module [10]. Based on this model, an extended Kalman filter (EKF) battery SOC estimator is developed for BMSs. The second model is an auto-regressive moving average with exogenous input (ARMAX) model developed in [12]. The adaptability of ARX battery models developed in [10] for designing a robust and accurate EKF SOC estimator is rigorously assessed in the same reference [10]. Some simulation results indicate that the proposed EKF SOC battery module estimator based on the ARX model shows a “great performance” in terms of robustness and SOC accuracy [10]. Additionally, the proposed EKF battery estimator “increases the model output voltage accuracy, thereby having the potential to be used in real applications, such as EVs and HEVs” [10]. Two MIMO ARMAX models are developed in [12] for modeling and identification of heating, ventilation, and air-conditioning (HVAC) multi-input multi-output (MIMO) centrifugal chiller plant. This model is built and implemented in a MATLAB simulation environment to develop two accurate MIMO proportional integral-plus (PIP) control strategies in a closed loop for temperature control and refrigerant liquid control level. For comparison purposes in [11], ARX and ARMAX polynomial discrete-time plant representations are built as decorrelation models for detecting model-plant mismatch for a column distillation integrated into a model predictive control (MPC) strategy. Detailed simulations in [11] show that the ARMAX models provide:

- Higher accuracy
- Less computational complexity
- Less processing power is required with less model order than ARX.

Moreover, in [12], ARMAX models are developed for an MIMO HVAC centrifugal chiller open-loop control system using the identification techniques presented in MATLAB Identification Toolbox [13]. Also, for the same HVAC plant, an MIMO ARMAX open-loop polynomial model helps implement an interesting closed-loop proportional integral-plus (PIP) control strategy of chiller plant temperature and liquid-level refrigerant. Both ARX and ARMAX models are helpful in [12] for implementing an extended MIMO PIP control strategy as a new modeling approach in a non-minimal discrete-time state-space system representation (NMSS). The MATLAB simulation results show a superior accuracy of the MIMO NMSS centrifugal chiller model compared with the ARMAX models. Therefore, the MIMO PIP closed-loop control strategy based on the MIMO NMSS models performs better than those built on the MIMO ARMAX models of the MIMO chiller plant, as is proved in [12, 13].

Taking advantage of the considerable advances in modeling, identification, and control systems developed in the field of literature, thanks to the latest achievements in artificial intelligence, statistics and machine learning, deep learning, signal process analysis, our research objectives diversify with new approaches. The most recent results in modeling and identification for various industrial applications reported in the literature field motivate us to investigate attractive new modeling approaches.

Then remains to adapt these approaches to our research topic of developing new Li-ion battery models. Furthermore, the proposed Li-ion battery SOC estimator for a Rint SAFT model of 6 Ah and 11 V nominal voltage in the selected case study is expected to perform much better in terms of accuracy and robustness of the battery SOC estimates for different operating conditions [7]. For simulation and comparison results purposes, as a case study of Li-ion battery, a third-order resistor-capacitor (RC) equivalent circuit model (ECM) (in abbreviated notation 3RC ECM) is considered. It combines three parallel polarization circuits R-C connected in series with the battery's internal resistance (Rint) and voltage source, i.e., as a similar 3RC ECM battery model developed in [7]. The model selection is suggested due to its simplicity and ability to describe the static and dynamic behavior of the Li-ion battery accurately.

Since the proposed Li-ion battery's open-circuit voltage (OCV) has highly nonlinear dependence on the battery SOC, as an alternative block model developed in [7], it is an adaptive neuro-fuzzy inference system (ANFIS) model. It is a hybrid neuro-fuzzy technique that brings the learning capabilities of neural networks to fuzzy inference systems. The learning algorithm tunes the membership functions of a Sugeno-type fuzzy inference system using the training input/output data [14]. More precisely, the learning algorithm teaches the ANFIS to map the input (current driving cycle profile) to the Li-ion battery SOC and terminal voltage through training. At the end of the training, the trained ANFIS network would have learned the input-output map and be ready to be deployed into the Kalman filter SOC estimator solution. The architecture, design, and implementation of the proposed ANFIS battery model are developed in an attractive MATLAB R2021b simulation environment [14–16]. This new battery model adjusts the design techniques and guidelines inspired from [14–33] to the selected model adopted in the case study from [7]. The accuracy of the ANFIS battery model has a significant impact on the SOC Li-ion battery Kalman Filter estimator accuracy performance built on this model. Its effectiveness is proved through extensive simulations and comparisons conducted on the same MATLAB platform. In this research, our motivation for using adaptive neuro-fuzzy training of Sugano-type fuzzy inference system (ANFIS) modeling comes from the preliminary results obtained for similar investigations on the impact of nonlinearities and uncertainties actuators [18]. The ANFIS modeling is well documented in the most recent MATLAB release versions that use the fuzzy logic toolbox and fuzzy inference tuning procedure [14–16]. Handy tutorials of using ANFIS modeling architectures are presented in [14–17]. For MATLAB implementation and simulation intent, as well as “proof concept” in this research, the accuracy of the Li-ion battery ANFIS model is tested for a battery urban dynamometer driving schedule (UDDS) input current profile.

In the proposed case study, for both ARX and ANFIS models an adaptive EKF (AEKF) SOC estimator is adopted attached to Li-ion battery used for creating fault detection and isolation (FDI) control strategies in [12], preferred for its simplicity, SOC accuracy, real-time implementation capability, and robustness. Its robustness is tested for four different scenarios, such as to changes in SOC initial values (guess values), ranging 70–40%, 20, 90, and 100%, to federal test procedure for 75 F (FTP-75) degree Fahrenheit driving cycle profile test, changes in measurement-level noise (from 0.001 to 0.01), to changes in the battery capacity value from 6 Ah to 4.8 Ah due to aging effects, and changes in internal resistance due to temperature effects, and also for simultaneous changes [7, 29]. Based on a rigorous performance

analysis of SOC residual error compared with the similar results reported in the literature with a typically 2% error, in some situations, the AEKF estimator SOC residual error reached values smaller than 1%, such as shown in [29]. Since of the lack of data in the literature field for similar situations developed in our research for Li-ion battery, it is not easy to make a state-of-the-art analysis of the results reported in the literature related to Li-ion battery SAFT 6 Ah and 11 V nominal voltage AEKF SOC estimators based on ANFIS models analysis. The overall ANFIS battery model consists of two ANFIS models, the first one attached to the battery Rint-3RC active part and the second to OCV(SOC) nonlinear block. The SOC and terminal voltages accuracy of the overall battery ANFIS model and AEKF SOC estimators, as well as their robustness to changes in the initial values of the battery SOC from 70 to 40%, are proved in this research paper based on extensive simulations conducted on MATLAB R2021b platform.

## **1.2 Statistical criteria for evaluating the performance of Li-ion battery – SOC and terminal voltage**

Based on MATLAB simulation results useful information on SOC and battery terminal voltage accuracy can be extracted based on SOC and terminal voltage residuals and based on four statistic criteria values shown in eight tables, defined in [29, 30], and grouped as:

- Root mean squared error (RMSE)
- Mean squared error (MSE)
- Mean absolute error (MAE)
- Mean average percentage error (MAPE)

For each Li-ion battery model developed in this research, the SOC and terminal voltage performance are evaluated by simulations conducted on MATLAB Simulink platform. The information extracted from these simulations is beneficial for a rigorous comparison of performance, so that the reader has a better perspective on the modeling, design, and implementation of the battery. From a variety of battery models, the reader has the ability to decide which model and estimator are best for a particular application.

## **1.3 Manuscript structure, objectives, and performed results**

The paper is organized as follows: Section 2 gives a brief description of Rint Li-ion SAFT 6 Ah 11 V nominal voltage and battery selection for the case study, model option, and its validation using the National Renewable Energy Laboratory (NREL) ADVANCED SIMULATOR (ADVISOR) 2003 for HEVs and EVs design. An equivalent electric circuit model (ECM) for the Li-ion battery SAFT Rint model is preferred due to its simplicity and ability to capture all the battery dynamics such that its SOC and the predicted terminal cell voltage are of high accuracy. The dynamics battery part ARX and ANFIS models, the ANFIS battery OCV(SOC) model, their order

selection, parameters identification and model implementation, ANFIS models' generation and performance, and the MATLAB simulation results are shown and discussed in Sections 2 and 3, respectively. For the ARX model and hybrid combinations of the ARX model and ANFIS model of OCV(SOC) nonlinear block, an overall ANFIS battery model consisting of ANFIS dynamic battery part model and ANFIS OCV(SOC) nonlinear battery block models are considered. A rigorous analysis of AEKF SOC estimator adaptability for all these models is evaluated based on simulation results conducted on MATLAB R2021b and Simulink environments that provide valuable information on SOC and battery terminal voltage accuracy and robustness performance. Also, a comparison of the evaluation of the results is made based on the SOC and battery voltage residuals and statistics criteria values summarized in almost eight tables in the last subsection 2.1.3 of Section 2 and all Section 3. Section 4 is dedicated to Conclusions supporting all the previous MATLAB results. In summary, in this research paper an impressive number of investigations are done on the accuracy and adaptability of six alternative Li-ion batteries models to the original NREL Li-ion Rint SAFT-type 6 Ah 11 V rated voltage battery model. The main reason of this selection is that the Li-ion batteries are very common in a wide variety of HEVs/EVs applications in the automotive industry, Also, it is a beneficial option to be used as a baseline model of Li-ion battery for performance comparison and validation of alternative models, among them the linear, simple, and accurate 3RC ECM Li-ion battery model developed in this research work. This alternative model is designed by using one of the most used designing tools very spread in the automotive industry, created by NREL, known as ADVANCED SIMULATOR (ADVISOR) with the final launch in 2003 for HEVs/EVs design. The Li-ion battery model 3RC ECM model is selected for simulation purpose and "proof" concept for developing new alternative battery models. Five alternative models that derivate from 3RC ECM Li-ion battery model are developed in this research work: (a) ARX-ECM that models the dynamic part of the battery represented by the Rint-3RC circuit using an equivalent ARX model; (b) ANFIS-ECM replacing the Rint-3RC circuit with an ANFIS model; (c) ARX-ANFIS hybrid structure that is a combination of ARX model for Rint-3RC dynamic part and an ANFIS model of the nonlinear static block OCV (SOC); (d) Rint-3RC -ANFIS model that keeps the dynamic part of the battery combined with the ANFIS model of OCV(SOC) static block; (e) full ANFIS model structure derived from ARX-ANFIS, which replaces the ARX model with an ANFIS model. The MATLAB simulation results for each model provide a large database stored in 10 useful tables for a rigorous analysis of the performance of the Li-ion battery in terms of SOC accuracy and terminal voltage, as well as the robustness of the AEKF algorithm for estimating the SOC of the selected battery.

## **2. Li-ion battery selection, modeling, MATLAB implementation, and ADVISOR simulator experimental test setup validation**

### **2.1 Li-ion battery model selection, description, and validation: case study**

In this section, we focus our attention on the Li-ion battery selection for the case study, its description, and developing the most suitable battery model of high accuracy. The selected model is validated through an impressive number of simulations conducted on the MATLAB R2021b platform. Then will compare the MATLAB simulations result to an experimental test performed in a similar MATLAB

environment integrated with a specialized simulator ADVISOR for batteries design of different chemistry, which is very spread in the automotive industry. National Renewable Energy Laboratory (NREL) developed this simulator in 1983 and improved its performance until the last release in 2003-00-r0116. A 6 Ah nominal capacity and 11 V nominal voltage SAFT Li-ion battery integrated into the hybrid electric vehicle (HEV) BMS structure, namely a Japanese Toyota Prius, one of the most spread commercial hybrid electric cars on the automotive industry market. It is equipped with an MC-AC75 motor of 75 kW and a powertrain control version, TX-5SPD manual transmission with five speeds and frontal wheel drive, as shown in **Figure 1**. In this figure on the right side, the reader can see the type of vehicle in the database of the ADVISOR simulator considered one of its primary inputs; also, at the bottom side is shown the open-circuit voltage (OCV) graph of the proposed SAFT Li-ion battery as the most suitable for the HEV car selected in the case study.

**Figure 2** shows the Simulink diagram of the Toyota Prius HEV car configuration. In **Figure 3**, you can see the graphical user interface that selects the urban dynamometer driving schedule (UDDS) of cycle speed profile for a driving test, the initial temperature, state of charge (SOC), and the ambient conditions.

In **Figure 4**, the MATLAB simulations results are displayed. Among these results two of the variables of interest can be emphasized, such as the UDDS driving cycle input current profile (ess\_current) and the battery SOC evolution (ess\_soc\_hist).

The UDDS driving cycle of the current profile shown in **Figure 5** is the equivalent of the UDDS driving cycle speed profile shown in the graph in **Figure 3**. It represents

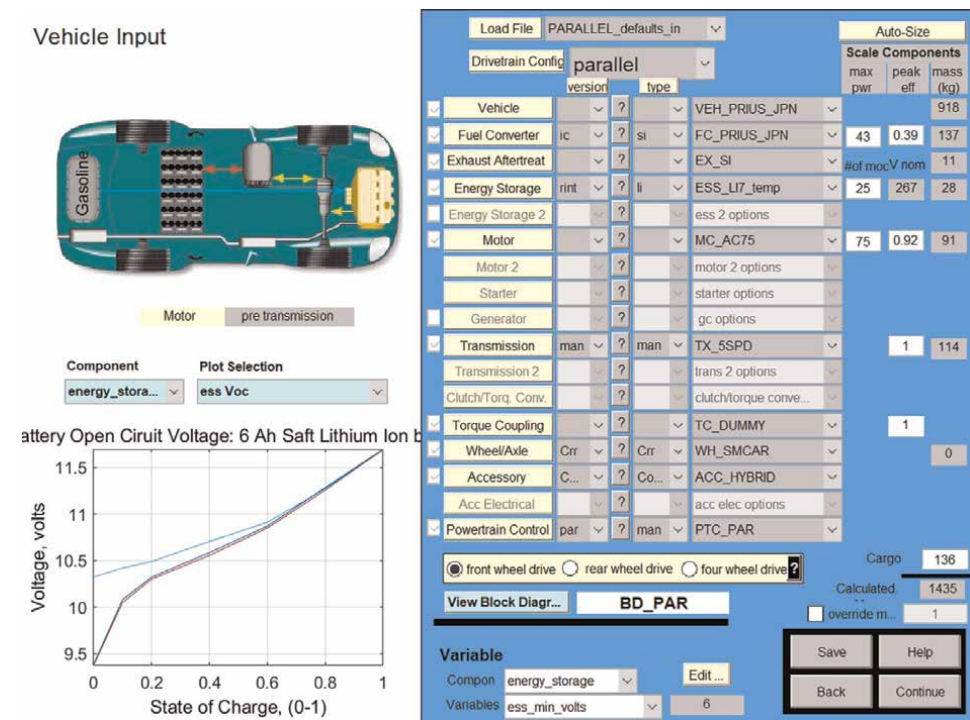


**Figure 1.**  
 The ADVISOR 3.2 simulator -input interface set up.

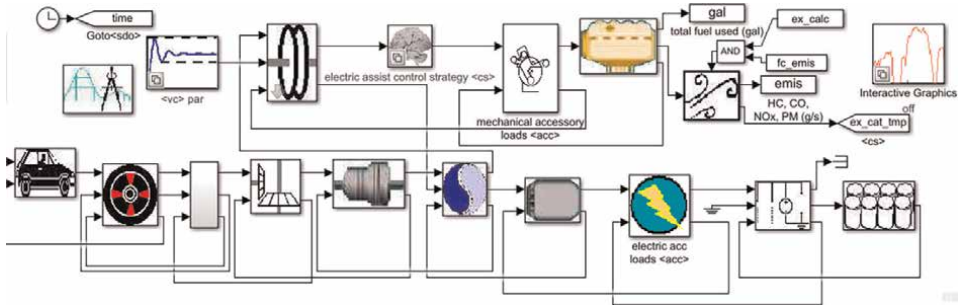


**Figure 2.** Block diagram of HEV powertrain configuration.

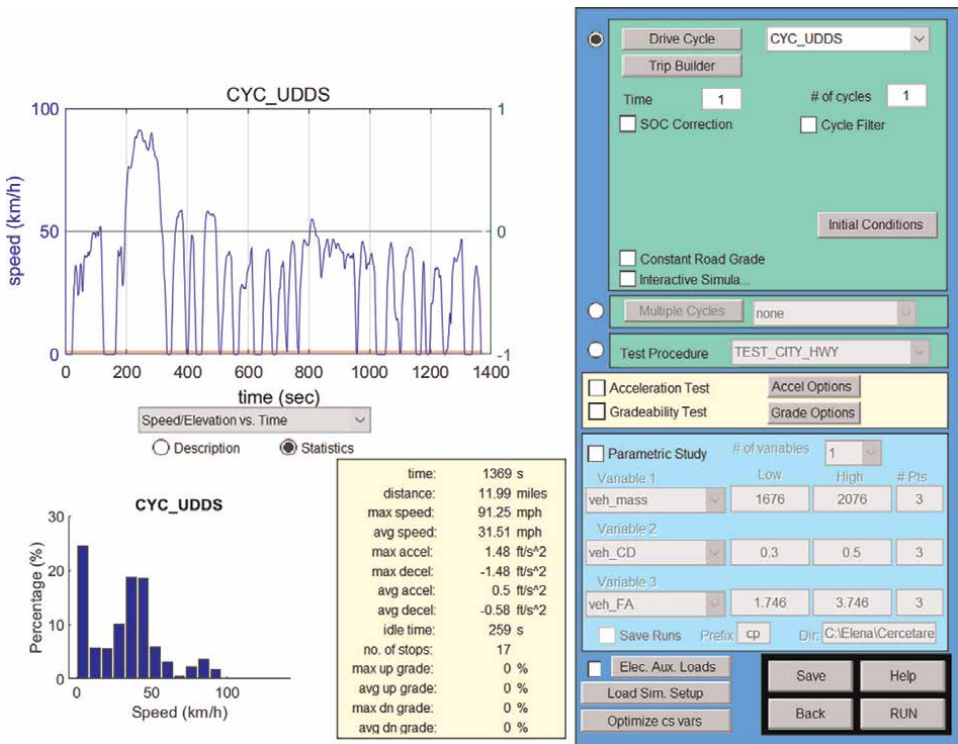


**Figure 3.** Graphical user interface with the ADVISOR simulator parameters.

the evolution of the input battery current during a repeated sequence of charging and discharging the battery for different periods.

More precisely, the ADVISOR 3.2 Simulator provides an extensive Database of different types of HEV cars, driving cycles speed tests, and input currents profiles for battery charging and discharging cycles.

### 2.1.1 Li-ion battery electrical equivalent circuit model

For simulation purposes and “proof concept,” a starting point for developing new Li-ion battery alternative models might be a linear electrical circuit consisting of one

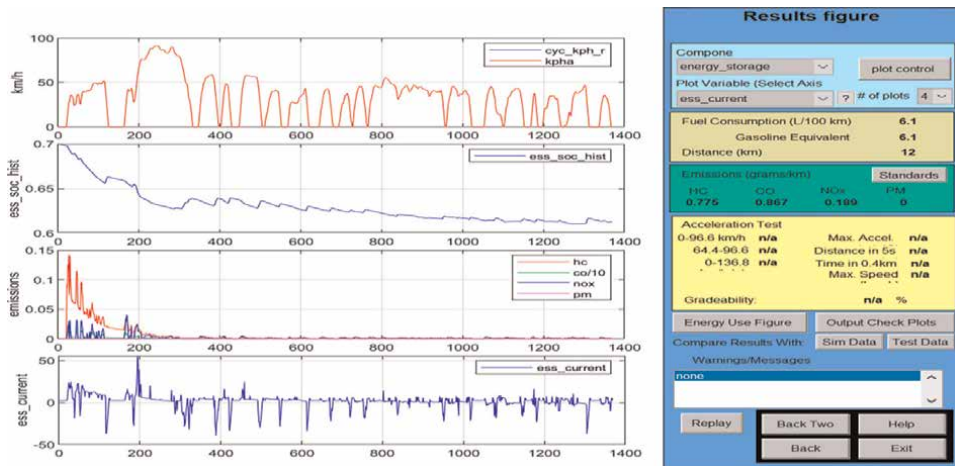


**Figure 4.**  
 MATLAB input-output simulation results.

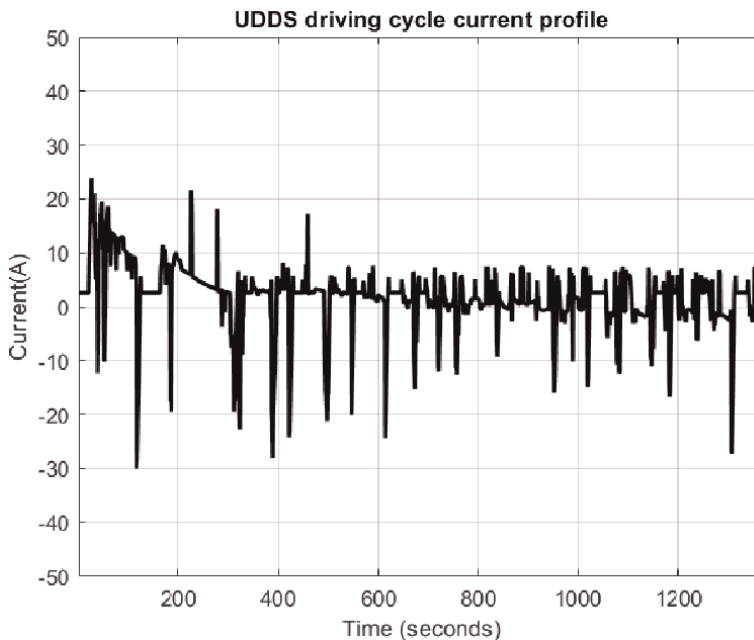


**Figure 5.**  
 The input UDDS driving cycle current profile (battery charging and discharging periods).

of the combinations of an open-circuit voltage (OCV) controlled source, known in the literature as Thevenin voltage source, connected in series with the internal resistance ( $R_{int}$ ) of the battery, followed by one, two, or three parallel resistive and capacitive polarization cells (RC). These combinations lead to a simple electrical equivalent circuit models (ECMs) very spread in the literature field as is shown in **Figure 6** [7]. Until now, the ECMs proved that they are of the high simplicity and are the most suitable models to capture the battery's dynamic electrochemical behavior and increase the model's accuracy. Since in **Figure 6**, the ECM has three parallel RC bias

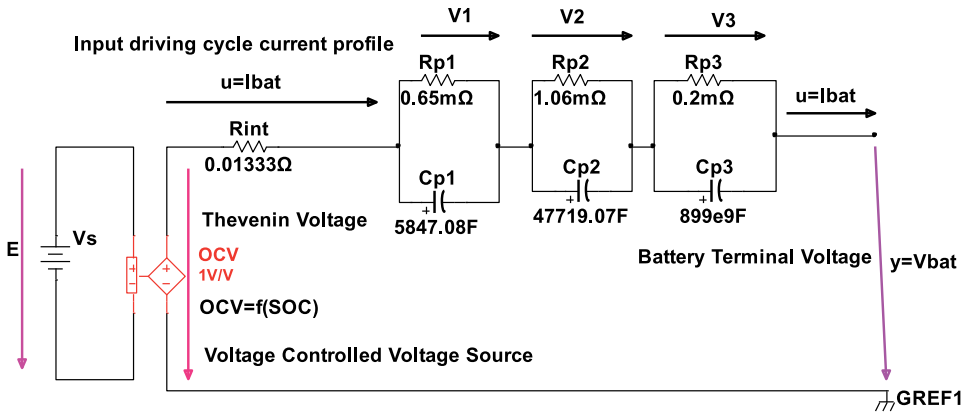


**Figure 6.** Electrical schematic of third-order 3RC ECM battery selection (see [7]).

polarization cells, it is known in the literature field as a three-order RC (3RC) ECM Li-ion battery model. The ECM schematic is built using the Multisim 14.1 software package provided by the well-known National Instruments (NI) company. The first R1pC1p polarization parallel cell captures the fast transient of the battery compared with the last two RC cells that capture only the slow steady state with a great impact in the increase of the battery model accuracy [7]. Since most HEV/EV technologies are very dependent on batteries nowadays, it is crucial for developing and implementing accurate Li-ion battery models. These models must suit better the BMS requirements to be easily deployed on-board power simulators and electronic on-board power systems. Moreover, the 3RC ECM accuracy performance is a baseline for all other alternative battery models developed in this research paper for comparison purposes. For MATLAB simulation’s goal, a similar setup for the 3RC ECM Li-ion battery model parameters used in [7], shown in **Table 1** or directly on the electrical schematics from **Figure 6**, is considered to prove the effectiveness and the robustness of an adaptive extended Kalman filter SOC estimation strategy, similar to those used in [9] for a generic Li-ion cobalt battery and adapted to the 3RC ECM model, presented in Appendix A. This setup is achieved from a generic ECM by changing only the values of the model parameters in state-space equations.

### 2.1.2 Li-ion battery 3RC ECM validation

The Li-ion battery 3RC ECM model parameters and the OCV nonlinear model coefficients are given in **Tables 1** and **2**. The OCV shown in **Figure 7** is a nonlinear function of SOC that combines three additional well-known models, namely Shepherd, Unnewehr universal and Nernst (SUN-OCV) models, defined in [3, 5, 7, 9] with the coefficients set at same values as in [3, 7, 9].

According to the values of the parameters and coefficients set in the **Table 1** the Li-ion battery model dynamics is described by the following discrete-time Eqs. [7]:

$$x_1(k + 1) = a_{11}x_1(k) + b_1u(k) = V_1(k) \quad (1)$$

$$x_2(k + 1) = a_{22}x_2(k) + b_2u(k) = V_2(k) \quad (2)$$

$$x_3(k + 1) = a_{33}x_3(k) + b_3u(k) = V_3(k) \quad (3)$$

Item	Parameters/Coefficients	Symbol	Value	Unit Measure
1	Li-ion battery ECM parameters			
1.1	Internal ohmic resistance	Rint+	13.333	mΩ (milliohm)
1.2	First cell polarization resistance	Rp1	0.65	mΩ
1.3	Second cell polarization resistance	Rp2	1.06	mΩ
1.4	Third cell polarization resistance	Rp3	0.2	mΩ
1.5	First cell polarization capacitance	Cp1	5847.08	F (Farad)
1.6	Second cell polarization capacitance	Cp2	47719.07	F
1.7	Third cell polarization capacitance	Cp3	8.99e9	F
2	Li-ion battery OCV coefficients			
2.1	k0			11.38
2.2	k1			3.86e-5
2.3	k2			0.24
2.4	k3			0.22
2.5	k4			0.04

**Table 1.**  
 The 3RC ECM parameters and OCV coefficients [3, 7, 9].

Criteria indices	Acronyms		Values
	ARX-ECM		ANFIS combined model
IC1	RMSE	8%	2.2%
IC2	MSE	0.64%	0.051%
IC3	MAE	4.17%	1.1%
IC4	MAPE	8.12%	1.73%

**Table 2.**  
 Performance of the Li-ion AEKF SOC ARX model compared with AEKF SOC estimator ANFIS model for UDDS driving cycle test [7].

$$x_4(k+1) = x_4(k) + \frac{\eta T_s u(k)}{C_{nom}}, x_4(k) = SOC(k) = SOC(kT_s) \quad (4)$$

$$OCV(k) = k_0 - k_2 x_4(k) - \frac{k_1}{x_4(k)} + k \ln(x_4(k)) + k \ln(1 - x_4(k)) \quad (5)$$

$$y(k) = OCV(k) - R_{in} u(k) = V_{bat}(k), u(k) = I_{bat}(k) \quad (6)$$

where  $T_s = 1 [s]$  is the sampling time, and the values of the equations' coefficients (1)–(6) are given by  $a_{11} = 1 - \frac{T_s}{T_1}$ ,  $a_{22} = 1 - \frac{T_s}{T_2}$ ,  $a_{33} = 1 - \frac{T_s}{T_3}$ ,  $a_{44} = 1$ ,  $b_1 = \frac{T_s}{C_{p1}}$ ,  $b_2 = \frac{T_s}{C_{p2}}$ ,  $b_3 = \frac{T_s}{C_{p3}}$ , and  $b_4 = -\frac{\eta T_s}{3600 Q_{nom}}$ . In the expression of the coefficient  $b_4$ ,  $\eta$  is the Coulombic efficiency, and  $Q_{nom}$  represents the nominal capacity of the battery, set to the following values:  $\eta = 0.85$ , and  $Q_{nom} = 6Ah$ . Also, the time constants of the polarization cells  $T_1$ ,  $T_2$ , and  $T_3$  are given by:  $T_1 = R_{p1} C_{p1}$ ,  $T_2 = R_{p2} C_{p2}$ , and  $T_3 = R_{p3} C_{p3}$ .

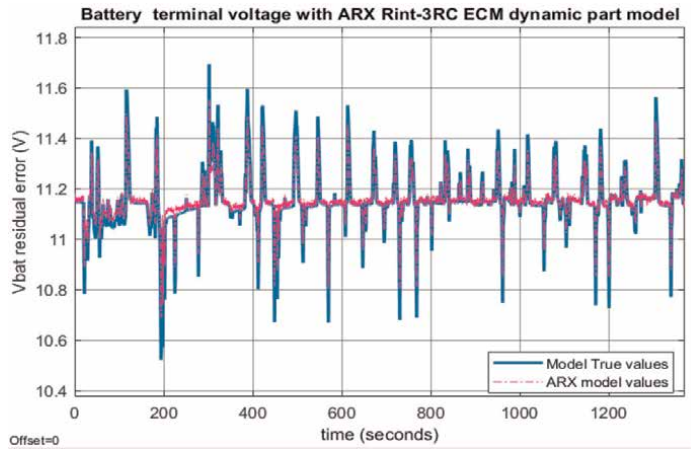


**Figure 7.** Battery terminal Rint-3RC ECM voltage versus ARX – ECM for the dynamic part of the battery.

A Simulink model based on these previous equations is shown in **Figure 8a**, compact in compact form, and in **Figure 8b**, for a detailed form.

The MATLAB simulation results are shown in **Figure 9**. In **Figure 9a** and **b** are depicted the SOC of the battery 3RC model versus SOC estimated by the ADVISOR simulator. In **Figure 9c** and **d** are presented the OCV =  $f(\text{SOC})$  curve and the battery SOC for a complete UDDS discharge cycle respectively. In **Figure 9e** is shown only the terminal voltage for a single UDDS cycle. The SOC residual represented in **Figure 9b** reveals a good SOC accuracy performance of the 3RC EMC battery model with respect to the estimated battery SOC on the ADVISOR simulator integrated with the MATLAB platform. This excellent result is a realistic argument that validates certainly the proposed 3RC ECM Li-ion battery attached to the generic Rint model of SAFT-type battery.

### 2.1.3 Li-ion battery 3RC ECM SOC estimation using an adaptive extended Kalman filter (AEKF)

The main goal of this section is to estimate the battery SOC and analyze the AEKF SOC estimator accuracy compared with the actual value of the battery model validated in the previous section. It is essential to prove that an accurate battery model in terms of SOC and terminal voltage is vital for building the most accurate SOC estimator. To accomplish this goal, an adaptive extended Kalman filter (AEKF) SOC estimator is adopted in this research, encouraged by the preliminary results obtained in [9, 29] by using the same AEKF estimator for a similar application. The SOC estimator implementation is performed on the MATLAB R2018b platform, and the simulation results are depicted in **Figure 10**. Also, in **Figure 10a** is shown the SOC AEKF estimator accuracy and its robustness to changes in the SOC initial value from  $\text{SOC}_{\text{ini}} = 0.7$  to  $\text{SOC}_{\text{ini}} = 0.4$ , compared with the 3RC ECM model values. In **Figure 10b**, the battery model terminal voltage is compared with the AEKF estimate of the terminal voltage. Both **Figure 10a** and **b** reveal that the SOC AEKF estimator performs well with high SOC accuracy, evaluated also based on their errors shown in **Figure 10c** and **d**.

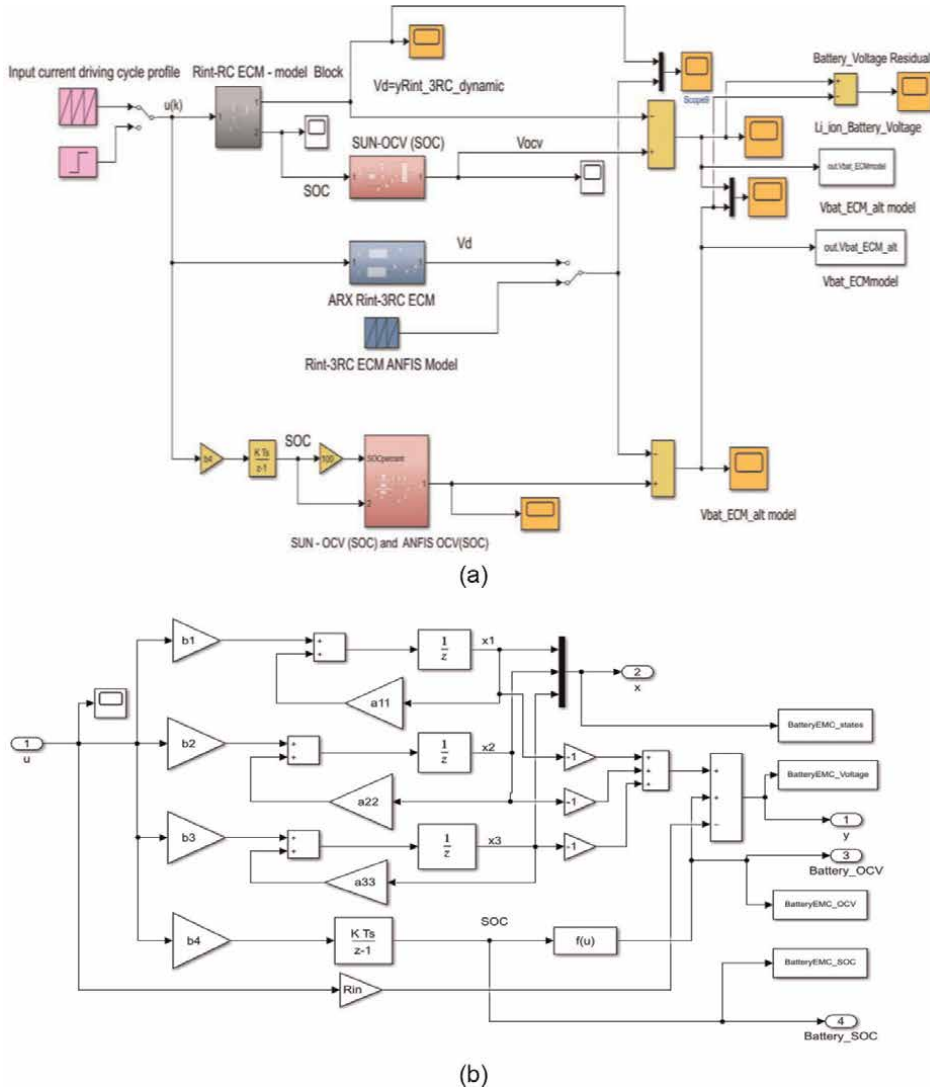


**Figure 8.** (a) The Simulink model of the 3RC ECM Li-ion battery in compact form; (b) the detailed Simulink model of the 3RC ECM Li-ion battery.

#### 2.1.4 The ARX model of the Rint-3RC ECM circuit dynamics (ARX-ECM)

An alternative to the battery model is a linear polynomial model in discrete-time state-space representation, namely an autoregressive with exogenous terms (ARX) model, which captures the dynamics impact on the series circuit Rint (internal battery resistance) and all three RC polarization cells. The linear discrete-time polynomial model ARX is one of the simplest models that incorporate the stimulus input signal to capture some stochastic dynamics as part of the 3RC ECM dynamics. Since the  $OCV = f(SOC)$  curve is of high nonlinearity, an ANFIS model is also assessed. A hybrid battery model structure ARX Rint-3RC ECM – ANFIS OCV(SOC) model will be developed as a challenge in this valuable research for the reader to have a good

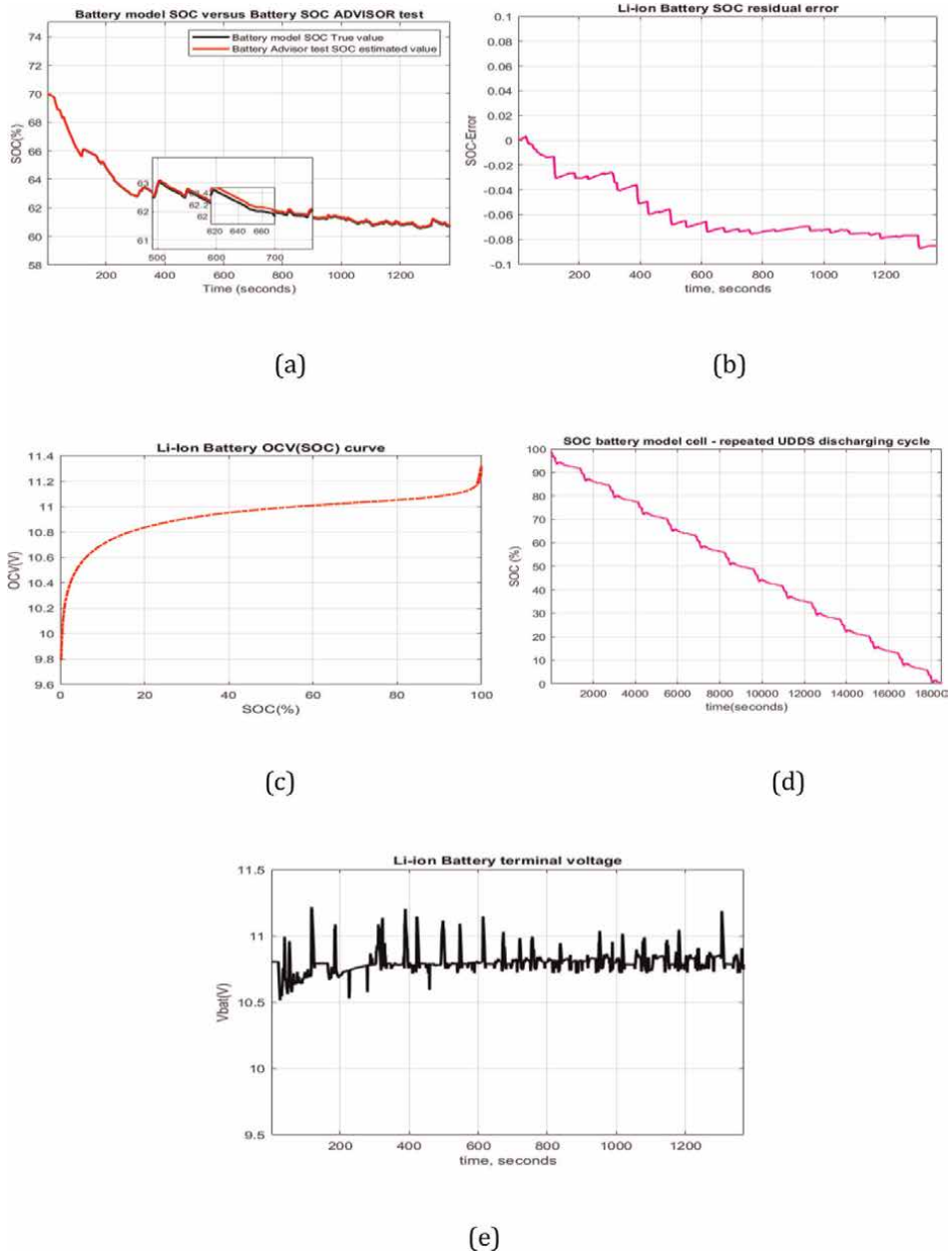


**Figure 9.** (a) Li-ion battery 3RC ECM model SOC versus battery ADVISOR simulator estimated; (b) SOC residual error; (c)  $OCV = f(SOC)$  curve for 5 hours full discharge of the battery to a UDDS driving multi-cycles; (d) SOC for a full battery discharge SOC; (e) SOC for a single UDDS driving cycle discharging input profile (1370 seconds).

insight on OCV(SOC) impact on battery SOC accuracy. Finally, a combined ARX Rint-3RC ECM – ANFIS OCV(SOC) model structure is investigated. The Simulink diagram with all these alternative modeling techniques is shown in **Figure 8**. To build a single-input single-output (SISO) ARX model, the system identification MATLAB toolbox and Simulink are the most precious tools [13]. Also, for good documentation,

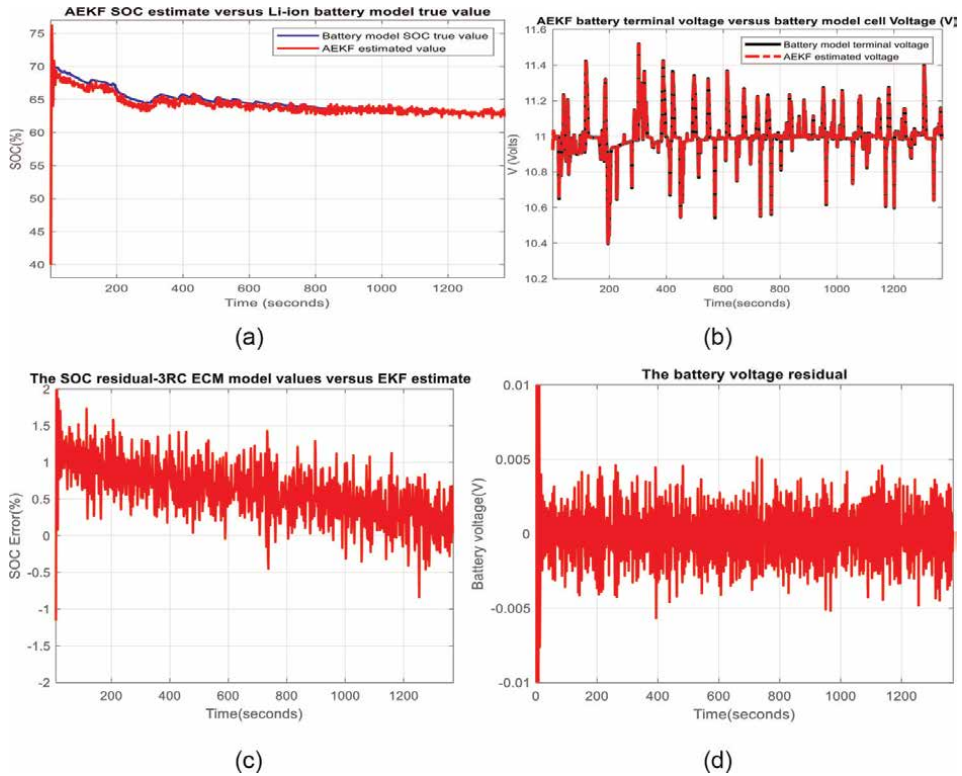


**Figure 10.** (a) SOC voltage; (b) battery terminal voltage versus AEKF estimated. (c) Terminal voltage residual error; (d) SOC residual error.

a piece of valuable information about ARX models is provided in the references [10–13, 31]. MATLAB’s arx command is helpful to generate and estimate the models’ parameters from the input-output data sets. This MATLAB command is a routine based on a prediction-error least-squares method and specified polynomial orders to estimate the parameters of ARX polynomial discrete-time models. The model properties include covariances (parameter uncertainties) and goodness of fit between the estimated and measured data. Fundamental work on systems identification is done in [31]. The MATLAB implementation and simulations of SISO polynomial ARX models can be performed on any recent MATLAB platforms available online at [www.mathworks.com/help/ident/ref/arx.html](http://www.mathworks.com/help/ident/ref/arx.html) [13]. A “trial and error” procedure is considered to select the most suitable ARX model order. This procedure is repetitive until the best match of the data set is found, provided by the following status indicators:

- Fit to data estimation (prediction focus)
- Final prediction error (FPE)
- Mean square error (MSE),

as recorded output data of ARX model. The ARX model can be represented in the discrete state-space by the following polynomial with constant coefficients:

$$A(q)y_d(t) = B(q)u(t) + e(t) \quad (7)$$

where  $y_d(t)$  is the output dynamics part of the series circuit Rint-3RC, given by

$$y_d(t) = R_{int}u(t) + V_1(t) + V_2(t) + V_3(t) = v_d(t) \quad (8)$$

where the voltages  $V_1(t)$ ,  $V_2(t)$ , and  $V_3(t)$  are given in Eq. (1), Eq. (2), and respectively Eq. (3). The Rint-3RC circuit input  $u(t)$  denotes the battery charging and discharging current input (e.g., UDDS driving cycle input current profile). The linear discrete time polynomials  $A(q)$  and  $B(q)$  in Eq. (7) have the degrees  $n_a$  (poles), respectively  $n_b$  (zeroes) and are described as,

$$A(q^{-1}) = 1 + a_1q^{-1} + \dots + a_{n_a}q^{-n_a} \quad (9)$$

$$B(q^{-1}) = b_1q^{-1-n_k} + \dots + b_{n_b}q^{-n_b-n_k+1} = q^{-n_k}(b_1q^{-1} + \dots + b_{n_b}q^{-n_b+1}) \quad (10)$$

where  $n_k$  designates an integer number of samples as a track record of pure transport signal flow delay between the system input-output measurement sensors. Also,  $u(t)$  and  $y_d(t)$  in Eq. (7) denote the Rint-3RC ECM input, respectively, its output at the discrete instant  $t = kT_s, k \in \mathbb{Z}^+$ ,  $q$  is a forward shift operator, i.e.,  $q(u(t)) = u(t+1)$ ,  $q(y_d(t)) = y_d(t+1)$ , and  $q^{-1}$  is backward shift operator, i.e.,  $q^{-1}(u(t)) = u(t-1)$ ,  $q^{-1}(y_d(t)) = y_d(t-1)$ .  $T_s$  represents the sampling period, and  $e(t)$  term denotes the white noise disturbance value at the discrete instant  $t$ . The values of  $n_a$  and  $n_b$  that signify the degrees of the polynomials  $A(q)$  and  $B(q)$ , respectively, are set to the arguments in the syntax of the specific MATLAB arx command from Control Systems Identification MATLAB Toolbox. To use MATLAB Simulink to build the 3RC ECM battery model based on ARX model of the Rint-3RC electrical circuit dynamic part, a transfer function representation of the linear discrete-time polynomial ARX model is required. Some of MATLAB simulations results obtained after the use for ARX Rint-3RC ECM model implementation of the identification systems toolbox arx command are shown below. Discrete-time ARX (2,2,1) (i.e., ARX ( $n_a = 2, n_b = 2, n_k = 1$ ) model [10, 12, 13]:

$$A(z)y_d(t) = B(z)u(t) + e(t) \quad (11)$$

$$A(z) = 1 - 1.121z^{-1} + 0.2837z^{-2}, a_1 = -1.121, a_2 = 0.2837 \quad (12)$$

$$B(z) = 0.006972z^{-1} - 0.005292z^{-2}, b_1 = 0.006972, b_2 = -0.005292 \quad (13)$$

Sample time: 1 seconds, Parameterization: polynomial orders:  $n_a = 2, n_b = 2, n_k = 1$ , Number of free coefficients: 4, Status: Estimated using ARX on time-domain data, Fit to estimation data: 33.89% (simulation focus), FPE: 0.007562, MSE: 0.004557.

**Remark:** Since the roots of the characteristic equation  $A(z^{-1}) = 0$  are equal to  $0 < z_1 = 0.735 < 1, < 0$  and  $z_2 = 0.385 < 1$ , then the dynamic part of the 3RC ECM model is stable. The Simulink model of the ARX Rint-3RC ECM dynamic model part is integrated into the overall Simulink diagram shown in **Figure 8**, and the MATLAB simulation results for the new Li-ion battery SAFT accurate model implementation are presented in **Figure 11** for the ARX model of Rint-3RC ECM dynamic part voltage versus the voltage measurement values. In **Figure 7**, the result of simulations is related to battery terminal voltage based on the original 3RC ECM model versus battery

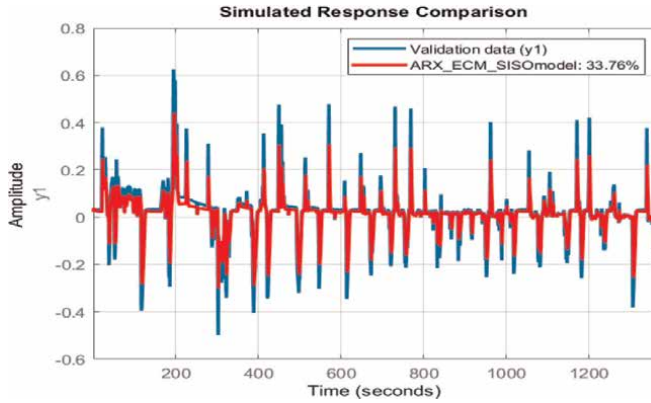


**Figure 11.**  
 The ARX – ECM model of 3RC ECM dynamic part voltage- MATLAB simulation result for validation.

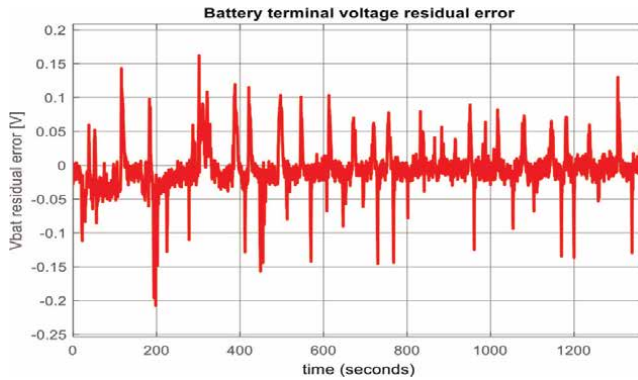


**Figure 12.**  
 Battery terminal voltage residual error.

terminal voltage in the integrated structure with ARX Rint-3RC ECM, the dynamic part model. For a good visualization of battery accuracy performance, the residual voltage between two previous voltages is depicted in **Figure 12**.

According to Eq. (4) and Eq. (6), an overall discrete-state space representation for the integrated ARX model structure of 3RC ECM SAFT Li-ion battery model can be written as follows:

$$soc(k + 1) = soc(k) - \frac{\eta T_s u(k)}{C_{nom}}, soc(0) = SOCini \quad (14)$$

$$y(k) = -V_d(k) + V_{OCV}(k) = -ARX(u(k)) + OCV(soc(k)) \quad (15)$$

where  $y_d(k) = V_d(k)$  represents the output voltage of the dynamic part Rint-3RC ECM, and  $u(k) = i(k)$  the input current profile of the battery. Also, a detailed discrete-time state-space representation has the following form:

$$x(k + 1) = Ax(k) + Bu(k) + w(k) \quad (16)$$

$$y(k) = Cx(k) + v(k) \quad (17)$$

where

$$A = \begin{bmatrix} 1 & 0 & 0 \\ 0 & a_1 & a_2 \\ 0 & 0.5 & 0 \end{bmatrix}, \quad B = \begin{bmatrix} -\frac{\eta T_s}{C_{nom}} \\ b_1 \\ 0 \end{bmatrix}, \quad C = \begin{bmatrix} \frac{OCV(soc(k))}{soc(k)} & c_1 & c_2 \end{bmatrix}, \quad (18)$$

$x(k) = \begin{bmatrix} soc(k) \\ x_1(k) \\ x_2(k) \end{bmatrix}$ ,  $u(k) = i(k)$  and represent the battery state vector and input

current driving cycle profile, respectively. The components  $x_1(k)$  and  $x_2(k)$  of the state vector describe the Rint-3RC ECM dynamics part of all three parallel polarization cells, and  $y(k)$  is the predicted battery terminal voltage. The new model parameters have the following values:  $a_1 = 1.121$ ,  $a_2 = -0.5674$ ,  $c_1 = 0.058578$ , and  $c_2 = -0.08467$ . The advantage of the new discrete-time state-space representation compared with 3RC ECM battery original model is its third-order simplified structure. This structure is used to estimate the battery SOC using an AEKF SOC state estimator and then to compare its

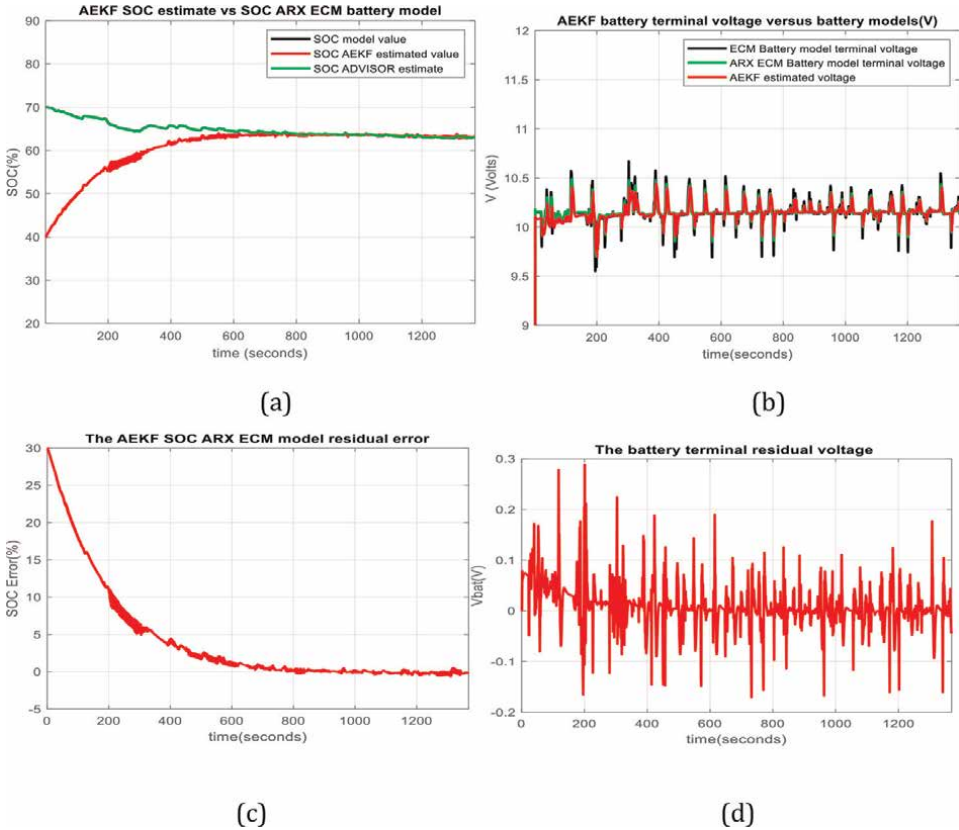


**Figure 13.** (a) The battery SOC true values versus SOC AEKF estimated values and SOC ADVISOR estimate for  $SOC_{ini} = 40\%$ ; (b) AEKF battery terminal voltage versus battery ARX ECM and 3RC ECM models terminal voltages; (c) SOC battery residual between ARX model SOC and AEKF SOC estimator; (d) terminal voltage error between ARX model and AEKF estimator.

accuracy performance with 3RC ECM Li-ion battery original model. For comparison purposes, the MATLAB simulation results of AEKF SOC estimator based on ARX battery model are shown in **Figure 13**. To also highlight the robustness of the AEKF SOC estimator to the changes in the initial value of battery SOC, in **Figure 13a** is depicted the battery SOC true values versus SOC AEKF estimated values and SOC ADVISOR estimate for an  $SOC_{ini} = 40\%$ . The simulation results reveal an excellent robustness and SOC accuracy of the adopted AEKF SOC estimator. Moreover, the simulation results are shown in **Figure 13b–d** that highlight the accuracy of battery terminal voltage of ARX ECM model compared with 3RC ECM and AEKF SOC estimator based on ARX model, as well as both residuals SOC and battery terminal voltage.

### **3. ANFIS Li-ion battery model design for dynamic part Rint-3RC ECM and OCV(SOC) nonlinear block**

As an alternative to 3RC ECM and ARX battery models, the ANFIS modeling techniques are based on specific MATLAB commands provided by fuzzy logic toolbox and based on fuzzy inference tuning procedures [14–16]. The Sugeno-type inference system FIS is tuned based on an input-output training data set collected in open-loop from 3RC ECM Li-ion battery model. From our most recent preliminary results in the Li-ion battery field, modeling and SOC estimators disseminated in [12, 25, 26], an interesting state-of-the-art analysis of similar SOC AEKF estimators performance reported in the literature is done in terms of statistical performance criteria values, such as root mean square error (RMSE), mean square error (MSE), mean absolute error (MAE), standard deviation (std), mean fundamental percentage error (MAPE), and R2 (R-squared). Among three SOC Li-ion battery estimators, the AEKF, adaptive unscented Kalman filter (AUKF), and particle filter (PF) SOC estimators, the AEKF proved that is the most suitable for HEVs applications [29].

#### **3.1 Detailed ANFIS Li-ion battery model design steps**

##### *3.1.1 ECM hybrid and combined Li-ion battery models structures: Training phase and battery terminal voltage accuracy*

A specific MATLAB function *anfis(trainingData)* that has as argument the *TrainingData* generates a single-output Sugeno fuzzy inference system (FIS) and tunes the system parameters using the specified input-output training data. The FIS object is automatically generated using the grid partitioning method. The training algorithm uses a combination of the least-squares and back propagation gradient descent methods to model the training data. Also, the same MATLAB function could have a second argument called *options* with the syntax *anfis(trainingData, options)* and tunes an FIS using the specified trainingData and options. Using this syntax, the user can select an initial FIS object to tune, validate the data to prevent overfitting to training data, the training algorithm options, and display training progress information. In the last two decades, an impressive amount of research was done by researchers, developers, and implementers in the artificial intelligence field to develop a robust theoretical background on neural network architectures, fuzzy logic design, and ANFIS modeling approach, as well as to create the most suitable algorithms and techniques to be implemented in an extensive palette of applications

[14, 18]. The following summarizes some of the key lines of MATLAB code that are much easier for MATLAB readers and users to understand a quick implementation of the online generation of the ANFIS model based exclusively on the input-output measurement data set suggested in [14]. The MATLAB implementation steps required to generate an ANFIS plant/process model, the actions that guide the reader/implementer are:

Step 1: Set up the driving cycle profile for Li-ion battery as input  $u$ , and the battery SOC ( $y_1$ ) and terminal voltage ( $y_2$ ) as battery outputs; The Li-ion battery input-output measurements data set will be collected from a 3RC ECM original battery model given by Eq. (1)–Eq. (7) from previous section through several extensive simulations conducted on MATLAB platform.

Step 2: Generate the ANFIS model grid partition method-based options using the specific MATLAB function:

```
options = genfisOptions('GridPartition')
```

```
options.NumMembershipFunctions = 5 or greater than this
```

Step 3: Construct the FIS input attached to the battery SOC and terminal voltage

```
in_fis1 = genfis (u, y1, options)
```

```
in_fis2 = genfis (u, y2, options)
```

Step 3: Select for training the ANFIS model options

```
options = anfisOptions.
```

```
options.InitialFIS1 = in_fis1
```

```
options.InitialFIS2 = in_fis2
```

```
options.EpochNumber = 20 or greater to get a reasonable accuracy
```

Step 4: Construct the FIS output attached to the battery SOC and terminal voltage

```
out_fis1 = anfis ([u y1], options)
```

```
out_fis2 = anfis ([u y2], options)
```

Step 5: Plot the input-output measurements data set versus input-output of both ANFIS models

```
plot (u, y1, u, evalfis (u, out_fis1))
```

```
plot (u, y2, u, evalfis (u, out_fis2))
```

```
legend ('trainingData', 'ANFIS Output').
```

The previous steps must be adapted to generate both ANFIS models of the Rint-3RC ECM dynamic part and the OCV(SOC) nonlinear function. The MATLAB simulation results are depicted in Figure. **Figure 14a** presents the ANFIS Rint-3RC ECM dynamic part model output and voltage training data set measurements, and **Figure 14b** shows only the ANFIS model output. The impact on battery terminal voltage accuracy using the ANFIS -ECM model compared with ARX -ECM developed in the last Section 2.1.4 is shown in **Figure 14c**. The accuracy of ANFIS -ECM model is revealed in **Figure 14d**, which presents the battery terminal voltage residual.

Also, for building some interesting Li-ion SAFT battery structures, an ANFIS model is developed for OCV(SOC) nonlinear function block in **Figure 15a** for training data phase, and in **Figure 15b** for OCV(SOC) ANFIS output model. Both ANFIS models are based on a repeated UDDS driving cycles input current profile for almost 5 hours to assure a large interval of input-output data set measurements for SOC, OCV, and battery dynamic part voltage. The impact of OCV(SOC) ANFIS block on battery terminal voltage accuracy based on 3RC ECM is revealed in **Figure 15c** and **d**. In **Figure 15c** it is very difficult to distinguish between ECM battery terminal voltage graph and the second one ECM Li-ion battery terminal voltage that integrates the

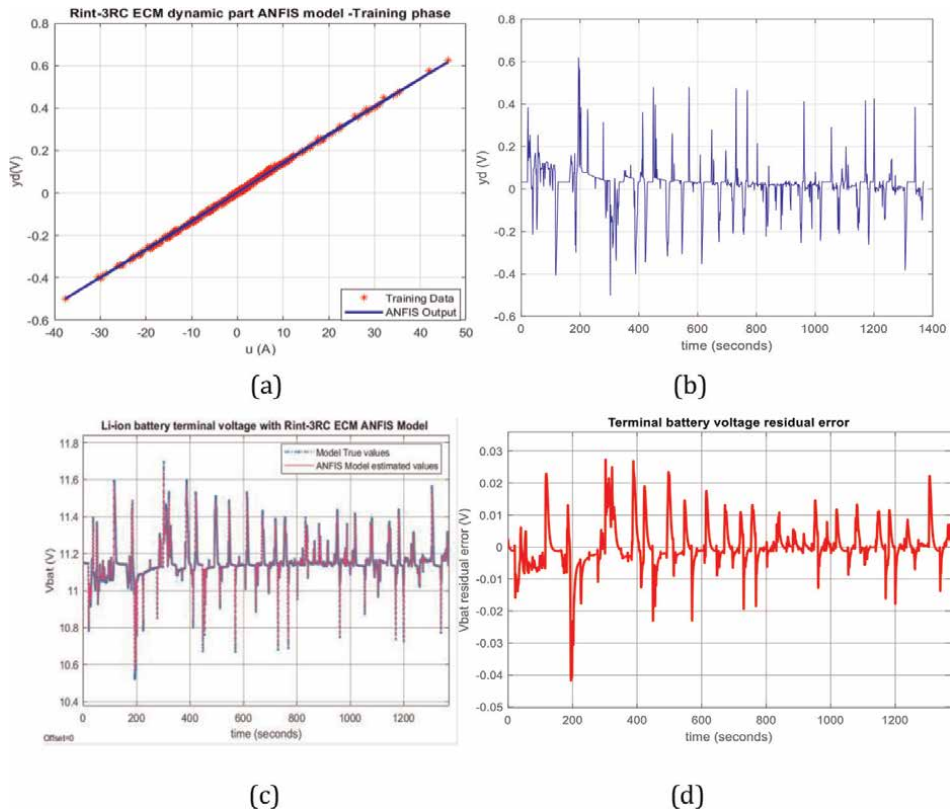


**Figure 14.** (a) ANFIS ECM dynamic part model output and voltage training data set measurements; (b) Rint-3RC ECM dynamic part ANFIS model  $y_d$  circuit output; (c) terminal battery voltage  $V_{bat}$  with Rint-3RC ECM dynamic part ANFIS model (ANFIS-ECM); (d) terminal voltage residual error.

OCV(SOC) block ANFIS model due to the high ANFIS OCV(SOC) model block accuracy. The reader can have a better insight on the battery terminal voltage accuracy in **Figure 15d** that reveals a very small battery terminal voltage residual error compared with the ARX ECM dynamic part battery model terminal voltage shown in previous **Figure 14d**.

Let us discuss why the ANFIS battery integrated model is the most suitable to build hybrid integrated battery Li-ion structures in terms of high accuracy.

An exciting hybrid battery Li-ion structure can incorporate into the ARX ECM dynamic part model and an ANFIS OCV(SOC) nonlinear block model. The MATLAB simulations result of the Li-ion battery hybrid structure is presented in **Figure 16a** and **b**.

A rigorous analysis of MATLAB simulation results from **Figure 15c** and **d** shows a high battery terminal voltage accuracy compared with the battery hybrid structure, as can be seen in **Figure 16a** and **b**.

The last combined battery structure consists of two ANFIS models, the first one for Rint-3RC ECM active battery part and the second one that replaces the Li-ion SAFT ECM SUN OCV(SOC) nonlinear block with an ANFIS model block. The MATLAB simulation results are depicted in the **Figure 17a** and **b**.

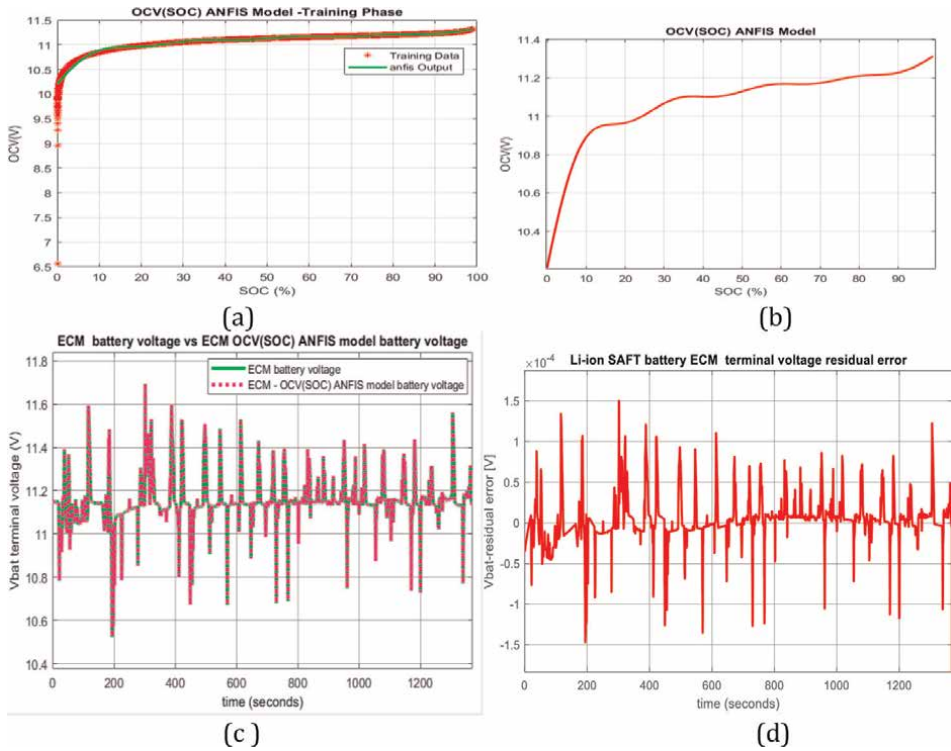


**Figure 15.** (a)  $OCV = f(SOC)$  ANFIS model versus OCV measurements; (b)  $OCV = f(SOC)$  ANFIS model; (d) ECM Li-ion SAFT battery terminal voltage versus ECM-OCV(SOC) ANFIS model ( $R_{int}$ -3RC -ANFIS) terminal battery voltage; (e) ECM Li-ion SAFT battery terminal voltage residual error versus ECM-OCV(SOC) ANFIS model ( $R_{int}$ -3RC - ANFIS) integrated structure.

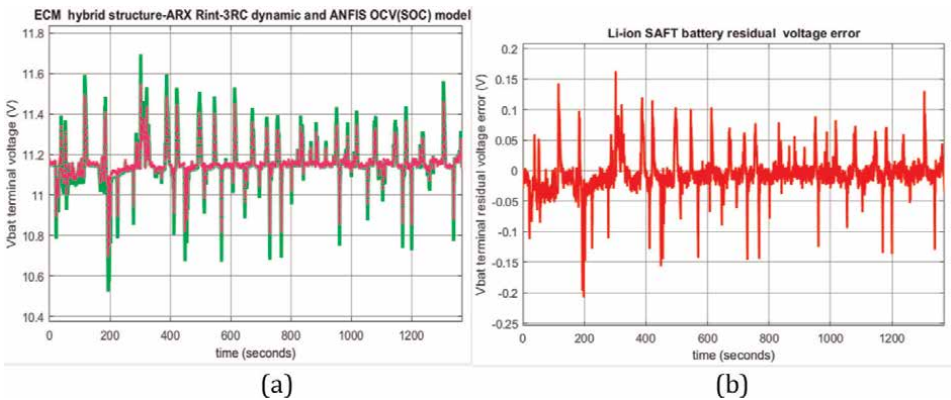


**Figure 16.** (a). ECM Li-ion SAFT hybrid structure – ARX  $R_{int}$ -3RC dynamic part and ANFIS OCV (SOC) nonlinear block model (ARX-ANFIS); (b) Li-ion SAFT battery terminal residual voltage error for hybrid structure.

The voltage accuracy performance revealed by simulation results from **Figure 17a** and **b** seems to be better than the previous hybrid ARX and ANFIS battery structure. Still, it is slightly inferior compared with the design that integrates only the ANFIS model for SOC(OCV) nonlinear battery block.

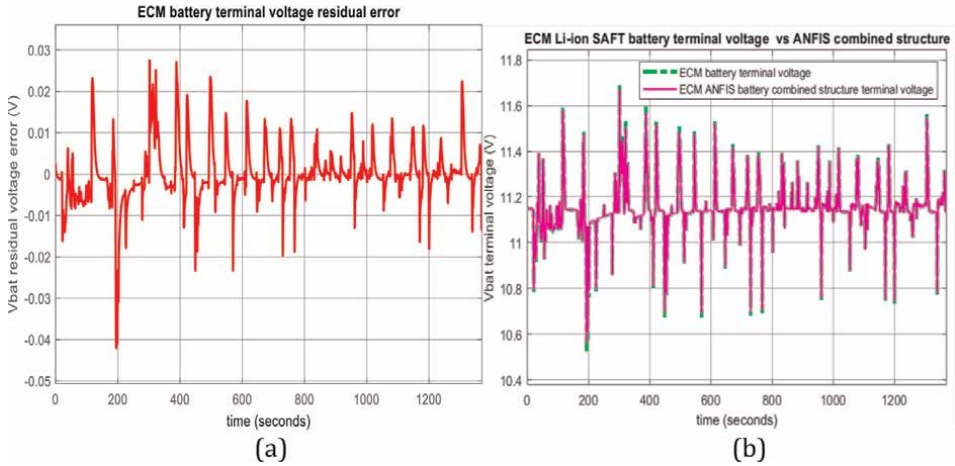


**Figure 17.** (a) ECM Li-ion SAFT battery terminal voltage versus ECM ANFIS combined structure terminal voltage; (b) ECM Li-ion SAFT battery terminal residual voltage error for ECM ANFIS combined structure.

### 3.1.2 AEKF SOC estimator for ANFIS 3RC ECM SAFT Li-ion battery model: accuracy performance

For simplification purpose and SOC and battery terminal voltage accuracy, as alternative Li-ion 3RC ECM structure required to implement the AEKF SOC estimator on a MATLAB R2021b platform is considered the ANFIS 3RC ECM SAFT Li-ion battery model consisting of Rint-3RC ECM dynamic part block, and second ANFIS model attached to OCV(SOC) nonlinear block. The overall simplified ANFIS 3RC ECM battery model structure is described by the following equations:

$$soc(k + 1) = soc(k) - \frac{\eta T_s u(k)}{C_{nom}}, soc(0) = SOCini \quad (19)$$

$$y(k) = V_{OCV}(k) - V_d(k) = \left( \frac{anfis(soc(k))}{soc(k)} \right) soc(k) - anfis(u(k)) \quad (20)$$

In all the MATLAB simulations for implementing the AEKF SOC estimator are considered the following parameters values:

- SOC initial value = 0.4,

Covariance of estimated value of SOC,  $Phat = 1e-10$ ,

- Covariance process noise  $Qw = 0.01$ ,
- Measurement noise  $Rv = 0.001$ .
- $\alpha = 0.791$ ,  $r = 5$ .

The MATLAB simulations results are presented in **Figure 18a–c**. Similar to ARX model developed in previous chapter 2, in **Figure 18** the robustness of AEKF

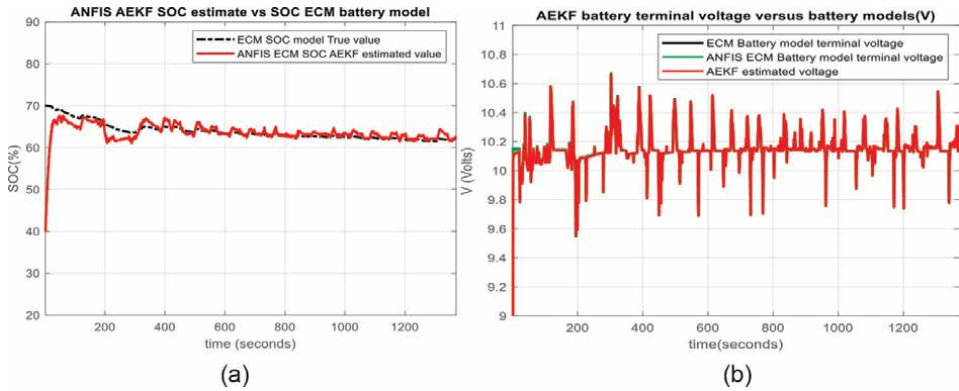


**Figure 18.** (a) Robustness of ANFIS AEKF SOC estimator to changes in SOC initial values from  $SOC_{ini} = 0.7$  to  $SOC_{ini} = 0.4$ ; (b) the ANFIS 3RC ECM Li-ion battery OCV voltage accuracy.

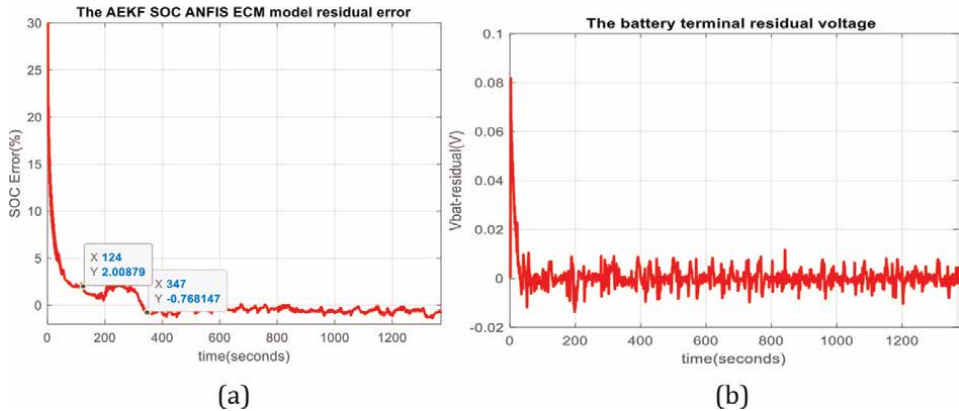


**Figure 19.** (a) The ANFIS 3RC ECM Li-ion battery SOC residual error; (b) the ANFIS 3RC ECM Li-ion battery terminal voltage residual error with respect with the battery terminal voltage estimated by AEKF.

SOC estimator to changes in the battery SOC initial values from  $SOC_{ini} = 0.7$  to  $SOC_{ini} = 0.4$  is shown. In **Figure 18b** the predicted values of battery terminal and OCV voltages cell by AEKF and ANFIS are compared with 3RC ECM true values.

The battery SOC and terminal voltage accuracy are revealed in **Figure 19a** and **b**, respectively, based on SOC and battery terminal voltage residuals.

### 3.2 Discussion: ANFIS models and AEKF SOC estimator performance analysis

Based on the information accessible from the battery SOC and terminal voltage residual errors presented in the first two subsections of Section 3, more precisely the MATLAB simulation results and the statistics criteria values RMSE, RSE, MAE, MAPE, collected in **Table 2**, can be made a rigorous performance analysis of both ANFIS models and AEKF SOC estimator.

### 3.2.1 ANFIS models performance accuracy analysis

The performance analysis is made on the information provided by the battery terminal voltage residuals errors. The MATLAB simulation results reveal a battery terminal voltage prediction accuracy for ANFIS Rint-3RC ECM dynamic part model of an absolute residual error less than 0.03 volts and greater than  $-0.04$  volts, compared with ARX model of same structure that is situated in the range  $(-0.2, 0.15)$  volts. The voltage error of OCV(SOC) ANFIS model is very small ranged inside the interval  $(-1.5 \times 10^{-4}, 1.5 \times 10^{-4})$  volts. For the ANFIS combined structure (ANFIS-ANFIS), the residual error remains in the same range as Rint-3RC ECM dynamic part model, i.e.,  $(-0.04, 0.03)$  volts.

### 3.2.2 AEKF based on ANFIS combined model (ANFIS-ANFIS) performance accuracy analysis

The performance analysis is made on the information provided by the battery SOC and terminal voltage residuals errors shown in **Figure 19a** and **b**. During the steady state, more precisely after 347 seconds, the SOC residual error is less than 1% smaller

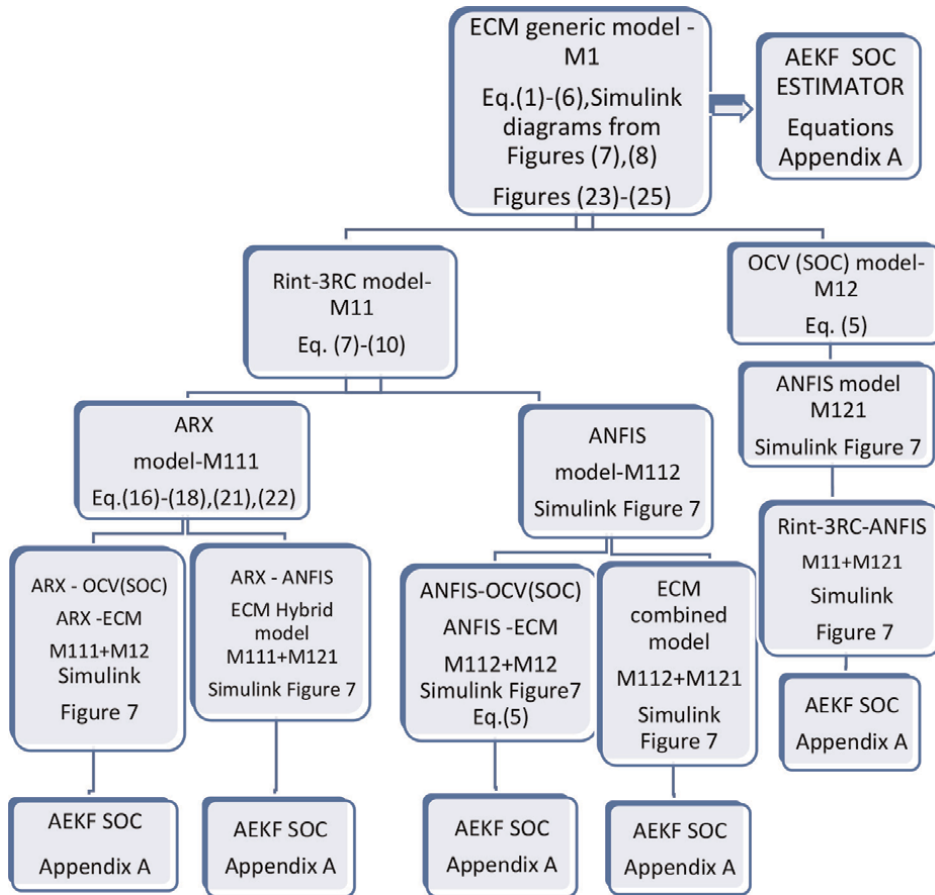


**Figure 20.** System-level flowchart diagram.

than usual SOC residual error of 2% value reported in the literature field. Since the SOC residual error of AEKF based on ARX ECM battery model that is less than 1% during the steady state after 600 s, as is shown in **Figure 13c**, it is obviously that the AEKF based on ANFIS battery model performs better. For a complete information about the suitability of AEKF SOC estimator based on ANFIS battery model is built in the **Table 2**, which incorporates all the statistics of criteria values RMSE (IC1), MSE (IC2), MAE (IC3), and MAPE (IC4), the most common criteria that have been used in the literature field to measure model performance and select the best model from a set of potential candidate models [7, 29, 30]. Comparing both statistics criteria values (third and fourth columns) is straightforward that the AEKF SOC estimator based on ANFIS battery model performs better than AEKF SOC estimator based on ARX battery model.

By comparing the terminal battery voltage residuals shown in **Figure 12** for AEKF based on ARX model and AEKF based on ANFIS model depicted in **Figure 19b**, they are ranged inside the intervals  $(-0.2, 0.3)$  volts and  $(-0.01, 0.08)$  volts, respectively; thus, the second SOC estimator based ANFIS battery model performs better than the first one. Based on the performance analysis of SOC accuracy, robustness to changes in SOCini value and terminal battery voltage prediction accuracy it can conclude that the AEKF SOC estimator based on ANFIS model is the most suitable SOC estimator for HEVs/EVs applications.

A system-level flowchart/flow diagram is shown in **Figure 20**. It indicates the major steps involved in the key sections of the last two chapters to provide an overview of the differences in steps between generic ECM, ARX ECM, ANFIS ECM, hybrid (ARX-ANFIS), and combined (ANFIS-ANFIS) models.

A detailed description for each small block of the overall diagram of the models along with a flow of the equations is also considered in the overall diagram shown in **Figure 20**.

## **4. Conclusions**

This research paper has opened a new Li-ion battery modeling research direction in the HEV BMS applications field by performing several investigations on ARX and ANFIS alternative accurate battery models with a high impact on improving the battery SOC estimators' accuracy and their robustness, design, and real-time implementation in MATLAB and Simulink environments.

The effectiveness of the modeling and SOC estimation strategies is demonstrated through an extensive number of simulations in a MATLAB R2021b software environment. The preliminary simulation results are encouraging, and extensive investigations will be done in future work to extend the applications area. The performance analysis from the last section reveals that ANFIS battery models overpass the second-order linear ARX polynomial battery model in terms of SOC and terminal voltage accuracy and by their capability and suitability to simplify the battery model structure and build robust and accurate SOC Li-ion battery estimators with a high terminal voltage prediction accuracy. The AEKF SOC estimator accuracy based on combined ANFIS model structure is also very accurate compared with AEKF SOC estimator based on ARX dynamic part model with the SOC absolute value lower than 1%, better than the usual 2% SOC value reported in the literature field. Both alternative models are based only on the measurement input-output data set collected by a data acquisition (DAQ) system incorporated in the BMS of HEVs. Besides, the battery SOC and output voltage signals' accuracy is not affected by noise as long as the AEKF SOC estimator is very robust.

## **Conflict of interest**

The authors declare no conflict of interest.

## **Abbreviations/Acronyms**

EV	electric vehicle
HEV	hybrid electric vehicle
BMS	battery management system
FTP-75	Federal test procedure at 75 F
UDDS	Urban Dynamometer Driving Schedule
OCV	open-circuit voltage
SUN-OCV	Shepherd, Unnewehr universal and Nernst open-circuit voltage
SOC	state of charge
ARX	autoregressive exogenous
NREL's	ADVISOR National Renewable Energy Laboratory Advanced Vehicle Simulator
AEKF	adaptive extended Kalman filter
ANFIS	adaptive neuro-fuzzy inference system
ECM	equivalent circuit model
MPC	model predictive control
3RC	ECM third-order RC ECM
Rint-3RC	ECM third-order internal resistance RC ECM
FDI	fault detection isolation
RMSE	root mean square error
MSE	mean square error
MAE	mean absolute error
MAPE	mean absolute percentage error
std.	standard deviation
R <sup>2</sup>	R-squared
ARX-ECM	Rint-3RC replaced by ARX model
Rint-3RC-ANFIS	OCV(SOC) block replaced by ANSIM model
ARX-ANFIS	Rint-3RC replaced by ARX and OCV (SOC) by ANFIS (hybrid structure)
ANFIS-ANFIS	Rint-3RC replaced by ANFIS and OCV (SOC) by ANFIS (combined structure)

## **Author details**

Roxana-Elena Tudoroiu<sup>1</sup>, Mohammed Zaheeruddin<sup>2</sup>, Nicolae Tudoroiu<sup>3\*</sup>  
and Sorin Mihai Radu<sup>1</sup>

1 University of Petrosani, Petrosani, Romania

2 Concordia University from Montreal, Montreal, Canada

3 John Abbott College, Sainte-Anne-de-Bellevue, Canada

\*Address all correspondence to: ntudoroiu@gmail.com

## **IntechOpen**

---

© 2022 The Author(s). Licensee IntechOpen. This chapter is distributed under the terms of the Creative Commons Attribution License (<http://creativecommons.org/licenses/by/3.0>), which permits unrestricted use, distribution, and reproduction in any medium, provided the original work is properly cited. 

## References

- [1] Xia B, Zheng W, Zhang R, Lao Z, Sun Z. Mint: A novel observer for Lithium-ion battery state of charge estimation in electric vehicles based on a second-order equivalent circuit model. *Energies*. 2017;**10**(8):1150. DOI: 10.3390/en10081150. Available from: <http://www.mdpi.com/1996-1073/10/8/1150/htm>
- [2] Young K, Wang C, Wang LY, Strunz K. Electric vehicle battery technologies—chapter 2. In: Garcia-Valle R, JAP L, editors. *Electric Vehicle Integration into Modern Power Networks*. 1st, 9, and 325 ed. New-York, USA: Springer Link: Springer-Verlag; 2013. pp. 15-26. DOI: 10.1007/978-1-4614-0134-6.ch.2
- [3] Farag M. Lithium-ion batteries. In: *Modeling and State of Charge Estimation*, (Thesis). Ontario, Canada: McMaster University of Hamilton; 2013. p. 169
- [4] Tudoroiu R-E, Zaheeruddin M, Radu SM. In: Louis Romeral Martinez TN, Prieto MD, editors. *New Trends in Electrical Vehicle Powertrains*, Vol. 4. London, UK: IntechOpen Limited; 2019. pp. 55-81. DOI: 10.5772/intechopen.76230.ch4
- [5] Plett GL. Extended Kalman filtering for battery management systems of LiPB-based HEV battery packs: Part 2. Modeling and identification. *Journal of Power Sources*. 2004;**134**:262-276. DOI: 10.1016/j.jpowsour.2004.02.032
- [6] Zhang R, Xia B, Li B, Cao L, Lai Y, Zheng W, et al. State of the art of Li-ion battery SOC estimation for electrical vehicles. *Energies*. 2018;**11**:1820
- [7] Tudoroiu R-E, Zaheeruddin M, Tudoroiu N, Radu S-M. SOC estimation of a rechargeable Li-ion battery used in fuel-cell hybrid electric vehicles—Comparative study of accuracy and robustness performance based on statistical criteria. Part I: Equivalent models. *Batteries*. 2020;**6**(3):42. DOI: 10.3390/batteries6030042
- [8] Wu C, Zhu C, Ge Y, Zhao Y. A review on fault mechanism and diagnosis approach for Li-ion batteries. *Journal of Nanomaterials*. 2015;**2015**:1-9. DOI: 10.1155/2015/631263
- [9] Tudoroiu N, Zaheeruddin M, Tudoroiu R-E, Radu S-M. Fault detection, diagnosis, and isolation strategy in Li-ion battery management systems of HEVs using 1-D wavelet signals analysis. In: Mohammady S, editor. *Wavelet Theory*. London, UK: IntechOpen; 2021. DOI: 10.5772/intechopen.94554. Available from: <https://www.intechopen.com/chapters/74031>
- [10] Yuan S, Wu H, Yin C. State of charge estimation using the extended Kalman filter for battery management systems based on the ARX battery model. *MDPI, Energies Journal*. 2013;**6**:444-470. DOI: 10.3390/en6010444
- [11] Uddina F, Tufaa LD, Yousifa SMT, Mauluda AS. Comparison of ARX and ARMAX decorrelation models for detecting model-plant mismatch. In: *4th International Conference on Process Engineering and Advanced Materials*, Procedia Engineering. Vol. 148. Amsterdam, Nederland: Elsevier Ltd, ScienceDirect; 2016. pp. 985-991. DOI: 10.1016/j.proeng.2016.06.536
- [12] Tudoroiu N, Zaheeruddin M, Tudoroiu R-E. Modelling, identification, implementation, and MATLAB simulations of multi-input multi-output proportional integral-plus control strategies for a centrifugal chiller system.

- Int. J. Modelling, Identification and Control. 2020;**35**(1):64-91. DOI: 10.1504/ijmic.2020.10035847
- [13] MathWorks MATLAB Version R2019b On-Line Documentation, Available from: <https://www.mathworks.com/help/ident/ref/arx.html>
- [14] MathWorks MATLAB Version R2021b on-line Documentation, Neuro-Adaptive Learning and ANFIS. Available from: <https://www.mathworks.com/help/fuzzy/neuro-adaptive-learning-and-anfis.html>
- [15] Konsoulas Ilias S. Adaptive Neuro-Fuzzy Inference Systems (ANFIS) Library for Simulink. Available from: <https://www.mathworks.com/matlabcentral/fileexchange/36098-adaptive-neuro-fuzzy-inference-systems-anfis-library-for-simulink>, MATLAB Central File Exchange. [Accessed: January 19, 2022]
- [16] MathWorks MATLAB Version R2021b on-line Documentation, Neuro-Fuzzy Designer. Available from: <https://www.mathworks.com/help/fuzzy/neurofuzzydesigner-app.html>.
- [17] Bellali B, Hazzab A, Bousserhane IK, Lefebvre D. A decoupled parameters estimators for in nonlinear systems fault diagnosis by ANFIS. *International Journal of Electrical and Computer Engineering (IJECE)*. 2012;**2**(2):166-174. DOI: 10.11591/ijece.v2i2.221
- [18] Tudoroiu R-E, Zaheeruddin M, Tudoroiu N, Burdescu DD. MATLAB implementation of an adaptive neuro-fuzzy Modeling approach applied on nonlinear dynamic systems – A case study. In: *Proceedings of the Federated Conference on Computer Science and Information Systems*. Vol. 15. Poznan: ACSIS; 2018. pp. 577-583. DOI: 10.15439/2018F38
- [19] Nourani V, Uzelaltinbulat S, Sadikoglu F, Behfar N. Artificial intelligence based ensemble Modeling for Multi-Station prediction of precipitation. *Atmosphere*. 2019;**10**:80. DOI: 10.3390/atmos10020080
- [20] Chang F-J, Chang Y-T. Adaptive neuro-fuzzy inference system for prediction of water level in reservoir. In: *Advances in Water Resources*. Vol. 29. Amsterdam, Nederland: Elsevier Ltd; 2005. pp. 1-10. DOI: 10.1016/j.advwatres.2005.04.015
- [21] Mosavi A, Ozturk P, Chau K-W. Flood prediction using machine learning models: Literature review. *Water*. 2018;**10**:1536. DOI: 10.3390/w10111536
- [22] Huang C-L, Hsu N-S, Wei C-C, Lo C-W. Using artificial intelligence to retrieve the optimal parameters and structures of adaptive network-based fuzzy inference system for typhoon precipitation forecast Modeling. *Advances in Meteorology*. 2015;**9**:1-22. DOI: 10.1155/2015/472523
- [23] Chen S-H, Lin Y-H, Chang L-C, Chang F-J. The strategy of building a flood forecast model by neuro-fuzzy network. *Hydrological Processes*. 2006; **20**:1525-1540. DOI: 10.1002/hyp.5942
- [24] Ilias Konsoulas. Recurrent Fuzzy Neural Network (RFNN) Library for Simulink. Available from: <https://www.mathworks.com/matlabcentral/fileexchange/43021-recurrent-fuzzy-neural-network-rfnn-library-for-simulink>, MATLAB Central File Exchange. [Accessed: January 19, 2022]
- [25] Appiah R, Panford JK, Riverson K. Implementation of adaptive neuro fuzzy inference system for malaria diagnosis. Case study: Kwesimintsim polyclinic. *International Journal of Computer*

Applications India. 2015;**115**(7):33-37.  
DOI: 10.5120/20166-2284

[26] Jang J-SR. ANFIS: Adaptive-network-based fuzzy inference system. IEEE Transactions on System, Man, and Cybernetics. 1993;**23**:665-685. DOI: 10.1109/21.256541

[27] Karathanasopoulos A, Zaremba A, Osman M, Mikutowski M. Oil forecasting using artificial intelligence. Theoretical Economics Letters. 2019; **09**(07):2283-2290. DOI: 10.4236/tel.2019.97144

[28] Nahr ST, Pahlavani P, Amirkalayi A. A comparative study of adaptive neuro-fuzzy inference Systems in Object Detection of complex City scenes using digital aerial images and LiDAR data. Journal of the Indian Society of Remote Sensing. 2015;**43**(4):1-13. DOI: 10.1007/s12524-015-0457-1

[29] Tudoroiu R-E, Zaheeruddin M, Tudoroiu N, Radu S-M. SOC estimation of a rechargeable Li-ion battery used in fuel-cell hybrid electric vehicles—Comparative study of accuracy and robustness performance based on statistical criteria. Part II: SOC estimators. Batteries. 2020;**6**(3):42. DOI: 10.3390/batteries6030041

[30] Pham H. A new criterion for model selection. Mathematics. 2019;**7**(12):1215. DOI: 10.3390/math7121215

[31] Ljung L. System Identification: Theory for the User, Upper Saddle River. 2nd edition. NJ: Prentice-Hall PTR; 1999

[32] Zhang C, Jiang J, Zhang W, Sharkh SM. Estimation of state of charge of lithium-ion batteries used in HEV using robust extended Kalman filtering. Energies. 2012;**5**:1098-1115. DOI: 10.3390/en5041098

[33] Wu T, Wang M, Xiao Q, Wang X. The SOC estimation of power Li-ion battery based on ANFIS model. Smart Grid and Renewable Energy. 2012;**3**: 51-55. DOI: 10.4236/sgre.2012.31007



---

Section 2

# Safety and Perspectives

---



# Halide Perovskites as Emerging Anti-Counterfeiting Materials Contribute to Smart Flow of Goods

*Ziren Zhou, Jin Xie and Yu Hou*

## Abstract

The counterfeiting of goods is a fast-growing issue worldwide, being a risk to human health, financial safety, and national security. Customized anti-counterfeiting patterning technologies enable unclonable tags on products, which ensure the reliable and convenient flow of goods such as daily foods, prescription medicines, and value-added components. In this chapter, we start with the introduction of recent advances of anti-counterfeiting technologies that generate unique physical tags on products for encryption and information storage. Various halide perovskite-based materials and their fabrication techniques for unreplicable luminescent patterns are then discussed, with a particular focus on the intelligent encoding principles that correlate with the chromism and other special optical readout of materials. The multilevel anti-counterfeiting functions that allow high-throughput authentication of products within a single tag are also exemplified, through which the increasing security demands can be fulfilled. We finally discuss the current issues encountered by perovskite anti-counterfeiting technologies and outline their future directions toward smarter and safer flow of goods.

**Keywords:** halide perovskites, luminescence, security tags, anti-counterfeiting, smart flow

## 1. Introduction

The booming global businesses have largely facilitated the cross-border flow of goods, but meanwhile are threatened by the dramatically increased intellectual property (IP) crimes nowadays. According to the study by Organization for Economic Cooperation and Development (OECD), the value of counterfeit and pirated products is amounted to USD 464 billion in 2019, equal to 2.5% of world trade and more than half of the total value is carried by containerships between countries [1, 2]. The illicit trade hits company profits and nation tax revenue and endangers public health when pharmaceuticals and medical equipment are involved. For these reasons, advanced technologies that combat fake products demand prompt development to ensure reliable flow of goods while maintain its convenience.

Anti-counterfeiting idea was early raised by Philadelphia printer Benjamin Franklin in the 1700s [3], at that time colonies in North America were troubled by the circulation of counterfeit bills. Franklin deliberately misspelled Pennsylvania in the printed bills to baffle less-literate criminals. Meanwhile, he engraved the fine detail of copper on the leaf vein at the back of each bill, making these bills hard to be reproduced by counterfeiters. The unique copper engraving created by blocky lead printer has been regarded as a prototype for contemporary anti-counterfeiting patterning technologies. Since the 1950s, the development of holograms [4–7], ink printing [8–11], and exquisite laser engraving [12–14] have offered practical solutions to protect the market from malicious third parties.

Halide perovskites as an emerging family of semiconductor materials have achieved notable success in photovoltaics and other optoelectronics over the past decade [15–20]. The intriguing photophysical property of perovskites, such as widely tunable bandgaps [21–26], high photoluminescence quantum yield (PLQY) [27–29], and narrow emission width [30–32], are making them promising candidates for fabricating luminescent security tags. Meanwhile, the solution/ink processability of perovskites imparts them feasibility with a variety of printing technologies, enabling high-throughput generation of customized labels with enhanced encoding capacity and lowered processing cost [33–35].

Here, we give a retrospect to the recent advances of halide perovskite-based materials for anti-counterfeiting applications. Low-dimensional perovskites and double perovskites that are structural analogs to three-dimensional (3D) ones as well as other perovskite-like materials are included in the discussion. We summarize the patterning techniques that can lead to precise control of tag fabrication at high dim either flat surface or closed space. The luminescent security tags of perovskites are categorized by different encryption principles, with detailed phase transformation or compositional variation of materials being provided for each chromic case. Integration of luminescent properties that gives rise to multimodal anti-counterfeiting is discussed in respect of goods being strictly confidential. We then survey the special optical readout of security tags that is enabled by the exciton relaxation behavior and carrier dynamic of perovskites.

## **2. Perovskites for anti-counterfeiting applications**

Taking advantage of the high PLQY of halide perovskites, security information in a luminescent tag can be easily and rapidly identified by the human eye or spectrum. The excitation-dependent emission of perovskites can also be tuned from the monochromatic to broadband white light [36–38], giving an added complexity to the optical readout of tags. Combined with versatile encryption and decryption strategies, the security level of an individual tag can be enhanced multidimensionally and output in a simplified digital form [39]. The anti-counterfeiting mechanism of security tags during the flow of goods is illustrated in **Figure 1**, where the authentication is implemented by the communication between preloaded database and third parties.

### **2.1 Fundamental structure of perovskites and their luminescent properties**

Perovskite mineral (calcium titanium oxide,  $\text{CaTiO}_3$ ) was discovered in the Ural Mountains by German mineralogist Gustav Rose in 1839 [40]. The crystal structure of perovskite oxide was not determined by X-ray diffraction until nearly a century later [41] and was proved to comprise three fundamental phases, i.e. cubic,

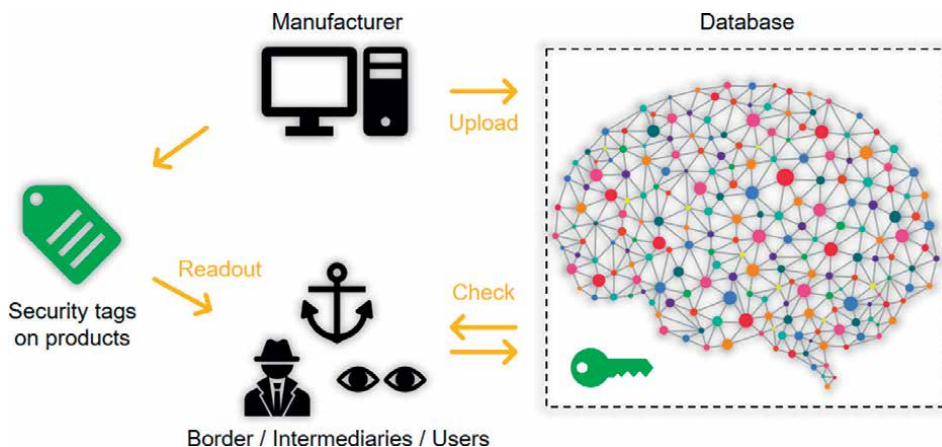


**Figure 1.**  
*Anti-counterfeiting mechanism of security tags during the flow of goods.*

tetragonal, and orthorhombic based on the rigid 3D lattice. Halide perovskites share the similar crystal structure to perovskite oxide, of which the compounds were first synthesized in the late nineteenth century by H. L. Wells [42]. Typically, 3D perovskites (defined by a chemical formula of  $ABX_3$ , where A is a monovalent cation, B is a divalent cation, and X is a halide anion) have direct bandgaps that can be widely tuned by altering the composition of A- and B-site cations and halide anions [21, 24, 43, 44]. Besides, 3D perovskites normally feature low exciton binding energy ( $E_b$ ) of dozens of millielectronvolts. Relaxation of an exciting photon in 3D perovskites normally releases a photon with equal energy, making the band maximum of PL spectra representative of their bandgaps. These properties are important for accurate encryption of perovskite patterns for wide-color-gamut luminescence.

Two-dimensional (2D) perovskites feature corner-sharing metal-halide octahedra intercalated by the bulky cations. Emission spectra of 2D perovskites can be structurally correlated with the interlayer spacing, quantum well (QW) thickness, and its distribution [45, 46]. Strong electron-photon coupling that originated from the deformable lattice was previously demonstrated for some 2D perovskite single crystals, which introduces permanent trap states [47]. The self-trapped excitons (STEs) were later revealed to be a type of transient defect driven by the electron-photon coupling and will contribute to the broadband emission of 2D perovskites [48, 49]. Further lowering the dimensionality of 2D perovskites leads to one-dimensional (1D) and zero-dimensional (0D) perovskites whose octahedra are shared by edge or face. STEs can also be responsible for the broadband emission of these materials with large Stokes shift [50–53]. The white light or dual-/multiband emissions under different excitations are favorable for those luminescent tags that demand a high security level.

Double perovskites are defined by a chemical formula of  $A_2BB'X_6$ , where B is a monovalent cation and B' is a trivalent cation and feature a rock salt arrangement of  $BX_6$  and  $B'X_6$  octahedra. In addition,  $A_2B(IV)X_6$  compounds are also grouped as double perovskites because of their vacancy-ordered structure [54, 55]. The phase-pure double perovskites usually have room-temperature (RT) indirect bandgaps and exhibit band-to-band or downshifting emissions that can be strongly influenced by the specific metal dopants [55–59]. The in-depth reason was ascribed to lattice distortion since metal dopants will basically affect the length and angle of B – X – B' bonds and hence change the electronic wave function coupling of metal cations [60].

## 2.2 Patterning techniques for perovskite security tags

Halide perovskites possess a high compatibility with printing techniques, since both the precursor solution and synthesized colloidal nanocrystals (NCs) can serve as inks. Using  $\text{CsPbX}_3\text{:Mn}^{2+}$  ( $X = \text{Cl, Br, I}$ ) NCs inks, Wang et al. [34] previously reported the fabrication of various patterns by screen, inkjet, and roll-to-roll printing techniques on flexible substrate (e.g. paper, polyethylene terephthalate, and banknotes). The patterns showed fluorescence as response to 254-nm and 365-nm ultraviolet (UV) light, and the  $\text{CsPbBr}_3\text{:Mn}^{2+}$ -based on maintained bright fluorescence after continuous UV irradiation for 60 days. Shi et al. [61] demonstrated an *in situ* growth of  $\text{MAPbX}_3$  ( $\text{MA} = \text{methylammonium}$ ,  $X = \text{Cl, Br, I}$ ) quantum dots (QDs) in polymer scaffold by directly inkjet printing precursor solution on polymer layer. The microdisk arrays of perovskite QDs showed high PLQY up to 80% and can be integrated for a variety of luminescent patterns. Specifically, the 2D code pattern fabricated on polyvinylidene chloride showed excellent water endurance and was still luminescent after being dipping in water for 100 days.

Nanoscale 3D printing technique was recently reported to fabricate perovskite nanopixels with programmed vertical height, location, and emission characteristics [35], which overcomes the low-resolution problem of conventional printing techniques. The authors of this study used femtoliter meniscus to guide the out-of-plane growth of  $\text{MAPbX}_3$  ( $X = \text{Cl, Br, I}$ ) crystals from precursor solution, enabling ultrahigh integration density of red, green, and blue (RGB) nanopixel arrays with spacing of  $\sim 5 \mu\text{m}$  while maintaining its lateral resolution (**Figure 2a**). Numbers can be encoded for

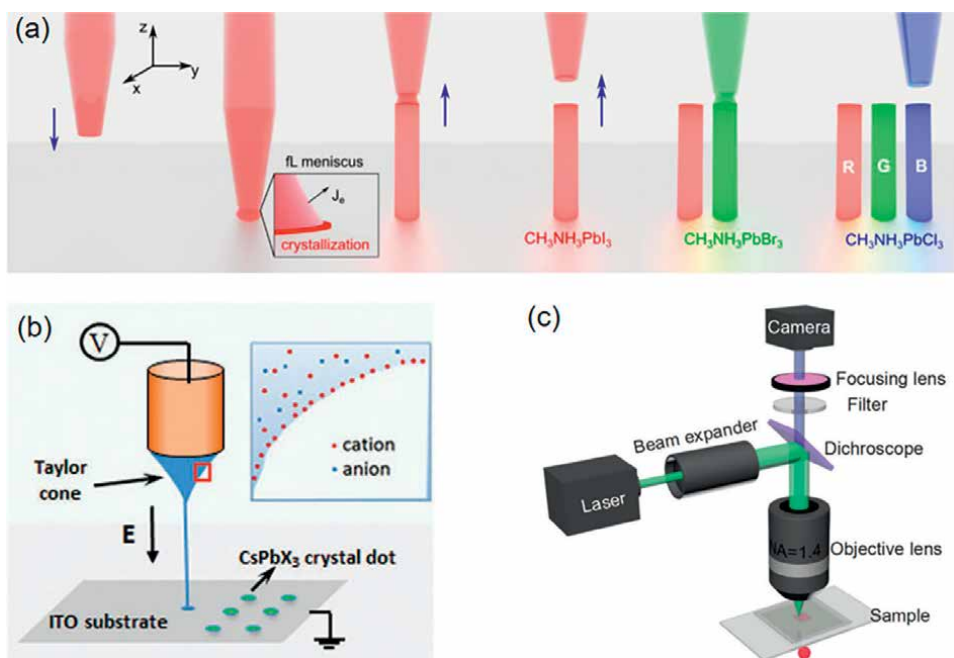


**Figure 2.** (a) Schematic illustration of 3D printing of perovskite nanopixels. (b) Schematic illustration of EHD printing technique for perovskite patterning. (c) Representative laser processing system for perovskite patterning. Reprinted with permission from ref. [35, 62, 63]. Copyright 2021 American Chemical Society; copyright 2019 WILEY-VCH Verlag GmbH & Co. KGaA, Weinheim; copyright 2020 Royal Society of Chemistry.

each discrete height of nanopixels and thus adds an additional level for encryption. Electrohydrodynamic (EHD) printing as another advanced printing technique was also reported to fabricate high-resolution  $\text{CsPbX}_3$  ( $X = \text{Cl, Br, I}$ ) dot arrays with full-color display (**Figure 2b**) [62]. The size of a single dot was precisely controlled by the frequency and peak values of pulse voltage for precursor solution, and a minimum size of  $5 \mu\text{m}$  can be achieved.

Laser beam was previously used to trigger the ultrafast crystallization of perovskite for both patterning and photovoltaic applications [64]. **Figure 2c** shows a typical laser processing system for perovskite patterning. Without any heat treatment, Zhang et al. [63] demonstrated the fabrication of  $\text{CsPbBr}_3/\text{CsPb}_2\text{Br}_5$ -polymer nanocomposites fluorescent pattern by 532-nm femtosecond laser irradiation. Localized crystallization of perovskite was observed in the irradiated pathway, which was accompanied by the laser-induced polymerization of  $\gamma$ -butyrolactone solvent. The width of perovskite line was lowered down to  $1.2 \mu\text{m}$ , and both the crystal quality and luminescent intensity can be fine-tuned by the power and moving speed of laser beam. In addition, laser engraving was introduced to directly create patterns on  $\text{CsPbBr}_3$  microplates [65]. The hidden security information provides a guidance for encryption on a miniaturized pattern.

Most recently, Sun et al. [66] reported the use of 3D lithography technique to fabricated separated  $\text{CsPbX}_3$  ( $X = \text{Cl, Br, I}$ ) NCs in glass matrix. The strong thermal accumulation at the laser-irradiated region of borophosphate glass leads to local pressure and temperature above the liquidus of materials, which induces liquid nanophase separation of glass and perovskite. By tailoring the parameters of pulse duration, repetition rate, pulse energy, and irradiation time, the emission color of pattern was tuned from blue to red under 405-nm excitation. Perovskite NCs in glass matrix exhibited notable phase stability against long-term UV irradiation, organic solution, and high temperature. The patterns were used for both 3D multicolor and dynamic holographic displays, showing huge potential for stereoscopic optical storage and authentication. Accordingly, we provide an overall assessment of existing printing and laser processing techniques for perovskite security tags in **Table 1**.

## 2.3 Encryption principles of perovskite security tags

With the assistance of advanced patterning techniques, the intriguing luminescent properties found on perovskites can be transformed into security information for encryption and decryption of tags. Normally, these tags are invisible under visible light but can emit light under UV, visible, or near-infrared (NIR) excitations. In this section, we provide an overview of encryption principle of perovskite security tags, including pattern, thermochromism, solvatochromism, photochromism, and multimodal luminescence. Other optical readout, such as long-lived emission (after-glow) phenomenon and carrier lifetime gating, are discussed as special encryption methods for delicate authentication of goods. **Figure 3** shows the representative cases of encryption principles being reported over the past few years.

### 2.3.1 Pattern

Shape design of a pattern is a fundamental approach to encode the security data relative to the complexity of contours. Printing or laser processing techniques have been developed to create customized pattern shapes whose resolution now reach a few micropixels or below. Lin et al. [33] raised the concept of clonable shape,

Approach	Technique	Dimensionality	Advantage	Disadvantage
Printing	Handwriting [67]	2D	Easy fabrication, low processing cost	Low-resolution display
	Screen, inkjet, and roll-to-roll printing [34, 61]	2D	High-throughput fabrication, large-area display	Only available for liquid precursors
	Electrohydrodynamic printing [62]	2D	High-resolution display	Conductive substrate required
	Meniscus-guided printing [35]	3D	Multidimensional display	Delicate mechanical control of pipet
Laser processing	Laser annealing [63, 64]	2D	Ultrafast fabrication, high-resolution display	Heavy crystallization impact from laser beam
	Laser engraving [33, 65]	2D	High-resolution display	Flat pattern required
	Lithography [66]	3D	Holographic display, high encoding capacity	High-energy laser source required, sophisticated optical paths and machines

**Table 1.**  
Technical assessment of patterning methods.

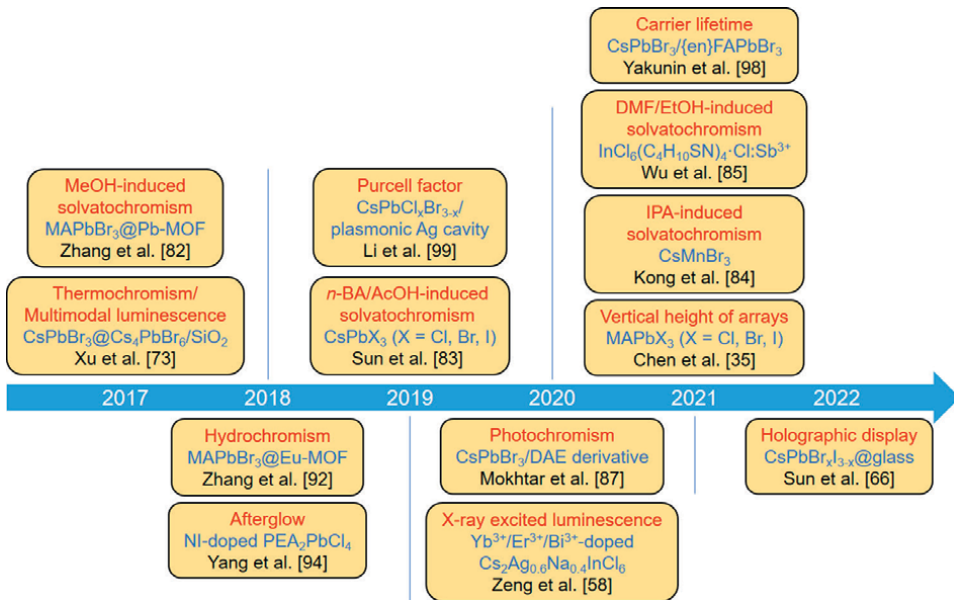


**Figure 3.**  
Timeline of pioneering works with new encryption principles being reported for perovskite security tags.

while unclonable texture for anti-counterfeiting tags is based on CsPbBr<sub>3</sub> patterns. A large amount of patterns that grown on laser-engraved lyophilic 1H,1H,2H,2H-perfluorooctyltriethoxysilane (POTS) layer are grouped by the number of edges for both polygon and complex contour design. Using portable microscope and

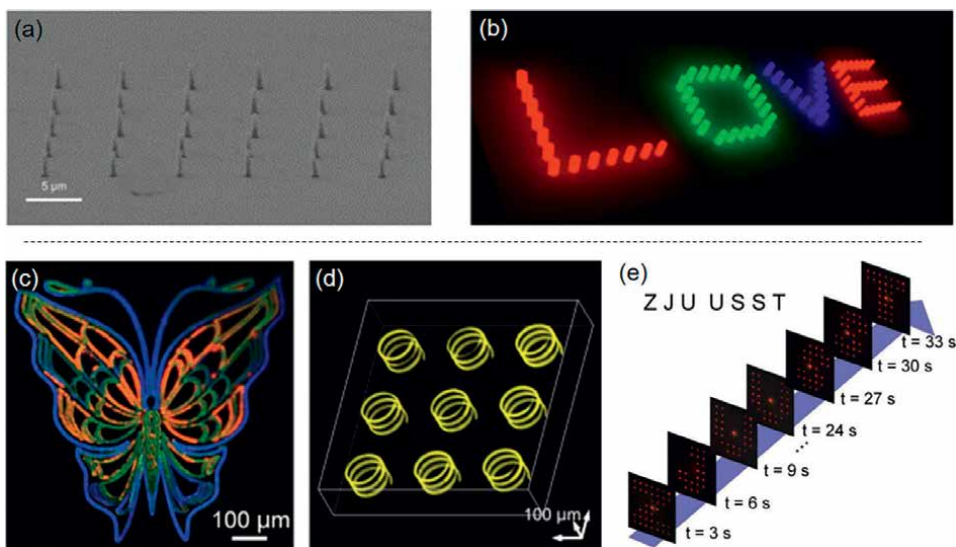


**Figure 4.** (a) Tilt-view SEM image of as-printed perovskite nanopixel arrays. (b) Multicolor display of perovskite nanopixel arrays with different halide components under UV light. (c) Multicolor pattern with  $\text{CsPbCl}_x\text{Br}_{3-x}$  nanophasers in glass under UV light. (d) 3D microhelix arrays of  $\text{CsPbCl}_x\text{Br}_{3-x}$  under UV light. (e) Dynamic holographic display of as-patterned “ZJUUSST” characters under 532-nm light. Reprinted with permission from ref. [35, 66] copyright 2021 American Chemical Society; copyright 2022 American Association for the Advancement of Science.

ShaptexMatch authentication software, the authors of this study matched the shape and texture of patterns, respectively, from the establishing database of 61st type of graphics. The effective encoding capacity of patterns was estimated up to  $2.1 \times 10^{623}$ , and the authentication time was only 12.17 s for 4000 samples.

The vertical height of a single perovskite pixel can be also encoded as specific numbers [35], which is regarded as a complementary encryption strategy to lateral shape design of a pattern (**Figure 4a** and **b**). 3D confocal PL imaging was applied to recognize the height variation of perovskite pixels with the height interval of 5  $\mu\text{m}$ . The height values were further converted into binary information matrix for digitalized decryption. As we have mentioned in Section 2.2, the pattern design at three dimensionalities enabled by 3D lithography technique allows more complex encryption on a security tag (**Figure 4c–e**) [66]. Random 3D luminescent patterns can therefore be spatially and temporally identified, offering an innovative platform for smart authentication of goods.

### 2.3.2 Thermochromism

Halide perovskites, especially organic–inorganic hybrid ones, feature considerably large thermal expansion coefficients [68, 69]. The thermochromic property of perovskites was first observed in thin film due to the phase transition between transparent hydrated phase ( $\text{MA}_4\text{PbI}_6 \cdot 2\text{H}_2\text{O}$ ) and dark perovskite phase ( $\text{MAPbI}_3$ ) [70]. This phenomenon can be reversible by exposing perovskite film to ambient moisture at RT or heating condition at 60°C repeatably and was explored as the switchable photovoltaic performance for perovskite solar cells. The discoloration mechanism was recently developed for smart window applications based on hydrated  $\text{MAPbCl}_x\text{I}_{3-x}$  [71]. Similarly, Lin et al. [72] demonstrated the reversible thermochromic property

of  $\text{CsPbBr}_x\text{I}_{3-x}$  film coupled with dynamic transition of RT non-perovskite phase and high-temperature perovskite phase, which is also switched by the moisture and thermal annealing.

Above cases show the thermochromic phenomena of perovskites in the presence of moisture but may not be applicable to anti-counterfeiting tags that are fully encapsulated. Taking advantage of the inverse temperature crystallization (ITC) of hybrid perovskites, Bastiani et al. [73] reported the chromatic inks with wide color variation that depend on the halide constituent of perovskite precipitate. The RT yellow inks turned to orange, red, and black when temperature reached 60°C, 90°C, and 120°C, corresponding to the extrapolated absorption edges of  $\text{MAPbBr}_{2.7}\text{I}_{0.3}$  at 597 nm,  $\text{MAPbBr}_{2.4}\text{I}_{0.6}$  at 615 nm, and  $\text{MAPbBr}_{1.8}\text{I}_{1.2}$  at 651 nm, respectively. The thermochromic behavior of perovskite inks showed consecutive cycling between RT and 60°C for several times.

The reversible thermochromic phenomena was also observed in diphasic perovskite material ( $\text{CsPbBr}_3/\text{Cs}_4\text{PbBr}_6$ ) wrapped by silica nanosphere [74]. The strong RT PL emission (at 525 nm) of composited patterns gradually decreased when temperature was elevated and almost disappeared at 150°C. Temperature-dependent PL spectra revealed the relatively low activation energy ( $E_a$ , 38 meV) of thermal quenching of composites, being ascribed to the thermal-sensitive nature of  $\text{Cs}_4\text{PbBr}_6$  and should be responsible for the thermal-switchable PL emission. In addition, thermochromism can be found in both lead-based and lead-free 2D perovskites and double perovskites. Octahedral distortion and interlayer distance of 2D perovskites are strongly related to temperature and hence will result in phase transition during thermal heating or cooling [75, 76]. The structural change is accompanied by the bandgap variation of materials, leading to thermochromic behavior that can be identified by CIE coordinates. Ning et al. [77] reported the thermochromism of double-perovskite single crystal and thin film from RT to 250°C. The synergistic effect of anharmonic fluctuation and electron-phonon coupling as well as the spin-orbit coupling effect were unveiled to explain the thermochromic behavior of  $\text{Cs}_2\text{AgBiBr}_6$  upon the bond length change of Ag-Br and Bi-Br. Security tags based on thermochromic perovskites enable the decryption through the information of discoloration or photoexcited emission relative to temperature.

### 2.3.3 Solvatochromism

Solvatochromism refers to chromic behavior of materials as response to water or other organic solvents. As we mentioned in Section 2.3.2, hybrid perovskites feature hydrochromism due to the formation of hydrated or non-perovskite phases in moisture atmosphere [70, 72]. Reversibly decomposition-induced hydrochromism was recently reported for  $\text{CsPbBr}_3$  NCs confined in mesoporous silica nanospheres (MSNs) [78]. Orthorhombic  $\text{CsPbBr}_3$  will decompose into nonluminescent tetragonal  $\text{CsPb}_2\text{Br}_5$  and  $\text{CsBr}$  in the presence of water, and the dissolved  $\text{CsBr}$  component can be confined in MSNs. As a result, the green emission pattern turned to dark in moisture condition and recovered when water was removed (**Figure 5a**). Similar hydrochromic mechanism was also reported for  $\text{CsPbBr}_3/\text{Cs}_4\text{PbBr}_6$  nanocomposites, which maintained about half of its initial PL intensity after 10 wetting-drying cycles [80].  $\text{Cs}_3\text{Cu}_2\text{I}_5$  as lead-free perovskite-like material was recently exploited for hydrochromism-based encryption and decryption of security tags [81–83]. Water functions as a switch of phase transition between blue emission  $\text{Cs}_3\text{Cu}_2\text{I}_5$  and yellow emission  $\text{CsCu}_2\text{I}_3$  under UV excitation. Combined with water-resistant polymethyl methacrylate (PMMA) coating layer, moreover, the microarray

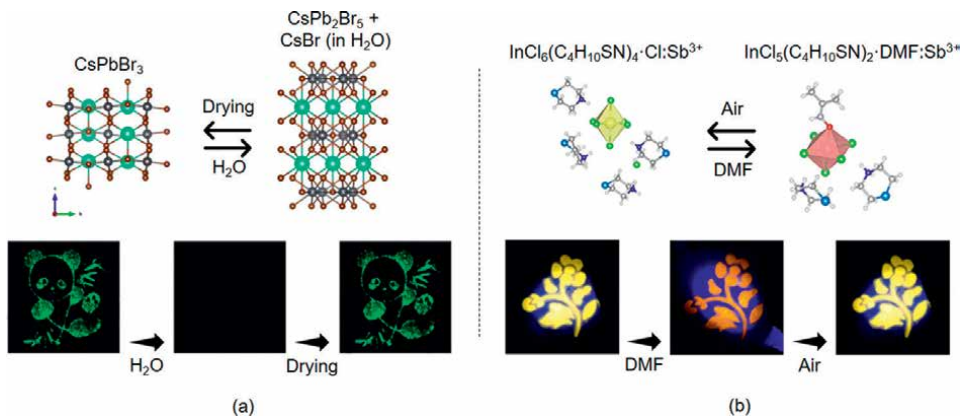


**Figure 5.** (a) Reversible hydrochromism of CsPbBr<sub>3</sub> pattern under 365-nm UV light and the corresponding phase transformation. (b) Reversible DMF-induced solvatochromism of InCl<sub>6</sub>(C<sub>4</sub>H<sub>10</sub>SN)<sub>4</sub>·Cl·Sb<sup>3+</sup> pattern under 365-nm UV light and the corresponding phase transformation. Reprinted with permission from refs. [78, 79]. Copyright 2020 Wiley-VCH Verlag GmbH & Co. KGaA, Weinheim; copyright 2021 American Chemical Society.

patterns can be tailored for dual-color emission toward various shapes and characters in moisture atmosphere [82].

Besides water, methanol (MeOH) was previously demonstrated capable to trigger the solvatochromism of MAPbBr<sub>3</sub> NCs that are converted from lead-based metal–organic framework (MOF) [84]. The authors of this study found that MeOH impregnation can remove the organic perovskite species while leave lead ions in MOF matrix. The green emission of pattern under UV excitation therefore quickly quenched after impregnation but can be recovered by loading MABr solution (10 mg mL<sup>-1</sup> in *n*-butanol) on top. Using *n*-butylamine (*n*-BA) and acetic acid (AcOH) as encryption and decryption reagents, respectively, Sun et al. [85] reported the solvatochromism of patterns based on CsPbX<sub>3</sub> (X = Cl, Br, I) QDs. The RGB emission colors disappeared after *n*-BA treatment and then recovered by AcOH treatment. Specifically, the as-fabricated multicolor quick response (QR) code still showed clear optical readout after 100 times crumpling. Isopropanol (IPA)-induced solvatochromism was observed in 1D CsMnBr<sub>3</sub> NCs which underwent phase decomposition to 0D Cs<sub>3</sub>MnBr<sub>5</sub> and MnBr<sub>2</sub> [86]. The pattern showed emission color changing from red to green under 365-nm UV light.

Solvatochromism can also be induced by new phase formation where solvent molecules are incorporated into perovskite lattice [79]. The 0D InCl<sub>6</sub>(C<sub>4</sub>H<sub>10</sub>SN)<sub>4</sub>·Cl·Sb<sup>3+</sup> showed red-shifted emission peak from 550 nm to 580 nm and 600 nm when being exposed to ethanol (EtOH) and *N,N*-dimethylformamide (DMF) vapor, corresponding to the new phases of InCl<sub>6</sub>(C<sub>4</sub>H<sub>10</sub>SN)<sub>3</sub>·EtOH·Sb<sup>3+</sup> and InCl<sub>5</sub>(C<sub>4</sub>H<sub>10</sub>SN)<sub>2</sub>·DMF·Sb<sup>3+</sup>, respectively. Pattern based on this environmentally friendly material displayed reversible emission colors between yellow and orange under 365-nm excitation, which was enabled by the alternate incorporation and release of DMF species (**Figure 5b**). Considering the peculiar chemical reaction between perovskites and solvents, solvatochromism of perovskite security tags provides an additional route for authentication of goods.

### 2.3.4 Photochromism

Photochromic property has been found in a variety of organics and organic–metal complexes in the case of light-mediated configuration change of molecules [87].

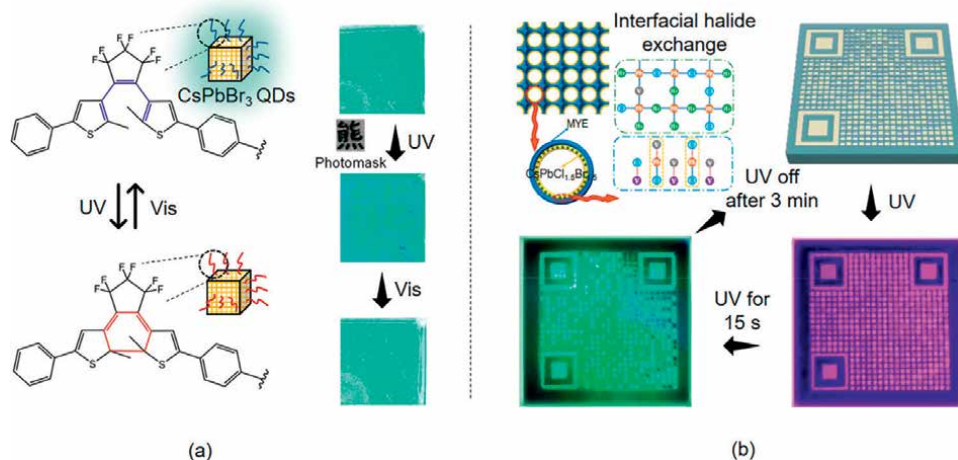


**Figure 6.** (a) Photoswitchable cyclization and cycloreversion of DAE surfactant and the resultant photochromism of pattern based on CsPbBr<sub>3</sub>-DAE hybrids. (b) UV irradiation-induced reversible halide exchange at CsPbCl<sub>1.5</sub>Br<sub>1.5</sub>/MYE interface and the photochromism of QR code patterned by CsPbCl<sub>1.5</sub>Br<sub>1.5</sub>/MYE composites. Reprinted with permission from refs. [88, 89]. Copyright 2020 American Chemical Society; copyright 2021 American Chemical Society.

By anchoring the diarylethene (DAE) derivative onto CsPbBr<sub>3</sub> QDs surface, Mokhtar et al. [88] observed the reversible photoswitchable luminescence of QDs-DAE hybrids. The open-ring isomer of DAE underwent cyclization under UV light and quickly turned off the green emission of printed pattern, while the green emission can be switched on again by exposing the pattern to visible light for DAE cycloreversion (**Figure 6a**). Similar photochromic behavior was reported for DAE derivative whose triethoxysilane (TEOS) moiety is altered by alkyl amine [90]. Following this strategy, a majority of photochromic molecules may be introduced as the surfactant to achieve the photochromism of perovskite QDs/NCs.

Photochromism also occurs under the circumstance of photoinduced compositional variation of perovskites. The emission color of CsPbCl<sub>1.5</sub>Br<sub>1.5</sub> NCs that confined in macroporous Y<sub>2</sub>O<sub>3</sub>:Eu<sup>3+</sup> (MYE) changed from red to green under continuous UV irradiation, which was explained by the halide migration between perovskite NCs and MYE matrix [89]. The small  $E_a$  of halide vacancy defects allows bromine ions to segregate to NCs domain, while the chlorine ions are fixed on MYE surface due to the stable Y-Cl bond. Therefore, the red emission is contributed by MYE matrix at the first stage, and the subsequent strong green emission that originated from Br-rich perovskite NCs will dominate the composites (**Figure 6b**). The QR code fabricated by stereolithography printing technique maintained 61% of the maximum green emission intensity after 25 encryption/decryption cycles. Yang et al. [91] reported the irreversible photochromism of CsPbCl<sub>1.5</sub>Br<sub>1.5</sub>@Ca<sub>0.9</sub>Eu<sub>0.1</sub>MoO<sub>4</sub> (CEMO) composites enabled by interfacial redox reaction of  $\text{Eu}^{3+} + \text{Pb}^0 \rightarrow \text{Eu}^{2+} + \text{Pb}^{2+}$ . The emission peak at 615 nm dominated the composites at the initial stage for a few seconds but was quickly overwhelmed by the emission peak at 519 nm during continuous UV irradiation, and patterns based on such composites ultimately displayed a mixed color of cyan.

The bandgap of perovskites is structurally dependent on the QW thickness; in this view, photochromism can be achieved in dimensionality-mixed perovskites whose QW thickness and distribution are self-adapted to light stimulus. The emission

behavior of layered  $\text{FA}_{n+2}\text{Pb}_n\text{Br}_{3n+2}$  (FA = formamidinium) was recently studied with respect to its structural transformation under light irradiation [92]. The authors of this study demonstrated the UV damage to perovskite that can convert wide-bandgap 2D phase to narrow-bandgap 3D phase. Accordingly, perovskite film showed emission color changed from blue to green as response to the elongated irradiation time. The metastable 2D phase can meanwhile be transformed back by dark storage, showing reversible photochromism that is applicable for anti-counterfeiting patterns.

### 2.3.5 Multimodal luminescence

Unlike unidirectional authentication methods, multimodal luminescence of perovskites allows the encryption and decryption to be conducted through multiple excited sources. Xu et al. [74] first demonstrated the triple-modal anti-counterfeiting of  $\text{CsPbBr}_3@\text{Cs}_4\text{PbBr}_6/\text{SiO}_2$  composites in 2017, since the as-patterned codes showed reversible and switchable luminescence to heating, UV, and NIR irradiation. In addition, the dual-color emission of green and red of  $\text{MAPbBr}_3@\text{Eu-MOF}$  composites was reported under 365-nm and 254-nm UV lamp [93], respectively, where the red emission under 254-nm excitation primarily comes from the photon upconversion (UC) of Eu-MOF species (**Figure 7a** and **b**). Solvatochromism was also observed for the composites, and the written pattern on paper showed reversible green emission via

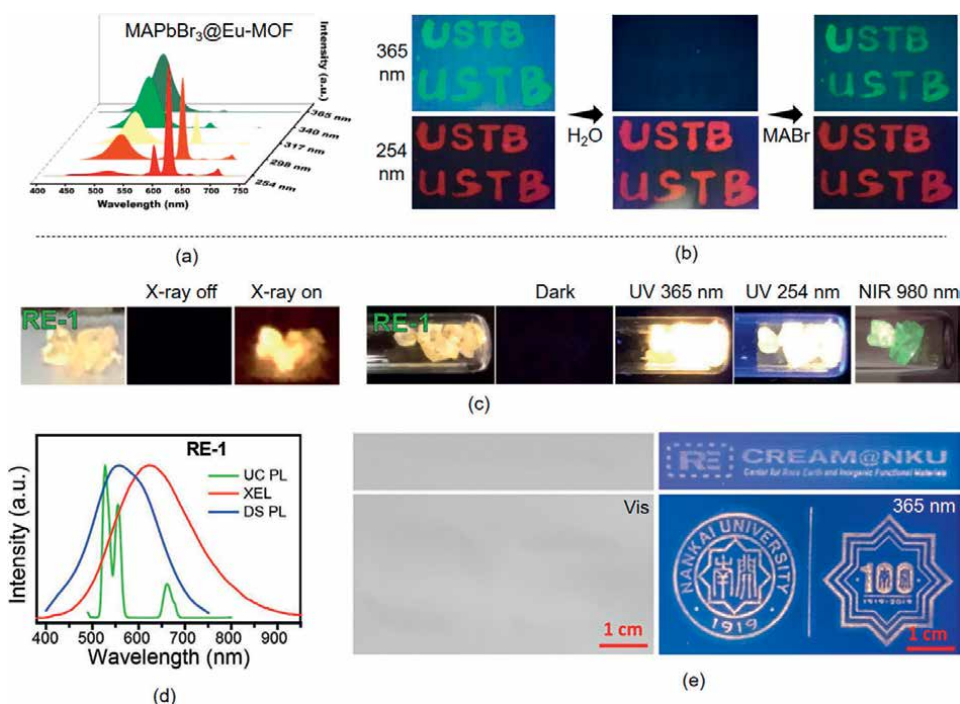


**Figure 7.**  
 (a) The dependence of PL spectra of  $\text{MAPbBr}_3@\text{Eu-MOF}$  composites on the UV excitation wavelength.  
 (b) Hydrochromism of “USTB” characters based on  $\text{MAPbBr}_3@\text{Eu-MOF}$  composites and the MABr-induced recovery under 254-nm and 365-nm UV light. (c) Photographs of  $\text{Cs}_2\text{Ag}_{0.6}\text{Na}_{0.4}\text{InCl}_6\text{Yb}^{3+}/\text{Er}^{3+}/\text{Bi}^{3+}$  (RE-1) under different excitations. (d) XEL, DS-PL, and UC-PL spectra of RE-1. (e) Photographs of RE-1 pattern under visible and 365 nm UV light. Reprinted with permission from refs. [58, 93]. Copyright 2018 American Chemical Society; copyright 2020 Wiley-VCH GmbH.

water and MABr treatment. Notably, the UC luminescent component of perovskites can be further tuned by rational doping of lanthanides [94].

Overcoming the limited response range of conventional perovskite materials, the excitation source of  $\text{Yb}^{3+}/\text{Er}^{3+}/\text{Bi}^{3+}$  co-doped  $\text{Cs}_2\text{Ag}_{0.6}\text{Na}_{0.4}\text{InCl}_6$  double perovskite was reported to be extended to X-ray, as a complementary to UV and NIR [58].  $\text{Bi}^{3+}$  ions were demonstrated to reduce the structural disorder, promote the exciton localization, and lead to strong Jahn-Teller effect that would benefit both UC and X-ray excited luminescence (XEL) (Figure 7c and d). The as-synthesized double-perovskite single crystals were ground and dispersed in organic solvent for ink printing, and the patterns showed exceptional luminescent stability in thermal heating (up to  $400^\circ\text{C}$ ), moisture, and high-dosage radiation conditions (Figure 7e). The combination of X-ray excited luminescence (XEL), downshifting (DS), UC luminescence, and other routine encryption methods enhance the confidential level of tags considerably, which offers a reliable solution for customized authentication of high-value products.

### 2.3.6 Other optical readout

Some special optical readout of perovskites can be transformed into security information for anti-counterfeiting applications. Here, we exemplify the encryption principles of patterns based on afterglow phenomenon and carrier lifetime gating. The RT afterglow of perovskites was first reported for 2D  $\text{PEA}_2\text{PbCl}_4$  (PEA = phenylethylammonium) perovskite doped with 1,8-naphthalimide (NI) spacers [95]. The as-printed pattern on paper showed UV-excited white emission in nitrogen atmosphere that comprises blue fluorescence from perovskite and yellow phosphorescence from NI organic cations. After UV light off, however, the blue fluorescence (PLQY: 25.6%) quenched quickly, while the yellow phosphorescence (PLQY: 56.1%) can maintain for a few seconds. This property caused the yellow afterglow of pattern that can be identified by both spectrum and human eye. Wei et al. [96] recently found the RT greenish afterglow of 0D  $\text{BAPPIn}_{1.996}\text{Sb}_{0.004}\text{Cl}_{10}$  (BAPP =  $\text{C}_{10}\text{H}_{28}\text{N}_4$ ) perovskite-like material after UV

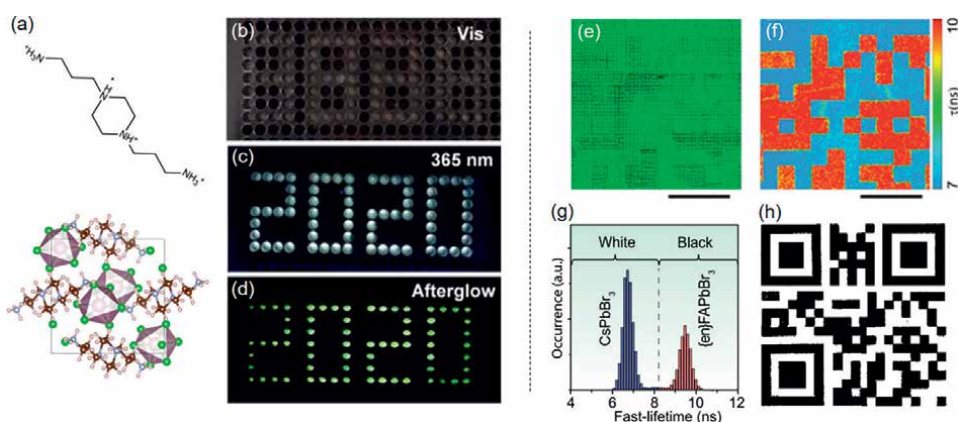


**Figure 8.** (a) Molecular configuration of  $\text{BAPP}^{4+}$  cation and crystal structure of  $\text{BAPPIn}_2\text{Cl}_{10}$ . (b–d) Photographs of  $\text{BAPPIn}_{1.996}\text{Sb}_{0.004}\text{Cl}_{10}$  pattern under visible light, 365-nm UV light, and 365-nm UV light off (afterglow), respectively. (e) FLIM image and (f) time-correlated single-photon counting fluorescence lifetime imaging (TCSPC-FLI) image of tag patterned by  $\text{CsPbBr}_3$  and  $\{\text{en}\}\text{FAPbBr}_3$  NCs inks. (g) Fast-lifetime histograms of as-patterned inks and (h) binarization of lifetime for QR code generation. Reprinted with permission from refs. [96, 97]. Copyright 2021 American Association for the Advancement of Science; copyright 2021 Springer Nature.

light off, where the relaxation of excitons from BAPP organic cations were demonstrated to be responsible for the afterglow (**Figure 8a–d**). For CsPbBr<sub>3</sub> NCs doped by lanthanide ions (Ln<sup>3+</sup>), the persistent time of afterglow is even up to 1800 s [98]. In addition, X-ray-induced afterglow was also reported for 0D Cs<sub>4</sub>EuX<sub>6</sub> (X = Br, I) perovskite single crystals, despite the case did not involve anti-counterfeiting applications [99].

The carrier lifetime of perovskites is influenced by a variety of factors, among which the composition of perovskite can be the deterministic one. The EHD-printed security tags were reported to be encrypted based on the different carrier lifetime of CsPbBr<sub>3</sub> and hollowed {en}FAPbBr<sub>3</sub> NCs, which can then be decrypted by either fluorescence-lifetime imaging microscopy (FLIM) or time-of-flight fluorescence-lifetime imaging (ToF-FLI) (**Figure 8e–h**) [97]. These two imaging techniques enabled machine-readable lifetime of QR code that cannot be readily decoded by routine methods. Moreover, the system is highly reconfigurable due to the compositional versatility of perovskite NCs. The enhancement and Purcell factors of CsPbCl<sub>x</sub>Br<sub>3-x</sub> QDs that coupled to plasmonic silver cavity were also extracted for the encryption of QR code, where the factors are defined by the relationship among excitation efficiency, light extraction efficiency, quantum efficiency, and radiative rate [100].

### **3. Challenges of anti-counterfeiting technology based on halide perovskites**

We hereby briefly discuss the current challenges encountered by perovskite fluorescent tags prior to their real-world applications, including the potential overuse of toxic lead, the poor durability, and many clonable functions that can be easily reproduced by counterfeiters. Possible solutions are also provided with respect to each challenging case.

#### **3.1 Lead contamination**

Lead's toxicity has been widely recognized due to its damage to the nervous system of biological individuals. Therefore, lead-based wastes are now under strict control in many developed countries. Despite perovskite security tags made by lead compounds feature many intriguing fluorescent properties, they can be highly risky when adhere to daily goods and cause potential lead leakage. Alternatively, more environmental-friendly perovskites (e.g. tin-, antimony-, bismuth-, and copper-based) can be developed to replace lead-based ones while maintaining the bright luminescence and high processability of tags [55, 57, 58, 79, 82, 83, 96].

#### **3.2 Poor durability**

The phase stability of halide perovskites, especially 3D ones, can be susceptible to environmental perturbations and hence fail to work during long term or repeated authentication. Lowering down the dimensionality of perovskites as well as composite strategies enable more robust perovskite phase, yet the stability of fluorescent tags can hardly rival the simple-patterned tags (e.g. QR code). Advanced sealing techniques alleviate this problem by isolating perovskites from environment; however, they are limit for those tags that need direct exposure to atmosphere, chemicals, or solvents. Inert matrix has been demonstrated to enhance the durability of both common and special perovskite fluorescent tags. Beside glass, silica, and polymers [66, 82, 101], other durable matrix materials remain to be exploited.

### **3.3 Clonable functions**

Single-mode perovskite fluorescent tags work as response to certain stimulus, making their functions clonable by commercial phosphors or other functionalized luminescent materials. A safer communication between users and server database requires physically unclonable functions (PUFs) that generated by irregular encryption and decryption methods. In this view, multimodal anti-counterfeiting that combines two or more encoding and decoding pathways (see Section 2.3) is prompt to be developed for highly confidential security tags. In addition, authentication based on the digital readout of sophisticated machines can also fulfill the demands of PUFs [97, 100].

## **4. Summary**

Increasingly rich encryption principles have been exploited for halide perovskite-based security tags owing to their intriguing luminescent properties as response to a wide range of stimuli. Apart from the existing cases, the mechanochromism upon mechanical stress as well as the magnetochromism under altered magnetic field can be studied for perovskites with the aim of further enriching the diversity of authentication methods [102, 103]. Perovskite memristors as a new rising technology was also demonstrated to deliver switching electronic signals relative to the charged defects and halide motions inside the materials, providing an additional solution toward the design of PUF system [104]. All these unique optical and digital readout may overcome the limit of conventional clonable tags such as QR codes, watermarks, and raised print.

Future development of perovskite security tags is supposed to follow the taxonomy of predominant PUFs, including high encoding capacity, tunable security level, logically/physically reconfigurable functions, and switchable access between private and public. Based on the rational screening strategy of perovskite materials, micro- and nanoscale patterning techniques allow these functions to be multidimensionally integrated in a minimized tag, making security information more robust against third parties. Halide perovskites are bound to play a more important role in anti-counterfeiting arena and contribute to future smart flow of goods in a more fair and orderly global market.

## **Acknowledgements**

YH thanks the support by National Ten Thousand Talent Program for Young Topnotch Talent.

## **Conflict of interest**

The authors declare no conflict of interest.

## Author details

Ziren Zhou<sup>1</sup>, Jin Xie<sup>2</sup> and Yu Hou<sup>2\*</sup>

1 Department of Physics, Chemistry and Biology (IFM), Linköping University, Linköping, Sweden

2 Key Laboratory for Ultrafine Materials of Ministry of Education, Shanghai Engineering Research Center of Hierarchical Nanomaterials, School of Materials Science and Engineering, East China University of Science and Technology, Shanghai, China

\*Address all correspondence to: [yhou@ecust.edu.cn](mailto:yhou@ecust.edu.cn)

## IntechOpen

---

© 2022 The Author(s). Licensee IntechOpen. This chapter is distributed under the terms of the Creative Commons Attribution License (<http://creativecommons.org/licenses/by/3.0>), which permits unrestricted use, distribution, and reproduction in any medium, provided the original work is properly cited. 

## References

- [1] OECD, European Union Intellectual Property Office. Trends in Trade in Counterfeit and Pirated Goods, Illicit Trade. Paris: OECD Publishing; 2019. DOI: 10.1787/g2g9f533-en
- [2] OECD, European Union Intellectual Property Office. Misuse of Containerized Maritime Shipping in the Global Trade of Counterfeits, Illicit Trade. Paris: OECD Publishing; 2021. DOI: 10.1787/e39d8939-en
- [3] Glyn D. A History of Money. 4th ed. Cardiff: University of Wales Press; 2016 p. 800
- [4] Grier DG. A revolution in optical manipulation. *Nature*. 2003;**424**:810-816. DOI: 10.1038/nature01935
- [5] Midgley PA, Dunin-Borkowski RE. Electron tomography and holography in materials science. *Nature Materials*. 2009;**8**:271-280. DOI: 10.1038/nmat2406
- [6] Zheng G, Muhlenbernd H, Kenney M, Li G, Zentgraf T, Zhang S. Metasurface holograms reaching 80% efficiency. *Nature Nanotechnology*. 2015;**10**:308-312. DOI: 10.1038/nnano.2015.2
- [7] Rivenson Y, Zhang Y, Gunaydin H, Teng D, Ozcan A. Phase recovery and holographic image reconstruction using deep learning in neural networks. *Light: Science & Applications*. 2018;**7**:17141. DOI: 10.1038/lsa.2017.141
- [8] Nam H, Song K, Ha D, Kim T. Inkjet printing based mono-layered photonic crystal patterning for anti-counterfeiting structural colors. *Scientific Reports*. 2016;**6**:30885. DOI: 10.1038/srep30885
- [9] You M, Zhong J, Hong Y, Duan Z, Lin M, Xu F. Inkjet printing of upconversion nanoparticles for anti-counterfeit applications. *Nanoscale*. 2015;**7**:4423-4431. DOI: 10.1039/c4nr06944g
- [10] Kumar P, Singh S, Gupta BK. Future prospects of luminescent nanomaterial based security inks: From synthesis to anti-counterfeiting applications. *Nanoscale*. 2016;**8**:14297-14340. DOI: 10.1039/c5nr06965c
- [11] Liu Y, Han F, Li F, Zhao Y, Chen M, Xu Z, et al. Inkjet-printed unclonable quantum dot fluorescent anti-counterfeiting labels with artificial intelligence authentication. *Nature Communications*. 2019;**10**:2409. DOI: 10.1038/s41467-019-10406-7
- [12] Ecker M, Pretsch T. Multifunctional poly(ester urethane) laminates with encoded information. *RSC Advances*. 2014;**4**:286-292. DOI: 10.1039/c3ra45651j
- [13] Ha BH, Ahn S, Bae HS, Kang HS, Kim JO, Noh J. Fast and direct engraving of iridescent lettering on original product surface using laser interference to prevent counterfeiting. *Optics and Lasers in Engineering*. 2018;**107**:214-220. DOI: 10.1016/j.optlaseng.2018.03.024
- [14] Zhu CC, Tao LQ, Peng ZR, Wang GY, Huang YX, Zou SM, et al. An integrated luminescent information encryption-decryption and anticounterfeiting chip based on laser induced graphene. *Advanced Functional Materials*. 2021;**31**:2103255. DOI: 10.1002/adfm.202103255
- [15] Zhou Z, Qiao HW, Hou Y, Yang HG, Yang S. Epitaxial halide perovskite-based materials for photoelectric energy conversion. *Energy &*

- Environmental Science. 2021;**14**: 127-157. DOI: 10.1039/d0ee02902e
- [16] Hassan Y, Park JH, Crawford ML, Sadhanala A, Lee J, Sadighian JC, et al. Ligand-engineered bandgap stability in mixed-halide perovskite LEDs. *Nature*. 2021;**591**:72-77. DOI: 10.1038/s41586-021-03217-8
- [17] Kim YH, Zhai Y, Lu H, Pan X, Xiao C, Gauldin EA, et al. Chiral-induced spin selectivity enables a room-temperature spin light-emitting diode. *Science*. 2021;**371**:1129-1133. DOI: 10.1126/science.abf5291
- [18] Yoo JJ, Seo G, Chua MR, Park TG, Lu Y, Rotermund F, et al. Efficient perovskite solar cells via improved carrier management. *Nature*. 2021;**590**:587-593. DOI: 10.1038/s41586-021-03285-w
- [19] Lei Y, Chen Y, Zhang R, Li Y, Yan Q, Lee S, et al. A fabrication process for flexible single-crystal perovskite devices. *Nature*. 2020;**583**:790-795. DOI: 10.1038/s41586-020-2526-z
- [20] García de Arquer FP, Armin A, Meredith P, Sargent EH. Solution-processed semiconductors for next-generation photodetectors. *Nature Reviews Materials*. 2017;**2**:16100. DOI: 10.1038/natrevmats.2016.100
- [21] Noh JH, Im SH, Heo JH, Mandal TN, Seok SI. Chemical management for colorful, efficient, and stable inorganic-organic hybrid nanostructured solar cells. *Nano Letters*. 2013;**13**:1764-1769. DOI: 10.1021/nl400349b
- [22] Wang H, Yin X, Wang L. Highly stable perovskite nanogels as inks for multicolor luminescent authentication applications. *Journal of Materials Chemistry C*. 2018;**6**:11569-11574. DOI: 10.1039/c8tc04420a
- [23] Filip MR, Eperon GE, Snaith HJ, Giustino F. Steric engineering of metal-halide perovskites with tunable optical band gaps. *Nature Communications*. 2014;**5**:5757. DOI: 10.1038/ncomms6757
- [24] Eperon GE, Stranks SD, Menelaou C, Johnston MB, Herz LM, Snaith HJ. Formamidinium lead trihalide: A broadly tunable perovskite for efficient planar heterojunction solar cells. *Energy & Environmental Science*. 2014;**7**:982-988. DOI: 10.1039/c3ee43822h
- [25] Ito N, Kamarudin MA, Hirotani D, Zhang Y, Shen Q, Ogomi Y, et al. Mixed Sn-Ge perovskite for enhanced perovskite solar cell performance in air. *The Journal of Physical Chemistry Letters*. 2018;**9**:1682-1688. DOI: 10.1021/acs.jpcllett.8b00275
- [26] Ke W, Stoumpos CC, Zhu M, Mao L, Spanopoulos I, Liu J, et al. Enhanced photovoltaic performance and stability with a new type of hollow 3D perovskite {en}FASnI<sub>3</sub>. *Science Advances*. 2017;**3**:e1701293. DOI: 10.1126/sciadv.1701293
- [27] Zhou C, Lin H, Tian Y, Yuan Z, Clark R, Chen B, et al. Luminescent zero-dimensional organic metal halide hybrids with near-unity quantum efficiency. *Chemical Science*. 2018;**9**:586-593. DOI: 10.1039/c7sc04539e
- [28] Mondal N, De A, Samanta A. Achieving near-unity photoluminescence efficiency for blue-violet-emitting perovskite nanocrystals. *ACS Energy Letters*. 2018;**4**:32-39. DOI: 10.1021/acscenergylett.8b01909
- [29] Pang P, Jin G, Liang C, Wang B, Xiang W, Zhang D, et al. Rearranging low-dimensional phase distribution of quasi-2D perovskites for efficient sky-blue perovskite light-emitting diodes. *ACS Nano*. 2020;**14**:11420-11430. DOI: 10.1021/acsnano.0c03765

- [30] Liu MM, Wan Q, Wang HM, Carulli F, Sun XC, Zheng WL, et al. Suppression of temperature quenching in perovskite nanocrystals for efficient and thermally stable light-emitting diodes. *Nature Photonics*. 2021;**15**:379-385. DOI: 10.1038/s41566-021-00766-2
- [31] Chu Z, Ye Q, Zhao Y, Ma F, Yin Z, Zhang X, et al. Perovskite light-emitting diodes with external quantum efficiency exceeding 22% via small-molecule passivation. *Advanced Materials*. 2021;**33**:2007169. DOI: 10.1002/adma.202007169
- [32] Chen Q, Wu J, Ou X, Huang B, Almutlaq J, Zhumekenov AA, et al. All-inorganic perovskite nanocrystal scintillators. *Nature*. 2018;**561**:88-93. DOI: 10.1038/s41586-018-0451-1
- [33] Lin Y, Zhang H, Feng J, Shi B, Zhang M, Han Y, et al. Unclonable micro-texture with clonable micro-shape towards rapid, convenient, and low-cost fluorescent anti-counterfeiting labels. *Small*. 2021;**17**:2100244. DOI: 10.1002/smll.202100244
- [34] Wang HJ, Yao WJ, Tian QY, Li MX, Tian B, Liu L, et al. Printable monodisperse all-inorganic perovskite quantum dots: Synthesis and banknotes protection applications. *Advanced Materials Technologies*. 2018;**3**:1800150. DOI: 10.1002/admt.201800150
- [35] Chen M, Hu S, Zhou Z, Huang N, Lee S, Zhang Y, et al. Three-dimensional perovskite nanopixels for ultrahigh-resolution color displays and multilevel anticounterfeiting. *Nano Letters*. 2021;**21**:5186-5194. DOI: 10.1021/acs.nanolett.1c01261
- [36] Shamsi J, Urban AS, Imran M, De Trizio L, Manna L. Metal halide perovskite nanocrystals: Synthesis, post-synthesis modifications, and their optical properties. *Chemical Reviews*. 2019;**119**:3296-3348. DOI: 10.1021/acs.chemrev.8b00644
- [37] Smith MD, Karunadasa HI. White-light emission from layered halide perovskites. *Accounts of Chemical Research*. 2018;**51**:619-627. DOI: 10.1021/acs.accounts.7b00433
- [38] Dohner ER, Hoke ET, Karunadasa HI. Self-assembly of broadband white-light emitters. *Journal of the American Ceramic Society*. 2014;**136**:1718-1721. DOI: 10.1021/ja411045r
- [39] Wan W, Han XX, Zhou YY, Chen FR, Jing XP, Ye S. Constructing perovskite-like oxide  $\text{CsCa}_2\text{Ta}_3\text{O}_{10}$ :  $\text{Yb, Er}@\text{Cs}(\text{Pb}_x\text{Mn}_{1-x})(\text{Cl}_y\text{Br}_{1-y})_3$  perovskite halide composites for five-dimensional anti-counterfeiting barcodes applications. *Chemical Engineering Journal*. 2021;**409**:128165. DOI: 10.1016/j.cej.2020.128165
- [40] Anthony JW, Bideaux RA, Bladh KW, Nichols MC. *Handbook of Mineralogy*. Chantilly, VA: Mineralogical Society of America; 2003. pp. 20151-21110
- [41] Megaw HD. Crystal structure of barium titanate. *Nature*. 1945;**155**:484-485. DOI: 10.1038/155484b0
- [42] Wells HL. Über die cäsium- und kalium-bleihalogenide. *Zeitschrift für anorganische Chemie*. 1893;**3**:195-210. DOI: 10.1002/zaac.18930030124
- [43] Saliba M, Matsui T, Seo JY, Domanski K, Correa-Baena JP, Nazeeruddin MK, et al. Cesium-containing triple cation perovskite solar cells: Improved stability, reproducibility and high efficiency. *Energy & Environmental Science*. 2016;**9**:1989-1997. DOI: 10.1039/c5ee03874j
- [44] Anaya M, Correa-Baena JP, Lozano G, Saliba M, Anguita P, Roose B, et al. Optical

analysis of  $\text{CH}_3\text{NH}_3\text{Sn}_x\text{Pb}_{1-x}\text{I}_3$  absorbers: A roadmap for perovskite-on-perovskite tandem solar cells. *Journal of Materials Chemistry A*. 2016;**4**:11214-11221. DOI: 10.1039/c6ta04840d

[45] Yuan M, Quan LN, Comin R, Walters G, Sabatini R, Voznyy O, et al. Perovskite energy funnels for efficient light-emitting diodes. *Nature Nanotechnology*. 2016;**11**:872-877. DOI: 10.1038/nnano.2016.110

[46] Ng YF, Febriansyah B, Jamaludin NF, Giovanni D, Yantara N, Chin XY, et al. Design of 2D templating molecules for mixed-dimensional perovskite light-emitting diodes. *Chemistry of Materials*. 2020;**32**:8097-8105. DOI: 10.1021/acs.chemmater.0c00513

[47] Dohner ER, Jaffe A, Bradshaw LR, Karunadasa HI. Intrinsic white-light emission from layered hybrid perovskites. *Journal of the American Ceramic Society*. 2014;**136**:13154-13157. DOI: 10.1021/ja507086b

[48] Hu T, Smith MD, Dohner ER, Sher MJ, Wu X, Trinh MT, et al. Mechanism for broadband white-light emission from two-dimensional (110) hybrid perovskites. *The Journal of Physical Chemistry Letters*. 2016;**7**:2258-2263. DOI: 10.1021/acs.jpcclett.6b00793

[49] Yu J, Kong J, Hao W, Guo X, He H, Leow WR, et al. Broadband extrinsic self-trapped exciton emission in Sn-doped 2D lead-halide perovskites. *Advanced Materials*. 2019;**31**:1806385. DOI: 10.1002/adma.201806385

[50] Li Z, Li Y, Liang P, Zhou T, Wang L, Xie R-J. Dual-band luminescent lead-free antimony chloride halides with near-unity photoluminescence quantum efficiency. *Chemistry of Materials*. 2019;**31**:9363-9371. DOI: 10.1021/acs.chemmater.9b02935

[51] Zhang R, Mao X, Yang Y, Yang S, Zhao W, Wumaier T, et al. Air-stable, lead-free zero-dimensional mixed bismuth-antimony perovskite single crystals with ultra-broadband emission. *Angewandte Chemie International Edition*. 2019;**58**:2725-2729. DOI: 10.1002/anie.201812865

[52] Klement P, Dehnhardt N, Dong CD, Dobener F, Bayliff S, Winkler J, et al. Atomically thin sheets of lead-free 1D hybrid perovskites feature tunable white-light emission from self-trapped excitons. *Advanced Materials*. 2021;**33**:e2100518. DOI: 10.1002/adma.202100518

[53] Zhao S, Jiang S, Cai W, Li R, Mo Q, Wang B, et al. Intrinsic white-light emission from low-dimensional perovskites for white-light-emitting diodes with high-color-rendering index. *Cell Reports Physical Science*. 2021;**2**:100585. DOI: 10.1016/j.xcrp.2021.100585

[54] Maughan AE, Ganose AM, Bordelon MM, Miller EM, Scanlon DO, Neilson JR. Defect tolerance to intolerance in the vacancy-ordered double perovskite semiconductors  $\text{Cs}_2\text{SnI}_6$  and  $\text{Cs}_2\text{TeI}_6$ . *Journal of the American Ceramic Society*. 2016;**138**:8453-8464. DOI: 10.1021/jacs.6b03207

[55] Liu R, Zhang W, Li G, Liu W. An ultraviolet excitation anti-counterfeiting material of  $\text{Sb}^{3+}$  doped  $\text{Cs}_2\text{ZrCl}_6$  vacancy-ordered double perovskite. *Inorganic Chemistry Frontiers*. 2021;**8**:4035-4043. DOI: 10.1039/d1qi00639h

[56] Luo J, Wang X, Li S, Liu J, Guo Y, Niu G, et al. Efficient and stable emission of warm-white light from lead-free halide double perovskites. *Nature*. 2018;**563**:541-545. DOI: 10.1038/s41586-018-0691-0

- [57] Li X, Xu S, Liu F, Qu J, Shao H, Wang Z, et al. Bi and Sb codoped  $\text{Cs}_2\text{Ag}_{0.1}\text{Na}_{0.9}\text{InCl}_6$  double perovskite with excitation-wavelength-dependent dual-emission for anti-counterfeiting application. *ACS Applied Materials & Interfaces*. 2021;13:31031-31037. DOI: 10.1021/acsami.1c07809
- [58] Zeng Z, Huang B, Wang X, Lu L, Lu Q, Sun M, et al. Multimodal luminescent  $\text{Yb}^{3+}/\text{Er}^{3+}/\text{Bi}^{3+}$ -doped perovskite single crystals for X-ray detection and anti-counterfeiting. *Advanced Materials*. 2020;32:2004506. DOI: 10.1002/adma.202004506
- [59] Cong M, Yang B, Hong F, Zheng T, Sang Y, Guo J, et al. Self-trapped exciton engineering for white-light emission in colloidal lead-free double perovskite nanocrystals. *Science Bulletin*. 2020;65:1078-1084. DOI: 10.1016/j.scib.2020.03.010
- [60] Zhang L, Liu Z, Sun X, Niu G, Jiang J, Fang Y, et al. Retainable bandgap narrowing and enhanced photoluminescence in Mn-doped and undoped  $\text{Cs}_2\text{NaBiCl}_6$  double perovskites by pressure engineering. *Advanced Optical Materials*. 2022;10:2101892. DOI: 10.1002/adom.202101892
- [61] Shi LF, Meng LH, Jiang F, Ge Y, Li F, Wu XG, et al. In situ inkjet printing strategy for fabricating perovskite quantum dot patterns. *Advanced Functional Materials*. 2019;29:1903648. DOI: 10.1002/adfm.201903648
- [62] Zhu M, Duan Y, Liu N, Li H, Li J, Du P, et al. Electrohydrodynamically printed high-resolution full-color hybrid perovskites. *Advanced Functional Materials*. 2019;29:1903294. DOI: 10.1002/adfm.201903294
- [63] Zhang L, Liu Y, Gan Z, Su J, Gao Y. In situ localized formation of cesium lead bromide nanocomposites for fluorescence micro-patterning technology achieved by organic solvent polymerization. *Journal of Materials Chemistry C*. 2020;8:3409-3417. DOI: 10.1039/c9tc06687j
- [64] You P, Li G, Tang G, Cao J, Yan F. Ultrafast laser-annealing of perovskite films for efficient perovskite solar cells. *Energy & Environmental Science*. 2020;13:1187-1196. DOI: 10.1039/c9ee02324k
- [65] Sheng Y, Liu C, Yu L, Yang Y, Hu F, Sheng C, et al. Microsteganography on all inorganic perovskite micro-platelets by direct laser writing. *Nanoscale*. 2021;13:14450-14459. DOI: 10.1039/d1nr02511b
- [66] Sun K, Tan D, Fang X, Xia X, Lin D, Song J, et al. Three-dimensional direct lithography of stable perovskite nanocrystals in glass. *Science*. 2022;375:307-310. DOI: 10.1126/science.abj2691
- [67] Wang K, Wu C, Hou Y, Yang D, Ye T, Yoon J, et al. Isothermally crystallized perovskites at room-temperature. *Energy & Environmental Science*. 2020;13:3412-3422. DOI: 10.1039/d0ee01967d
- [68] Jacobsson TJ, Schwan LJ, Ottosson M, Hagfeldt A, Edvinsson T. Determination of thermal expansion coefficients and locating the temperature-induced phase transition in methylammonium lead perovskites using X-ray diffraction. *Inorganic Chemistry*. 2015;54:10678-10685. DOI: 10.1021/acs.inorgchem.5b01481
- [69] Schueller EC, Laurita G, Fabini DH, Stoumpos CC, Kanatzidis MG, Seshadri R. Crystal structure evolution and notable thermal expansion in hybrid perovskites formamidinium tin iodide and formamidinium lead bromide. *Inorganic Chemistry*. 2018;57:695-701. DOI: 10.1021/acs.inorgchem.7b02576

- [70] Halder A, Choudhury D, Ghosh S, Subbiah AS, Sarkar SK. Exploring thermochromic behavior of hydrated hybrid perovskites in solar cells. *The Journal of Physical Chemistry Letters*. 2015;6:3180-3184. DOI: 10.1021/acs.jpcclett.5b01426
- [71] Liu S, Du YW, Tso CY, Lee HH, Cheng R, Feng SP, et al. Organic hybrid perovskite (MAPbI<sub>3-x</sub>Cl<sub>x</sub>) for thermochromic smart window with strong optical regulation ability, low transition temperature, and narrow hysteresis width. *Advanced Functional Materials*. 2021;31:2010426. DOI: 10.1002/adfm.202010426
- [72] Lin J, Lai M, Dou L, Kley CS, Chen H, Peng F, et al. Thermochromic halide perovskite solar cells. *Nature Materials*. 2018;17:261-267. DOI: 10.1038/s41563-017-0006-0
- [73] De Bastiani M, Saidaminov MI, Dursun I, Sinatra L, Peng W, Buttner U, et al. Thermochromic perovskite inks for reversible smart window applications. *Chemistry of Materials*. 2017;29:3367-3370. DOI: 10.1021/acs.chemmater.6b05112
- [74] Xu L, Chen J, Song J, Li J, Xue J, Dong Y, et al. Double-protected all-inorganic perovskite nanocrystals by crystalline matrix and silica for triple-modal anti-counterfeiting codes. *ACS Applied Materials & Interfaces*. 2017;9:26556-26564. DOI: 10.1021/acsami.7b06436
- [75] Mączka M, Ptak M, Gaḡor A, Stefańska D, Sieradzki A. Layered lead iodide of [methylhydrazinium]2pbI<sub>4</sub> with a reduced band gap: Thermochromic luminescence and switchable dielectric properties triggered by structural phase transitions. *Chemistry of Materials*. 2019;31:8563-8575. DOI: 10.1021/acs.chemmater.9b03775
- [76] Elattar A, Suzuki H, Mishima R, Nakao K, Ota H, Nishikawa T, et al. Single crystal of two-dimensional mixed-halide copper-based perovskites with reversible thermochromism. *Journal of Materials Chemistry C*. 2021;9:3264-3270. DOI: 10.1039/d0tc04307a
- [77] Ning W, Zhao XG, Klarbring J, Bai S, Ji F, Wang F, et al. Thermochromic lead-free halide double perovskites. *Advanced Functional Materials*. 2019;29:1807375. DOI: 10.1002/adfm.201807375
- [78] Yu X, Wu L, Yang D, Cao M, Fan X, Lin H, et al. Hydrochromic CsPbBr<sub>3</sub> nanocrystals for anti-counterfeiting. *Angewandte Chemie International Edition*. 2020;59:14527-14532. DOI: 10.1002/anie.202005120
- [79] Wu Y, Shi CM, Xu LJ, Yang M, Chen ZN. Reversible luminescent vapochromism of a zero-dimensional Sb<sup>3+</sup>-doped organic-inorganic hybrid. *The Journal of Physical Chemistry Letters*. 2021;12:3288-3294. DOI: 10.1021/acs.jpcclett.1c00418
- [80] Wang Z, Zhang YQ, Liu XD, Yu YX, Xu FC, Ding J, et al. High stability and strong luminescence CsPbBr<sub>3</sub>/Cs<sub>4</sub>PbBr<sub>6</sub> perovskite nanocomposite: Large-scale synthesis, reversible luminescence, and anti-counterfeiting application. *Advanced Materials Technologies*. 2021;6:2100654. DOI: 10.1002/admt.202100654
- [81] Wang Y, Yan Y, Li D, Zhao W, Chen S, Zhong Q, et al. Reversible transformation of all-inorganic copper halide perovskite nanocrystals for anti-counterfeiting. *Dalton Transactions*. 2021;50:12826-12830. DOI: 10.1039/d1dt02386a
- [82] Zhang F, Liang WQ, Wang LT, Ma ZZ, Ji XZ, Wang M, et al. Moisture-induced reversible phase conversion

of cesium copper iodine nanocrystals enables advanced anti-counterfeiting. *Advanced Functional Materials*. 2021;**31**:2105771. DOI: 10.1002/adfm.202105771

[83] Feng JL, Wang JX, Wang D, Han MN, Qian GS, Wu F, et al. Reversible phase transitions of all inorganic copper-based perovskites: Water-triggered fluorochromism for advanced anticounterfeiting applications. *ACS Applied Electronic Materials*. 2022;**4**:225-232. DOI: 10.1021/acsaelm.1c00967

[84] Zhang C, Wang B, Li W, Huang S, Kong L, Li Z, et al. Conversion of invisible metal-organic frameworks to luminescent perovskite nanocrystals for confidential information encryption and decryption. *Nature Communications*. 2017;**8**:1138. DOI: 10.1038/s41467-017-01248-2

[85] Sun C, Su S, Gao Z, Liu H, Wu H, Shen X, et al. Stimuli-responsive inks based on perovskite quantum dots for advanced full-color information encryption and decryption. *ACS Applied Materials & Interfaces*. 2019;**11**:8210-8216. DOI: 10.1021/acsaami.8b19317

[86] Kong Q, Yang B, Chen J, Zhang R, Liu S, Zheng D, et al. Phase engineering of cesium manganese bromides nanocrystals with color-tunable emission. *Angewandte Chemie International Edition*. 2021;**60**:19653-19659. DOI: 10.1002/anie.202105413

[87] Abdollahi A, Roghani-Mamaqani H, Razavi B, Salami-Kalajahi M. Photoluminescent and chromic nanomaterials for anticounterfeiting technologies: Recent advances and future challenges. *ACS Nano*. 2020;**14**:14417-14492. DOI: 10.1021/acsnano.0c07289

[88] Mokhtar A, Morinaga R, Akaishi Y, Shimoyoshi M, Kim S, Kurihara S, et al.

Reversible luminescence photoswitching of colloidal CsPbBr<sub>3</sub> nanocrystals hybridized with a diarylethene photoswitch. *ACS Materials Letters*. 2020;**2**:727-735. DOI: 10.1021/acsmaterialslett.0c00131

[89] Li M, Zhao Y, Zhang S, Yang R, Qiu W, Wang P, et al. Understanding the energy barriers of the reversible ion exchange process in CsPbBr<sub>1.5</sub>Cl<sub>1.5</sub>@Y<sub>2</sub>O<sub>3</sub>:Eu<sup>3+</sup> macroporous composites and their application in anti-counterfeiting codes. *ACS Applied Materials & Interfaces*. 2021;**13**:60362-60372. DOI: 10.1021/acsaami.1c18030

[90] Mokhtar A, Morinaga R, Akaishi Y, Koinuma M, Kim S, Kurihara S, et al. Luminescence photoswitching of colloidal CsPbBr<sub>3</sub> nanocrystals by photochromic diarylethene ligands. *Chemistry Letters*. 2021;**50**:1534-1538. DOI: 10.1246/cl.210254

[91] Yang RR, Li M, Zhao YF, Wang P, Ye S. Regulating synthesis and photochromic behavior via interfacial Eu<sup>3+</sup>/Eu<sup>2+</sup>-Pb<sup>0</sup>/Pb<sup>2+</sup> redox of the CsPbCl<sub>1.5</sub>Br<sub>1.5</sub>@Ca<sub>0.9</sub>Eu<sub>0.1</sub>MoO<sub>4</sub> porous composites. *Materials Today Chemistry*. 2022;**23**:100721. DOI: 10.1016/j.mtchem.2021.100721

[92] Kanwat A, Ghosh B, Ng SE, Rana PJS, Lekina Y, Hooper TJN, et al. Reversible photochromism in 110 oriented layered halide perovskite. *ACS Nano*. 2022;**16**:2942-2952. DOI: 10.1021/acsnano.1c10098

[93] Zhang D, Zhou W, Liu Q, Xia Z. CH<sub>3</sub>NH<sub>3</sub>PbBr<sub>3</sub> perovskite nanocrystals encapsulated in lanthanide metal-organic frameworks as a photoluminescence converter for anti-counterfeiting. *ACS Applied Materials & Interfaces*. 2018;**10**:27875-27884. DOI: 10.1021/acsaami.8b10517

[94] Han X, Song E, Zhou B, Zhang Q. Color tunable upconversion luminescent

perovskite fluoride with long-/short-lived emissions toward multiple anti-counterfeiting. *Journal of Materials Chemistry C*. 2019;7:8226-8235. DOI: 10.1039/c9tc02171j

[95] Yang S, Wu D, Gong W, Huang Q, Zhen H, Ling Q, et al. Highly efficient room-temperature phosphorescence and afterglow luminescence from common organic fluorophores in 2D hybrid perovskites. *Chemical Science*. 2018;9:8975-8981. DOI: 10.1039/c8sc03563f

[96] Wei JH, Liao JF, Zhou L, Luo JB, Wang XD, Kuang DB. Indium-antimony-halide single crystals for high-efficiency white-light emission and anti-counterfeiting. *Science. Advances*. 2021;7:eabg3989. DOI: 10.1126/sciadv.abg3989

[97] Yakunin S, Chaaban J, Benin BM, Cherniukh I, Bernasconi C, Landuyt A, et al. Radiative lifetime-encoded unicolour security tags using perovskite nanocrystals. *Nature Communications*. 2021;12:981. DOI: 10.1038/s41467-021-21214-3

[98] Zhang H, Yang Z, Zhao L, Cao JY, Yu X, Yang Y, et al. Long persistent luminescence from all-inorganic perovskite nanocrystals. *Advanced Optical Materials*. 2020;8:2000585. DOI: 10.1002/adom.202000585

[99] Wu Y, Han D, Chakoumakos BC, Shi H, Chen S, Du M-H, et al. Zero-dimensional Cs<sub>4</sub>EuX<sub>6</sub> (X = Br, I) all-inorganic perovskite single crystals for gamma-ray spectroscopy. *Journal of Materials Chemistry C*. 2018;6:6647-6655. DOI: 10.1039/c8tc01458b

[100] Li HM, He FT, Ji CK, Zhu WW, Xu YQ, Zhang WK, et al. Purcell-enhanced spontaneous emission from perovskite quantum dots coupled to plasmonic

crystal. *The Journal of Physical Chemistry C*. 2019;123:25359-25365. DOI: 10.1021/acs.jpcc.9b06919

[101] Pan A, Li Y, Wu Y, Yan K, Jurow MJ, Liu Y, et al. Stable luminous nanocomposites of CsPbX<sub>3</sub> perovskite nanocrystals anchored on silica for multicolor anti-counterfeit ink and white-LEDs. *Materials Chemistry Frontiers*. 2019;3:414-419. DOI: 10.1039/c8qm00591e

[102] Ben Haj Salah M, Mercier N, Dittmer J, Zouari N, Botta C. The key role of the interface in the highly sensitive mechanochromic luminescence properties of hybrid perovskites. *Angewandte Chemie International Edition*. 2021;60:834-839. DOI: 10.1002/anie.202006184

[103] Xu XS, Brinzari TV, Lee S, Chu YH, Martin LW, Kumar A, et al. Optical properties and magnetochromism in multiferroic BiFeO<sub>3</sub>. *Physical Review B*. 2009;79:134425. DOI: 10.1103/PhysRevB.79.134425

[104] John RA, Shah N, Vishwanath SK, Ng SE, Febriansyah B, Jagadeeswararao M, et al. Halide perovskite memristors as flexible and reconfigurable physical unclonable functions. *Nature Communications*. 2021;12:3681. DOI: 10.1038/s41467-021-24057-0



# Accidental Injury Analysis and Protection for Automated Vehicles

*Jay Zhao and Francis Scott Gayzik*

## Abstract

This chapter summarizes our recent research on accidental injury analysis and new passive restraint concepts for automated vehicle occupant protection. Recent trends to develop highly automated driving systems (ADS) may enable occupants to sit in non-conventional ways with various seating positions. Such seating position may subject occupants to 360 degree of principal direction of force (PDOF). Current government regulatory crash tests and evaluation standards known as New Car Assessment Programs (NCAP) and other motor safety regulations have been implemented in the automotive industry mainly for the protection of forward-facing seated occupants in frontal, side, and rollover vehicle crashes. Automated vehicles will pose challenges and opportunities for occupant protection. In addition, automation may lead to an increase in occupants from more diverse populations in crash conditions and seating arrangements. More studies are required to better understand the kinematics, injuries, and protection for the ADS occupants on other new seating positions and postures from various crashes. Our latest research focused on occupant injury risk analysis and new restraint concepts for the ADS occupants at different seating positions, especially at the side-facing seat. This chapter summarizes our major findings from the research, including occupant injury risk assessment methods, estimated injury patterns and severities at different PDOF and seating arrangements, as well as new restraint concepts for mitigation of the ADS occupant injuries.

**Keywords:** occupant safety, automated vehicle safety, human body model, accidental injury prevention, restraint systems

## 1. Introduction

In the past decades extensive research and development (R&D) has made for effective protection of the occupants in conventional vehicles. Through analytical and experimental investigations on the kinematics response and injuries of postmortem human subject (PMHS) in forward-facing seating under different frontal, oblique, side, and rear impacts, the injury measures and criteria for the trauma of each body region at Abbreviated Injury Scale (AIS) with the injury risk probability function have been defined. The families of the anthropomorphic test devices (ATDs) have been developed as the laboratory test tools for surrogate human occupants representing a population of different gender and ages. These ATDs included advanced THOR dummies for the 50th%ile adult male and 5th%ile female and Hybrid-III dummies for

95th%ile and 50th%ile adult males, 5th%ile female, 10 year old, 6 year-old, 3 year-old, and 1 year children, mainly for the frontal impact applications; WorldSID, Eurosid, US-Sid dummies of the 50th%ile male and 5th%ile female for the side impacts; and BioRid dummy for the rear impacts. Dummy based measures and criteria for the human body injuries have been developed from the paired studies of the PMHS tests and dummy tests at laboratory impact test conditions.

Based on the research and development, the government regulatory crash tests and evaluation standards known as New Car Assessment Programs (NCAP) and other motor safety regulations have been implemented in industry for nearly three decades, mainly for occupant protection of the forward-facing seated occupants in conventional vehicles, including the first-row driver and passenger and the second-row occupants, for vehicle frontal, side and rollover crashes. It was estimated to have saved hundreds of thousands of lives in the field each year [1].

As new automated vehicles technologies are accelerating in recent years, the National Highway Traffic Safety Administration (NHTSA) [2] released new federal guidance for Automated Driving Systems (ADS) on September 12, 2017, prioritizing occupant safety with the vision for safe deployment of automated vehicle technologies to a future with fewer traffic fatalities and increased mobility for all occupants. The new guidance supports further development of this important new technology, and offers a voluntary guidance for twelve priority safety design elements of the ADS, including new occupant protection systems that provide enhanced protection to occupants of all ages and sizes, additional countermeasures that will protect all occupants in any alternative planned seating or interior configurations, and the tools to demonstrate such due care not only limited to physical testing but also including virtual tests with vehicle and human body models.

Automated vehicles (AV) will pose challenges and opportunities for occupant protection since an AV could involve in different crash conditions, occupants could be from more diverse population, and seating arrangements could be free of restriction.

Recent trends in AV interior seating configurations bring more innovative and versatile design options than the conventional vehicles. In addition to the traditional forward-facing seats, AV seating designs may consider oblique-facing, rear-facing, and side facing or any other angle-oriented seating positions. The occupant postures in an AV could also vary at great extent, from normal seated to leaning backward until lying down. Jorlöv et al. [3] investigated user desires and attitudes to seating positions and activities in future highly automated cars. The survey found that during long drives, with several occupants in the car, there is a desire to rotate the seats to a living room position. During shorter drives alone, users would prefer to maintain the forward-facing position, but with the seat reclined to a more relaxed position.

For effective protection to all occupants of all ages and sizes in any alternative planned seating or interior configurations from various vehicle crashes, it is necessary for us to understand better the kinematics and injury patterns and outcomes of AV occupants at new seating configurations, and to develop better biofidelic tools and occupant injury evaluation methods.

In the past several years some fundamental biomechanics research has been performed on the PMHS and dummies in oblique facing, rear facing, and side-facing seating positions and reclined postures. Jason et al. [4] studied kinematic occupant responses and injury outcomes from 3-point seatbelt restrained PMHS in a forward-facing seat subjected to lateral and oblique far-side vehicle crash pulses of 6.6 mph and 14 mph. Humm et al. [5] studied kinetic and kinematic occupant responses, and injury outcomes from the lap-restrained PMHS in the oblique and side-facing seats subjected

to a frontal pulse with 16 g peak, 13.4 m/s (48 km/h or 30 mph) change in velocity, and 90 ms rise time (USCFR-1988) in an aviation environment. The sustained injuries included spinal injuries for all subjects varying with vertebral level, rib fractures, pelvic injuries, and leg injuries. Kang et al. [6, 7] studied kinematic responses and injury outcomes from the 3-point seatbelt restrained PMHS in the rear-seats subjected to frontal pulses of 16 mph, 24 mph and 35 mph crash severities of a represented vehicle. Minor c-spine injuries and transverse process fractures, 3–15 ribs fractures were observed from the PMHS at the rear seat under the 35 mph crash pulse. More injuries (Clavicle, scapula, and pelvis fractures) were observed from the PMHS at same test condition with the reclined 45 deg. seating.

Good progress has also been made in development of omni-directionally biofidelic human body models (HBMs). In the past decades, several finite element human body models for the occupants and pedestrians have been developed worldwide. Most recently, Global Human Body Model Consortium (GHBMC) have developed a family of HBMs in total of 13 models representing the 95th%ile and 50th%ile male and 5th%ile female occupants and pedestrians, and a six-year old child pedestrian. Biofidelity of the GHBMC 50th%ile male detailed occupant model (M50-O v4.5) was evaluated for the responses to the UVA PMHS farside sled tests condition [8], as well as to the rear impact sled tests by Kang et al. [9]. These results indicated better biofidelity of the HBMs than the dummies at these conditions.

In this research, we have used the GHBMC HBMs as a tool for assessment of the occupant kinematics and injuries, and for evaluation of the restraint performance.

The objectives of this research were the following

- to develop the accidental injury risk assessment method with the GHBMC HBMs,
- to better understand the body injury patterns and severities for a belted 50th%ile male occupant at various orientated seating positions under a vehicle frontal crash pulse and at a side-facing seating position under frontal, oblique, side, and rear vehicle crashes, and
- to develop new concepts of effective restraints for the AV occupant protection.

In this chapter, Section 2 summarizes the GHBMC HBM validations and the occupant injury risk assessment methods. Section 3 states the occupant injury analysis for the seating in various 360 degree orientated seating positions. Section 4 focuses on the occupant injury analysis for the side-facing seat occupant. Section 5 demonstrates the evaluation methods and results for new restraint concepts for protection of the side-facing seat occupants.

## **2. Occupant accidental injury risk assessment methods**

In this study we used the GHBMC 50th%ile male occupant human body models in two versions – detailed M50-O v4.5 and simplified M50-OS v1.8.4. The M50-O v4.5 model has 2,187,596 elements and 1,263,445 nodes, while the M50-OS v1.8.4 FE model has 338,814 elements and 299,095 nodes.

### **2.1 Occupant model validation**

The Global Human Body Models Consortium (GHBMC) M50-O average male seated occupant is a widely used and validated HBM. The detailed M50-O v4.5

occupant model has been validated at the tissue, component, and full body crash test levels during the development. GHBMCM models were developed from external anthropometry and posture specific medical image data [10, 11]. A multi-modality image dataset from volunteers representing various target anthropometries were used. Over 14 thousand images across three imaging modalities (CT, MRI, and upright MRI) were collected for the M50 model including scans in the supine, standing, and seated postures [12]. Geometries for the M50 were developed from these image datasets using a variety of segmentation techniques. Segmented data were verified against or augmented with data from literature sources [13].

Component level validation has been conducted in each major body region. In the head, the model was validated by comparing the response in matched simulation of impacts to bony structures (e.g. maxilla [14], zygoma [10], nasal bone [15], and skull [16]). Various soft tissue injuries were validated including intracranial pressures [17, 18], and relative brain to skull motion [19, 20]. In the neck, segment level tests were validated using individual functional units [21–24], functional units and full spine in tension [25], ligamentous strain [26–29], and axial rotation [30, 31]. The full cervical spine was tested in various configurations including rear impact [32, 33], lateral impact, and frontal impact [34, 35]. The thorax was validated at the rib cage level using a denuded rib cage study [36], pendulum impacts [37–39], and table top impacts [40]. The individual response of a single rib was the subject of an optimization study [41]. The abdomen was validated in various tests using bar impacts with a free back [42, 43], belt loading with a free back [43], airbag loading with a fixed back [43], belt loading at the mid abdomen [44, 45], pendulum impact [46], organ level validation at impact [47], lumbar flexion [48], lateral impact [49] and side airbag loading [50]. The pelvis was validated in lateral compression at the acetabulum [51–53] and pubic symphysis [54]. The lower extremity has been validated in various loading conditions including axial loading. The ankle has been specifically studied in impacts for axial loading, ankle inversion, eversion, dorsiflexion, and rotation [55–58]. Furthermore, the tibia has been validated in a three-point bending setup as well as axial loading for the entire leg [59, 60].

The model has also been extensively validated at the full body level in classical macro-level injury biomechanics studies [61]. Along with validation in dynamic simulations, the mass distribution of the GHBMCM M50 model was validated [62] by virtually sectioning the model into body regions and comparing masses to anthropometric PMHS data from McConville et al. [63] and Robbins [64]. Rigid impacts to body regions (e.g. thorax, pelvis, etc.) in frontal, oblique, and lateral directions were applied to the model based on experimental designs in the literature [43, 65–69]. Care was taken to closely approximate the experiment, including considerations of motion constraints on impactors and the inclusion of gravity, seat backs, etc. Three sled tests in frontal [70, 71] and lateral [72] directions have been validated. An example of these simulations is shown below (**Figure 1**).

The M50-OS v1.8.3 model provides relevant biomechanical output data from the same body habitus as the detailed model, but at a substantially reduced computational cost. The simplification process included reducing the total number of elements through re-meshing, consolidating contact definitions, utilizing simplified material properties, and implementing kinematic joints throughout the body. The M50-OS model exhibits roughly a 40-fold decrease in run time (**Table 1**). Since joint definitions and meshes were designed to maximize the ability to position the model, a semi-automated positioning “tree” was programmed into LS-PrePost allowing the user to dynamically adjust joint angles prior to running a simulation.

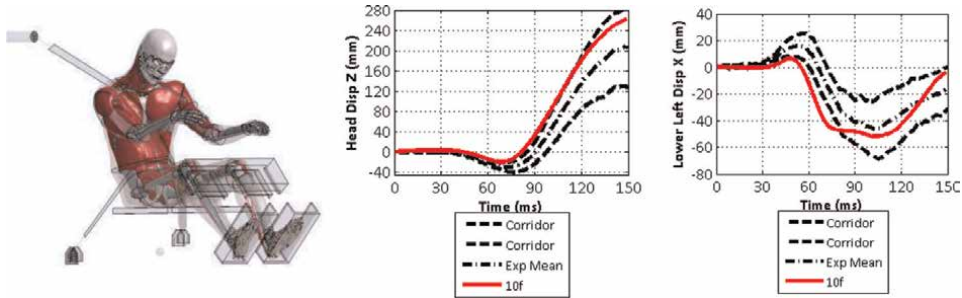


**Figure 1.** Sample validation using the GHBMCM50 model. Left to right: Shaw et al. sled buck model setup, head Z displacement and lower left rib displacement.

Test	Detailed Model Run Time (min)	Simplified Model Run Time (min)	Run Time Reduction (Detailed/Simplified)
Thorax hub impact	583	15	38.9
Lateral sled impact	1554	40	38.9

**Table 1.** Run time results for the simplified M50 occupant model.

The published work on the M50-OS v1.8.3 model [73] reported thirteen validations and robustness simulations, which included denuded rib compression at 7 discrete sites, 5 rigid body impacts, and one sled simulation. Perez-Rapela et al. [74] compared simulated kinematics in their far-side impact sled tests with the M50-OS v1.8.3 model to the PMHS responses. Results showed that, in general, the model captured lateral excursion in oblique impact conditions but overpredicted in purely lateral impact conditions. The human body model obtained a “good” CORA score for the correlation of their evaluation.

### 2.2 Injury risks assessment

The injury measures are Head Injury Criterion (HIC36 for side and HIC15 for frontal) and Brain Injury Criterion (BrIC) for the head region, Chest Lateral Deflections (side and frontal) for the chest, Abdominal VC for the abdomen, Pubic symphysis peak force for the pelvis, and Femur Force for the KTH region, and Upper Tibia Force and RTI for the lower extremities, respectively. The Full Body Injury Index FBII was defined as a summation of all the body region injury probabilities. **Table 2** summarizes these injury measures and the body region injury risk functions.

In this study, the human occupant injury risks were estimated with these probability functions. The estimations served as comparative measures for the body region injury severities among different analysis cases.

### 3. Occupant injury analysis for the seating subject to PDOF 360 degree

An occupant could be injured at a vehicle crash when the external impact forces on his/her body regions exceed the tolerances. The force magnitude related to the vehicle crash severity and the principal direction of force (PDOF) affect the body region

Injury Type	Injury Measure	Injury Risk Function	Ref.
Head AIS 3+	HIC36 (side) HIC15 (Frontal)	$\Phi \left[ \frac{\ln(HIC) - 7.45231}{0.73998} \right]$	[75]
	BrIC	$1 - e^{-\left(\frac{BrIC - 0.523}{0.531}\right)^{1.8}}$	[76]
Chest AIS 3+ - - Frontal	CD	$0.5 * \left( 1 + erf \left( \frac{\ln \left[ \frac{CHD_{front}}{\sqrt{2 * (e^{-0.67464})^2}} \right]} - (4.16985 - 0.198331) \right) \right)$	[77]
Chest AIS 3+ - - Side	CD	$\frac{1}{1 + e^{(9.02937 - 0.03705 * 45 - 36.8232 * CHD_{side} / 327)}}$	[77]
Abdomen AIS 2+	VC	$\frac{1}{1 + e^{(-8.07553 + 2.77263 * V_{max} C_{max})}}$	[78]
Pelvis AIS 2+	Pubic Force Fp	$\frac{1}{1 + e^{4.70 - 1.50 * F_{pubic}}}$	[79]
KTH AIS 2+	Femur Fz	$\frac{1}{1 + e^{5.7949 - 0.5396 * F_{femur}}}$	[80]
Tibia AIS 2+	Upper Tibia Force	$\frac{1}{1 + e^{0.5204 - 0.8189 * F_{upibia} + 0.06586 * max}}$	[80]
Tibia/Fibula Shaft fracture AIS 2+	Tibia Index RTI	$1 - \exp \left( -e^{\frac{\ln(RTI) - 0.2728}{0.2468}} \right)$ , $RTI = \frac{M}{240} + \frac{F}{12}$	[80]
Ankle AIS 2+	Lower Tibia Fz	$\frac{1}{1 + e^{4.572 - 0.670 * F_{lotibia}}}$	[80]
Full Body Index	FBII	$\sum_{i=1}^7 P_i$	

**Table 2.**  
The human body region injury risk functions for the 50th%ile male occupant.

injury patterns and severities. The PDOF could vary for an occupant on a given seating position with different crash scenarios (frontal, oblique, side, or rear impacts to the vehicle), or vary with different seating orientations under one vehicle crash. In the real-world, there are more occurrences of vehicle frontal crashes than other impacts.

Kitagawa et al. [81] analyzed occupant kinematics in simulated frontal collisions with three speeds assumed (56 km/h, 40 km/h and 30 km/h) using the THUMS Version 4 AM50 occupant human model representing the 50th%ile male occupant seated varying seating orientations with every 45-degree increment from 0 degree (forward-facing) to ±180 degrees (rear-facing) with respect to the impact direction, and with three angles of the seatback from 24 degrees to 36 degrees for two seating positions. The results showed that the occupant had the largest torso lateral excursion (up to 700 mm at a 56 km/h frontal crash) at -45 degrees and -90 degrees orientated (side-facing) seating positions.

In this study, we focused on analysis of occupant injury patterns and risks for a mid-size male occupant on a seat with the orientations varying to the PDOF 360 degree under a moderate frontal crash pulse.

### 3.1 Methods

We simulated a belted mid-size male occupant on a seat in a conceptual automated vehicle subject to the 40 km/h (25 mph) frontal crash pulse from Shaw PMHS golden test [70] as shown in **Figure 2** (left graph). The 3-point seatbelt restraint was with pretensioner and 3.5 kN load limiter. **Figure 2** (right graph) shows the simulation cases with the GHBMCM50-O v4.5 model representing the male occupant. For each

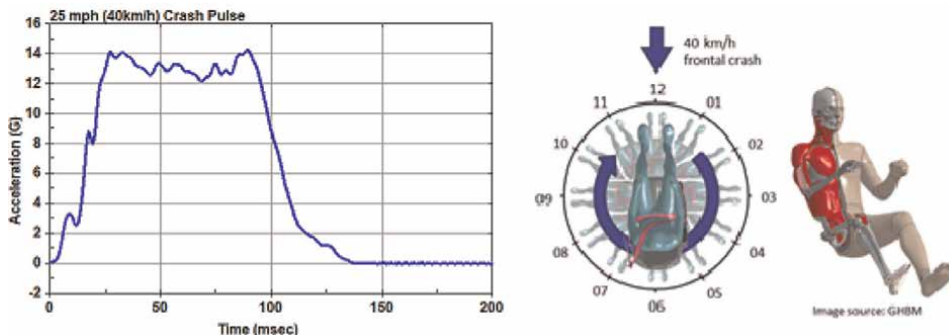


**Figure 2.** The 40 kph (25mph) frontal crash pulse (left graph) and the 50th%ile occupant seating positions considered in this study (right graph).

simulation case, the seat was rotated with every 30-degree increment from 0 degree to 360 degrees respect to the frontal impact. It is noted that each case number is named same as the clock number.

The models of the seat and seatbelt were used the same as what have been validated from the NHTSA's Advanced Adaptive Restraint Program (AARP) [82]. For the seat model, additional validation was made for the rotational stiffness of the seat back against the published body block test data [83], in which the seat back forward-rearward rotation was allowed within +20 degrees.

From the simulations for the twelve cases with the defined different seating orientations, analyses were made on the occupant kinematics, forces on the occupant, and injury patterns and severities for each case.

## 3.2 Results

### 3.2.1 Occupant kinematics and external forces

Respect to the impact direction, the seating orientations could be classified as the frontal/oblique facing (within  $0\text{---}\pm 60$  degree orientations or 10, 11, 12, 01, 02 O'clock (OC)), side facing (within  $\pm 90\text{---}\pm 120$  or 03, 04, 08, 09 OC), and rear-facing (within  $\pm 120\text{---}180$  degrees or 05, 06, 07 OC). **Figure 3** shows the maximum human body movement of each case varying with seat orientations. Significant kinematics differences of the human occupant among the seat facing classifications were observed.

**Figure 4** (left graph) shows the time-history traces of the head, T1, and pelvis of the frontal/oblique facing seated occupant during the crash. **Figure 4** (right graph) depicts the maximum external forces on the occupant from the seatbelt and the seat back. As the occupant faced more obliquely, the Head/T1 displacements increased while the pelvis displacement slightly decreased. The seatbelt routing obviously affected the kinematics. It was observed that the occupant at 11 & 10 OC had larger displacement than 01 & 02 OC. The seatbelt shoulder forces were all above 5 KN, while the seat back force to the occupant increased as the occupant had more side facing.

**Figure 5** (left graph) shows the time-history traces of the head, T1, and pelvis of the side facing seated occupant during the crash. **Figure 5** (right graph) depicts the external forces on the occupant from the seatbelt and the seat back. The occupant at

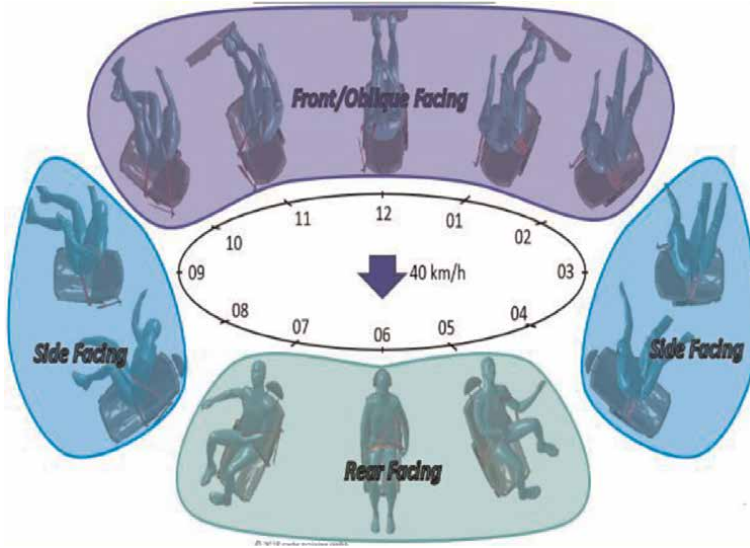


**Figure 3.** The seat facing classifications and the 50th%ile occupant kinematics under the 40 km/h frontal crash pulse.

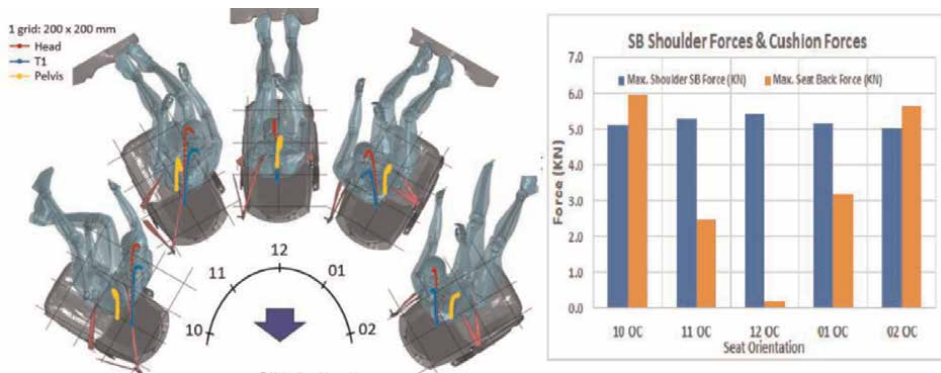


**Figure 4.** The 50th%ile occupant kinematics (left graph) and maximum forces on the occupant (right graph) at the frontal/oblique facing seating positions under the 40 km/h frontal crash pulse.

03 & 04 OC showed twisting head while the torso was restrained by the seat belt and the seat back. The occupant seating at 09 & 08 OC showed shoulder belt slip-off and significantly larger displacement than 03 & 04 OC. In these side facing seat positions, the seatbelt restraint forces were reduced to 2–3 KN, while the seat back forces on the occupant increased to 7.1–8.7 KN.

**Figure 6** (left graph) shows the time-history traces of the head, T1, and pelvis of the rear facing seated occupant during the crash. **Figure 6** (right graph) depicts the maximum seatbelt shoulder forces and the seat back forces on the occupant. No significant difference between 05 OC and far-side 07 OC was shown. In this seat facing group, much larger head and T1 displacement occurred compared to the other two groups. The restraint forces from the seat back increased significantly to 15.5–22.7 KN, while the seatbelt forces were below 1 KN. Hyperextension of the neck was observed.

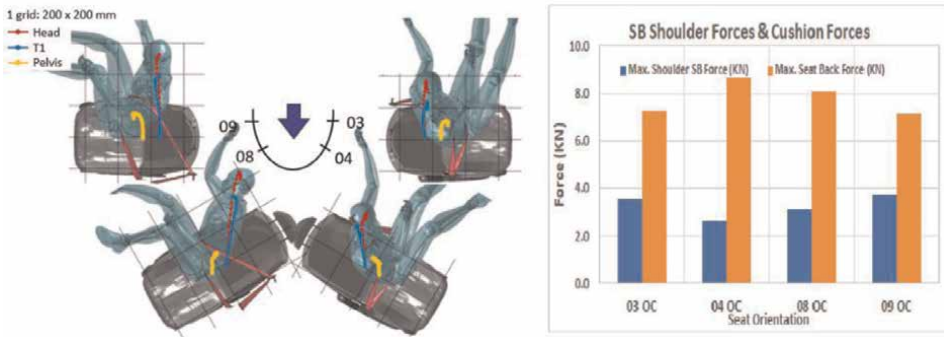


**Figure 5.** The 50th percentile occupant kinematics (left graph) and maximum forces on the occupant (right graph) at the side facing seating positions under the 40 km/h frontal crash pulse.

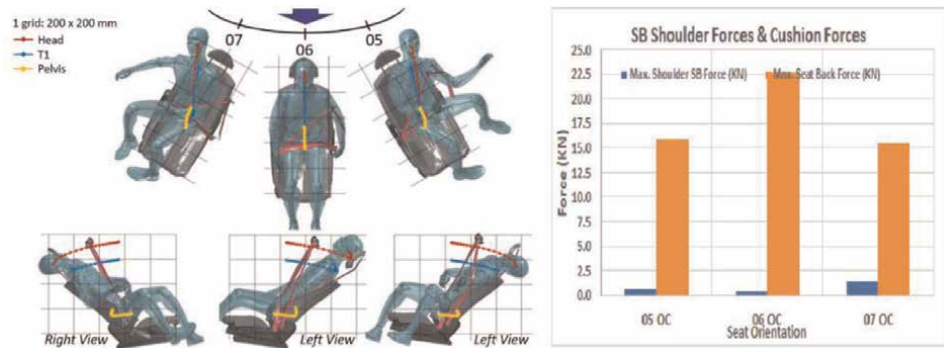


**Figure 6.** The 50th percentile occupant kinematics (left graph) and maximum forces on the occupant (right graph) at the rear facing seating positions under the 40 km/h frontal crash pulse.

### 3.2.2 Occupant injury patterns

For each case, the body injury measures, HIC, BrIC, Chest Deflection and Femur Load, were calculated. **Figure 7** plots these normalized injury measures varying with the seating orientations. From the HIC and BrIC plots, we see that the more rearward the occupant faced, the larger HIC and BrIC had. The occupant at the front/oblique facing (12–02 OC) showed largest anterior-posterior chest deflection, followed by pure rear facing (06 OC) due to the restraints from the seatbelt or seat back. The occupant at the side facing (04 & 08 OC) showed largest lateral chest deflection, followed by front/oblique facing (11 & 10 OC) because the torso moved laterally to the seat and contacted the seat side structure.

### 3.2.3 Discussion

**Figures 3–6** show that the occupant had the largest torso excursion laterally in the  $-90$  degrees (or 09 OC side-facing) orientated seating position. The maximum Y-displacement of the T1 kinematics target reached 751 mm. This trend was same as what Kitagawa, Y., et al. found in their study similar to this setup [81].

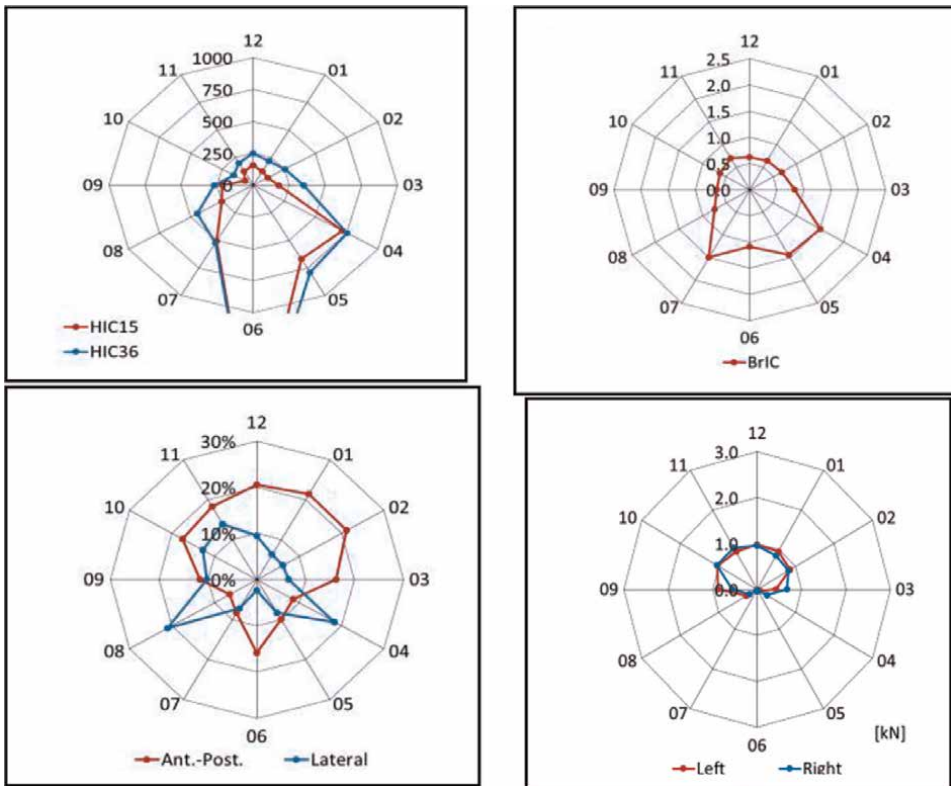


**Figure 7.**  
The 50th percentile occupant body region injury measures at all the seating positions under the 40 km/h frontal crash pulse.

Figures 3–6 show that the shoulder seatbelt had the largest restraint force on the occupant at the 12 OC seating position under the frontal loading, while the restraint force on the occupant from the seat back reached the maximum at the 06 OC seating position.

From Figure 7, the worst cases were identified as

- side facing (04 OC) having the highest risks of combination of the head and chest injuries indicated with the largest BrIC and lateral chest deflection, and
- rear facing (06 OC) having the highest risks of head and neck injuries due to neck hyperextension.

#### 4. Injury analysis for the side-facing seated occupant

The results in Section 3 show that a side facing seated occupant could have high risk of head and chest injuries even at a moderate severity frontal crash. Our other previous study [84] concluded that as a frontal crash severity increased above 40 kph or 25 mph delta velocity, the estimated injury risks for the body regions of head, chest, abdomen, pelvis, and knee-thigh-hip of the side-facing seated occupant increased significantly.

In real-world vehicle crashes, a lateral-facing seated occupant could also be exposed to various impacts other than a frontal crash, such as the oblique, side, and rear vehicle crashes. In this study, we investigated a mid-size male occupant on a 2nd row side-facing seat in a minivan subject to various crash pulses from the current US regulatory vehicle crash tests. The objective was to better understand the body injury risks and restraint protection effectiveness for such a side-facing seated occupant.

The general approach went through the three phases: 1) selected the vehicle crash test cases, collected the test data, and performed the vehicle crash test simulations; 2) performed the occupant simulations and injury analysis; 3) developed new restraint concepts for the occupant protection (the methods and results from this phase will be summarized in Section 5).

#### 4.1 Methods

In this study, the case vehicle was a US minivan with redesigned seating arrangement for a conceptual automated vehicle.

Eight US regulatory vehicle crash tests for the minivan were considered, as listed in **Table 3**, including the US NCAP rigid barrier frontal crash (FC-RB), the IIHS 40% offset deformable barrier frontal crash (FC-ODB), the IIHS small overlap rigid barrier frontal crash (FC-SOB), the US NCAP moving deformable barrier near side crash (NS-DB), the IIHS moving deformable high barrier near side crash (NS-IDB), the US NCAP moving deformable barrier far side crash (FS-DB), the IIHS moving deformable high barrier far side crash (FS-IDB), and the NHTSA rear crash sled test (RC-RL).

The vehicle side crash tests listed in **Table 3** were simulated. The vehicle FE model was originally obtained from the public resource hosted by George Washington University National Crash Analysis Center (NCAC). Further updates were made on the side door structures of the minivan model. Correlation of the maximum side door

Case Ref. Name	Crash Test Description	Crash Type	Crash Mode	Delta Velocity	Ref. Test #
FC-RB	Frontal Crash, US NCAP Rigid Barrier	Frontal	NCAP Barrier	56 kph	[85]
FC-ODB	Frontal Crash, IIHS 40% Offset Deformable Barrier	Frontal oblique	IIHS ODB	64 kph	[CEF0806]
FC-SOB	Frontal Crash, IIHS Small Overlap Rigid Barrier	Near side	IIHS SOB	64 kph	[CEN1438]
NS-DB	Near Side Crash, US NCAP Moving Deformable Barrier	Near side	NCAP MDB	61.6 kph	[86]
NS-IDB	Near Side Crash, IIHS Moving Deformable High Barrier	Near side	IIHS High MDB	50 kph	[CES0813]
FS-DB	Far Side Crash, NCAP Moving Deformable Barrier	Far side	NCAP MDB	61.6 kph	[87]
FS-IDB	Far Side Crash, IIHS Moving Deformable High Barrier	Far side	IIHS High MDB	50 kph	[CES0813]
RC-RL	Rear Crash, Rear Sled test	Rear	Rear Sled	40 kph	[88]

**Table 3.**  
 The US regulatory vehicle crash tests for the minivan investigated in this study.

structure deformation against the measured data were achieved. The updated vehicle FE model consisted of 572,555 elements, 604,821 nodes and 694 parts. **Figure 8** shows the vehicle crash simulation model setup for the four side crash tests, in which coupled vehicle crash and occupant simulations were performed.

For simulations of the vehicle frontal, oblique and rear crash tests listed in **Table 3**, a simplified vehicle FE model with 148,437 elements, 153,155 nodes and 47 parts was developed from the original NCAC model. The vehicle crash pulses from the frontal and oblique tests were collected and applied to the vehicle model, as shown in **Figure 9**.

For the occupant simulations, the GHBMCM50-OS v1.8.4 model (updated internally) was used to represent a 50th%ile male occupant. **Figure 10** shows the occupant model setup with the interior seating configuration of the minivan. The occupant restrained with a 3-point seatbelt was placed on a concept bench seat (case seat) on the frontal right side in the middle of the vehicle, surrounded by a 1st row right hand side (RHS) seat on his right, a 2nd row rear-facing seat on his front, and the rear-seat on his left.

The case seat model consisted of the cushion, seat pan and seatback. The material models of the cushion foam and the cover fabric were carried over from the validated mechanical properties of a passenger seat. The 1st row RHS seat was represented by a validated production passenger seat FE model as a surrogate.

The occupant seating under gravity was simulated initially. Each simulation run through 150 msec of termination time. The final occupant seating position and posture were then defined along with the seat cushion and seatback geometry profiles from the seating simulation at the time when the occupant achieved his equilibrium seating position.

For each of all the US regulatory vehicle crash tests listed in **Table 3**, the vehicle and occupant simulations were conducted. From the occupant simulation results, we analyzed the occupant kinematic and kinetic response, as well as the injury measures and risks estimated from the injury risk functions summarized in **Table 2**.

## 4.2 Results

### 4.2.1 Kinematics

**Figure 11** compares the kinematics snapshots at 115 msec of the 50th%ile male occupant at the side facing seat responding to the US NCAP rigid barrier frontal crash

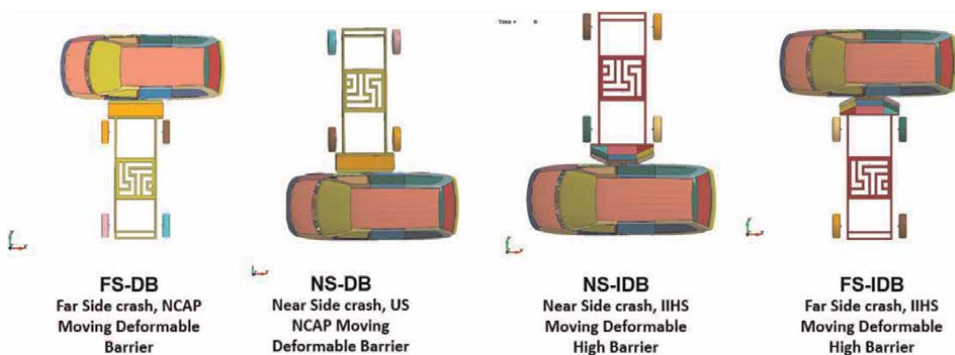


**Figure 8.**  
*Simulation models for the four US regulatory vehicle side crash tests.*

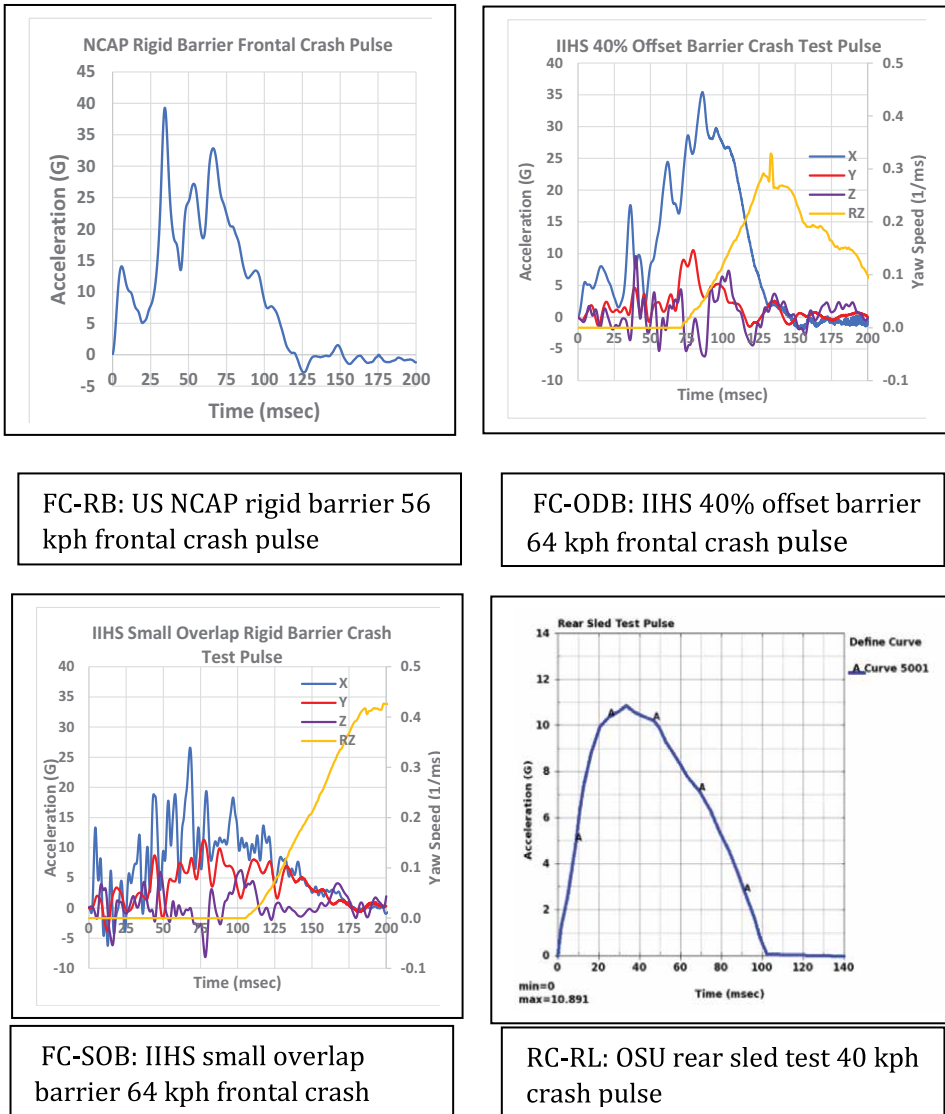


**Figure 9.** The vehicle frontal and oblique crash pulses from the four US regulatory vehicle crash tests used for the occupant simulations in this study.

(FC-RB), the IIHS 40% offset deformable barrier (FC-ODB) frontal crash, the IIHS small overlap rigid barrier frontal crash (FC-SOB), and the rear impact (RC-RL), respectively. In all the three frontal and oblique crashes, the occupant impacted to the 1st row seat back on his right, while in the rear impact he moved laterally to his left.

**Figure 12** compares the kinematics of the side-facing seated 50th%ile male occupant at 150 msec responding to the US NCAP moving deformable barrier near side crash (NS-DB), the IIHS moving deformable high barrier near side crash (NS-IDB), the US NCAP moving deformable barrier far side crash (FS-DB), and the IIHS moving deformable high barrier far side crash (FS-IDB), respectively. Under the near side crashes, the occupant firstly moved back toward the seatback during about 80 msec and then bounced forward driven by the seatback force. Under the farside crashes, the

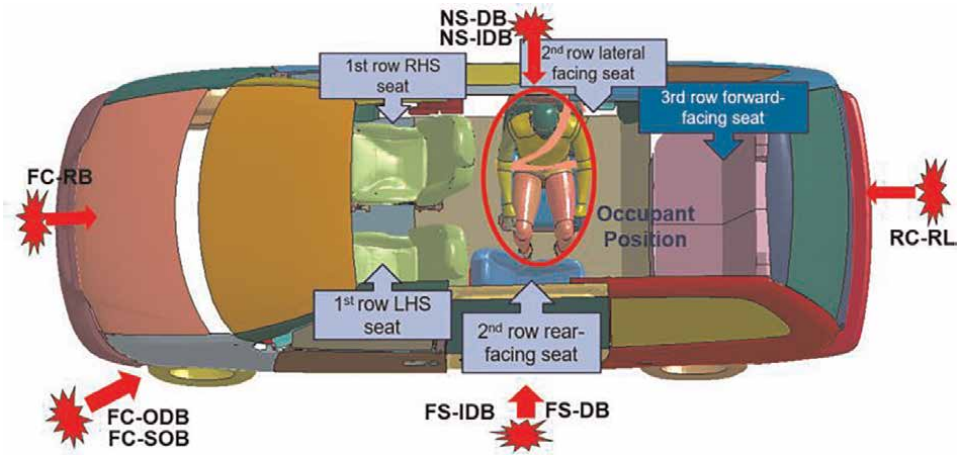


**Figure 10.**  
The crash cases and interior seating configuration of a conceptual automated minivan investigated in this study.

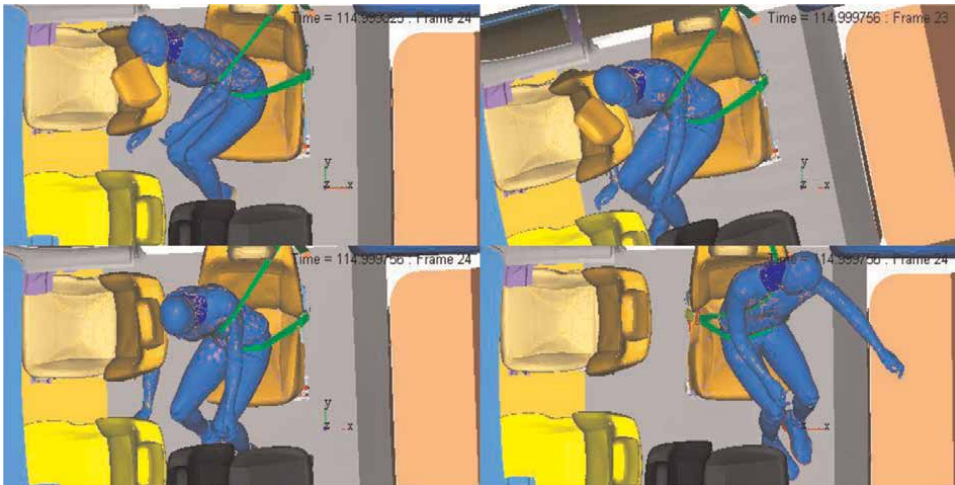


**Figure 11.**  
The kinematics snapshots at 115 msec of the 50th percentile male occupant at the side facing seat under various vehicle frontal and rear crashes—FC-RB (upper left), FC-ODB (lower left), FC-IDB (upper right), and RC-RL (lower right).

occupant moved forward all the way from the beginning. His lower legs impacted the side of the 2nd row LHS seat that was pushed toward the occupant by the deforming LHS side door structures of the vehicle.

#### 4.2.2 Injury analysis

**Table 4** summarizes the injury measures for the body regions of head, neck, Thorax, abdomen, pelvis, and lower extremities, outputted from the belted GHMBC M50-OS v1.8.4 (modified) model for the eight crash cases.

With the body injury risk functions listed **Table 2**, we calculated the body region injury risks and the Full Body Injury Index FBII of the 50th percentile mid-size male occupant for each crash case.

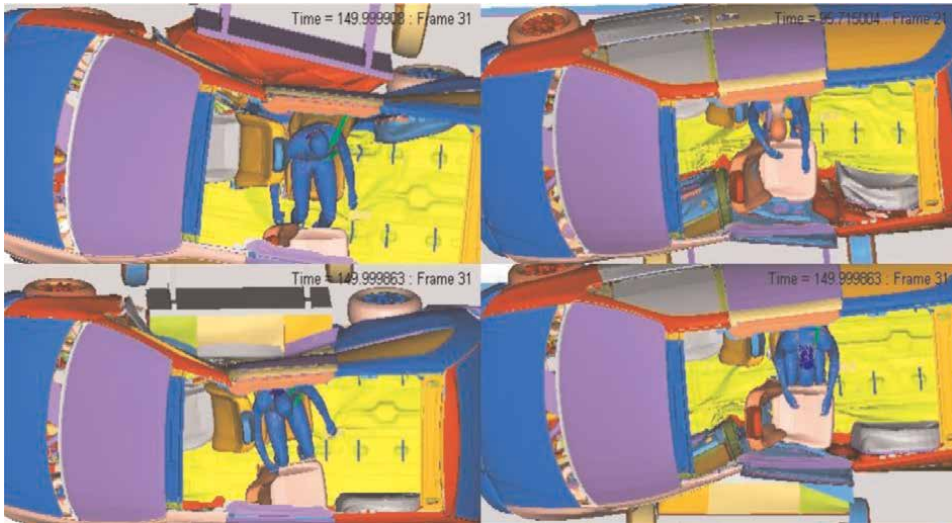


**Figure 12.**  
 The kinematics snapshots at 150 msec of the 50th%ile male occupant at the side facing seat under various vehicle side crashes—NS-DB (upper left), NS-IDB (lower right), FS-DB (upper right), and FS-IDB (lower right).

Injury	Injury Measure	1-FCRB	2-FCOD	3-FCSOB	4-NSDB	5-FSDB	6-RCRL	7-NSIDB	8-FSIDB
Head AIS3+ (Side)	HIC36	1977.6	1673.4	519.2	116.3	95.7	121.4	159.6	150
Head AIS3+ (Front)	HIC15	1483.1	1493.2	578.4	7.4	95.7	100.3	103.2	140.1
Brain injury	BrIC	1.3	1.34	0.89	0.53	0.39	0.55	0.46	0.45
Neck AIS 2+	IV-INC	1.87	1.9	1.85	1.12	1.2	1.82	1.39	1.8
Chest AIS3+ (Front)	Chest Dmax	55.9	55.3	30.7	30.1	46.6	57.1	36.6	47.3
Chest AIS3+ (Side)	Chest Half Dmax	96.3	80.5	56.3	31.5	64.5	65.4	32.2	64.8
Abdomen AIS3+	Vmax*Cmax	1.174	1.917	2.287	0.509	2.698	0.615	0.875	1.44
Pelvis AIS2+ (Side)	Pubic Force	3.585	4.807	2.751	0.555	0.737	1.098	0.881	0.593
KTH AIS2+ (Front)	Femur Force	4.974	4.547	3.334	2.055	5.42	3.39	1.895	5.107
Tibial Plateau/Condyle fracture AIS2+	Tibia Upp Fz	5.18	5.423	2.598	3.324	7.957	1.396	2.38	9.263
Tibia/Fibula shaft fracture AIS2+	Tibia Index RTI	0.24	0.184	0.179	0.325	0.749	0.082	0.248	0.862
Calcaneus, Talus, Ankle and Midfoot fracture AIS2+	Tibia lower Fz	3.94	1.321	2.005	1.076	1.932	0.366	0.978	1.358

**Table 4.**  
 The injury measures for the body regions of head, neck, thorax, abdomen, pelvis, and lower extremities from the GHBMC M50-OS v1.8.4 (modified) model restrained with the 3 pt. seatbelt for the eight crash cases.

**Figure 13** (Left plot) compares all the injury risks of the head (P\_head), chest (P\_chest), abdomen (P\_abd), pelvis (P\_pelvis), tibial (P\_tibial), ankle (P\_ankle) among the eight crash cases. It shows that the chest injury risks were relatively high across all the cases. Higher head and pelvis injury risks were observed at all the frontal crash cases. Higher lower extremity injury risks were seen at the far side crash cases.

**Figure 13** (Right plot) compares the Full Body Injury Index FBII among the eight crash cases. It is indicated that the US NCAP rigid barrier frontal crash (FCRB) caused the highest FBII value while the US NCAP moving deformable barrier near side crash (NS-DB) had the lowest FBII value.

4.2.3 Discussion

**Table 5** summarizes the estimated vulnerable body regions and injury severity for the side-facing seated 50th%ile male occupant responding to the frontal/oblique, rear, near side and farside side crashes, respectively. It is noted that the impacts to the occupant were completely different from the forward-facing seated due to the side-facing seat orientation. The occupant experienced the side impacts from the frontal and oblique vehicle crashes and the frontal impacts from the farside crashes. Severe body injuries for the side-facing occupant were caused the most by the frontal and oblique crashes, followed by the farside crashes, rear crashes, and near-side crashes.

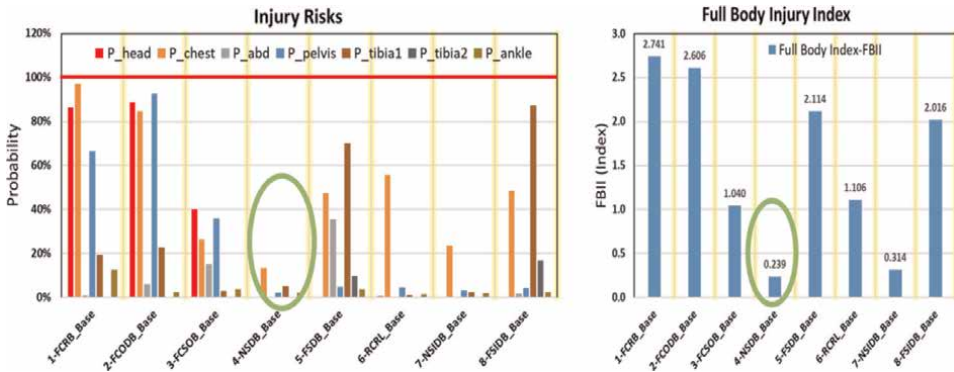


**Figure 13.** (left plot): The 50th%ile male occupant body region injury risks of the head (P\_head), chest (P\_chest), abdomen (P\_abd), pelvis (P\_pelvis), tibial (P\_tibial), ankle (P\_ankle), and (right plot): The full body injury index FBII among the eight crash cases.

Vehicle Crash	Impact to Occupant	Vulnerable Body Region	Injury Severity
Frontal & Frontal Oblique Crashes	Side from Right	Head, Neck, Chest, Pelvis, Lower Extremity	Very High
Far Side Crashes	Frontal	Head, Chest, Lower Extremity	High
Rear Crashes	Side from Left	Neck, Chest	Moderate
Near Side Crashes	Rear	Chest	Low

**Table 5.** The estimated vulnerable body regions and injury severity for the side-facing seated 50th%ile male occupant responding to various vehicle crashes.

The severe body injuries for the side-facing seated occupant restrained with 3-point seatbelt from the frontal, oblique and rear crashes indicated ineffectiveness of the seatbelt restraint for such crash scenarios.

For the farside crashes, the seatbelt performed better for the frontal impacted experienced occupant. The high injury risk value of the lower extremity was caused by contact of the legs to the 2nd row seat.

The near-side crashes caused less severe injuries to the rear impacted experienced occupant possibly due to mitigation of the impact energy by the seat back and the vehicle side structures.

The estimated outcomes of the body injury risks were limited to one case vehicle interior configuration. Further investigation on different vehicle crashes and seating configurations should be performed.

## 5. New restraint concepts for the side-facing seat occupant

To protect the side-facing seated occupant better, we developed new restraint concepts and evaluated the effectiveness based on understanding of the results from the phase 1–2 presented in Section 4.

### 5.1 New restraint concepts

First of all, design guidelines for new restraint devices were defined specifically for the side-facing occupant. The requirements for the restraints' performances are such that: 1) the pelvis lateral movement should be restrained earlier and properly; 2) the head/torso lateral displacements should be minimized to prevent the head/torso contact to any laterally nearby objects; 3) the lower legs/foot lateral failing motion and impact to the 2nd row LHS seat should be minimized.

Four new restraint concept designs highlighted below were developed:

- Seat-mounted Side Airbag (SSAB)—integrated to the occupant seat, designed for protection of the occupant from side impacts.
- Torso Restrain Airbag (TRAB)—integrated with the lap-seatbelt or to the occupant seat, designed for protection of the occupant from frontal and oblique impacts.
- Seat-mounted Head Airbag (HAB)—mounted on the side door structure, designed for protection of the occupant from rear impacts.
- Leg Restraint Device (LRD)—mounted beneath of the floor, designed for control of the lower legs/foot lateral failing motion from high severe side impacts.

**Figure 14** shows snapshots of the deployed restraints of the SSAB, TRAB, HAB, and LRD, respective.

### 5.2 Evaluation methods

Evaluation of the restraint effectiveness was performed in two steps: 1) new restraint concept evaluation; 2) integrated restraint system performance evaluation.

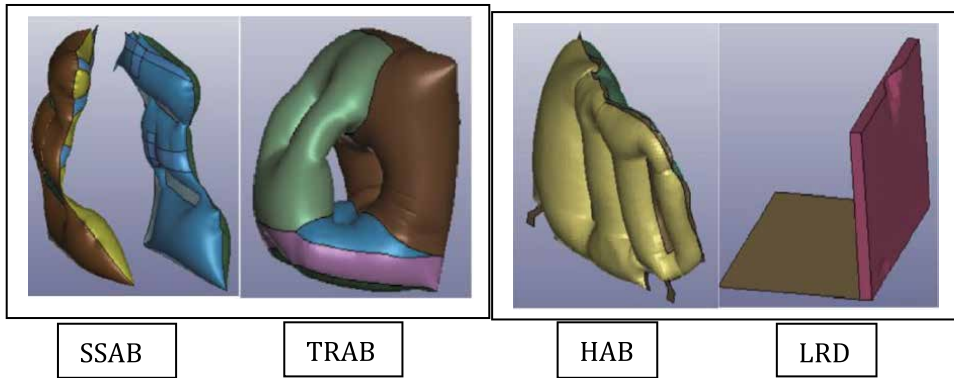


**Figure 14.**  
The new concepts of restraint devices.

The 1st step was development of the new restraint concepts one by one, for which a component model was created. Its system performance was then evaluated only at one worst vehicle crash test case. For each protection type, the restraint system integration and performance were optimized. The best performed integrated restraints were then selected for the next step study. **Table 6** shows the new restraint concept evaluation matrix.

The 2nd step was to verify the system performance of the integrated restraints across all the eight crashes in **Table 3**. **Table 7** shows the evaluation matrix for the three integrated restraint systems—the baseline 3 pt. seatbelt from Section 4, a 4 pt. seatbelt and the “optimal” new restraint system from Step 1 of current study.

### 5.3 Results

#### 5.3.1 Kinematics

**Figure 15** compares the kinematics snapshots at 120 msec of the side-facing seated 50th%ile male occupant with the three restraint systems under the US NCAP rigid barrier frontal crash (FC-RB) (worst case). With the new restraint system, the occupant was protected from being impacted from the 1st row seat on his right side, while

Protection Type	Frontal Protection	Side Protection - Right	Side Protection - Left	Rear Protection
Restraint Device	3 pt. Seatbelt	3 pt. Seatbelt	3 pt. Seatbelt	3 pt. Seatbelt
	Torso Restrain Airbag (TRAB)	Seat-mounted Side Airbag (SSAB)	Seat-mounted Side Airbag (SSAB)	Seat-mounted Head Airbag (HAB)
		Leg Restraint Device (LRD)	Leg Restraint Device (LRD)	
Test Case for Evaluation	FS-DB	FC-RB	RR-SL	NS-DB
CAE Cases	12	32	12	8

**Table 6.**  
New restraint concept evaluation matrix.

	Baseline	4 pt. Seatbelt (SB)	New Constraints
Restraint Device	3 pt. Seatbelt (Baseline)	4 pt. Seatbelt	3 pt. Seatbelt SSAB, TRAB, LRD,HAB
Crash Cases for Evaluation	FC-RB	FC-RB	FC-RB
	FC-ODB	FC-ODB	FC-ODB
	FC-SOB	FC-SOB	FC-SOB
	NS-DB	NS-DB	NS-DB
	NS-IDB	NS-IDB	NS-IDB
	FS-DB	FS-DB	FS-DB
	FS-IDB	FS-IDB	FS-IDB
	RC-RL	RC-RL	RC-RL
CAE Cases	8	8	8

**Table 7.**  
 Integrated restraint system performance evaluation matrix.



**Figure 15.**  
 The kinematics snapshots at 120 msec of the side-facing seated 50th%ile male occupant under the US NCAP rigid barrier frontal crash (FC-RB) with the three restraint systems—3 pt. SB (left), 4 pt. SB (middle), and new restraints (right).

the occupant with the other two restraints (3 pt. and 4 pt. seatbelt) impacted heavily to the 1st row right seat on his right.

### 5.3.2 Injury analysis

**Table 8** summarizes the injury measures for the body regions of head, neck, Thorax, abdomen, pelvis, and lower extremities, outputted from the GHMCM50-OS v1.8.4 (modified) model restrained with the new restraints for the eight crash cases.

**Figure 16** compares the body injury risks of the side-facing seated 50th%ile male occupant for the vehicle frontal & rear crash cases, restrained with 1) baseline 3 pt. SB

Injury	Injury Measure	17-FCRB_NEWRS	18-FCODB_NEWRS	19-FCSOB_NEWRS	20-NSDB_NEWRS	21-FSDB_NEWRS	22-RCRL_NEWRS	23-NSIDB_NEWRS	24-FSIDB_NEWRS
Head AIS3+ (Side)	HIC36	250.5	204.5	150	113.3	117.4	76.1	150.1	104.1
Head AIS3+ (Fronta)	HIC15	174.4	132.9	150	75.7	93.6	65.9	91.9	58.6
Brain injury AIS 4+	BrIC	0.81	0.76	0.83	0.52	0.52	0.33	0.49	0.59
Neck AIS 2+	IV-INC	1.11	1.22	1.5	1.79	1.52	1.52	1.43	1.3
Chest AIS3+ (Front)	Chest Dmax	35.6	38.4	28.3	23.1	34.4	17.4	32.1	43.1
Chest AIS3+ (Side)	ChestHalf Dmax	56.3	58.0	34.9	29.2	44.8	25.1	25.2	47.9
Abdomen AIS 2+	Vmax*Cmax	0.623	0.615	0.381	0.288	1.529	0.125	0.877	1.313
Pelvis AIS2+ -(side)	Pubic Force	2.935	1.423	2.109	0.666	0.743	0.560	1.004	0.951
KTH AIS2+ (front)	Femur Force	3.548	4.704	3.310	2.019	5.933	1.856	2.160	4.476
Tibial Plateau/Condyle fracture AIS2+	Tibia Upp Fz	3.584	2.740	3.837	2.642	4.721	1.567	1.891	4.731
Tibia/Fibula shaft fracture AIS2+	Tibia Index RTI	0.413	0.443	0.281	0.124	0.950	0.232	0.158	0.622
Calcaneus, Talus, Ankle & Midfoot fracture AIS 2+	Tibia lower Fz	1.293	0.733	2.195	1.029	1.125	0.467	1.127	1.350

**Table 8.** The injury measures for the body regions of the side-facing seated 50th%ile occupant restrained with the new restraints for the eight crash cases.

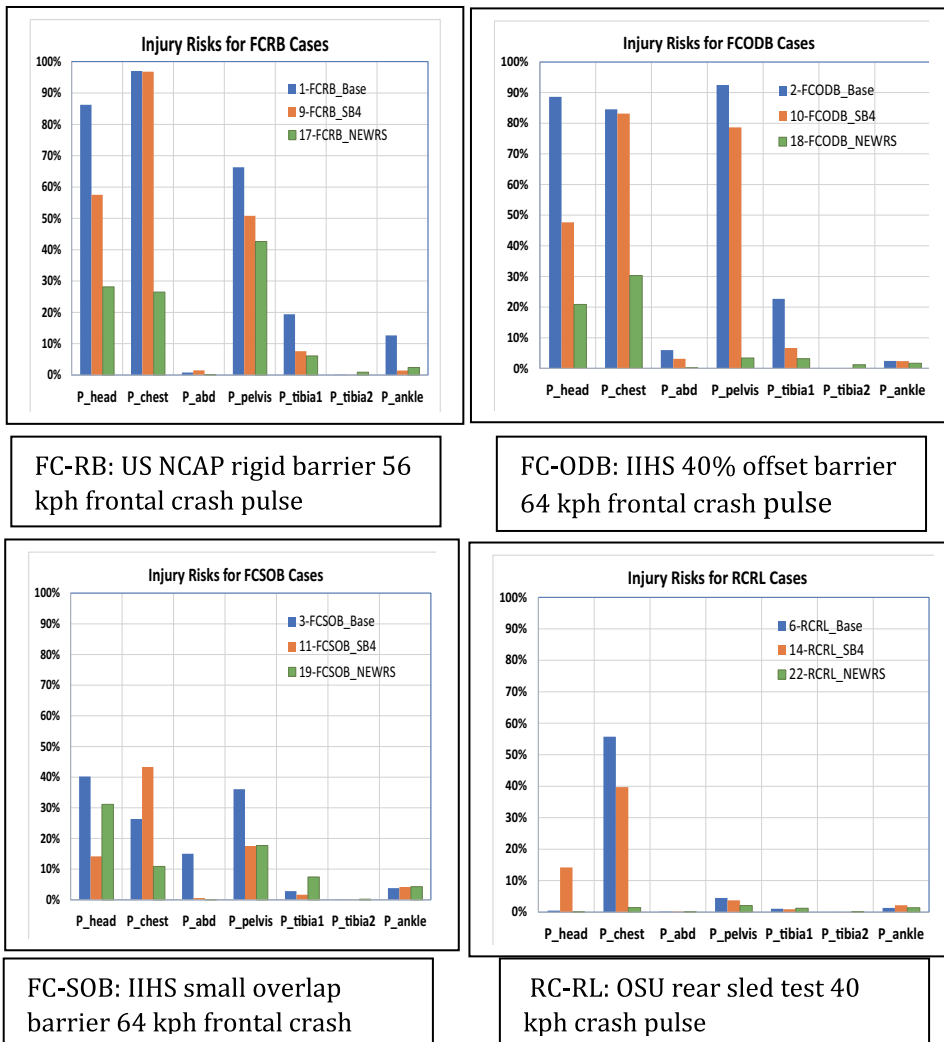


**Figure 16.** Comparison of the body injury risks of the side-facing seated 50th%ile male occupant for the vehicle frontal & rear crash cases, restrained with baseline 3 pt. SB (blue), 4 pt. SB (Orange), and new restraints (green).

(in blue), 2) 4 ps SB (in Orange), and 3) new restraints. We see that the new restraint system significantly reduced all the body region risks compared to the 3 pt. SB restraint system.

**Figure 17** compares the body injury risks of the side-facing seated 50th%ile male occupant for the vehicle side crash cases, restrained with 1) baseline 3 pt. SB (in blue), 2) 4 ps SB (in Orange), and 3) new restraints. It showed that under all the side crash conditions the new restraint system also worked effectively for reducing the severe injury risks compared to the 3 pt. SB restraint baseline.

**Figure 18** compares the Full Body Injury Index of the side-facing seated 50th%ile male occupant with three restraint systems from all the vehicle crash cases. Overall, the new restraint system significantly reduced the risks from all the vehicle crash tests in **Table 3** compared to the other evaluated seatbelt only restraints.

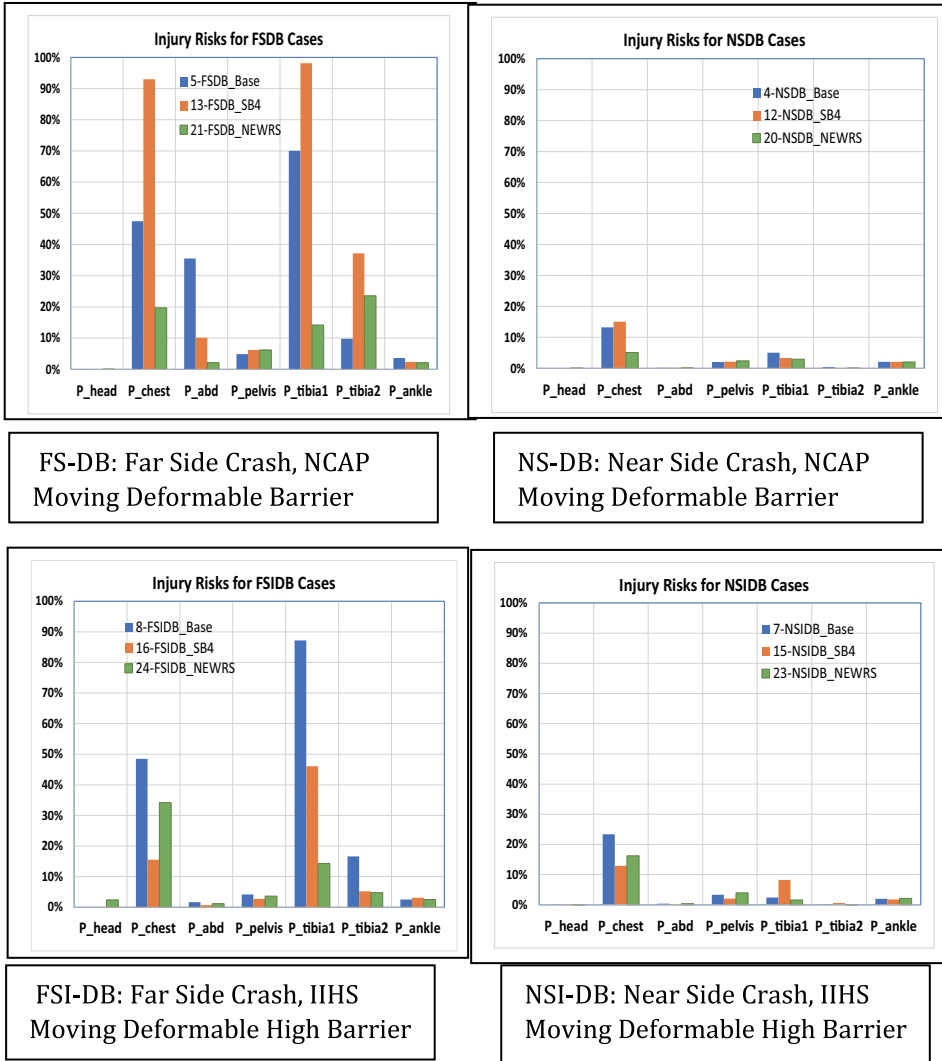


**Figure 17.** Comparison of the side-facing seated 50th%ile male occupant body injury risks for the vehicle near side and far side crash cases, restrained with baseline 3 pt. SB (blue), 4 pt. SB (Orange), and new restraints (green).

### 5.3.3 Discussion

This study indicated that the conventional seatbelt system (with baseline 3-pt seatbelt alone) did not provide sufficient protection for the side-facing seated occupant. The same conclusion was also obtained from our other study on both 50th%ile male and 5th%ile female human occupants in a side-facing seat [84].

The 4-pt seatbelt restrain system investigated from this study did not show good performance. Further work was needed to improve the 4-pt restraint design and the restraint component model validation.

The new restraints concepts developed in this study were shown to be capable of effectively protecting the far-side seating occupant at different vehicle crash conditions. The restraint system consisted of the three restraint components, among which

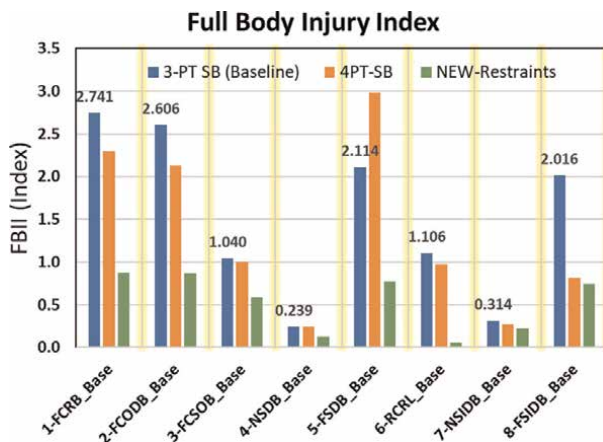


**Figure 18.** Comparison of the full body injury index of the side-facing seated 50th%ile male occupant across all the vehicle crash cases, restrained with baseline 3 pt. SB (blue), 4 pt. SB (Orange), and new restraints (green).

the seat-mounted side airbag (SSAB) was a key component that protected the head/neck and torso more effectively. To further develop this concept design into a product in mass protection, more future work is required to resolve possible issues in the packaging and the manufacturing.

## 6. Conclusions

Among different seating orientations of 360 degrees respect to the impact direction under the 40 kph frontal crash pulse, the side-facing positions were identified as worst cases in which the occupant had the highest risks of combination of the head and chest injuries indicated with the largest BrIC and lateral chest deflection, while the rear facing seated occupant had the highest risk of cervical spinal neck injury due to the neck hyperextension.

For the US regulatory (NCAP and IIHS) vehicle frontal and oblique crash tests (including NCAP rigid barrier frontal crash, the IIHS 40% offset deformable barrier frontal crash, and the IIHS small overlap rigid barrier frontal crash), as well as the vehicle rear crash test, side protection of a side-facing seated occupant is required. As the crash severities increased to 65kph or 35 mph of delta velocity, the side-facing occupant with the 3 pt. seatbelt alone could suffer high injury risks for the multiple body regions of head, chest, abdomen, pelvis, and the lower extremities.

Under the US regulatory (NCAP and IIHS) vehicle far side crash tests (including the US NCAP moving deformable barrier far side crash and the IIHS moving deformable high barrier far side crash), frontal protection for a side-facing seated occupant restrained with a 3 pt. seatbelt is necessary. Such an occupant could suffer moderate to high injury risks for the head, chest, and the lower extremities.

Under the US regulatory (NCAP and IIHS) vehicle near side crash tests (including the US NCAP moving deformable barrier near side crash and the IIHS moving deformable high barrier near side crash), a side-facing seated occupant will experience the rear impact under large pushing force from the seat due to the side door structure intrusion. With the seat and 3 pt. seatbelt restrains, such an occupant could suffer moderate injury risks for the head, neck and chest.

The new restraint concepts developed for the side-facing seat occupant in Section 5 demonstrated significant improvement for mitigation of the occupant's body injuries for all the vehicle crash test conditions considered in this study.

## **Acknowledgements**

We acknowledge Sungwoo Lee and Maika Katagiri who helped analyzing the occupant injury analysis data and Parred Kumar Jakkamsetti who helped modeling and analyzing of the restraint concept models in this research.

## **Author details**

Jay Zhao<sup>1\*</sup> and Francis Scott Gayzik<sup>2</sup>

1 Joyson Safety Systems, Auburn Hills, MI, USA

2 Wake Forest University School of Medicine, Center for Injury Biomechanics, Winston-Salem, NC, USA

\*Address all correspondence to: jay.zhao@joysonssafety.com

## **IntechOpen**

---

© 2022 The Author(s). Licensee IntechOpen. This chapter is distributed under the terms of the Creative Commons Attribution License (<http://creativecommons.org/licenses/by/3.0>), which permits unrestricted use, distribution, and reproduction in any medium, provided the original work is properly cited. 

## References

- [1] American Samoa Highway Safety Plan FFY 2018. Annual Report, US Department of Transportation. 2018. Available from: [https://www.nhtsa.gov/sites/nhtsa.gov/files/documents/american\\_samoa\\_fy2018\\_hsp.pdf](https://www.nhtsa.gov/sites/nhtsa.gov/files/documents/american_samoa_fy2018_hsp.pdf)
- [2] US Department of Transportation. Preparing for the Future of Transportation Automated Vehicles 3.0, October 2018 [Internet]. Available from: <http://www.transportation.gov/av>
- [3] Jorlöv S, Bohman K, Larsson A. Seating positions and activities in highly automated cars – A qualitative study of future automated driving scenarios. In: IRCOBI conference 2017. Antwerp: IRC-17-11; 2017
- [4] Forman J, Lopez-Valdes F, et al. Occupant kinematics and shoulder belt retention in far-side lateral and oblique collisions: A parametric study. *Stapp Car Crash Journal*. 2013;**57**:343-385
- [5] Humm JR, Yoganandan N, Pintar FA, et al. Responses and injuries to PMHS in side-facing and oblique seats in horizontal longitudinal sled tests per FAA emergency landing conditions. *Stapp Car Crash Journal*. 2016;**60**: 135-163
- [6] Kang Y et al. Biomechanical responses of PMHS in moderate-speed rear impacts and development of response targets for evaluating the internal and external biofidelity of ATDs. *Stapp Car Crash Journal*. 2012;**56**:105-170
- [7] Kang Y, Stammen J, Ramachandra R, Agnew AM, Hagedorn A, Thomas C, et al. Biomechanical Responses and Injury Assessment of Post Mortem Human Subjects in Various Rear-facing Seating Configurations. *Stapp Car Crash Journal*. 2020;**64**:155-212
- [8] Katagiri M, Zhao J, Kerrigan J, Kent R, Forman J. Comparison of whole-body kinematic behavior of the GHBM occupant model to PMHS in far-side sled tests. In: IRCOBI conference 2016. Malaga: IRC; 2016. pp. 16-88
- [9] Katagiri M, Zhao J, Lee S, Moorhouse K, Kang Y. Biofidelity evaluation of GHBM male occupant models in rear impacts. In: IRCOBI conference 2019. Florence: IRC; 2019. pp. 19-52
- [10] Gayzik FS et al. Development of a full body CAD dataset for computational modeling: A multi-modality approach. *Annals of Biomedical Engineering*. 2011; **39**(10):2568-2583.2
- [11] Gayzik FS et al. External landmark, body surface, and volume data of a mid-sized male in seated and standing postures. *Annals of Biomedical Engineering*. 2012;**40**(9):2019-2032
- [12] Hayes AR et al. Abdominal organ location, morphology, and rib coverage for the 5(th), 50(th), and 95(th) percentile males and females in the supine and seated posture using multi-modality imaging. *Annals of Advances in Automotive Medicine*. 2013; **57**:111-122
- [13] Gayzik F, Hoth J, Stitzel J. Finite element-based injury metrics for pulmonary contusion via concurrent model optimization. *Biomech Model Mechanobiology*. 2011;**10**(4):505-520
- [14] Allsop DL et al. Facial impact response—A comparison of the hybrid III dummy and human cadaver. *SAE Transactions*. 1988;**97**:1224-1240
- [15] Hodgson V, Brinn J, Thomas L, Greenberg S. Fracture Behavior of the Skull Frontal Bone Against Cylindrical

Surfaces. SAE Technical Paper 700909. 1970. DOI: 10.4271/700909

[16] Yoganandan N et al. Biomechanics of skull fracture. *Journal of Neurotrauma*. 1995;**12**(4):659-668

[17] Nahum A, Smith R, Ward C. Intracranial Pressure Dynamics During Head Impact. SAE Technical Paper 770922. 1977. DOI: 10.4271/770922

[18] Trosseille X et al. Development of a FEM of the human head according to a specific test protocol. *SAE Transactions*. 1992;**101**(6):1801-1819

[19] Hardy WN et al. A study of the response of the human cadaver head to impact. *Stapp Car Crash Journal*. 2007; **51**:17

[20] Hardy WN et al. Investigation of head injury mechanisms using neutral density technology and high-speed Biplanar X-ray. *Stapp Car Crash Journal*. 2001;**45**:337

[21] Camacho DL et al. Experimental flexibility measurements for the development of a computational head-neck model validated for near-vertex head impact. In: *Proceedings of the 41st Stapp Car Crash Conference*, November 13-14, 1997. Orlando, Florida, USA: SAE Technical Paper 973345; 1997

[22] Nightingale RW et al. Flexion and extension structural properties and strengths for male cervical spine segments. *Journal of Biomechanics*. 2007;**40**(3):535-542

[23] Nightingale RW et al. Comparative strengths and structural properties of the upper and lower cervical spine in flexion and extension. *Journal of Biomechanics*. 2002;**35**(6):725-732

[24] Wheeldon JA et al. Experimental flexion/extension data corridors for

validation of finite element models of the young, normal cervical spine. *Journal of Biomechanics*. 2006;**39**(2):375-380

[25] Dibb AT et al. Tension and combined tension-extension structural response and tolerance properties of the human male ligamentous cervical spine. *Journal of Biomechanical Engineering*. 2009;**131**(8)

[26] Ivancic P et al. Biofidelic whole cervical spine model with muscle force replication for whiplash simulation. *European Spine Journal*. 2005;**14**(4):346-355

[27] Panjabi MM et al. Cervical spine ligament injury during simulated frontal impact. *Spine*. 2004;**29**(21):2395-2403

[28] Panjabi MM et al. Injury mechanisms of the cervical intervertebral disc during simulated whiplash. *Spine*. 2004;**29**(11): 1217-1225

[29] Pearson AM et al. Facet joint kinematics and injury mechanisms during simulated whiplash. *Spine*. 2004; **29**(4):390-397

[30] Ivancic PC et al. Predicting multiplanar cervical spine injury due to head-turned rear impacts using IV-NIC. *Traffic Injury Prevention*. 2006;**7**(3): 264-275

[31] Ivancic PC et al. Effect of rotated head posture on dynamic vertebral artery elongation during simulated rear impact. *Clinical Biomechanics*. 2006; **21**(3):213-220

[32] Davidsson J et al. Human volunteer kinematics in rear-end sled collisions. *Crash Prevention and Injury Control*. 2001;**2**(4):319-333

[33] Hynd D et al. Dummy requirements and injury criteria for a low-speed rear

- impact whiplash dummy. European Enhanced Vehicle-safety Committee. 2007
- [34] Wismans J, Van Oorschot H, Woltring H. Omni-directional human head-neck response. *SAE Transactions*. 1986;**95**(5):5.819-5.837
- [35] Thunnissen J et al. Human volunteer head-neck response in frontal flexion: A new analysis. in proceedings: Stapp car crash conference. Society of Automotive Engineers SAE. 1995
- [36] Kindig MW et al. Structural response of cadaveric ribcages under a localized loading: Stiffness and kinematic trends. *Stapp Car Crash Journal*. 2010;**54**:337-380
- [37] Kroell C, Schneider D, Nahum A. Impact Tolerance and Response of the Human Thorax II. *SAE Technical Paper* 741187. 1974. DOI: 10.4271/741187
- [38] Shaw JM et al. Oblique and lateral impact response of the PMHS thorax. *Stapp Car Crash Journal*. 2006;**50**:147
- [39] Yoganandan N et al. Impact biomechanics of the human thorax-abdomen complex. *International Journal of Crashworthiness*. 1997;**2**(2):219-228
- [40] Kent R, Lessley D, Sherwood C. Thoracic response to dynamic, non-impact loading from a hub, distributed belt, diagonal belt, and double diagonal belts. *Stapp Car Crash Journal*. 2004;**48**: 495
- [41] Li Z et al. Influence of mesh density, cortical thickness and material properties on human rib fracture prediction. *Medical Engineering & Physics*. 2010;**32**(9):998-1008
- [42] Cavanaugh JM et al. Lower abdominal tolerance and response. *SAE Transactions*. 1986;**95**(5):5.611-5.633
- [43] Hardy WN, Schneider LW, Rouhana SW. Abdominal impact response to rigid-bar, seatbelt, and airbag loading. *Stapp Car Crash Journal*. 2001;**45**:1-32
- [44] Foster CD et al. High-speed seatbelt pretensioner loading of the abdomen. *Stapp Car Crash Journal*. 2006;**50**:27-51
- [45] Lamielle S et al. 3D deformation and dynamics of the human cadaver abdomen under seatbelt loading. *Stapp Car Crash Journal*. 2008;**52**:267
- [46] Viano DC. Biomechanical responses and injuries in blunt lateral impact. *SAE Transactions*. 1989;**98**(6):1690-1719
- [47] Howes MK et al. Kinematics of the thoracoabdominal contents under various loading scenarios. *Stapp Car Crash Journal*. 2012;**56**:1-48
- [48] Luet C et al. Kinematics and dynamics of the pelvis in the process of submarining using PMHS sled tests. *Stapp Car Crash Journal*. 2012;**56**:411-442
- [49] Kremer MA et al. Pressure-based abdominal injury criteria using isolated liver and full-body post-mortem human subject impact tests. *Stapp Car Crash Journal*. 2011;**55**:317
- [50] Hallman JJ, Yoganandan N, Pintar FA. Biomechanical and injury response to posterolateral loading from torso side airbags. *Stapp Car Crash Journal*. 2010;**54**:227
- [51] Guillemot H et al. Pelvic injuries in side impact collisions: A field accident analyze and dynamic tests on isolated pelvic bones. In: *Proceedings of the 41st Stapp Car Crash Conference*, November 13–15, 1997. Orlando, Florida, USA: SAE Technical Paper 973322; 1997
- [52] Guillemot H et al. Pelvic behavior inside collisions: Static and dynamic tests

- on isolated pelvic bones. In: Proceedings of the 16th International Technical Conference of the Enhanced Safety of Vehicles. Windsor, ON, Canada: NHTSA; 1998. Paper Number 98-S6-W-37. NHTSA | The 16th ESV Conference Proceedings (dot.gov)
- [53] Beason DP et al. Bone mineral density correlates with fracture load in experimental side impacts of the pelvis. *Journal of Biomechanics*. 2003;**36**(2): 219-227
- [54] Dakin GJ et al. Elastic and viscoelastic properties of the human pubic symphysis joint: Effects of lateral impact joint loading. *Journal of Biomechanical Engineering*. 2001; **123**(3):218-226
- [55] Funk JR et al. The role of axial loading in malleolar fractures. *SAE Transactions*. 2000;**109**:212-223
- [56] Funk JR et al. The axial injury tolerance of the human foot/ankle complex and the effect of Achilles tension. *Journal of Biomechanical Engineering*. 2002;**124**(6):750-757
- [57] Rudd R et al. Injury tolerance and response of the ankle joint in dynamic dorsiflexion. *SAE Technical Paper*. 2004
- [58] Siegler S, Chen J, Schneck C. The three-dimensional kinematics and flexibility characteristics of the human ankle and subtalar joints—Part I. *Kinema*. 1988
- [59] Kerrigan JR et al. Experiments for establishing pedestrian-impact lower limb injury criteria. *SAE Technical Paper*. 2003
- [60] Untaroiu C et al. A finite element model of the lower limb for simulating pedestrian impacts. *SAE Technical Paper*. 2005
- [61] Vavalle NA et al. Lateral impact validation of a geometrically accurate full body finite element model for blunt injury prediction. *Annals of Biomedical Engineering*. 2013;**41**(3):497-512
- [62] Vavalle NA et al. Investigation of the mass distribution of a detailed seated male finite element model. *Journal of Applied Biomechanics*. 2013
- [63] McConville JT et al. Anthropometry Relationships of Body and Body Segment Moments of Inertia, Report AD A097238, US Department of Transportation. 1980. Available from: <https://apps.dtic.mil/sti/pdfs/ADA097238.pdf>
- [64] Robbins DH. Anthropometric specifications for mid-sized male dummy. US Department of Transportation. 1983. p. 134. Available from: <https://deepblue.lib.umich.edu/bitstream/handle/2027.42/260/72269.0001.001.pdf;jsessionid=2EDE7B338736E2EACDA885894222F93?sequence=2>
- [65] Koh SW et al. Shoulder injury and response due to lateral glenohumeral joint impact: An analysis of combined data. *Stapp Car Crash Journal*. 2005;**49**: 291-322
- [66] Kroell C, Schneider D, Nahum A. Impact tolerance and response of the human thorax. *Stapp Car Crash Journal*. 1971;**15**
- [67] Viano DC. Biomechanical responses and injuries in blunt lateral impact. *Stapp Car Crash Journal*. 1989;**33**
- [68] Kemper AR et al. The influence of arm position on thoracic response in side impacts. *Stapp Car Crash Journal*. 2008; **52**:379-420
- [69] Bouquet R, Ramet M, Bermond F, Caire Y, Talantikite Y, Robin S, et al.

- Pelvis human response to lateral impact. In: 16th International Technical Conference on the Enhanced Safety of Vehicles. Windsor, ON, Canada: NHTSA; 1998. Paper Number 98-S7-W-16. NHTSA | The 16th ESV Conference Proceedings ([dot.gov](http://www.nhtsa.gov))
- [70] Shaw G et al. Impact response of restrained PMHS in frontal sled tests: Skeletal deformation patterns under Seat Belt loading. *Stapp Car Crash Journal*. 2009;53:1-48
- [71] Shaw G, Parent D, Purtsezov S, Lessley D, Crandall J, Kent R, et al. Rear seat occupant safety: An investigation of a progressive force-limiting, pretensioning 3-point belt system using adult PMHS in frontal sled tests. *Stapp Car Crash Journal*. 2009;53(2009-22-0001):49-74
- [72] Cavanaugh JM, Walilko TJ, Malhotra A, Zhu Y, King AI. Biomechanical response and injury tolerance of the thorax in twelve sled side impacts. *SAE*, 1990
- [73] Schwartz D, Guleyupoglu B, Koya B, Joel D, Stitzel J, et al. Development of a computationally efficient full human body finite element model. *Traffic Injury Prevention*. 2015;16(sup1):S49-S56. DOI: 10.1080/15389588.2015.1021418
- [74] Perez-Rapela D, Markusic C, Whitcomb B, Pipkorn B, et al. Comparison of the simplified GHBM to PMHS kinematics in far-side impact. In: IRCOB conference 2019. Florence: IRC; 2019. pp. 19-42
- [75] Eppinger R, Sun E, Bandak F, Haffner M. Development of improved injury criteria for the assessment of advanced automotive restraint systems-II. National Highway Traffic Safety Administration. 1999
- [76] Takhounts E, Craig M, Moorhouse K, McFadden J. Development of brain injury criteria (BrIC). *Stapp Car Crash Journal*. 2013;57:243-266
- [77] Kuppas S. Injury Criteria for Side Impact Dummies. May: National Highway Traffic Safety Administration NPRM; 2004
- [78] Rouhana SW, El-Jawahri R, Laituri T. Biomechanical considerations for abdominal loading by Seat Belt Pretensioners. *Stapp Car Crash Journal*. 2010;54:381-406
- [79] Leport T, Baudrit P, Trosseille X, Petit P, et al. Assessment of the pubic force as a pelvic injury criterion in side impact. *Stapp Car Crash Journal*. 2007; 51:467-488
- [80] Kuppas S, Wang J, Haffner M, Eppinger R. Lower extremity injuries and associated injury criteria. In: Proceedings of 17<sup>th</sup> International Technical Conference on the Enhanced Safety of Vehicles. Amsterdam; Paper No. 457; 2001
- [81] Kitagawa Y, Hayashi S, Yamada K, et al. Occupant kinematics in simulated autonomous driving vehicle collisions: Influence of seating position, direction and angle. *Stapp Car Crash Journal*. 2017; 61:101-155
- [82] Zhao J, Jakkamsetti PK, Katagiri M, Lee S. New passenger restraints with Adaptivity to occupant size, seating positions and crash scenarios through paired ATD-HM study. In: Proceedings of 26<sup>th</sup> International Technical Conference on the Enhanced Safety of Vehicles. Eindhoven. Paper No. 19-0322; 2019
- [83] Viano DC, White AD. Seat Strength in Rear Body Block Tests. *Traffic Injury Prevention*; 2016. pp. 502-507. DOI: 10.1080/15389588.2015.1111513

[84] Zhao J, Katagiri M, Decker W, Lee S, Gayzik F. A Human Body Study on Restraints for Side-Facing Occupants in Frontal Crashes of an Automatic Vehicle. SAE Technical Paper 2020-01-0980; 2020. DOI: 10.4271/2020-01-0980

[85] NHTSA Vehicle Test Database: Test 2335 [Internet]. 1995. Available from: <https://www-nrd.nhtsa.dot.gov/database/VSR/veh/QueryTest.aspx>

[86] NHTSA Vehicle Test Database: Test 7461 [Internet]. 2011. Available from: <https://www-nrd.nhtsa.dot.gov/database/VSR/veh/QueryTest.aspx>

[87] NHTSA Vehicle Test Database: Test 3249 [Internet]. 2000. Available from: <https://www-nrd.nhtsa.dot.gov/database/VSR/veh/QueryTest.aspx>

[88] NHTSA Vehicle Test Database: Test 3789 [Internet]. 2001. Available from: <https://www-nrd.nhtsa.dot.gov/database/VSR/veh/QueryTest.aspx>

## Chapter 6

# Parent Opinions of Automated Vehicles and Young Driver Mobility

*Allegra Ayala and Yi-Ching Lee*

### Abstract

Previous research has identified that autonomous vehicles (AVs) may be useful in increasing the mobility of certain groups, including children. Teenagers present a unique ridership case, as many teenagers hold a form of driver's license although they are still children. Using an online survey, parents were asked about their general opinions of AV as well as several questions regarding their willingness to transport their teenagers in an AV unattended. Results indicated that factors such as early adopter status, the potential to delay teenager licensing, and perceived safety were related to parent willingness. These findings may be used to shape future research into using AVs to increase the mobility of teenagers.

**Keywords:** parents, children's mobility, teenager's mobility, autonomous vehicle, young driver

### 1. Introduction

When discussing smart mobility, there is an ever-increasing presence of autonomous vehicles (AVs) on the roadway and in development. Interest in the design and implementation of AVs increases each year as this innovative technology is applied to new contexts and user groups [1]. While there are many specifics that could be discussed regarding the hardware and function of AVs, this chapter will focus on parents' opinions of the use of AVs for their teenage children in various contexts and transportation scenarios.

The design and intended use of any vehicle largely depends on the user group the vehicle is targeted at. In the case of AVs, specific applications such as the creation of an innovative personal vehicle or improved long-haul trucking have received attention in recent years [2, 3]. Applications such as a shared autonomous bus (AB) or autonomous shuttle (AS) have also been examined both theoretically and in practice with potential riders [4–6]. Potential benefits for the implementation of AV on the roadways include an increase in safety and convenience, as well as the possibility of increased mobility [7, 8]. Automation makes the very inaccessible task of driving available to many groups who are currently unable to drive or have limited access to driving such as the elderly, disabled individuals, and children [7]. While some research examines the potential for this mobility increase, one particular area that has yet to be explored thoroughly concerns family mobility and the potential for AVs to increase it.

When considering the transportation of children of all ages in an AV, the relationship between parents and children's mobility must be examined. Generally, children have a large number of transportation needs such as school, extracurriculars, and social activities. For a number of reasons, parents are reliant on their personal vehicles to meet all of their families transportation needs, often seeing personal vehicle use as the only acceptable way to take their children to activities [9, 10]. In the context of school, the number of children who are able to transport themselves through walking or biking has decreased drastically over time due to increasing travel distances and parent concern regarding traffic dangers [11, 12]. Children who live close to their school are often still driven by a parent out of concern for the child's safety [13]. Even while many parents report issues managing these rides alongside their work and personal transportation needs, many still elect to transport their children personally [13, 14].

After school, tasks like extracurriculars, medical appointments, and social events add even more trips to a family's schedule. The use of public transportation options brings up concerns of safety with strangers and the difficulty of navigating some systems, while considering that many of these options do not allow unaccompanied minors [10]. Even rideshare services which utilize a private vehicle, such as Uber, do not allow for the transportation of unaccompanied children [15, 16]. For many families, a personal vehicle is the only available transportation method that meets the need for convenience and flexibility, while also quelling parent safety concerns. The option of utilizing an AV offers a solution to help lighten the load of transportation needs on the parent, while addressing many of their concerns regarding other methods of transportation.

In order to offer this potential solution to parents, AVs must be designed with parent concerns in mind. Prior research has suggested that parents are gatekeepers to this mobility and dictate the methods by which their children travel and therefore must feel that their children are safe in an AV [8, 17, 18]. Some research has been conducted to examine parent opinions of transporting young children in AVs independently which has uncovered several perceived concerns and benefits from parent groups. Prior literature suggests that parents were most interested in the possibility that this presented a convenient option to transport their children when they are unable to drive and that their children could carpool with other families children [8, 18, 19]. Excluding general barriers to acceptance of AV such as hacking, parents were often concerned about child maturity level and the distance of the journey [19]. Reported concerns about child safety included issues of how the AV would respond to threats and ensuring that a child gets to their final destination after exiting the vehicle [8].

Additionally, issues of technological acceptance and social desirability may play a role in parents' standpoint on transporting their children in AVs [20, 21]. Previous research suggests that children influence parent's decisions to adopt digital technologies [22]. Adoption of technology refers to an individual deciding to make use of a technology in their lives [23]. In this case, early adoption would refer to individuals who decide to use new technologies before the majority of the population. Parents who identify with this concept of early adoption may be more likely to make use of AVs, as they are an emerging technology.

When considering child transportation, teenagers present a unique challenge. Teenagers have more transportation needs than young children, as many have the addition of a work schedule and increased social obligations, but many are able to drive themselves after the age of 15 depending on the state. Despite this vastly different scenario, there is no research solely focused on transporting teenagers in AVs. Due to their ability to become licensed, it may be thought that teenagers have

a lesser need for AVs than young children, but teenagers would also benefit from this technology in unique ways.

One way that parents overcome traditional barriers to child mobility is encouraging their teenagers to receive learner's permits. Whether parents are busy or simply do not want to drive their older children around, learning to drive removes the need for a parent to be involved in their transportation. This also creates another driver in the family to transport younger children or individuals in the family who are unable to drive. Unfortunately, teenagers are among the most high-risk drivers. Some of this is due to lack of experience, but teenagers are also more likely to exhibit risk-taking behavior than their adult counterparts [24, 25]. CDC data collected from 2016 to 2017 shows that 16 year-old drivers were 1.5 times more likely to have an accident per mile driven than drivers in the 18–19 year-old category [26]. While some may attribute this to driving experience, it has also been found that teenagers who waited longer to obtain their learner's permits were shown to exhibit less risky driving behavior [27]. This suggests that the difference in driving behavior and accident rates are due to more than just experience gained. Adoption of AV transportation would lessen the need for these teenagers to get licensed as soon as they are of age while still offering independent mobility.

Teenagers who have already been licensed would also benefit from this technology, as they fall under the same high accident and risky driving behavior statistics. In the case of these teenagers, or teenagers who would still like to get their license and use an AV, this would create a unique group of users who are qualified to drive the vehicle should an emergency arise that requires a driver. Parents may also feel safer transporting young children in AVs if an older, teenaged sibling is there to monitor the ride, enforce safety rules, and ensure that the younger child reaches their destination. Overall, the use of personal AVs for transporting teenagers would greatly increase the entire family's mobility. To make this a reality for families, the needs and wants of parents must be addressed first.

The current study is an attempt to begin to understand parent opinions on transporting teenagers in AVs unaccompanied. Parent willingness will be measured, along with data regarding their child's transportation needs and driving habits. Additionally, parent opinions on teenagers using AV as a way to delay the need to drive will be examined.

## **2. Methods**

### **2.1 Data collection**

Participants were recruited through Amazon Mechanical Turk to take a survey hosted on Qualtrics from January 5th to February 7th, 2022. They were required to be between the ages of 18 and 99 years old, live in the United States of America, and be the parent of at least one child above the age of thirteen to participate in the study. Compensation was provided (4 USD per valid, complete response). This research was approved by the author's university Institutional Review Board.

Of the initial 315 responses, 38 participants were removed due to not meeting the participant criteria or declining to participate at the informed consent stage of the questionnaire. An additional 50 responses were removed due to failure of attention checks such as "What is the current month?" or "Please respond no to this question." Lastly, a final 34 participants were removed due to responding to the survey questions

for a child that was not within the acceptable age range of 13–19 years old. A total of 191 valid responses were used for the analysis.

## **2.2 Questionnaire development**

### *2.2.1 Parent demographics*

Before beginning the demographic section, participants were asked to confirm that they met the criteria to participate and agree to the terms laid out by an electronic informed consent form. Then, participants were asked to first answer a set of demographic questions regarding themselves. Parent demographic questions included age, sex, gender, ethnicity, and education level. Participants were also asked if they held a valid driver's license, which state this license was issued in, how many years of driving experience the participant had, and how many accidents they have caused. These questions were asked to gather information regarding the participants' driving experience.

### *2.2.2 Early adopters and autonomous vehicle opinions*

Participants were next asked to answer a set of questions regarding their general opinions about AVs. Willingness to adopt new technologies plays a role in opinions of AVs, as it is a relatively new innovation [23]. Parents were given a description of an early adopter of technology and then were asked if they considered themselves to be an early adopter. A description of AVs was given to define and frame the concept for the duration of the study [28]. Participants were then asked how familiar they were with AVs, how useful they found them, how safe they felt AVs were, and how likely they were to ride in one. Lastly, they were asked how likely they would be to purchase an AV if cost was no issue. The phrasing of this question aims to understand which participants would be inclined to purchase an AV if the issue of cost was removed, as this is one of the larger barriers to adoption [29].

### *2.2.3 Teenager demographics*

Parents were asked to answer the next section with information regarding their teenager. If the parent had more than one teenager, they were instructed to choose one to answer the questions for. Information was then collected regarding the demographics of the teenager such as sex, gender, ethnicity, and age. It was then asked what type of license this child had, if they held one and which state this was issued in. Years of driving experience and number of accidents were asked as well. Parents were then asked to subjectively rate their child's driving performance on a 5-point scale ranging from "far below average" to "far above average."

Having an older child who is able to drive has the potential to help increase the ability to meet a family's mobility needs. For this reason, parents were also asked if their child's ability to drive is helpful for meeting the family's transportation needs. Additionally, the number of vehicles a family has is relative to the number of drivers in the household with some families having as many vehicles as drivers [30]. Therefore, it was asked if the child has a designated vehicle to use when driving or if they would be using a car that would otherwise be used by the parent. In the case of the latter option, this indicates a potential need for more options for mobility within the family. Lastly, the parent was asked to rate how often their child needed

transportation to various activities per week, regardless of how this transportation is achieved, Activities including school, work, extracurriculars, and others were rated on a 5-point scale ranging from “Never” to “5+ times a week”.

#### *2.2.4 Willingness to use*

In the final section of the survey, parents were asked several questions to indicate their willingness to allow a teenager to use an AV in various contexts without a parent present. This included different destinations as well as different statuses of licensing, such as a learner’s permit or a full license. As many parents have more than one child, questions were also posed to gauge willingness to allow younger children to ride with a teenager in an AV unaccompanied by an adult. Parents were then asked if they would prefer for their child to wait to learn to drive until they are older if AVs were a readily available alternative for them. The final question gave a brief explanation of a take-over request, which occurs when an AV needs competent human driver to take over the task of driving due to an unexpected situation [31]. They were then asked if they would feel comfortable letting their child ride unattended in an AV if take-over request training were included in the curriculum to get the learner’s permit.

### **2.3 Data analysis**

Data cleaning was conducted using R. JASP was used to examine demographic information and descriptives of the sample. It was also used to conduct Chi-Square tests regarding early adopter status, perceived safety of AVs, and delayed licensing for teenage drivers. The Chi-Square statistic is used to analyze whether there is a statistically significant difference between the expected frequencies and the observed frequencies in one or more categories between groups in a contingency table. If significant, this test suggests that the distributions across categories and between groups are truly and significantly different [32].

## **3. Results**

### **3.1 Parent sample characteristics**

Of the valid 191 responses, just over half of the sample were male (53.40%). As for ethnicity, 72.78% of the participants were White, 12.57% were Asian, and 6.28% were Black or African American, 4.71% of participants identified as Mixed or Other, 2.09% were American Indian or Alaskan Native, 1.05% were Hispanic or Latino, and 0.52% were Native Hawaiian or Pacific Islander.

Education levels varied, with the largest grouping being a bachelor’s degree (52.88%), followed by an associate degree and a high school graduate, diploma or the equivalent (11.52% each). About one tenth (10.99%) of the sample held a master’s degree and 8.90% held some college credit. The smallest two groups included 2.62% holding a doctorate and 1.57% having trade, technical, or vocational training.

All participants were licensed drivers, with an average of 21.74 years of driving experience (SD = 9.35). When asked about the number of accidents they have personally caused, nearly half of the participants responded with none (47.64%). Less than 3.68% of respondents reported causing more than 2 accidents in their lifetime.

### 3.2 Teenager sample characteristics

The average age of the 191 teenagers that participants responded for was 15.75 years old (SD = 1.90). Slightly more than half (57.07%) of the sample was male. They also had a very similar breakdown of ethnicities as the parent group.

As some of the participants' children were not yet of legal driving age, 25.13% (n = 48) of the teenage sample consisted of non-drivers, 49.74% (n = 95) had their learner's permit or equivalent provisional license and the remaining 25.13% (n = 48) were fully licensed drivers (Figure 1). Among these teenagers, there was an average of 0.97 years of driving experience, with a standard deviation of 1.47 years (Figure 2). In parent's subjective report of their child's driving performance, over half of participants rated their child as an average driver as seen in Figure 3 (52.88%, n = 101). Participants also reported that 85.23% (n = 164) of the teenage sample had never caused an accident (Figure 4).

When asked if their child's ability to drive helps the family's overall transportation needs, many parents "somewhat agreed" (36.65%, n = 70) or "strongly agreed"

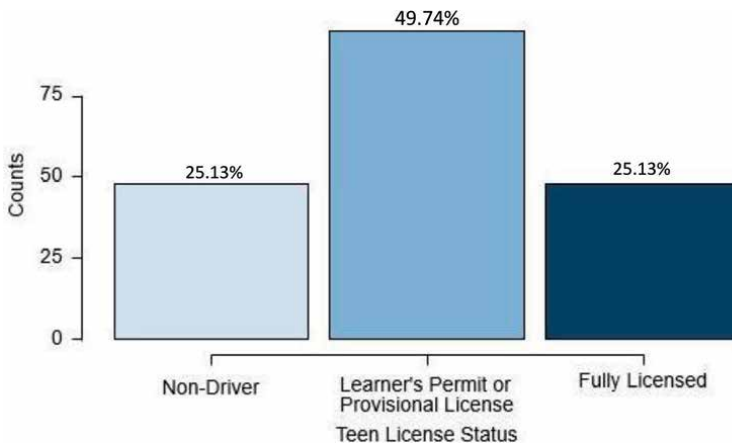


**Figure 1.**  
Teenager license status.

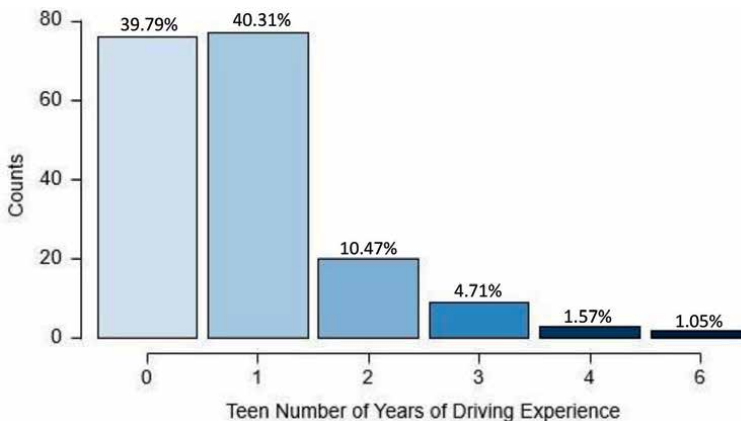


**Figure 2.**  
Number of years of driving experience for teenagers.

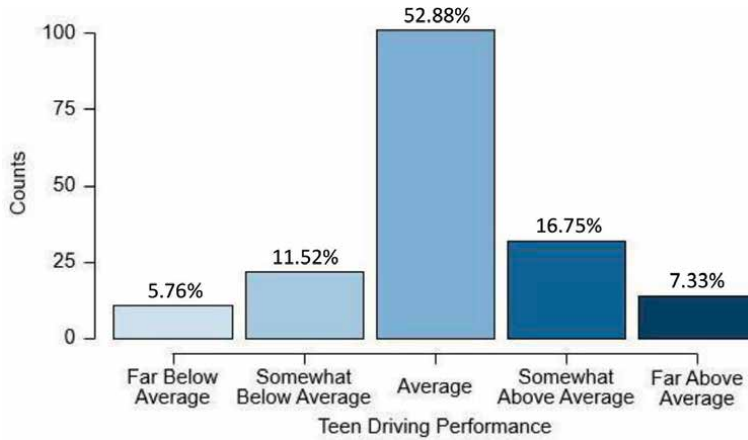


**Figure 3.**  
 Parent rating of driving performance for teenagers.

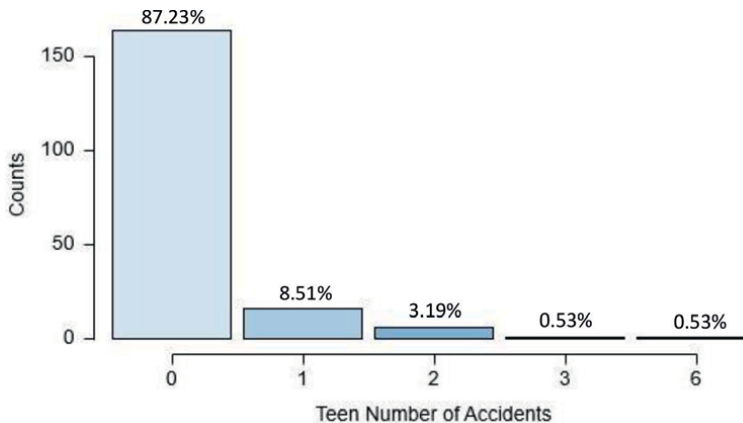


**Figure 4.**  
 Number of accidents teenagers have caused.

(20.94%, n = 40) that it was helpful to them. Parents were also asked if their child has their own personal vehicle (28.27%, n = 54), shares with siblings (5.24%, n = 10), or uses a vehicle that would otherwise be used by a parent (51.83%, n = 99); 11.52% (n = 22) of the sample indicated that their teenager typically used other vehicles outside of the immediate family when driving.

Finally, participants were asked if they would prefer for their child to wait to learn to drive until they are older if they could use an AV to retain the same level of mobility: 31.94% (n = 61) of parents said “yes,” 50.26% (n = 96) said “no,” and 17.28% (n = 33) were unsure (**Figure 5**).

### 3.3 Early adoption and autonomous vehicle opinions

Participants were asked a number of questions regarding their familiarity with AV as well as if they considered themselves to be early adopters. All responses fell on a 5-point Likert scale ranging from positive to negative, in relation to the nature

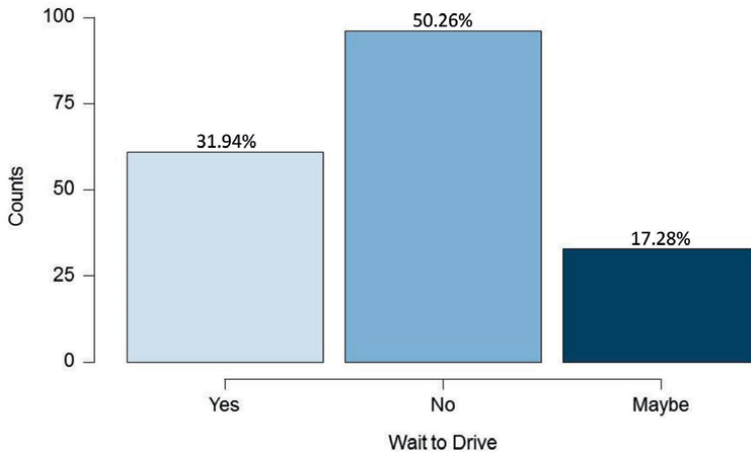


**Figure 5.**  
Participant responses to delayed licensing.

of the question. When asked about usefulness, 80% of participants responded with “somewhat useful” (n = 114) or “extremely useful” (n = 40). Respondents also largely felt that AVs were safe, with 89 saying “somewhat safe” and 23 saying “extremely safe.” When asked how familiar they were with AVs, a large number of participants reported being at least moderately familiar with the technology as seen in **Figure 6** (n = 88).

Participants were then asked if they themselves would likely be riding in an AV. The responses were diverse: 40 participants felt that they were extremely likely to be users, while 72 felt that it was somewhat likely; 22 chose the neutral category of neither likely nor unlikely and 38 felt that it would be somewhat unlikely. Only 18 individuals felt that it would be extremely unlikely for them to make use of an AV. Lastly, respondents were asked if they would be likely to purchase an AV if cost were no object. The results were the least varied of all the questions, with 52 “extremely likely,” 53 “somewhat likely,” 24 neutral responses, 33 “somewhat unlikely” and 29 “extremely unlikely” responses.

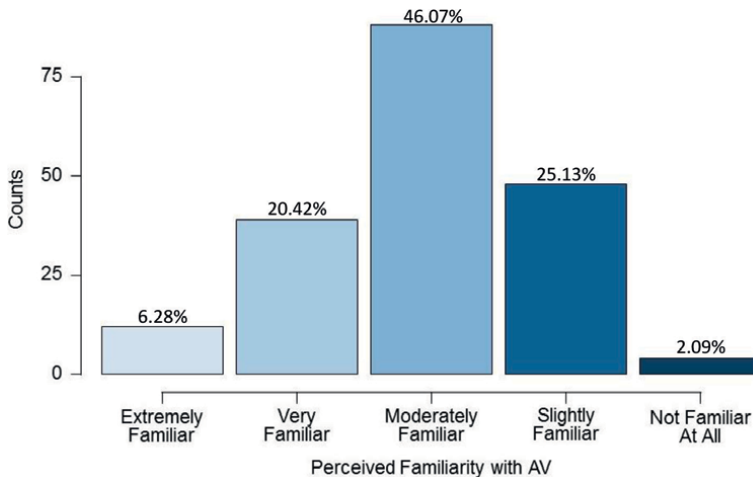


**Figure 6.**  
Perceived familiarity with AV.

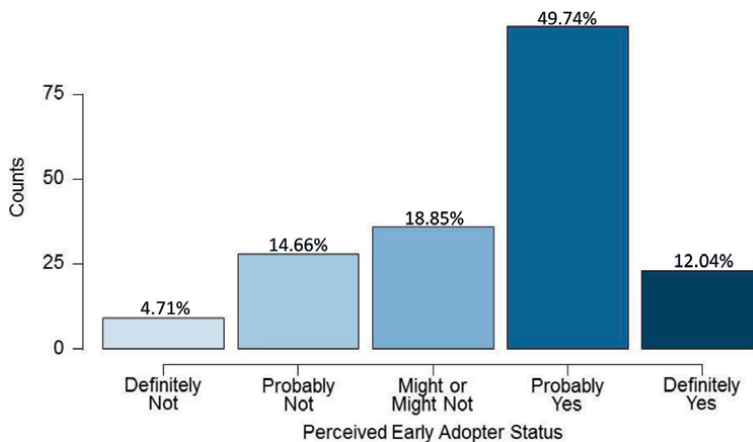


**Figure 7.**  
*Perceived early adopter status.*

In addition to these AV related questions, participants were asked if they would consider themselves to be an early adopter of technology. As seen in **Figure 7**, 95 individuals responded with “probably yes” and 23 with “definitely yes,” resulting in 61.78% of participants identifying with the concept of an early adopter of technology.

### 3.4 Comparison of parent willingness

A chi-square test showed significant differences in frequency distributions across participants self-reported early adopter status and their willingness to transport their licensed teenager in an AV ( $\chi^2(16, N = 190) = 31.97, p = 0.010$ ).

As seen in **Table 1**, a large number of parents who were unsure of their early adopter status (“might or might not”) were also fairly neutral on their willingness with 40% of this group selecting “neither comfortable nor uncomfortable” with transporting their teen this way. Interestingly, of the respondents who rated themselves as probably being early adopters (“probably yes”) there was quite a large divide between those who reported being “somewhat comfortable” ( $n = 32$ ) with the idea and those who reported “somewhat uncomfortable” ( $n = 25$ ). Overall, those who identified more with being an early adopter were more likely to feel comfortable with AV transportation.

Additionally, the perceived safety of AVs and parent willingness to use them for licensed teens were not equally distributed ( $\chi^2(16, N = 190) = 156.94, p < 0.001$ ). **Table 2** shows that participants who felt that AV is “extremely safe” felt “extremely comfortable” or “somewhat comfortable” with using the AVs except for one participant. Those who felt that AV was “somewhat safe” also had high rates of willingness with 52 participants feeling “somewhat comfortable” or “extremely comfortable.” In line with this, those who fell into the unsafe categories showed a tendency to be more uncomfortable with the idea of using this technology for their teenager’s transportation needs.

Lastly, parent willingness was compared to parent’s desire for their teen to wait to learn to drive if they could mitigate their mobility with an AV. There were significant group differences ( $\chi^2(8, N = 190) = 18.93, p = 0.015$ ), with most parents

Source	Definitely not		Probably not		Might or might not		Probably yes		Definitely yes		$\chi^2$	V
	n	%	n	%	n	%	n	%	n	%		
Extremely uncomfortable	4	15.39	7	26.92	3	11.54	11	42.31	1	3.85	31.969	0.205
Somewhat uncomfortable	4	8.70	7	15.22	5	10.87	25	54.35	5	10.87		
Neither comfortable or uncomfortable	0	0.00	4	13.33	12	40.00	11	36.67	3	10.00		
Somewhat comfortable	1	1.175	8	14.04	10	17.54	32	56.14	6	10.53		
Extremely comfortable	0	0.00	2	6.45	6	19.36	16	51.61	7	22.58		

*p* = 0.010.

**Table 1.** Frequencies and Chi-Square result for early adopter status & parent willingness with licensed child (N = 190).

Source	Extremely safe		Somewhat safe		Neither safe nor unsafe		Somewhat unsafe		Extremely unsafe		$\chi^2$	V
	n	%	n	%	n	%	n	%	n	%		
Extremely uncomfortable	1	3.85	3	11.54	1	3.85	12	46.15	9	34.62	156.94	0.454
Somewhat uncomfortable	0	0.00	22	47.83	8	17.39	15	32.61	1	2.17		
Neither comfortable nor uncomfortable	0	0.00	12	40.00	13	43.33	5	16.67	0	0.00		
Somewhat comfortable	5	8.77	41	71.93	3	5.26	7	12.28	1	1.75		
Extremely comfortable	17	54.84	11	35.48	2	6.45	0	0.00	1	3.23		

$p < 0.001$ .

**Table 2.** Frequencies and Chi-Square result for perceived safety & parent willingness with licensed child (N = 190).

Willingness	Yes		No		Maybe		$\chi^2$	V
	n	%	n	%	n	%		
Extremely uncomfortable	6	23.08	19	73.08	1	3.85	18.93	0.223
Somewhat uncomfortable	14	30.44	24	52.17	8	17.39		
Neither comfortable nor uncomfortable	6	20.00	13	43.33	11	36.67		
Somewhat comfortable	22	38.60	24	42.11	11	19.30		
Extremely comfortable	13	41.94	16	51.61	2	6.45		

*p* < 0.015.

**Table 3.** Frequencies and Chi-Square result for delayed licensing & parent willingness with licensed child (N = 190).

falling into the “somewhat comfortable” (n = 57) or “somewhat uncomfortable” (n = 46) responses regardless of whether they felt their child should wait to learn to drive or not (Table 3).

#### 4. Discussion

The current study was a cursory attempt at discovering the factors that contribute to parent willingness to transport teenagers in AVs unaccompanied. Overall, participants reported being moderately familiar with AV (46.07%) and generally perceived it to be safe (58.94%) and useful (80.63%). Respondents were in less agreement over if they would be likely to use an AV personally or likely to purchase an AV if cost were no issue. Although many parent participants (n = 118) reported identifying as an early adopter of technology, many were not in favor of their teenagers delaying their licensing by using AVs as a means of transportation.

When early adopter status was examined, results were congruent with previous research that those who self-identified as early adopters would display more willingness to make use of this technology [23]. The portion of participants who did consider themselves to be early adopters but still expressed discomfort for using AVs (22.11%) suggests that those who are more likely to adopt technology earlier than their peers may still have reservations about AV use specifically. Additionally, the group of participants who rated themselves neutrally on either early adoption status and willingness (34.74%) suggests that a large portion of the parents surveyed are not familiar enough with the technology to consider using it.

One of the key elements which contributes to parent acceptance of AVs identified in previous research is perceived safety [8, 18, 19]. Due to this, the current finding that participants who felt that AVs were safe (58.95%) were more inclined to let their children travel unattended in them is expected. There are still portions of the sample who were neutral or hesitant regardless of their opinion that AVs are generally safe which suggests that the safety is not the only factor which may inform parent decision making.

Due to the literature that discusses the risk taking behavior and lack of experience of teen drivers, it was hypothesized that parents may be in favor of using AV as a means of delaying the need for teenagers to become licensed at a young age [22, 24–26]. Interestingly, this was not the case. Many parents still wanted their child to learn to drive regardless of AV presence. Even when considering parent

willingness to transport their child in an AV, several parents who were in favor said that they would still want their child to get licensed. Based on participant feedback collected at the end of the survey, several parents who generally viewed AV favorably still wanted their child to learn to drive. They felt that it is an important skill which is crucial to learn at this age.

This study was limited in its sample size due to large numbers of failed attention checks and individuals responding for children who did not meet the age criteria. Additionally, there was likely a lack of uniformity in participant interpretations of AVs. While survey questions were posed to gain insight into participants AV opinions, an individual's level of prior knowledge and experience with an emerging technology is difficult to ascertain [8, 18]. Efforts were made to include descriptions of AVS and early adopter status, but it is difficult to provide a complete image of these subjects in a few sentences. Ultimately, this is a preliminary effort which hopes to inform directions for future studies in AV acceptance.

## **5. Conclusion**

This chapter focused on exploring parent opinions and willingness to transport teenagers in AVs independently. Results indicate that parents have varying opinions of transporting their teenagers in AVs. Early adopter status did express more comfort with using the technology, parents would still like their children to learn to drive traditional vehicles. These findings contribute to our understanding of the perceived AV usage, willingness, and adoption [28], as well as, the unique barriers from a family perspective which are largely centered around concerns about the AVs ability to safely transport children [8, 18–20]. Based on the findings, several suggestions for future research can be made. Firstly, an exploration into potential differences between parent's general ratings of AV safety compared to ratings of perceived safety specifically for transporting teenagers. In future iterations of this question, the focus can be shifted away from the idea of delaying one's licensing to using AV as a supplemental tool during more stressful or complex driving scenarios. Also, different ridership scenarios should be considered when a licensed teen is present or absent with younger siblings or other family members. Finally, more exploration is needed into early adoption of AVs specifically, as barriers may differ from general adoption of technology. We believe that these topics are important as we embrace AV technologies and the impact of AV-enhanced mobility on vulnerable road users, such as teenagers.

## **Acknowledgements**

The authors wish to thank Kyle Hickerson for his advice for statistical analysis.

## **Author details**

Allegra Ayala\* and Yi-Ching Lee  
George Mason University, Fairfax, VA, USA

\*Address all correspondence to: aayala21@gmu.edu

## **IntechOpen**

---

© 2022 The Author(s). Licensee IntechOpen. This chapter is distributed under the terms of the Creative Commons Attribution License (<http://creativecommons.org/licenses/by/3.0>), which permits unrestricted use, distribution, and reproduction in any medium, provided the original work is properly cited. 

## References

- [1] Bansal P, Kockelman KM. Forecasting Americans' long-term adoption of connected and autonomous vehicle technologies. *Transportation Research Part A: Policy and Practice*. 2017;**95**: 49-63. DOI: 10.1016/j.tra.2016.10.013
- [2] Slowik P, Sharpe B. Automation in the long haul: Challenges and opportunities of autonomous heavy-duty trucking in the United States. *The International Council on Clean Transportation*. 2018;1-30
- [3] Greenblatt JB, Shaheen S. Automated vehicles, on-demand mobility, and environmental impacts. *Current Sustainable/Renewable Energy Reports*. 2015;**2**(3):74-81. DOI: 10.1007/s40518-015-0038-5
- [4] Ayoub J, Mason B, Morse K, Kirchner A, Tumanyan N, Zhou F. Otto: An autonomous school bus system for parents and children. In: *Extended Abstracts of the 2020 CHI Conference on Human Factors in Computing Systems (CHI 2020)*; 25-30 April 2020; Honolulu HI, USA. New York: Association for Computing Machinery; 2020. p. 1-7. DOI: 10.1145/3334480.3382926
- [5] Francis S. Top 25 autonomous shuttle manufacturers. *Robotics & Automation News [Internet]*. 2020. Available from: <https://roboticsandautomationnews.com/2020/10/15/top-25-autonomousshuttle-manufacturers/37291/> [Accessed: January 19, 2021]
- [6] Salonen AO, Haavisto N. Towards autonomous transportation. Passengers' experiences, perceptions and feelings in a driverless shuttle bus in Finland. *Sustainability*. 2019;**11**(3):588-607. DOI: 10.3390/su11030588
- [7] Harper CD, Hendrickson CT, Mangones S, Samaras C. Estimating potential increases in travel with autonomous vehicles for the non-driving, elderly and people with travel-restrictive medical conditions. *Transportation Research Part C: Emerging Technologies*. 2016;**72**:1-9. DOI: 10.1016/j.trc.2016.09.003
- [8] Lee Y-C, Mirman JH. Parents' perspectives on using autonomous vehicles to enhance children's mobility. *Transportation Research Part C: Emerging Technologies*. 2018;**96**:415-431. DOI: 10.1016/j.trc.2018.10.001
- [9] Rosenbloom S. The impact of growing children on their parents' travel behavior: A comparative analysis. *Transportation Research Record*. 1987;**1135**:17-25
- [10] Dowling R. Cultures of mothering and car use in suburban Sydney: A preliminary investigation. *Geoforum*. 2000;**31**(3):345-353. DOI: 10.1016/S0016-7185(99)00048-2
- [11] Ham SA, Martin S, Kohl HW. Changes in the percentage of students who walk or bike to school—United States, 1969 and 2001. *Journal of Physical Activity and Health*. 2008;**5**(2):205-215. DOI: 10.1123/jpah.5.2.205
- [12] McDonald NC. Active transportation to school, trends among U.S. schoolchildren, 1969–2001. *American Journal Preventative Medicine*. 2007;**32**(6):8. DOI: 10.1016/j.amepre.2007.02.022
- [13] Faulkner GE, Richichi V, Buliung RN, Fusco C, Moola F. What's 'quickest and easiest?': Parental decision making about school trip mode. *International Journal of Behavioral Nutrition*

and Physical Activity. 2010;7(1):62.  
DOI: 10.1186/1479-5868-7-62

[14] Fyhri A, Hjorthol R, Mackett RL, Fotel TN, Kytta M. Children's active travel and independent mobility in four countries development, social contributing trends and measures. *Transport Policy*. 2011;18:703-710. DOI: 10.1016/j.tranpol.2011.01.005

[15] Haller S. Uber says 'no' to kids, but a growing number of ride apps say 'yes.' Parents are a 'maybe.' USA TODAY. 2019. Available from: <https://www.usatoday.com/story/life/parenting/2019/09/13/uber-kids-transportation-services-zum-hopskipdrive-kango-soar-how-they-work-are-they-safe/2268309001/>. [Accessed: January 18, 2021]

[16] Quander M. Ridesharing service for kids launches in the DC area. *wusa9.com*. 2019. Available from: <https://www.wusa9.com/article/news/local/ridesharing-service-for-kids-launches-in-the-dc-area/65-328f4c14-d97d-439e-86a5-876455fca066>. [Accessed: January 18, 2021]

[17] Mikkelsen MR, Christensen P. Is Children's independent mobility really independent? A study of children's mobility combining ethnography and GPS/mobile phone technologies. *Mobilities*. 2009;4(1):37-58. DOI: 10.1080/17450100802657954

[18] Hand SH, Lee Y-C. Who would put their child alone in an autonomous vehicle? Preliminary look at gender differences. *Proceedings of the Human Factors and Ergonomics Society Annual Meeting*. 2018;62(1):256-260. DOI: 10.1177/1541931218621059

[19] Tremoulet PD, Seacrist T, Ward McIntosh C, Loeb H, DiPietro A, Tushak S. Transporting children in autonomous vehicles: An exploratory study. *Human*

*Factors*. 2020;62(2):278-287. DOI: 10.1177/0018720819853993

[20] Ayala AM, Lee Y-C. Autonomous vehicles, children's mobility, and family perspective. In: *Proceedings of the Human Factors and Ergonomics Society, 65th Annual Meeting (HFES 2020)*; 4-7 October 2021; Baltimore MD, USA. California: SAGE; 2021. p. 747-751. DOI: 10.1177/1071181321651323

[21] Jing P, Du L, Chen Y, Shi Y, Zhan F, Xie J. Factors that influence parents' intentions of using autonomous vehicles to transport children to and from school. *Accident Analysis & Prevention*. 2021;152:105991. DOI: 10.1016/j.aap.2021.105991

[22] Correa T. Acquiring a new technology at home: A parent-child study about youths' influence on digital media adoption in a family. *Journal of Broadcasting & Electronic Media*. 2016;60(1):123-139. DOI: 10.1080/08838151.2015.1127238

[23] Carr VH Jr. Technology adoption and diffusion. In: *The Learning Center for Interactive Technology*. 1999. Available from: <https://www.icyte.com/system/snapshots/fs1/9/a/5/0/9a50b695f1be57ce369534ac73785801745a8180/index.html>

[24] Jonah BA. Accident risk and risk-taking behaviour among young drivers. *Accident Analysis & Prevention*. 1986;18(4):255-271. DOI: 10.1016/0001-4575(86)90041-2

[25] Williams AF. Teenage drivers: Patterns of risk. *Journal of Safety Research*. 2003;34:5-15. DOI: 10.1016/S0022-4375(02)00075-0

[26] CDC Injury Center. Teen Drivers: Get the Facts | Motor Vehicle Safety. 2021. Available from: [https://www.cdc.gov/transportationsafety/teen\\_drivers/](https://www.cdc.gov/transportationsafety/teen_drivers/)

teendrivers\_factsheet.html. [Accessed: January 05, 2022]

[27] Hartos JL, Eitel P, Simons-Morton B. Do parent-imposed delayed licensure and restricted driving reduce risky driving Behaviors among newly licensed teens? *Prevention Science*. 2001;2:113-122. DOI: 10.1023/A:1011595714636

[28] SAE. Taxonomy and Definitions for Terms Related to Driving Automation Systems for On-Road Motor Vehicles – SAE International. Pennsylvania: SAE International; 2016. Available from: [http://standards.sae.org/j3016\\_201609/](http://standards.sae.org/j3016_201609/)

[29] Fagnant DJ, Kockelman K. Preparing a nation for autonomous vehicles: Opportunities, barriers and policy recommendations. *Transportation Research Part A: Policy and Practice*. 2015;77:167-181. DOI: 10.1016/j.tra.2015.04.003

[30] Bureau of Transportation Statistics. Household, Individual, and Vehicle Characteristics. 2011. Available from: [https://www.bts.gov/archive/publications/highlights\\_of\\_the\\_2001\\_national\\_household\\_travel\\_survey/section\\_01](https://www.bts.gov/archive/publications/highlights_of_the_2001_national_household_travel_survey/section_01). [Accessed: January 05, 2022]

[31] SAE International. Taxonomy and Definitions for Terms Related to Driving Automation Systems for On-Road Motor Vehicles. J3016C, 04-21. Available from: [https://www.sae.org/standards/content/j3016\\_202104/](https://www.sae.org/standards/content/j3016_202104/). [Accessed: February 17, 2022]

[32] McHugh ML. The chi-square test of independence. *Biochemical Medicine*. 2013;23:143-149. DOI: 10.11613/BM.2013.018



---

Section 3

# Mobility Needs and Cybersecurity Applications

---



# IoT-Based Route Guidance Technology for the Visually Impaired in Indoor Area

*Jong-Gyu Hwang, Tae-Ki An, Kyeong-Hee Kim and Chung-Gi Yu*

## Abstract

The mobility handicapped, especially the visually impaired, are complaining of many difficulties and inconveniences in moving in underground spaces such as subway stations due to inconvenience in behavior and lack of guidance information. Route guidance for the visually impaired through various mobile apps using the newest global positioning system (GPS) is supported, but these apps cannot be used in areas where GPS signals are not received. To solve this problem, in this chapter, an Internet of things (IoT) sensor-based route guidance technology was presented to improve the mobility of the visually impaired in indoor areas such as railway stations and a mobile app has been developed, where an IoT-sensor-based user positioning algorithm and user convenience are considered. In addition, to evaluate the applicability of the developed system, the user satisfaction was measured through a test at the virtual Busan City Hall metro station for the visually impaired. The route guidance technology presented in this chapter is expected to contribute greatly to the improvement in the mobility of the visually impaired in indoor areas including railway stations.

**Keywords:** the visually impaired, route guidance, IoT-based technology, satisfaction ratio, positioning algorithm in indoor area

## 1. Introduction

The mobility handicapped refers to people who have temporary or continuous movement restrictions or inconveniences when using public transportation facilities due to behavioral inadequacies, and as of 2017 in Korea, the transportation vulnerable population is expected to reach 28.9% of the total population and an annual growth rate of 2% over the next 5 years. Accordingly, the improvement in convenience in the use of public transportation facilities such as railway stations for the mobility handicapped is becoming an urgent problem. Among the mobility handicapped, especially the visually impaired have many inconveniences in using public transportation such as railways due to their physical characteristics. In addition, it is difficult for the visually impaired to safely escape through various types of emergency evacuation information and escape systems in case of emergency situations such as fires in railway stations, so it has potential safety problems for them. Among the mobility

Division	Sum	Very satisfaction	Satisfaction	Normal	Unsatisfaction	Very unsatisfaction	No use	User satisfaction
The physically disabled	156	3	7	91	35	20	22	52
The visually disabled	69	0	7	42	13	7	5	54
The hearing disabled	63	3	3	42	12	3	9	57
The complex disabled	68	3	4	38	17	3	8	56
The pregnant	93	6	24	43	20	0	17	63
The older	374	45	105	165	50	9	83	67
The ordinary	430	68	188	160	11	3	63	72

**Table 1.** Usability evaluation results for each the mobility handicapped [1].

handicapped, especially the visually impaired feel more difficult and inconvenient in indoor activities than other mobility handicapped due to their lack of behavioral information and lack of information for them.

Recently, various walking-supported technologies for the visually impaired using global positioning system (GPS) signal-based location information have been introduced, helping them in their outdoor activities. However, since GPS signals cannot be used in underground or indoor areas such as railway stations, various walking support systems that have been introduced recently cannot be used. According to a survey report by the Ministry of Land, Infrastructure and Transport [1], as shown in **Table 1**, it is identified that the level of user satisfaction of the mobility handicapped including the visually impaired is 10–20% lower than that of the general public at railway station and bus terminal [1–4].

In order to increase the satisfaction ratio for the physical disabled, large-scale hardware investment such as the installation of elevators for interfloor movement and improvement in facilities such as application of barrier-free (BF) design is essential. However, on the other hand, the visually impaired need routes and risk information, not large-scale facility investors like the disabled. Various mobility convenience

<b>Nations</b>	<b>project of the visually impaired people</b>	<b>Institute</b>
Korea	Bus information terminal (BIT)	Rosisy Co., Ltd.
	Accessory technology for the visually impaired (NAVIWALK)	Naviworks Co., Ltd.
	Accessory technology for the visually impaired	Freemfor Co. & Isonic Co., Ltd.
	Accessory technology for the visually impaired (destination guidance sticks)	Daegu Univ.
	Accessory technology for the visually impaired (Smart-walk)	Daegu Univ.
	Voice guidance system for the visually impaired	Nowon-gu District Office
	Accessory technology for the visually impaired (Visually impaired Navigation)	HIMS International Co., Ltd.
	Sound signal for the blind using GPS	Korea Road Traffic Authority
USA	Wireless pedestrian navigation system (Drishti)	Univ. of Florida
	Trinetra project (the third eye)	CMU
	Seeing AI	MS
	Access program	Go-Metro
	Drone system to help blind people exercise	Univ. of Nevada
	Accessible pedestrian signals (APS)	USA Government
EU	GuideCane	World Int'l Sensory Aid
	Brumel navigation system	Brunel Univ.
	Walking guidance technology using Bluetooth-based beacons	Wayfindr
	OnTheBus System Project	Autonoma Tech. Univ.
	GPS-based visually impaired navigation app (Blindsquare)	Scandinavia

**Table 2.**  
*Technology development research and practical application examples.*

facilities to support the mobility of the visually impaired in indoor areas are continuously installed, but the level of the user satisfaction ratio is not improving as the facilities installation rate increases. Accordingly, although it is important to install hardware-based mobile convenience facilities, measures to improve the user satisfaction in view of software are required [3–5].

In order to solve these problems, various technologies for supporting independent walking for the visually impaired are being introduced and developed in many countries and institutes, as shown in **Table 2** [6–26]. It is confirmed that these various technologies are having difficulty in practical use in terms of usability, such as electronic sticks like NAVIWALK [14, 25], or still in the early stages of technology development. In particular, most of these are technologies for outdoor application, and except for some, it is analyzed that indoor technology is still in the early stages of development.

Recently, the use of smartphones has become common among visually impaired people in external activities in Korea. Accordingly, in this chapter, a technology for supporting mobility in indoor spaces of the visually impaired people based on smartphones that do not require large-scale facilities was presented, and its applicability was verified [7, 8, 13]. That is, Internet of things (IoT) sensor-based route guidance technology that can improve the satisfaction of the visually impaired in indoor space through smartphone-based technology and user satisfaction evaluation results was represented.

## 2. Technology trend analysis of support system for the mobility handicapped

In this section, the technology analysis through patent analysis and patent trend analysis for predicting future technology directions are conducted in relation to the support system technology for the mobility handicapped, centered on the visually impaired. In general, since related information is disclosed to the public after

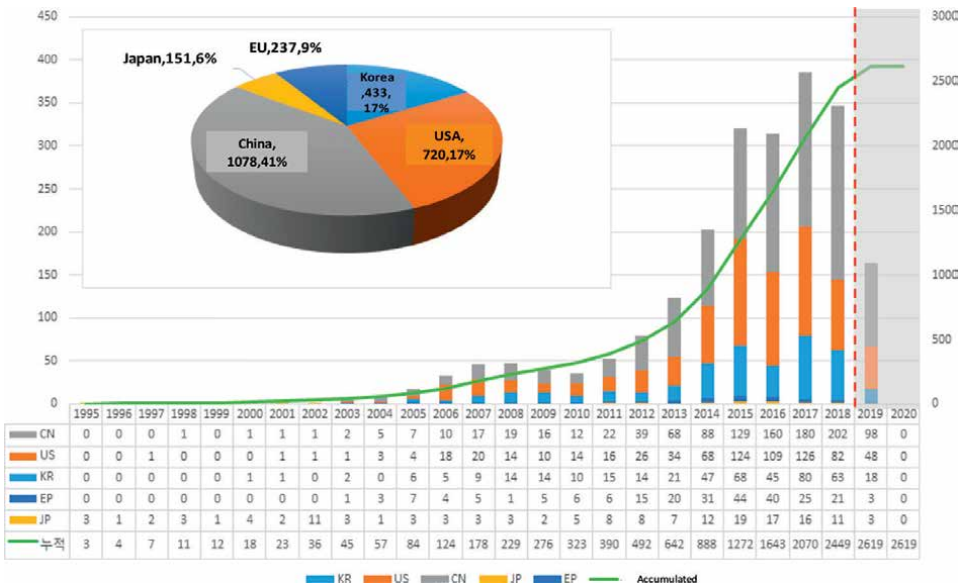
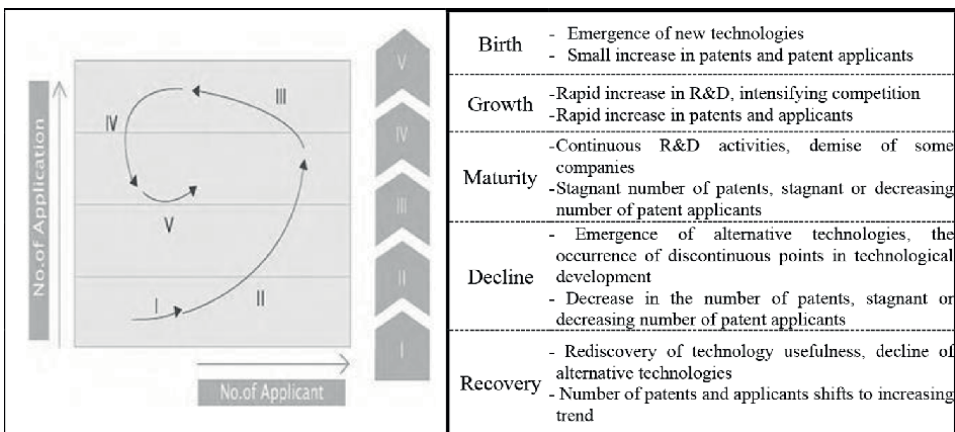


Figure 1. Patent application trends by year in major market countries [7].

18 months have elapsed since the patent application is filed, the quantitative meaning of patents filed in 2019–2020 is not valid, so quantitative analysis is limited to the end of 2018.

Looking at the overall patent trend by year of the support system technology for the mobility handicapped, from a macroscopic point of view, except for a brief decrease around 2010, the overall number of applications has been steadily increased, and it has been shown to have increased rapidly since 2010 (**Figure 1**). Korea has 433 cases, occupying 17% of the total valid patents; China has 1078 cases, occupying 41% of the total patents; Japan has 151 cases, occupying 6% of the total patents; the USA has 720 cases, occupying 27% of the total patents; and Europe has 237 cases, occupying 9% of the total patents. Looking at the patent trend by year in Korea, the number of patents increased from 2010, and after a sharp increase and peak in 2014, it decreased in 2016 and then increased again. In the USA, patents started to increase from 2006. In 2015, 102 applications were filed, the most among major market countries, and it appears to be declining in 2018. Patents in China started to increase from 2011, and in 2018, 202 applications were filed, the most among major market countries, and it is increasing steadily. In Japan, patents increased sharply in the early 2000s, since then increased and decreased repetitively, but, overall, it showed an increasing trend, but it has been decreasing since 2018. In Europe, the number of patents started to increase from 2011, and in 2015, 34 applications were filed, the most among major market countries, and it has been declining since 2016 [8, 27, 28].

The technology market generally goes through stages of “Birth ⇒ Growth ⇒ Maturity ⇒ Decline ⇒ Recovery” (**Figure 2**). In the field of interactive support system technology for the mobility handicapped, accordingly as it was investigated that the number of applicants as well as the number of applications continued to increase from Section 1 (2003–2006) to Section 4 (2015–2018), it was analyzed that currently it was located in the growth stage. The growth stages of the technology market by country seem to have entered a period of growth. That is, the technology position of Korea patent (KIPO), US patent (USPTO), Chinese patents (SIPO), Japanese patent (JPO), and European patents (EPO) is analyzed to have entered a period of growth, as both the number of applications and the number of applicants were increasing from Section 1 (2003–2006) to Section 4 (2015–2018).



**Figure 2.**  
*Growth stage of technology market.*

The main examples of development related to the mobility support system for the visually impaired are shown in **Table 3**, and only a few of them are introduced in this section.

Class	Nation	Project	Remark
The visually impaired	Korea	Bus Information Terminal (BIT)	LOGISYS
		Passage assistance technology for the visually impaired (NAVIWALK)	NAVIWORKS
		Passage assistance technology for the visually impaired	PRIMPO, ISONIC
		Passage assistance technology for the visually impaired (Destination Guide Cane)	Daegu University
		Smart-walk technology for the visually impaired	Daegu University
		Voice guidance system for the visually impaired	Nowon-gu Office
		Passage assistance technology for the visually impaired (only navigation for the visually impaired)	HIMS International
	A sound signal device for the visually impaired using GPS	Road Traffic Authority	
	USA	Wireless Pedestrian Navigation System (Drishti)	University of Florida
		Trinetra Project (the third eye)	Carnegie Mellon University
		Seeing AI	Microsoft
		Access program	Go-Metro
		Drone System that helps visually impaired people to exercise	University of Nevada
		Accessible Pedestrian Signals (APS)	USA Government
	Europe	GuideCane	Wormald International Sensory Aids
		Brumel navigation system	Brunel University
		Walking guidance technology using Bluetooth-based beacon	Wayfinder
		OnTheBus System Project	Universitat Autònoma
GPS-based navigation app for the visually impaired (Blindsquare)		Scandinavia	
Handicapped, Elderly, Infant	Korea	Bus boarding reservation service for the handicapped	Jeonju City
	USA	Senior Pedestrian Focus Areas for Senior Pedestrians	New York City
		Travel Assistance Device	University of North Florida
	Europe	SafeWalk and C-Walk sensors	Traficon
		SMART-WAY	Germany
		WAY4ALL	Austria
	Japan	Intelligent Wheelchair Robot (TAO Aicle)	AISIN SEIKI
		Current status of pedestrian facilities for the elderly	Japan Government

Class	Nation	Project	Remark	
Other	Korea	Development of customized public transportation service technology for the mobility handicapped	Ministry of Land, Infrastructure and Transport	
		USA	Pedestrian sanctuary	Department of Transportation
			School zone system	Department of Transportation
			Car swivel seat	Department of Transportation
			Policies and legal systems related to the mobility handicapped	Department of Transportation
	Europe		Mobility project to improve public transport accessibility	CIVITAS
			Intelligent bus stop system of the ACCESS2ALL project	European Commission
			HaptiMap project	Lund University
			PocketNavigator	European Commission
	Japan		Accessible Japan for the mobility handicapped	Japan Government
			Acoustic signal system technology development	Japan Government
			Pedestrian protection zone	Japan Government
			WHILL autonomous driving system	Japan Government
	China		Wheelchair Accessible Tour Guide	China Government
			Policies to increase accessibility for the mobility handicapped	China Government

**Table 3.**  
*Examples of technology development research and commercialization [9, 14–25].*

## 2.1 Passage assistance technology for the visually impaired of NAVIWORKS

When the NAVIWALK cane developed in Korea comes into contact with the radio frequency identification (RFID)-tag-inserted braille block, there is a product that reads the data of the current location and guide information stored in the tag and provides it with voice.

For this purpose, the RFID tag embedded in the braille block is detected through the antenna of the tip of the carrying cane (**Figure 3**). Because NAVIWALK is an offline system, it is easy to build and has low construction and operation costs, and it is easy to add, change, and modify location information and information messages wirelessly without physical changes, so because there are no restrictions on RFID tag installation, generally, it is suitable for commercialization. The principle of operation is that when the NAVIWALK cane comes into contact with the RFID-tag-inserted braille block, the data of the current location and guide information stored in the tag are read and provided as voice information to provide information to the visually impaired.

## 2.2 Passage assistance technology for the visually impaired of Primpo Co. (Isonic-Primpo)

In order to overcome the limitation that the existing canes for the visually impaired could not detect obstacles higher than waist height, as shown in **Figure 4**,

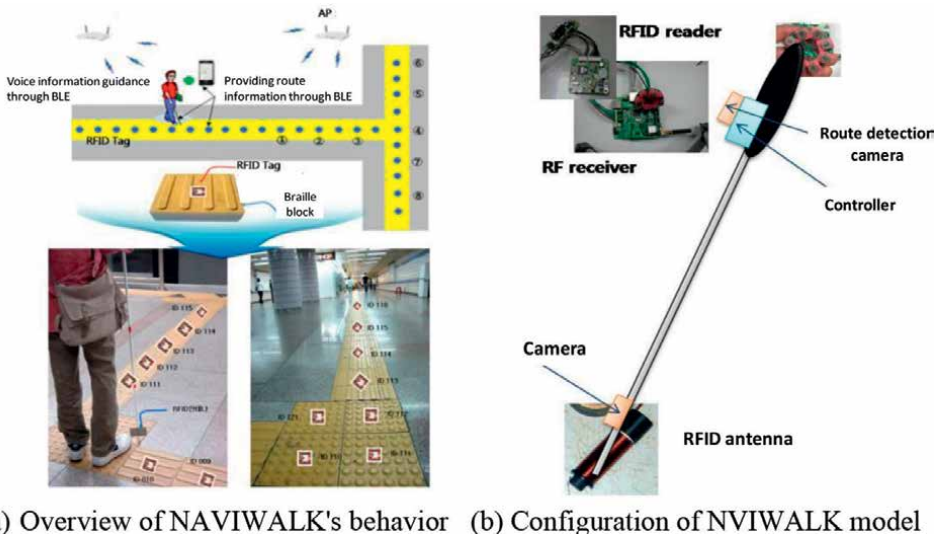


**Figure 3.** Smart cane configuration diagram of NAVIWALK model [14, 25].

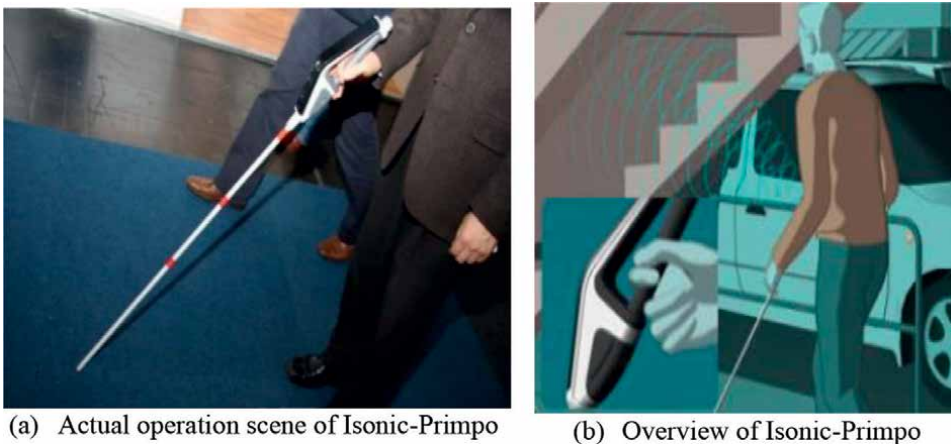


**Figure 4.** Isonic-Primpo voice recognition support for the visually impaired [15].

Isonic-Primpo is characterized by attaching an ultrasonic sensor to support a wider detection range [15]. It can detect obstacles located within 2 m from the user and even thin and slender obstacles with a thickness of 3 cm, and it can recognize up to an angle of 25° left and right. It can inform the user of the color of obstacles with a voice and can inform the user of brightness level with a voice. User-centered voice support is possible while delivering obstacle location information with a stronger vibration as it gets closer. In particular, as an obstacle detection electronic cane, it has the great advantages in its strong vibration tactile system and voice recognition support that can overcome visual limitations.

### 2.3 Drone system to help exercise of the visually impaired for the University of Nevada

The visually impaired people have limitations in some exercise, such as running outside without a guide, but it has been confirmed that the visually impaired have higher spatial localization skills than the general public. This study became the basis for the ability of the visually impaired people to follow drones in a running track environment. In fact, the University of Nevada, Reno (UNR), developed a drone system (**Figure 5**) that helps exercise of the visually impaired people through low-cost flying drones [15]. Equipped with a total of two cameras, a downward-facing camera that follows the track's line and a separate camera that focuses on the marker on the runner's shirt, the drone flies about 10 feet ahead of the runner running at eye level and provides sound guidance. As the runner speeds up or slows down, the drone adjusts its own speed to guide the movement of the visually impaired. The study was conducted with two visually impaired persons, and the results of the study confirmed that the visually impaired could accurately identify and follow the drone, and the qualitative results showed that the participants were accustomed to following the drone, and that the drone system had high efficiency when following and locating the drone.

### 2.4 Google's HearHere project

HearHere is a navigation system for the visually impaired, which proceeds in two steps [17]. **Figure 6** shows the overview of this project process. First, the hardware equipped with the sensor is installed on the glasses to measure the direction of the user with the sensor, and the measured information is transmitted to the smartphone through Bluetooth module, and the software installed on the smartphone creates small destinations at regular intervals on the route to the destination based on the transmitted location information.

When the destination is set, the walking route from the current location to the destination is calculated, and a virtual waypoint that will generate a sound in units of 10 m is created. A visually impaired person feels as if a sound is emitted from the nearest waypoint, and when the waypoint is reached, the next waypoint is updated to sound.



**Figure 5.** Conceptual diagram of UNR's drone system that helps exercise of the visually impaired [16].

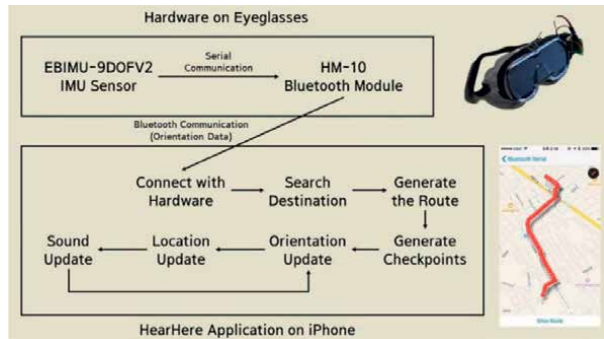


**Figure 6.** Google's HearHere project process [17].

### 2.5 Wormald international sensory Aid's robot GuideCane for the visually impaired

Initially, NavBelt, a combination of navigation and belt, was developed to search for obstacles in the path for the visually impaired to walk; however, since the walking part must also identify obstacles on the lower foot, a broader concept of GuideCane was developed [9]. The GuideCane and its functional components, as shown in **Figure 7**, are very similar to a white cane, in which the user holds the GuideCane in front of him while walking, but the details are different, although the GuideCane is considerably heavier than a regular cane, since it rolls on wheels that support the weight of the GuideCane during operation, it has normal weight. A submotor operating under the control of a built-in computer can move the wheels left and right based on the cane, and both wheels are equipped with encoders that determine the relative motion, and for obstacle detection, GuideCane is equipped with 10 ultrasonic

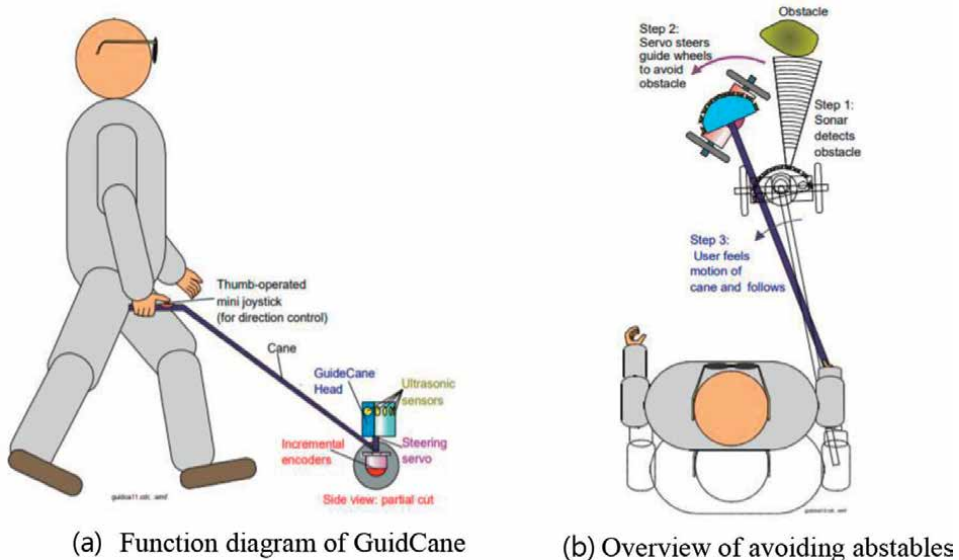


**Figure 7.** Configuration of GuideCane [9].

sensors, so it can detect dangerous obstacles. To specify the desired direction of motion, the user manipulates the mini joystick on the handle, and based on user input and sensor data from the encoder, the computer determines where to turn next.

### 3. Smart braille-block-based route guidance technology for the visually impaired

The visually impaired people have a lot of difficulties due to their visual limitations when moving outside. However, recently, various route guidance support systems using GPS signals have been developed and introduced to help them find their destination, but there are still many difficulties in mobility in underground and indoor areas such as railway stations where GPS signals cannot be used. Various technologies that can use location information in this indoor area are being developed, but most of them require the construction of many infrastructure facilities, and at the same time, users must have a dedicated terminal or additional device to use these services, etc. [6–9]. Therefore, it is difficult to put it into practical use. In this chapter, to increase practicality through the analysis of these existing studies, IoT-sensor-based route guidance technology was designed through positioning in the indoor space so that the user installs only the smartphone app and minimizes the construction of infrastructure facilities [7, 13].

#### 3.1 Overview of IoT-sensor-based route guidance technology

Braille blocks for the visually impaired are installed on the floor of most indoor areas, including railway stations, and rounded type is installed on the path of the braille blocks, and linear type is installed at junctions or end points to help the visually impaired. In this chapter, the IoT sensor is embedded in the braille block installed on the floor, and the mobile app determines the user's location and calculates the route to their destination based on the signal from the sensor. Following the confirmed user's current location and desired route, route information is guided through



**Figure 8.**  
*Configuration of IoT-based route guidance technology for the visually impaired.*

voice and screen of the mobile terminal. **Figure 8** shows the outline of the route guidance technology in the indoor area proposed in this chapter and the application screen of the mobile terminal.

The app screen is used by the visually impaired, not the general public, must be designed in accordance with the national app accessibility standard, and must also be certified by an authorized agency. The app developed in this chapter is designed and certified according to this standard. When the user's location information in the indoor area is confirmed, a route guidance service to the desired place is possible, and additionally, information on major facilities around the moving route and risk information can be provided. In other words, until now, it was impossible to provide various pieces of information to improve mobility as GPS signals were not available in indoor areas. However, through the location information through the IoT sensor proposed in this chapter, it is possible to apply various services for the visually impaired to support movement in indoor spaces. **Figure 1** shows an overview of route guidance technology for the visually impaired.

### **3.2 IoT sensor data structure**

As described in Section 3.1, the IoT sensor installed on the floor to identify the user's location in the indoor area is a Beacon (hereinafter referred to as Bluetooth Low Energy (BLE) in this chapter), and this sensor is based on the MAP of the indoor area that provides the route guidance service. As a result, IoT sensor mapping was done through the following appropriate zone design for each sensor:

- Zoning so that travel routes do not overlap
- Zoning by equalizing the installation interval of the sensor
- Mapping of direction information for each zone to provide user movement direction information
- Mapping with points of interest (POIs) management information by establishing standard identification code of sensor

After zoned on the MAP of the indoor area for location-based service in this way, the IoT sensors were mapped for each zone, and then, each identifier code system for each mapped sensor was designed. In this chapter, the BLE sensor standard data structure was applied in consideration of service scalability and terminal compatibility with the platform (Android and iOS). It was designed to use the identifier for classifying route guidance services for the visually impaired in the universally unique identifier (UUID) field of the data structure, the local information identifier for the area where the indoor area is located in the Major field, and the facility information identifier of the indoor area in the Minor field. The information in these two fields is configured differently depending on the characteristics of indoor areas such as railway stations, underground shopping malls, and buildings. In the figure, the allocation range means information about each zone zoned in the sensor mapping process. Each BLE sensor having information by such a standard identification code emits a radio frequency (RF) signal having physical location information by allocating it to each zone in the indoor area map. **Table 4** shows an example of designing an identifier code for the major and minor fields when the indoor area to be serviced is a metro

	Major	Minor
Structure	[J1] [J2] [J3] [J4] [J5]	[M1] [M2] [M3] [M4] [M5]
Allocation range	[J1]: 0–5, [J2]: 0–9 [J3]: 0–9, [J4]: 0–9 [J5]: 0–9	[M1]: 0–5, [M2]: 0–9 [M3]: 0–9, [M4]: 0–9 [M5]: 0–9
Code allocation	[J1][J2][J3]: Station Code(000–599) [J4][J5]: Region/Line Classification(00–99) *Region/Line Classification 00–29: Seoul area, 30–39: spare 40–49: Busan, 50–59: Daegu, ...	[M1][M2]: Consecutive numbers(00–59) [M3][M4]: Use classification(00–99) [M5]: Classification of floors *classifications of floors 0: top fourth floor, 1: top third floor 2: top second floor, 3: top first floor 5: bottom fourth floor, ...
Examples	[09801] Seoul area/line 1/Seoul station [02906] Seoul area/line 6/Bugok station, ...	[01014]: Platform Up/bottom first floor [01353]: Transfer parking/top first floor, ...

**Table 4.**  
*Example for Beacon identifier code in case metro station.*

station. If the area to be serviced is not a railway station, but a different area such as an underground shopping mall, the structure of the Major and Minor fields will be adjusted according to the characteristics of the target area.

### 3.3 IoT-based positioning algorithm in indoor area

In this chapter, the user’s location in the indoor area is confirmed based on the smart braille block with the built-in BLE sensor with the data structure presented in Section 3.2. Although the user’s location is identified based on a receiver signal strength indicator (RSSI) signal from a sensor installed on the floor, sensor signals of adjacent sections can be received at the same time, so a method of determining in which section the user is actually located is required. In addition, in order to increase the accuracy of the route guidance information, even if the area of the sensor where the user is located is determined, it is necessary to monitor how far away from the sensor and whether the user deviates from the set route while moving.

To measure the user’s moving direction and distance from the sensor, a hybrid positioning algorithm is applied through pedestrian dead reckoning (PDR) technology, which corrects the position through various sensors built into the mobile terminal. PDR is a technique for estimating the relative position change from the previous position through the detection of a pedestrian’s steps, estimation of the stride length to determine the distance traveled, and estimation of the direction to determine the direction of walking by using the measurement values of three sensors in the inertial measurement unit (IMU) built into the smartphone. For positioning error correction, Kalman filter (KF) was applied to remove the error included in the RSSI value measured by the inertial sensor of the mobile terminal, and an algorithm for correcting the accumulated error of the inertial sensor of the smartphone was applied. During positioning, error correction and algorithms are applied according to the situation such as the position of terminal, stride length, and speed. The user’s current location, movement direction, and movement distance are determined using map information based on the link information between nodes of the BLE sensors mapped to the indoor area map and a hybrid positioning algorithm. Route guidance is provided to

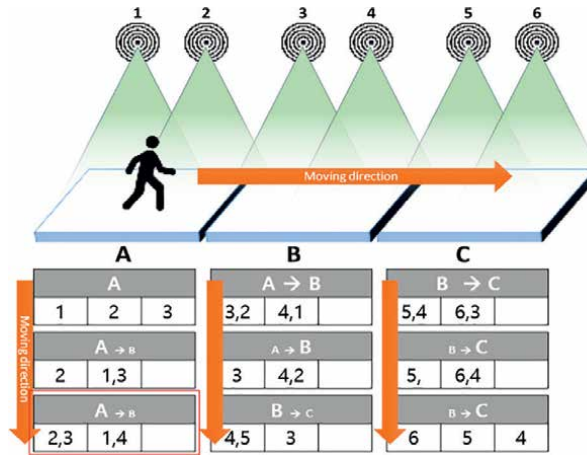


**Figure 9.**  
Concept of BLE-based tracking information.

the user through the app based on the user’s current location information determined by this algorithm.

The overview of the user tracking algorithm through the BLE signal is shown in **Figure 9**. It shows the concept of tracking information and area determination when a user enters area A and then moves to area C via area B. Multiple BLE signals are simultaneously received at the user’s current location; in consideration of the magnitude of these signals and the magnitude of the received signal of each signal in the previous position, the user’s moving position is estimated and which current sensor zone the user is in is determined. As shown in **Figure 10**, when the user enters area A and exits area C through area B, multiple BLE signals may be received by the user’s terminal, and some signals may be within the error range. The current user location is estimated in consideration of the strength of the received BLE signals, the mapped link information between the sensors, and area information from the previous location.

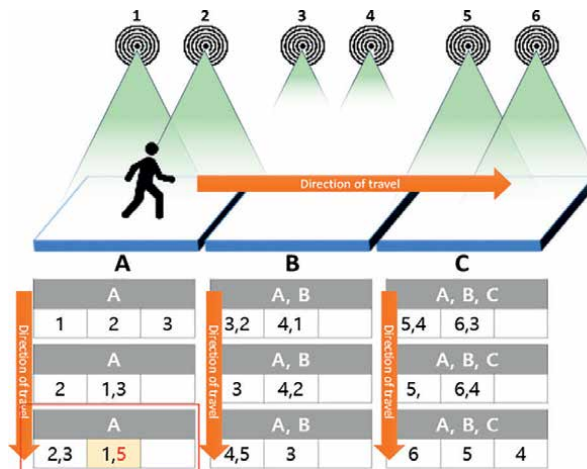


**Figure 10.**  
Calibration concept when ambient signals are measured higher.

As shown in **Figure 10**, based on the received sensor information, it is estimated which area the user is in now or from which area the user is moving to which area. In the figure, “A → B” means that, although it is estimated that the user is moving from area A to area B, the user is currently in area A. The part shown in **Figure 10** is the case that the signals of sensor No. 2 of A and No. 3 sensor of B and the signals of sensor No. 1 of A and No. 4 sensor of B are received within the error range, respectively; although it is ambiguous to determine where the signal is in A or B area from only this received signal, since the previous position is in area A, in this algorithm, it is determined that the user is moving to area B, while he is in region A.

As described above, after estimating the user’s location as a zone first, which sensor the user is located in is estimated in detail by the method shown in **Figure 11**. It is checked whether the sensor signal received from the terminal is a signal from a valid sensor, and if it is a valid signal, it is determined as the first priority signal of the user’s current location based on the received RSSI value through the above-described location correction algorithm. In addition, the sensor after ranking correction is compared with the previous tracking information to check whether there is a change, and finally, the user’s tracking information is updated.

**Figure 11** is an example of a case in which the BLE signal of area C is strongly measured in area A. In this case, since the strongest signal combination is No.1 and No.2 BLE of area A, the surrounding BLE information is searched. Through this, the nearest BLE after BLE No. 1 and No. 2 is determined as No. 3 and signal No. 5 is ignored. **Figure 12** shows the flowchart for checking the user’s tracking information based on the algorithm described so far. That is, it is checked whether the BLE signal received from the mobile phone is a valid BLE signal, and if it is a valid signal, it is determined as the first priority signal of the user’s current location based on the received RSSI value through the above-described location correction algorithm. In addition, the BLE after ranking correction is compared with the previous tracking information to check whether there is a change, and finally, the user’s tracking information is updated. That is, the BLE signal processing order for user tracking is processed according to the following order.

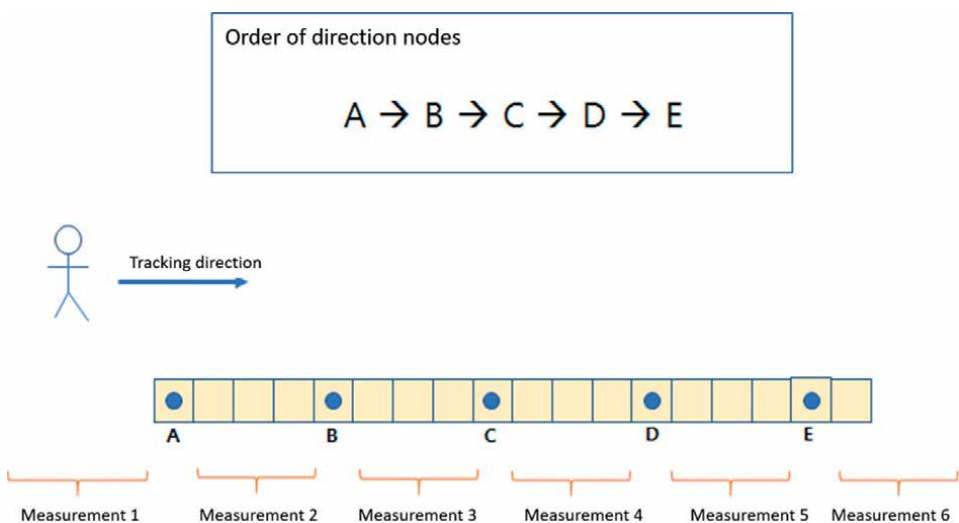


**Figure 11.**  
Node link of sensors when the desired route is straight line.

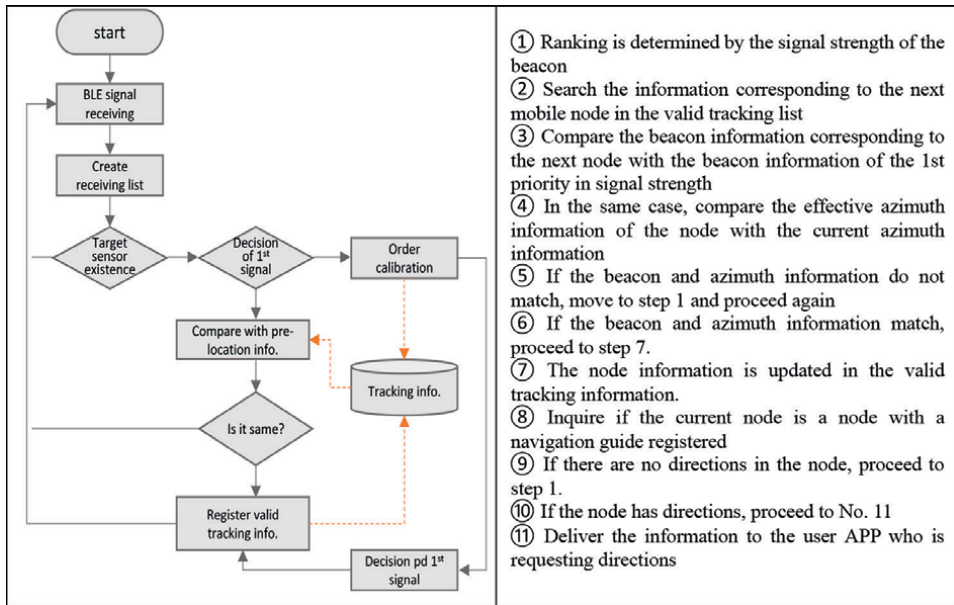


**Figure 12.**  
 Flowchart of user tracking information checking.

For route guidance in an indoor area, the criteria for continuous route guidance are divided into one unit through a smart braille block with built-in IoT sensors, and separate map node information is stored in the server for each divided unit. And when the user arrives at a location where route guidance is possible, the map node information of the corresponding unit is designed to be downloaded from the server to the mobile terminal. When the user's mobile terminal detects the sensor of the smart braille block, the current location is provided to the user by voice, and basic information and brief usage of the app are provided by voice. A list of facilities for a destination reachable from the current location is provided, and when the user selects a facility corresponding to the destination, route information is set up to that facility, and route guidance information can be provided in image and voice according to the user's movement.

#### 4. Simulation test and user satisfaction evaluation

For the evaluation of the system and algorithm presented in this chapter, a mobile app was produced based on the design presented in Section 3, and the user satisfaction was evaluated through a survey for the visually impaired before and after the application of the system of this chapter. For the user satisfaction survey, the waiting room of Busan City Hall Station was selected as an application target, and the nodes of the smart braille block were coded through the field survey, and route guidance information for the visually impaired to the destination could be provided through the connection of the coded nodes. **Figure 13** shows the mapping of IoT sensors and their connection status according to the smart braille block in the waiting room of Busan City Hall Station. The city hall, two ticket gates, toilets, and preferential ticketing machines, which are destinations that can be reached from ① of the station

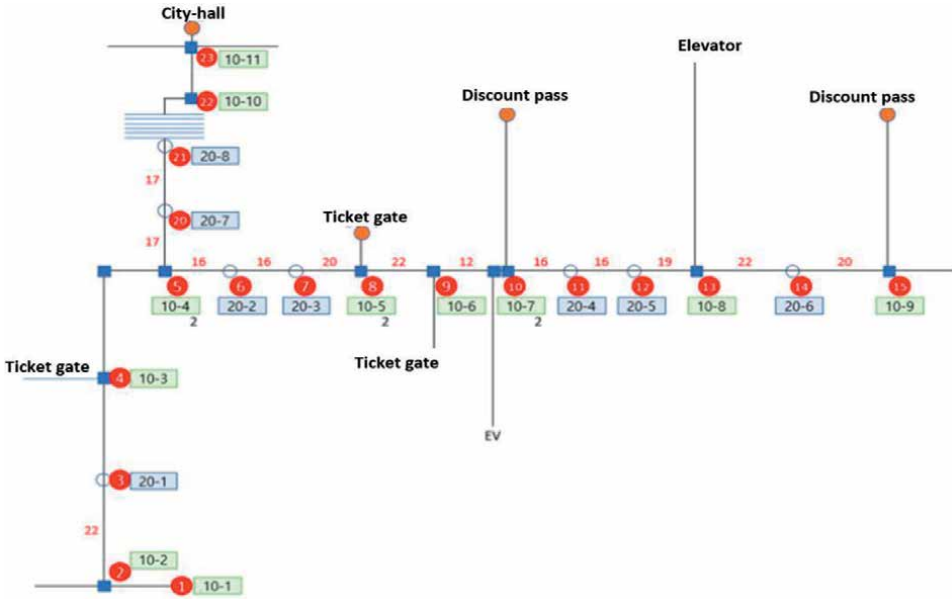


**Figure 13.**  
 Mapping of IoT sensors in case Busan City hall station.

exit gate 4, are displayed, and it can be confirmed that they are linked to each other. If a destination is selected from the location where the main facilities including the exit gate ①, which are each destination, are located, nodes are linked to the destination and route guidance is provided along the linked route.

**Figure 14** shows some part of the screen of the mobile app produced. The left first screen is the initial screen displayed when the user runs the app after arriving at the location of major facilities in the station; through voice recognition, the visually impaired people can easily select the destination they want to go to. Furthermore, it

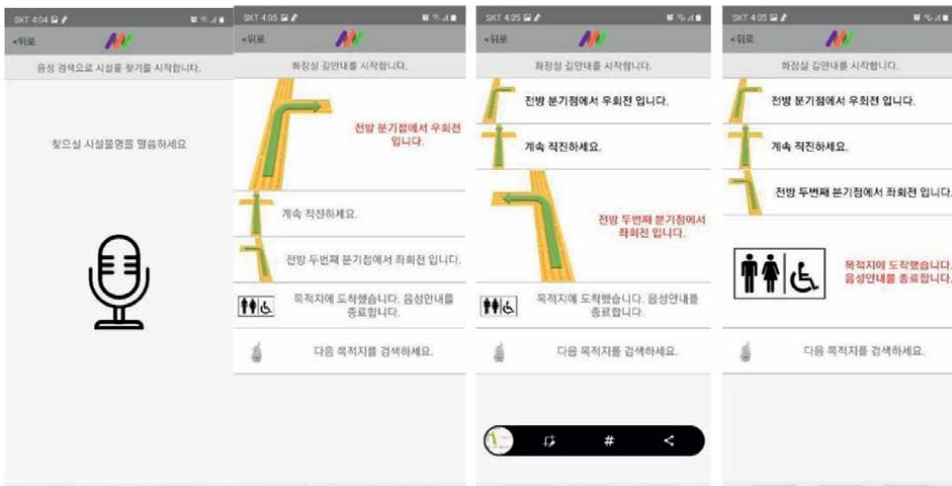


**Figure 14.**  
 Developed mobile app windows (in Korean).

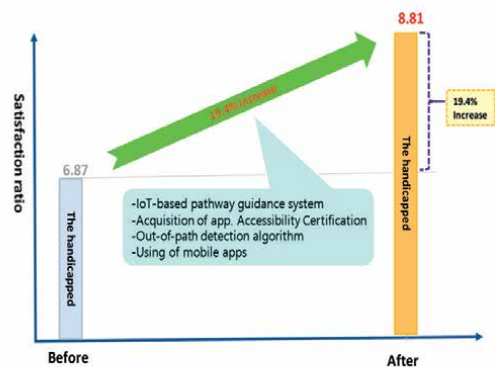
was also produced to provide a user interface (UI) that allows users to select and set destinations through screen touch rather than voice recognition. When a destination is selected through voice recognition or screen touch, the route is set by linking the sensor nodes as shown in **Figure 13** to the destination route, and the route to the destination is sequentially guided as shown in the middle two screens in **Figure 14**. In this case, route information is sequentially provided to the visually impaired through the voice displayed in red as well as the image to be guided, and when they finally arrive at the destination, the voice guidance is terminated.

Based on the produced mobile app, a simulation test was conducted to evaluate the development system targeting 23 visually impaired people in Busan through the Busan Blind Union. Although it is necessary to evaluate through the use of the development system in actual station, due to the corona situation, evaluation was conducted through a satisfaction survey through a simulation test. In the simulation test, an environment was established where the visually impaired could experience the voice route guidance system through a mobile app rather than the actual Busan City Hall station site. In other words, node information of the sensors installed in the actual Busan station was built in the actual Busan City Hall station server, and when the user selects a destination, the sensor node according to the route to the destination is linked as in reality. However, for location confirmation according to the user's movement, the movement was simulated in the app in consideration of the average movement speed of the visually impaired, and the link with the server was constructed so that route information could be provided according to the node link set identical to the actual station.

The design of the questionnaire is important in the user satisfaction survey according to the use of the development system. In this chapter, the basic survey items were applied mutatis mutandis by reviewing the "2017 Transportation Convenience Survey Study" conducted annually by the Ministry of Land, Infrastructure and Transport for the system use satisfaction survey for the test subjects. In order to understand the user satisfaction and the effect of the system on route movement, the NASA-TLX survey items were reflected as items for the satisfaction survey through the review of experts in related fields [4, 6, 23]. **Figure 15(a)** shows a photograph of the user satisfaction survey conducted by the Busan Blind Union for the 23 visually



(a) User satisfaction ratio survey photo



(b) Comparison of the results of the satisfaction ratio

**Figure 15.**  
Results of the satisfaction ratio survey.

impaired persons, and **Figure 15(b)** shows the results of the user satisfaction survey before and after the application of the development system of this chapter. As shown in the figure, the user satisfaction ratio before the application of the development system was 6.81 out of 10, but after using it, it was analyzed to be 8.81, which was an improvement of about 19.4%, confirming that the application effect of the proposed system was very good. In addition, the visually impaired people were reluctant to use railroad stations due to difficulties in finding routes when using them, but if the system of this chapter is applied to the field, a majority opinion that it would be very useful and helpful when moving at an actual station through a simulation walking through this app before going to the station was suggested.

## 5. Conclusion

In order to improve the mobility of the visually impaired in indoor area, an IoT-sensor-based route guidance technology was designed and presented in this chapter. To this end, a system was developed, such as an IoT-sensor-based user positioning algorithm and a mobile app that reflects the UI according to the app accessibility guidelines that reflect the user's convenience. For the evaluation of the developed technology, the IoT sensor map was mapped for the urban railway station, which is one of the representative indoor areas, and the app for the simulation test was additionally produced, and the user satisfaction level of the application of this developed system for the visually impaired was investigated. As a result of the user satisfaction survey, it was confirmed that the user satisfaction improved significantly compared to before the application of this developed system. In addition, with just the app for the simulation test the visually impaired people who participated in the simulation test could check the station and the route to destination before going out in advance and experience the route to the station they wanted to go, so it was possible to confirm the utility of the technology proposed in this chapter, such as many opinions were suggested that it can be usefully used. Moreover, if the improvement of the voice recognition rate specialized for the relevant indoor area, such as a railway station, is supplemented, it is expected that it will be possible to dramatically improve the mobility support of the visually impaired and user satisfaction through the minimum hardware installation in the indoor area and software technology.

## **Author details**

Jong-Gyu Hwang<sup>1\*</sup>, Tae-Ki An<sup>1</sup>, Kyeong-Hee Kim<sup>1</sup> and Chung-Gi Yu<sup>2</sup>

1 Korea Railroad Research Institute, Uiwang, Korea

2 Bluemobile Co., Ltd., Seoul, Korea

\*Address all correspondence to: [jghwang@krri.re.kr](mailto:jghwang@krri.re.kr)

## **IntechOpen**

---

© 2022 The Author(s). Licensee IntechOpen. This chapter is distributed under the terms of the Creative Commons Attribution License (<http://creativecommons.org/licenses/by/3.0>), which permits unrestricted use, distribution, and reproduction in any medium, provided the original work is properly cited. 

## References

- [1] Ministry of Land, Infrastructure and Transport, In year 2017 – A Study on the Actual Condition of Movement of the Traffic Handicapped. 2018. (in Korean)
- [2] Jung SB, Lee SO. A regression analysis study on customer satisfaction considering the mediation effect of safety of operation – Focusing on Subway line 9. *Journal of the Korean Society for Railway*. 2017;**20**(6):853-865. DOI: 10.7782/JKSR.17.6.853
- [3] Kim HC. Customer satisfaction analysis for urban railway service quality by IPA analysis. *Journal of the Korean Society for Railway*. 2015;**18**(5):502-511. DOI: 10.7782/JKSR.18.5.502
- [4] Jeong EB, Yu SY. Assessment of route guidance for mobility-handicapped passengers in railway stations based on user satisfaction survey. *Journal of Korean Society of Transportation*. 2020;**38**(4):309-323. DOI: 10.7470/jkst.2020.38.4.309
- [5] Kim HH. Study on the Usability Testing of User Interface Design Using NASA-LX [Thesis]. Korea: Korea Tech University; 2003
- [6] Ge T. Indoor Positioning System Based on BLE for Blind or Visually Impaired [Thesis]. Stockholm, Sweden: KTH Royal Institute of Technology; 2015
- [7] KRRI Research Report. Development in Interactive Route Guidance and Supporting System Technology for Mobility Handicapped in Railway Station. Korea: Korea Railroad Research Institute; 2021
- [8] Yu JW et al. Identification of vacant and emerging Technologies in Smart Mobility through the STM-based patent map development. Sustainability in MDPI. 2020;**12**:1-12. DOI: 10.3390/su14010476
- [9] Sgoval S, Ulrich I, Borenstein J. NavBelt and the guide-cane [obstacle-avoidance systems for the blind and visually impaired]. *IEEE Robotics & Automation Magazine*. 2003;**10**(1):9-20. DOI: 10.1109/MRA.2003.1191706
- [10] Rahman MA et al. Design and development of navigation guide for visually impaired people. In: *Proceeding of IEEE International Conference on Biomedical Engineering, Computer and Information Technology for Health*. IEEE; 2019. pp. 28-30. DOI: 10.1109/BECITHCON48839.2019.9063201
- [11] Okamoto T, Shimono T, Tsuboi Y, et al. Braille Block Recognition Using Convolutional Neural Network and Guide for Visually Impaired People. In: *Proceedings of IEEE 29th International Symposium on Industrial Electronics (ISIE)*. 2020. DOI: 10.1109/ISIE45063.2020.9152576
- [12] Kasthuri R, Nivetha B, et al. Smart device for visually impaired people. In: *Proceedings of International Conference on Science Technology Engineering & Management (ICONSTEM)*. IEEE; 2017. DOI: 10.1109/ICONSTEM.2017.8261257
- [13] Hwang JG et al. Design of Supporting System to improve the mobility handicapped satisfaction in Railway Station. *The Trans. of the KIEE*. 2019;**68P**(1):17-24. DOI: 10.5370/KIEEP.2019.68.1.017
- [14] Biconix, Gangnam Stick for The Blinded [Internet]. 2017. Available from: [http://play.google.com/store/apps/details?id=jh.com.beaconyx.gangnamsticks&hl=es\\_419](http://play.google.com/store/apps/details?id=jh.com.beaconyx.gangnamsticks&hl=es_419) [Accessed: December 20, 2020]

- [15] iSONIC [Internet]. 2010. Available from: <http://www.primpo.com/kr/index.html> [Accessed: May 2, 2022]
- [16] Al Zayer M et al. Exploring the use of a drone to guide blind runner. In: Proceedings of the 18th International ACM SIGACCESS Conference on Computers and Accessibility. ACM; 2016. pp. 263-264. DOI: 10.1145/2982142.2982204
- [17] Google's Hear Here Project [Internet]. 2016. Available from: <https://folio.openknowl.com/project/7950> [Accessed: May 2, 2022]
- [18] Aipoly. Vision through artificial intelligence [Internet]. 2016. Available from: <http://aipoly.com/> [Accessed: January, 4 2022]
- [19] Microsoft. Seeing AI [Internet]. 2017. Available from: <https://www.microsoft.com/en-us/ai/seeing-ai> [Accessed: January 4, 2022]
- [20] Google. Lookout [Internet]. 2018. Available from: <https://korea.googleblog.com/2018/05/lookout.html> [Accessed: January 4, 2022]
- [21] Be My Eyes [Internet]. 2015. Available from: <https://www.bemyeyes.com/> [Accessed: January 4, 2022]
- [22] Right-Hear [Internet]. 2015. Available from: <https://right-hear.com/> [Accessed: January 4, 2022]
- [23] Blind Pad [Internet]. 2017. Available from: <https://www.blindpad.eu/> [Accessed: January 4, 2022]
- [24] Soundplex [Internet]. 2018. Available from: <http://soundplex.co.kr/> [Accessed: January 4, 2022]
- [25] Beaconyx. Gangnam Stick. 2017. Available from: [https://play.google.com/store/apps/details?id=jh.com.beaconyx.gangnamsticks&hl=es\\_419](https://play.google.com/store/apps/details?id=jh.com.beaconyx.gangnamsticks&hl=es_419) [Accessed: January 4, 2022]
- [26] Elmannai W, Elleithy K. Sensor-based assistive devices for visually-impaired people - current status, challenges and future directions. *Sensors in MDPI*. 2017;17(3):565-573. DOI: 10.3390/s1730565
- [27] Smart Transportation Market-Global Industry Analysis, Size, Share, Growth, Trends and Forecast 2015-2021. Transparency Market Research. US: Markets and Markets; 2015
- [28] Visual Networking Index: Global Mobile Data Traffic Forecast Update 2016-2021. US: Cisco; 2017

# Intersection Management, Cybersecurity, and Local Government: ITS Applications, Critical Issues, and Regulatory Schemes

*Yunfei Hou, Kimberly Collins and Montgomery Van Wart*

## Abstract

This article focuses on the cybersecurity issues of intersection management—an element of transportation management systems—for local governments. Until relatively recently, concerns about and research needs for intersection cybersecurity have been largely ignored, and local governments have focused on other types of cyber threats, relying instead on private sector vendors to provide equipment that is safe against attacks. To address the gap in the literature, this article provides a short overview of the types of components used in intelligent transportation systems (ITS) and reviews the critical issues for local governments. Further, it discusses some current efforts to remediate the vulnerabilities in ITS and examines the current regulatory framework. This review of the issues is augmented by an analysis of local government perspectives using the Delphi method. The article concludes with some recommendations.

**Keywords:** transportation cybersecurity, transportation management systems, intelligent transportation systems, local government, intersection management

## 1. Introduction

As the transportation systems of the US grew and became more complicated to manage, intelligent management systems were used to more effectively and efficiently manage traffic. However, Intelligent transportation systems (ITS) technologies and applications have brought enormous opportunities and challenges. ITS deployment appears to have the most broad-based benefit in the area of improved mobility (ITS-JPO 2015–2019) [1], and in terms of opportunities and a sub-function of Smart Cities, intelligent systems are already providing advantages related to:

- Efficient timing/coordination of lights based on sensors, remote traffic monitoring and control,

- Traffic management based on road sensors, CCTV, satellites, cameras, metering, and electronic toll collections,
- Transit signal priority, and
- Traveler information systems (TIS).

Still, even while making the most of the technologies that already exist and integrating those advancements into vehicles and infrastructure where possible, the challenges of ITS technologies and their security implications are also enormous. A failure to identify significant vulnerabilities, and properly address them can leave a municipality at the mercy of a state actor or a misguided teen alike.

This article will present the challenges introduced by cyberspace and ITS. It will review cybersecurity incidents that have impacted local governments in the remaining of Section 1. It will provide an overview of ITS management and critical issues in Section 2 and 3 respectively. Then in Section 4 and 5, the results of a small but multi-perspective study of local government experiences and perceptions about local government cybersecurity issues and ITS are reported. The article ends with practical and research recommendations in Section 6, and Section 7 concludes this paper.

### **1.1 The challenges of cyberspace and ITS**

Cyberspace is a unique environment that easily and readily allows governments, criminals, terrorists, and even mischievous juveniles to mask their identity while they wreak havoc or disable a system [2]. Right now, the average breach in America takes around 5 months to discover [3, 4]. Public agencies historically relied on “security through obscurity” to avoid attack or exploitation, knowing that a system may be vulnerable, but relying on the thought that a system’s weaknesses were not common knowledge and persons with malicious intent were unlikely to find them [5]. This approach worked relatively well prior to the digital revolution, but from the late 1990s on, agencies have switched to extremely common commercial technologies such as Wi-Fi and Ethernet for field devices (traffic signals, sensors, dynamic messaging signs, etc.) that communicate with central monitoring systems. This resulted in a significant increase in the attack surface of ITS and thus a significant increase in the risk to ITS.

Cybersecurity threats present themselves in a variety of ways. They may be:

- External or internal attacks (bad actor(s) outside or inside the system)
- Software attacks (both immediate and ongoing or evasive by design)
- Physical manipulation (intentional and/or unintentional exploitation of hardware)
- Single acts or a combination of discrete steps threaded together [2]

The technologies that were once obscure and expensive are now readily available and low cost. As such, it has essentially eliminated any value from reliance on security through obscurity. The safe and efficient operation of a traffic management system relies largely on the application of advanced technologies [6]. And while new technologies have greatly enhanced how traffic signals work and efficiently operate, these

technologies have also increased the exposure to numerous cybersecurity threats [7]. Of specific interest here are the cybersecurity threats posed by various types of connectivity, not only external, but also from “credible” sources [8, 9]. Although these threats can extend in severity all the way to the level of terrorism, some of those primary threats include:

- Denial of Service, such as jamming Wi-Fi signals or blocking access to authorized users [10, 11].
- Traffic congestion, such as wrongly rerouting/timing vehicles
- Individual/multiple traffic signal control, such as changing all lights green [12].
- Autonomous/connected vehicle manipulation, such as seizing command of a vehicle’s braking system [13].
- Spear phishing, such as targeted online attempts to steal sensitive information, either directly from a credible actor/employee or from the system itself [14, 15].
- Privacy issues, such as bad actors tracking specific vehicles via different sensors in different positions [7].
- These issues are not just theoretical. There have been major incidents that have taken place in recent years throughout the United States. Local governments can be particularly vulnerable as they lack the resources both human and financial to prepare themselves against possible threats. The following section will present three short cases of cyber incidents in local governments.

## **1.2 Local government cybersecurity incidents**

Local governments have been shown to be susceptible to cyberattacks. According to a 2016 report [16], 44% percent of local governments said they experience cyberattacks at least daily. It is believed that the actual rate of cyberattacks is much higher, since less than 60.1% of local governments actually catalog or count how often their systems are attacked. The magnitude of cybersecurity incidents ranges from mischievous attacks (e.g., road signs manipulation) to attacks that interrupt the daily activities of governments (e.g., infected servers that interrupt activities). The following provides a famous example of hacking into the city of Atlanta, followed by some examples of agencies affected by hacking incidents in of ITS in Southern California.

### *1.2.1 The City of Atlanta*

Perhaps the most devastating known cyberattack in the United States against a government agency occurred against the city of Atlanta in March of 2018 [17, 18]. Atlanta was hit by a variation of ransomware called “SamSam” [19, 20]. The perpetrators of this attack are still at-large and unknown.

The city of Atlanta suffered major inconveniences as a result of the SamSam ransomware cyberattack. The security issues in the system had ironically been pointed out 2 months before the attack in January 2018 by the Atlanta City Auditor’s Information Security Management System Pre-Certification Audit. The most crucial

concerns noted in the audit report revolved around the disregard of establishing IT security control procedures [21]. The main issues listed included the lack of creating and maintaining Information Security Management System (ISMS) formal policies and procedures; lack of creating a comprehensive annual plan to aid in the meeting of security goals and compliance; and the lack of available staffing that “impact their ability to stay ahead of the security issues, such as migration of obsolete operating systems, patch management, and vulnerability management” ([21], p. 16). On March 22, 2018, the vulnerabilities were exploited by the SamSam ransomware, even though the city had been forewarned.

In June 2018, almost 3 months after the attack, it was reported that the city was still struggling to recover [22]. Over one-third of 424 software programs used by the city remain unusable or partly unusable. The ransomware attack took down crucial city systems that aid the city in managing police records, infrastructure maintenance requests, and revenue collection.

The ransom demanded by the SamSam hackers was a total of \$51,000 in Bitcoin. Atlanta reportedly did not pay the ransom, but the initial cost of restoring the city’s computer network amounted to \$2.7 million dollars [23]. In a recent budgetary meeting, the interim CIO requested an increase of \$9.5 million dollars to the \$35 million already allocated to the IT department. The extra budget allocation would serve to continue the city’s efforts of restoring the city’s computer network [24]. Overall, the SamSam ransomware cyberattack had significant impacts on the City of Atlanta’s computer network, showing local government agencies the importance in keeping their systems up-to-date.

### *1.2.2 California department of transportation*

One documented prominent instance of hacking in the study area caused an episode of public concern. In December 2015, an unknown person hacked into a California Department of Transportation (Caltrans) digital road sign in the City of Corona along the 15 freeway, a major arterial highway. The sign was hacked to display a political message endorsing the then-presidential candidate for office, current U.S. President Donald Trump. The sign displayed the message “The Inland Empire Supports Donald Trump, Merry Xmas”. The hacker was able to gain physical access to the road signal, hack the system, and obtain the security passcode to change the road sign message.

In a local news segment regarding the event, an official for the Riverside County Transportation Commission, explained that this hacking incident, although seemingly benign, is very much a public nuisance because it interferes with relaying drivers with vital information about transportation construction projects and delays that could be occurring [25]. Furthermore, the hacking of public signs by vandals is both a distraction to drivers and unsettling to public confidence. While a seeming minor nuisance, this type of act can create dangerous or even life-threatening situations. For example, signs can be used to redirect traffic to hazardous areas. They can also be used as part of complex coordinated attack, where creating traffic jams will slow or block responding vehicles.

### *1.2.3 Orange County transportation authority*

In another incident in the study region, the Orange County Transportation Authority (OCTA) had a bout with ransomware in February 2016. The attack, carried

out by unknown hackers, affected around 88 of OCTA's 400 servers. The ransomware affected approximately 20 internal applications that controlled payroll, email, etc. Fortunately, transportation systems were not affected [26].

The hackers demanded \$8500 dollars, but OCTA chose to ignore the ransom demand and had internal staff and contractors bring the system back to normal. It took approximately two and a half days to restore the system servers. The total cost of the ransomware attack was around \$660,000—approximately \$330,000 went to internal labor costs and contractors, and \$218,000 was paid to Microsoft and another contractor to eliminate any remaining malicious code, and to help them devise a plan to prevent another attack [27].

## 2. Overview of ITS applications at signalized intersections

In this section, an overview of ITS components and applications at signalized intersections is discussed. This overview will provide the needed foundation for understanding the major components of ITS to better appreciate the cybersecurity issues discussed in a later section.

### 2.1 Components in traffic signal systems

The modern traffic intersection consists of various sensors, controllers, malfunction management units, and communication devices. **Figure 1** illustrates some common devices found at intersections.

Sensors employing ultrasonic, microwave, and radar technology, as well as induction loops and video cameras are all used to detect traffic conditions at intersections. The induction loop is the most popular sensor for vehicle detection. These devices are buried under the pavement and detect vehicles by measuring a change in electric current due to the metal body of a vehicle. Video cameras are also frequently used at intersections, and rely on computer vision software to detect and classify vehicles. It is worth noting that video traffic detectors are usually stationary. Additionally, cameras are installed to provide live and steerable video feed to traffic management centers. Microwave, radar, and ultrasonic sensors are less common, but can be used for special applications. Aside from detecting fine-grained vehicle presence, Bluetooth/Wi-Fi traffic detectors are sometime installed at intersections to track vehicle travel time and speed. These sensors detect and time-stamp a Bluetooth/Wi-Fi MAC address from smartphones and in-vehicle hands-free audio, then use the time-stamps of subsequent detections of that address to determine vehicle travel time across known distances between sensors.

Controllers are responsible for setting light timing patterns at intersections. Sensors are directly connected to the controller, allowing it to adaptively adjust signal timings based on traffic conditions. Traffic signal controllers can operate in several modes: 1) pre-timed, e.g., signal states change with predetermined intervals; 2) actuated, e.g., one or more directions are green, based on sensor input; 3) coordinated, e.g., controllers of nearby intersections can be interconnected to share timing information and react to sensor input. Traffic signal controllers are typically locked in a metal cabinet by the side of the traffic signal's pole.

Networking equipment for traffic signals may include both hard-wired and wireless systems. In urban areas, traffic controllers are usually hard-wired through optical or cable networks. Traffic controllers may communicate with each other and with

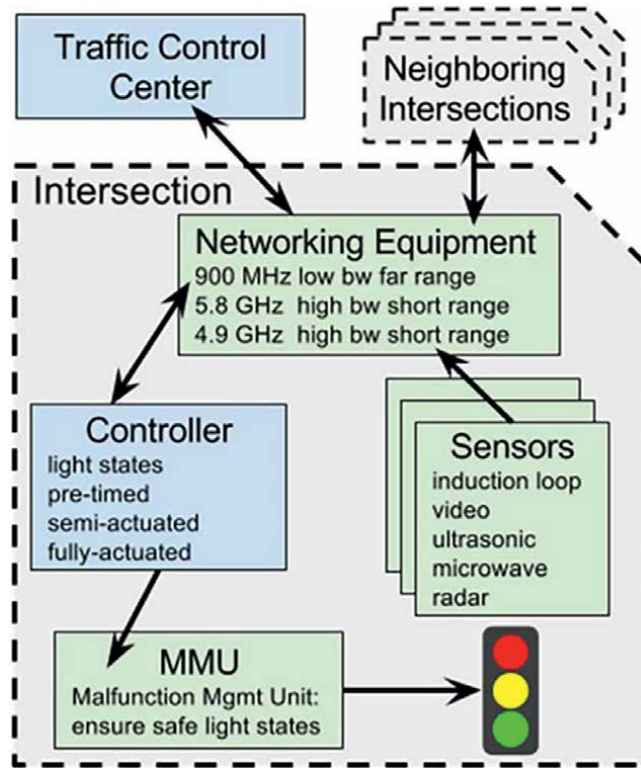


**Figure 1.**  
Main components of a traffic signal system [28].

traffic management centers. When intersections are geographically distant, wireless systems are frequently used. According to FCC regulations, these wireless systems operate on the ISM band at 900 MHz or 5.8 GHz, or in the 4.9 GHz band allocated for public safety. Communication between sensors has traditionally been connected to the traffic controller through a direct line. If wireless sensors are used, an intersection may be equipped with access points and repeaters to process, store, and relay data. Wireless systems for traffic signal controllers and sensors usually run on proprietary protocols derived from IEEE 802.11 or IEEE 802.15 standards.

Malfunction Management Units (MMU), also known as conflict monitor units (CMU), are hardware-level fail-safe mechanisms. The MMU monitors the outputs of the controller, and if a fault is detected (e.g., green signaling in all directions, or too short of a red light duration), the MMU overrides the controller and forces it to switch the intersection to a known-safe configuration (e.g., red lights flashing for all directions). While MMU prevents displaying a potentially hazardous combination of signals, its safe configurations are pre-defined and thus suboptimal. If the MMU detects a fault state, it requires manual intervention to reset.

Traffic Control Center, also known as traffic management center (TMC) or traffic operations center, is the facility that monitor and control transportation-related information, and coordinate responses to traffic incidents. Traditional traffic control center uses closed-loop network equipment (such as video camera and vehicle counters) to monitor traffic condition and coordinate construction activity, roadway advisories, incident management etc. As traffic control centers are moving toward

providing intermodal, interregional and interagency traffic management services, their increasing complexity leads to increases in vulnerability of cyber-attacks.

## **2.2 Technologies for signalized intersections**

While the traffic management infrastructure was traditionally built on closed, proprietary systems, the industry is currently on a journey to switch to more connected, responsive and secured networking. Virtually all aspects of a transportation management system are susceptible to cyber threats [2]. Nevertheless, the change to a connected system must happen due to increasing traffic demands, maintenance costs, and the complexity of legacy systems. On the other hand, consumers are demanding new transportation solutions that can provide safer, more efficient, and sustainable travel options. To this end, a wide range of transportation technologies have been proposed. What follows is a brief review some of the most important general applications.

**ATMS/Central System:** Advanced traffic management systems (ATMS) consist of transportation management centers, field infrastructure, and mobile units communicating in real time to monitor and manage transportation systems. Real-time traffic data from cameras, speed sensors, etc. are sent into a central system where it is integrated and processed (e.g., for incident detection), and may result in actions taken at traffic infrastructures (e.g., change of signal timing, roadside messages). ATMS are the command centers for reducing congestion, enhancing safety, and providing faster emergency response times. The main functions of an ATMS are: signal performance measurement, system assessment (collecting data), strategy determination, strategy execution, and strategy evaluation.

**Dynamic Message Signs:** Dynamic Message Signs, also known as Variable Message Signs, are the large, electronic signs which overhang or appear along roadways. The signs are typically used to display information about traffic conditions, travel times, construction, and road incidents.

**Adaptive and Coordinated Signal Control:** Adaptive signal control refers to technologies that capture current traffic demand data using sensors such as induction loops, and adjust traffic signal timing to optimize traffic flow accordingly. Coordinated traffic signal systems attempt to further improve efficiency by creating a green wave along multiple intersections (e.g., a long string of green lights) (e.g., progression) for drivers. The objective of adaptive and coordinated signal control is to provide effective signal timing settings within a range of operating conditions. It works by collecting current demand information from sensors (e.g., advance detection), evaluating performance using system specific algorithms at a central controller, and then implementing modifications based on the outcome of that evaluation via a communication network.

**Transit Signal Priority and Emergency Vehicle Priority:** Transit signal priority (TSP) is a set of operational improvements that modifies signal timing to favor transit vehicles (e.g., busses). TSP reduces dwell time for transit vehicles by holding green lights longer or shortening red lights. TSP systems require four components: a detection system aboard the transit vehicle; a priority request generator which can be aboard the vehicle or at a centralized management location; a strategy for prioritizing requests; and an overall TSP management system. Emergency Vehicle Priority (EVP, also known as signal preemption) is a similar application designed for special events such as a responding fire engine or police car. EVP and TSP applications can be built on a similar infrastructure, with the major difference being that signal preemption interrupts the normal signal operation rather than adjusting current signal timing.

**Eco-Signal:** The basic premise of the Eco-Signal concept is that if a driver has accurate information about the upcoming signal status, the vehicle speed can be adjusted accordingly to avoid stops and vehicle operation associated with increased fuel consumption (e.g., hard acceleration maneuvers). Eco-Signal application requires Signal Phase & Timing (SPaT) information from traffic controllers, which is a standard function of connected vehicle-ready traffic controllers (SAE J2735 standards). Several companies are working on commercializing such applications. They solicit traffic signal timing information from local agencies and offer a share of their revenue.

**V2V/V2I Communication:** V2V and V2I communication are the enabling technologies of Intelligent Transportation Systems. Vehicle to vehicle (V2V) communication is the ability to wirelessly exchange information such as speed and position between vehicles. This allows vehicles to broadcast and receive directional messages creating a net of “awareness” of other vehicles in proximity. Vehicle to infrastructure (V2I) communication is the ability to wirelessly exchange information with a structure such as a traffic signal. This can be used to gather information on traffic and road conditions. There are two mainstream technologies used in V2V/V2I communication: 1) cellular networks, such as 5G and 4G LTE, and 2) Dedicated Short Range Communication (DSRC). Cellular networks relies on cellular infrastructure along the road, while DSRC only connects vehicles in their vicinities and works in an ad-hoc manner.

**Bluetooth/Wi-Fi Traffic Probe:** As mentioned in Section 2.1, a basic Wi-Fi/Bluetooth sensor system for traffic monitoring consists of a Wi-Fi/Bluetooth probe device that scans for other Wi-Fi/Bluetooth-enabled devices in its radio proximity (usually within 90 feet), and then stores the data for future analysis and use. These applications may include measurements of traffic presence, density, and flow, as well as longitudinal and comparative traffic analysis.

**Third Party Traffic Data:** The rise of smartphone and in-vehicle apps allow large-scale vehicle probe data to be collected in real-time. Third party traffic data collected by companies such as Waze and INRIX can be used to improve traffic management.

Public agencies traditionally use third party data in an aggregated fashion such as origin-destination analysis, operation monitoring, and performance measurement. In recent years, there is a growing interest to integrate third party traffic information into Advanced Traffic Management Systems (ATMS) for real-time signal timing adjustments.

### **3. Critical issues related to the cybersecurity of intersection management**

As the components and technologies of intersection management have evolved to address the needs of a growing municipalities and transportation systems, new problems have been created. By having various elements of ITS connected via wireless and wired networks, threats of a cybersecurity nature are now a higher risk. This section will discuss the critical cybersecurity issues related to intersection management, and provides an overview of the current regulatory framework in California, USA.

Transportation systems include many modes: air, ships, and a variety of ground modes. In addition to roads, ground modes include trains, inland waterways, subways, bike ways, pedestrian travel, etc. Here we only focus on intersection management and upcoming Connected Automated Vehicles (CAV) issues. However, it should be noted that many reports focus on “critical” transportation systems. Such systems are generally thought to be air and train systems; while intersection management and TMS generally are considered significant, they are not as critical in terms of the

immediate, catastrophic consequences of cyber vulnerabilities. However, the field of TMS has become aware of: (1) the issues of cybersecurity related to intersection management, (2) the fact that vulnerabilities are extensive, (3) the increasing importance of cyber issues because of CAV and public information/service expectations, (4) the perception that public sector traffic experts do not have consistently adequate training and staff to deal with cyber issues, and (5) the fact that industry vendors have not been reliable partners in cybersecurity.

### 3.1 The magnitude

From an historical perspective, the number of reported attacks and incidents is still very small and non-catastrophic, despite the series of Hollywood movie portrayals of hijacked intersection management systems to the contrary. However, in 2014, cybersecurity expert Cesar Cerrudo presented the results of extensive white-hat hacking of Sensys intersection management systems at the DefCon 22 conference. An extensive YouTube video of that presentation has been watched over 15,000 times. He not only showed how the system he hacked was vulnerable to manipulation, ransom, and potential denial-of-service, but also showed that even the simplest security measures had not been taken in the primary field test site (Washington, DC) [29], and that the vendor was misleading about the level of security provided, and initially unresponsive about cybersecurity issues as not “their” problem. Cerrudo also pointed out that most deficient sensor systems could not be retrofitted, and would need to be completely replaced when more rigorous cybersecurity standards were implemented. He estimated the then-current replacement cost of the legacy sensors at \$100,000,000. Cerrudo’s presentation was highly reported on and put the industry on notice. It is hoped that improvements will be made by vendors to provide better cyber safeguards (such as simple encryption), and greater transparency [30]. While improvements in the industry are likely, the private sector also must improve. One cybersecurity expert reported that of the 250 traffic control systems he was able to discover on the internet, 49 had open devices because the username and password were disabled [31].

These are not one-off anomalies. There are numerous challenges to intersection management. While the following list is not comprehensive, it will sketch out the magnitude of the problem.

- The various devices used in intersection management frequently have low levels of cybersecurity built into them, and some legacy devices are essentially devoid of security.
- The industry has been slow to respond and be proactive in providing security controls that anticipate the next phase of black-hat hacking.
- Cyber threats to TMS systems are not only introduced by way of individual devices, but also through the amalgamations of various devices and systems that provide nexus-point vulnerabilities.
- Federal guidance on cybersecurity has tended to be generic to date. Cybersecurity testing results of devices in the form of qualified traffic control equipment lists normally comes from state agencies. It is unclear how in-depth their testing is, especially related to program error detection that can lead to

vulnerabilities. Qualified product lists, generally adopted by local governments from the state level, do not provide any information or guidance other than statements that they have been found to be acceptable on a variety of engineering factors, of which cybersecurity is only one.

- The public sector agencies who use intersection management the most are the smallest and most financially stretched. Municipalities have an enormous array of cyber threats and vulnerabilities, many of which they perceive as far more critical than traffic control systems.
- With a skills gap now estimated at 300,000 in the US [32, 33], smaller agencies (counties and municipalities) often cannot compete for top-notch cybersecurity experts because of an extremely tight market.
- Building cybersecurity awareness via training and quality control programs among TMS personnel is an aspect of the larger local government problem.

### 3.2 Assessing the risk: foreseeable attack scenarios

We conducted a literature review on cybersecurity vulnerabilities of traffic signal systems in recent years, and a high-level of summary is presented in **Table 1**. We then considered various types of attacks that could exploit those vulnerabilities and the consequences that could result. What follows is a description of several foreseeable attack scenarios and the damage that could be done.

- a. Controller attacks represent attacks that target at the light controller. An attacker may attempt to gain privileged access to the controllers. On a successful intrusion, lights could be changed to be green along the route the attacker is driving. An attacker may also initiate various denial of service (DoS) attacks on the traffic light system, causing the intersection to enter an undesired and potentially dangerous state. Alternatively, an attacker could trigger the MMU to take over, which will cause the lights to enter a safe but suboptimal state (e.g., flashing

Classification	Attack techniques	Consequences/use cases
Cyberattack on traffic controller [34, 35]	password cracking, social engineering to acquire device	control traffic signal, send commands to the controller
Cyberattack by sniffing [29, 30]	sniffing sensor identification information, commands, etc.	send falsifying commands and data, manipulation of devices
Cyberattack on traffic sensor [35, 36]	wireless sensors spoofing	destabilize the traffic network
Physical attack on traffic controller [35]	Sabotaging physical networking components	affect performance, availability of devices or services
Cyberattack on traffic controller [37]	denial-of-service attack	take down the network to which the traffic signal is connected
Cyberattack on traffic sensor [38]	data spoofing, masquerade as connected vehicles to send data	influence the signal control algorithms by sending invalid data

**Table 1.**  
*Cybersecurity vulnerabilities in traffic signal systems.*

all-red). Since MMU can only be reset with physical access to the controller while an attack can be triggered remotely, an adversary can disable traffic signals faster than technicians can be sent to repair them.

- b. Sensor data attacks are assaults on the sensor data being communicated to the controller. A malicious party can send bogus packets to the access point, thus leading the traffic controller to operate with misinformed traffic information. For example, in a spoofing attack, an attacker can trick the loop detector by pretending to be multiple vehicles going through a road segment. Additionally, sensors used in traffic signal systems may be susceptible to firmware modification; an attacker can modify the firmware with corrupted data which will cause the sensor to no longer function (also known as “bricking” a device).
- c. Physical attacks that directly tamper with the hardware such as vandalism and graffiti are common problems with public infrastructure, and traffic signal systems are designed with resiliency to handle such physical system issues. However, coordinated attacks performed through a combination of cyber and physical attacks present a significant threat to the systems. For instance, if the MMU (a hardware fail-safe device) is damaged or removed, a coordinated cyberattack can trigger dangerous light timing patterns, leading to potential massive damage and/or traffic disruption.

### **3.3 Efforts to address the issues**

While the challenges are numerous, there have been two ongoing efforts to address the TMS cybersecurity weaknesses worthy of mention. A state-funded initiative in Florida at the National Center for Transit Research is called Enhancing Cybersecurity in Public Transportation [14]. That initiative is to: identify and mitigate transit cybersecurity liabilities, and facilitate ongoing cybersecurity information exchange among Florida transit agencies, their vendors, and cybersecurity researchers. A second ongoing effort is being spearheaded by the Southwest Research Institute, funded by the National Cooperative Highway Research Program for approximately \$750,000 [39] and due to be completed 8/15/2019. The description of the project is to develop guidance for state and local transportation agencies on mitigating the risks from cyber-attacks on the field side of traffic management systems (including traffic signal systems, intelligent transportation systems, vehicle-to-infrastructure systems (V2I), and closed-circuit television systems) and, secondarily, on informing the agency’s response to an attack. The guidance will address the vulnerability of field devices (e.g., traffic signal controllers and cabinets, dynamic message signs, V2I roadside units, weigh-in-motion systems, road-weather information systems, remote processing and sensing units, and other IP-addressable devices), field communications networks, and field-to-center communications. It will not address vulnerabilities within a traffic management center, within center-to-center communications, or due to insider risk (accidental or intentional).

It is anticipated that the guidance will take the form of a web-based deliverable that uses a guided risk-based decision tree (similar to a capability maturity model) to identify the most relevant content for a user. The users will range from small, local agencies with limited risks and limited capabilities to those with substantial traffic management systems and more resources available to protect them. If a viable approach and host for the implementation and maintenance (including

updating content and addressing emerging technologies) of this type of product is not found, a traditional NCHRP document will be produced. NCHRP has begun discussions with the National Operations Center of Excellence as a possible host, but they should not be contacted by proposers regarding this effort (NCHRP 03-127). The most extensive and up-to-date listing of resources for TMS is the first draft of a Cybersecurity Literature Review and Efforts Report by Ramon and Zajac [40].

### 3.4 The current regulatory framework for intersection management

The dependence on and seamless integration of technology into everyday activities and operations has exposed the critical need to address cybersecurity [2]. The strategy at the national level has focused its regulatory schemes to aid cybersecurity by providing rules or guidance about security practices to be used by public agencies (based on ISO 27,001), and by providing legal standards or guidance about equipment to either/both vendors in terms of product standards, and public agencies in terms of qualified product lists (based on ISO 27002). This and more are captured in the National Institute of Standards and Technology, “*Framework for Improving Critical Infrastructure Cybersecurity (version 1.1)*” for the federal system (2018) [41].

To improve resilience to cyber-incidents and reduce cyber threats, at the federal level, rules have focused to date on consistent use of traffic control devices via the Manual on Uniform Traffic Control Devices (MUTCD) which is a part of 23 Code of Federal Regulations, Part 655, Subpart F [42]. While MUTCD rules are national in scope, they do not regulate cybersecurity standards at this point. Unlike some other highly critical areas of transportation such as the Cyber Air Act of 2016 in which cybersecurity standards were implemented via such agencies and government corporations as the National Institute of Standards and Technology and the Radio Technical Commission for Aeronautics, *cybersecurity of intersection management is not federally regulated*.

However, the federal government has provided general guidance about cybersecurity such as the Framework for Improving Critical Infrastructure Cybersecurity (2017), as have private organizations [43]. The federal guidance includes the Roadmap to Secure Control Systems in the Transportation Sector (2012), National Security Strategy for Transportation Security (2015), and the Federal Highway Administration Cybersecurity Program Handbook (2017).

Aligning with the DOT, DHS, and TSA, the American Public Transportation Association (APTA) has broadly identified four priorities for transportation agencies to consider, and at a minimum to address, regarding an agency’s information and communication technology (ICT) infrastructure [2]. The federal government is likely to issue some initial rules and guidance on connected and autonomous vehicles cybersecurity in the near future which will have an impact on TMS in the US and elsewhere.

States tend to have the best resources to provide qualified, preferred traffic control systems lists. In California (the location of the empirical in-depth study), that is the Caltrans Transportation Electrical Equipment Specification (TEES) report, last re-issued in 2009 [44], but with supplements (called Errata) in 2010, 2014, and 2018. California’s TEES guidance is used by many other states in the country, as well as local governments in California. Other than the brief mention of a password file (CA TEES, p. 46, 9.2.7.6.2), there had been no robust cybersecurity guidance in the 2014 revision (aka errata update). However, the recent errata report has included substantially enhanced cybersecurity specifications for equipment. The new standard promotes embedded cybersecurity systems and phase out customize-after-purchase approaches. Use of the TEES list by local government agencies is not mandated, but is frequently

voluntarily adopted. The state is taking an aggressive stand on cybersecurity in general at an enterprise level with a Security Operations Center in the CA Department of Technology's Office of Information Security. While this resource will likely bolster prevention of hacking of state agencies for private information and help prevent ransomware and denial-of-service attacks, it seems unlikely to have much effect in the near future on state or local intersection management issues. It should be noted that while most qualified equipment lists do not have an official regulatory status because they are dynamic, in practice they function like regulatory protocols at the time a contract is let.

Although city and county CIOs listed cybersecurity as their primary focus in 2017 [45], local governments do not seem to understand the scope of their problems, let alone have much in place beyond generic cybersecurity protocols, and few are equipped to stave off threats [4, 46]. Twenty-five years ago in the southwest US, a teenage computer whiz hacked into software that controlled city traffic signals. Since then, not much has changed [47]. Recent cyber-attacks (e.g., two LA traffic engineers were found guilty of intentionally creating massive delays by adjusting signal times [48], and reports (Cesar Cerrudo demonstrated how he accessed traffic-light systems in dozens of cities, and University of Michigan students conducted experiments that manipulated over 1000 lights in one city alone) have heightened cybersecurity concerns dramatically, making them the top priority according to some public officials perception surveys [47]. Striking shortages of IT and cybersecurity personnel have been widely reported [33]. Internal practices and policies with existing personnel create tremendous gaps in local government's cyber responses [4]. Further, local governments are cash-strapped and aren't easily convinced, for example, that they must manually update every signal controller to thwart vulnerabilities at intersections [10].

#### **4. Study of local government cybersecurity preparedness and concerns**

As a result of our review of the various issues described in previous sections, we chose to conduct a study of one local government region as a test case to see if what we were discovering was as prevalent as it seemed. We conducted a Delphi-expert type of study to investigate the status of local government cybersecurity preparedness and concerns. We collected 18 questionnaires from directors of public agency transportation systems, as well as conducted six Zoom interviews spanning 14 city/county transportation agencies in Riverside and San Bernardino Counties. We also interviewed two consulting companies in the area. A typical intersection management team in the study region consists of 2 to 4 traffic engineers and technicians who manage day-to-day operations for about 100 to 400 traffic signals. Regarding the traffic controller hardware, over 90% of surveyed intersections were found to be using McCain systems. The majority of them use McCain 170 series controllers. For new deployment and upgrade projects, McCain 170 models are usually replaced by the McCain 2070 series which supports McCain and third party application software (e.g., applications mentioned in Section 2.2), and meets ATC 5.2b standards.

#### **5. Study findings**

In this study we identified 3 significant findings, they were: 1) connected devices are named the top threats, 2) cities lack cybersecurity support, and 3) cities need to plan for future technology.

*Connected devices are named the top threats.* Among the 1157 traffic signals surveyed in this study (refer to **Figure 2**), 67.6% of them are connected (i.e., with signal coordination, remote traffic management capabilities), and about 10% support connected vehicle applications (which comes with newer models of traffic controllers such as the McCain 2070 series).

As transportation agencies build advanced and connected traffic signal infrastructure, they are becoming more aware of the potential threats to their systems. The majority of transportation professionals in this study agree that transportation cybersecurity is a priority for their organizations. In addition, 83% of transportation professionals said that connected devices and cloud infrastructure are among the most challenging risks to defend against attacks.

To meet demands for information access, traffic management teams recognize that data must be made available in real time. Controlling access to data, and making sure it's available to those who need it, is a key concern for system managers. They also recognize that this problem will continue to grow, as most agencies plan to replace closed, proprietary systems with connected and advanced systems. Although there is no incidence of transportation related cybersecurity breaches found in this survey, cybersecurity problems are a constant concern for local governments.

*Lack of cybersecurity support.* Experienced security personnel can help transportation professionals navigate through security challenges, but cybersecurity is lacking. All the transportation agencies participated in this survey rely on their agency's IT department for security tasks, and many agencies work with contractors to manage their network. Most of the transportation professionals in this survey said they are not aware if their agencies follow standardized information security practices or participate in a security standards body. Two out of the 11 cities have formal written security strategies. Transportation professionals recognize the impact of the dearth of expertise: 67% said they believe a lack of trained personnel is a major obstacle to adopting advanced security processes and technology.

As cybersecurity operations capabilities become more sophisticated and specific, transportation authorities need to be able to recruit, compensate, and retain the type of high-caliber talent necessary to protect critical infrastructure.

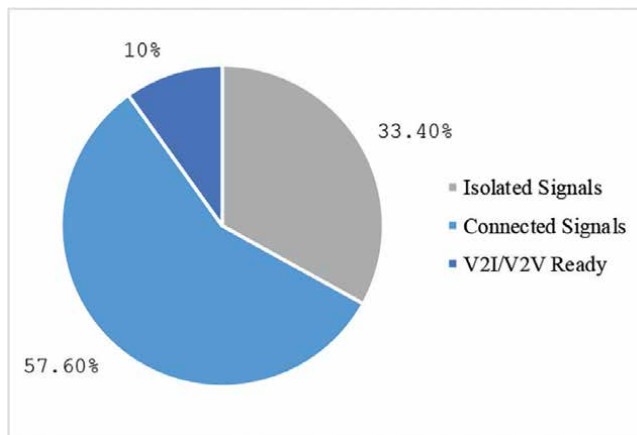


**Figure 2.**  
*Types of intersection controllers.*

*Need to plan for future technology.* The fact that transportation, like other critical infrastructure, requires new technologies to meet the ever-increasing demand may drive decisions about developing ITS applications. An overview of technologies surveyed in this study can be found in Section 2.2. Over half the cities have plans for Intelligent Transportation Systems or Traffic Signal Management. However, nearly 80% of the agencies said that they are underfunded for their transportation needs (**Figure 3**). At the city level, ATMS/Central system, Advance Detection, and Wireless

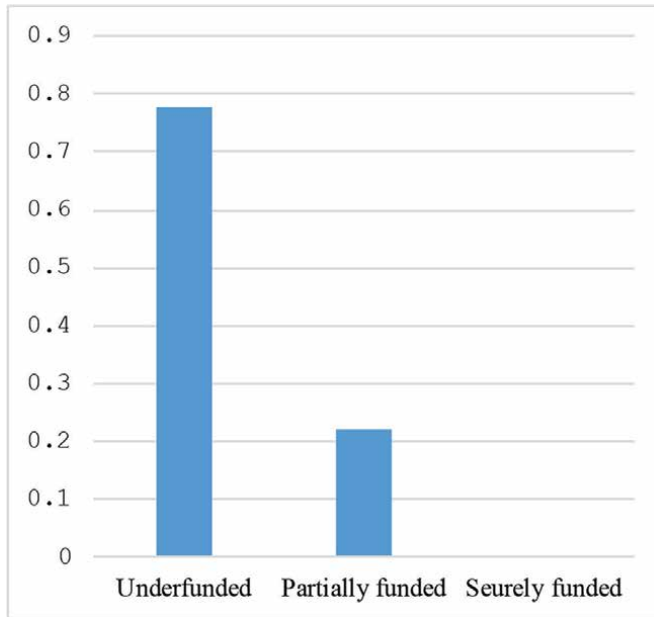


**Figure 3.**  
 Cities' funding status on transportation technology.

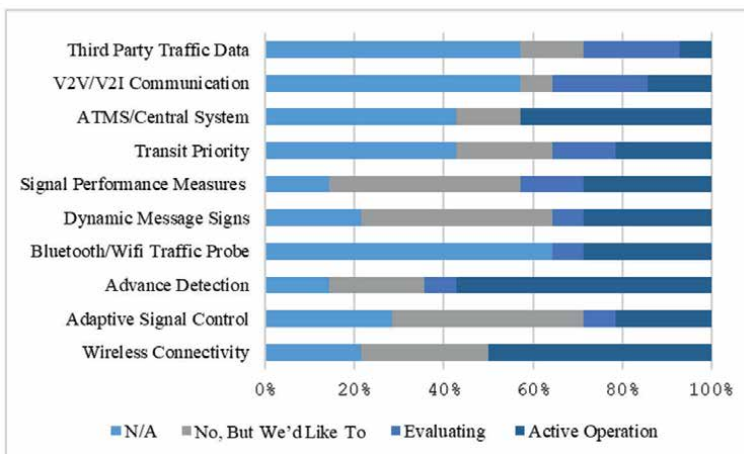


**Figure 4.**  
 Cities' plan for ITS applications.

Connectivity are listed as the top applications in active operation. As for future deployment, Signal Performance Measures, Dynamic Message Signs, and Adaptive Signal Control were noted as the technologies that cities would like to implement (refer to **Figure 4**). In order to move the implementation of these technologies forward, a number of actions need to be taken.

## **6. Recommendations**

While we have shown there to be numerous issues as it relates to cybersecurity and ITS, we provide several recommendations, each of which can go a long way toward improving the current state municipalities find themselves in.

- Cybersecurity audits and assessments

Perhaps the most important and the most immediate recommendation that can readily be implemented is to run comprehensive security audits and assessments. No organization wants or enjoys being audited. However, without conducting a structured, methodical audit, it will be difficult, if not impossible, to know just how serious the vulnerabilities are that a municipality is under. Audits may not need to be often. Just a baseline assessment and stock taking of what and where the issues are can go a long way toward making the ITS safer.

In the case of California and the hacking of the digital road signs, even a basic audit would have revealed the physical security and password issue that could easily been remedied. In the case of Atlanta, while they had an audit, they did not act on the findings of the audit. The reason for this, at least in part was due to funding.

This recommendation also supports each of the three findings from our study. Conducting an audit would help municipalities identify all of the connected devices and their associated risk which would be essential for making a case for supporting cybersecurity. The findings from an audit would be the basis for planning for what future technologies to implement.

- Funding

Throwing money at a problem usually will not solve it. However, not having enough money will almost certainly cause problems. If the TMS is understaffed and underfunded, then it is only a matter of time before more and likely graver events such as the one in Atlanta will take place. Likewise, continuing to operate on outdated equipment that lacks security and proper support presents significant risk. The bottom line is by not providing at least adequate funding for TMS is welcoming a catastrophe in the near future.

- Increase awareness

Knowing there is a problem is a major part of the battle. Many municipalities have many other pressing issues that require immediate attention. Limited resources and time make it unlikely that these local governments will discover on their own just how serious the problem can be. An informational website with

videos, research, and presentations materials should be made available. Local governments should have short presentations made to help them become aware and provide guidance on the steps to take to remediate current vulnerabilities and what to look for when implementing new systems in the future.

- Conferences with ITS security focus

As this paper has shown, there are so many aspects to cybersecurity and ITS that needs attention, that a conference would be a logical event address those issues. It could be a location that national experts can develop greater awareness of the vulnerabilities and threats local governments face, review ways to assess the risks they are under and give access to vendor demonstrations that can reduce exposure to threats. Provide mini-conference on transportation cybersecurity in the local regions to showcase local resources and to highlight local issues.

- More research is needed

The limitations of this study were its small scope and the focus on mid to small size jurisdictions. Additional review of large local governments would be highly useful. Also, the study region was dominated by a single provider; other areas with other providers may have different issues. Additional research opportunities exist to look at the coordination of technology risk assessments related to ITS; at an applied level, additional efforts to disseminate the information of risk assessments seems overdue.

## **7. Conclusion**

Cybersecurity issues are an ever-expanding part of the digital age, and intersection management is no exception. Hackers have shown themselves increasingly adept at infiltrating various systems, and intersection and sign management systems are likely to become prime targets if plans, devices, and protocols are not more highly protected. Currently, the prospects of having to retrofit some recently-acquired ITS systems are already looming because of complacent cyber concerns and insufficient design robustness.

From our regional study, we found evidence that indeed, many local governments are not prepared for cyber-attacks or have limited resources to prepare a comprehensive cybersecurity system. All too often, serious problems that exist go unnoticed, or ignored until it is too late. Let us hope that we do not wait for a catastrophic attack to occur before we do something about it.

## **Author details**

Yunfei Hou<sup>1\*</sup>, Kimberly Collins<sup>2</sup> and Montgomery Van Wart<sup>2</sup>

1 School of Computer Science and Engineering, California State University, San Bernardino, USA

2 Department of Public Administration, California State University, San Bernardino, USA

\*Address all correspondence to: hou@csusb.edu

## **IntechOpen**

---

© 2022 The Author(s). Licensee IntechOpen. This chapter is distributed under the terms of the Creative Commons Attribution License (<http://creativecommons.org/licenses/by/3.0>), which permits unrestricted use, distribution, and reproduction in any medium, provided the original work is properly cited. 

## References

- [1] Intelligent Transportation Systems Joint Program Office. ITS-JPO 2015-2019 ITS Strategic Plan, ITS Research Fact Sheets-Benefits of Intelligent Transportation Systems. ITS-JPO. Available from: [www.its.gov/communications/its\\_factsheets.htm](http://www.its.gov/communications/its_factsheets.htm)
- [2] American Public Transportation Program. APTA SS-ECS-RP-001-14, Cybersecurity Considerations for Public Transit. 2014. Available from: [www.apta.com/.../2014%20Q2%20Public%20Comment/RP\\_cyber\\_security\\_considera](http://www.apta.com/.../2014%20Q2%20Public%20Comment/RP_cyber_security_considera)
- [3] Ensey C. California Sets Cybersecurity Example for States to Follow. The Hill; 2016. Available from: [www.Thehill.com/blogs/.../289099-california-sets-cybersecurity-example-for-states-to-follo...](http://www.Thehill.com/blogs/.../289099-california-sets-cybersecurity-example-for-states-to-follo...)
- [4] Prall D. The Weakest Link in Your Cybersecurity Chain. American City and County; 2017. Available from: <https://www.americancityandcounty.com/2017/05/30/the-weakest-link-in-your-cybersecurity-chain/>
- [5] Fok E, Murphy R, Phomsavath K, Walker J. Taming cyber risks. Public Roads, Federal Highway Administration, FHWA-HRT-15-006. 2015;79(2). Available from: [www.fhwa.dot.gov/publications/publicroads/15sepoct/01.cfm](http://www.fhwa.dot.gov/publications/publicroads/15sepoct/01.cfm)
- [6] Nellore K, Hancke G. A Survey on urban traffic management system using wireless sensor networks. MDPI, Sensors. 2016;16(2):2016. Available from: [www.mdpi.com/1424-8220/16/2/157](http://www.mdpi.com/1424-8220/16/2/157)
- [7] Chandran D, Zhang Y, Cheng L-C. A survey on cybersecurity of traffic signal systems. In: The 30th Annual Conference of International Chinese Transportation Professionals Association; May 19-21, 2017; Houston, TX, USA. 2017. Available from: [www.uh.edu/technology/people/directory/\\_cv/zhang-yunpeng.pdf](http://www.uh.edu/technology/people/directory/_cv/zhang-yunpeng.pdf)
- [8] Gheyas I, Abdallah A. Detection and prediction of insider threats to cyber security: A systematic literature review and meta-analysis. Big Data Analytics. 2016;30:2016
- [9] Hill J. FBI: More Cyber Attacks Now Originate from Legitimate Credentials. Via Satellite; 2017. Available from: [www.satellitetoday.com/telecom/2017/11/08/fbi-cyber](http://www.satellitetoday.com/telecom/2017/11/08/fbi-cyber)
- [10] Pagliery J. Traffic Lights are Dangerously Easy to Hack. CNN Tech, The Cybercrime Economy; 2014. Available from: [www.money.cnn.com/2014/21/technology/security/traffic-lights-hack/](http://www.money.cnn.com/2014/21/technology/security/traffic-lights-hack/)
- [11] Rouse M. Denial-of-Service Attack. SearchSecurity.com; 2016. Available from: [www.searchsecurity.techtarget.com/contributor/Margaret-Rouse/2016](http://www.searchsecurity.techtarget.com/contributor/Margaret-Rouse/2016)
- [12] Schlack B. Cybersecurity issues in signal systems. In: Washtenaw County Road Commission Annual Meeting Presentation. 2015. Available from: [www.itscalifornia.org/contents/AnnualMeetings/2015/Presentations/TS7-2-WCRC-ATMSCyberSecurity.pdf](http://www.itscalifornia.org/contents/AnnualMeetings/2015/Presentations/TS7-2-WCRC-ATMSCyberSecurity.pdf)
- [13] Rockwell M. Traffic Cybersecurity Gets a Red Light. FCW, The Business of Federal Technology; 2014. Available from: [www.fcw.com/articles/2014/08/28/traffic-lights-cyber-risks.aspx](http://www.fcw.com/articles/2014/08/28/traffic-lights-cyber-risks.aspx)
- [14] Barbeau S, Ligatti J. Enhancing Cybersecurity in Public Transportation. National Center for Transit Research, Ongoing; 2017. Available from: [www.nctr.usf.edu/research/projectsopes](http://www.nctr.usf.edu/research/projectsopes)

- [15] Giandomenico N. What is spear-phishing? Defining and differentiating spear-phishing from phishing. *Digital Guardian*. 2016;27:2016. Available from: [www.digitalguardian.com/blog/wht-is-spear-phishing-defining](http://www.digitalguardian.com/blog/wht-is-spear-phishing-defining)
- [16] UMBC, University of Maryland, Baltimore County. Cybersecurity 2016 Survey. 2016. Available from: [https://icma.org/sites/default/files/309075\\_2016%20cybersecurity%20survey\\_summary%20report\\_final.pdf](https://icma.org/sites/default/files/309075_2016%20cybersecurity%20survey_summary%20report_final.pdf)
- [17] Blinder A, Perlroth N. A Cyberattack Hobbles Atlanta, and Security Experts Shudder. *The New York Times*; 2018. Available from: <https://www.nytimes.com/2018/03/27/us/cyberattack-atlanta-ransomware.html>
- [18] Kearney L. With Paper and Phones, Atlanta Struggles to Recover from Cyber Attack. *Reuters*; 2018. Available from: <https://www.reuters.com/article/us-usa-cyber-atlanta/with-paper-and-phones-atlanta-struggles-to-recover-from-cyber-attack-idUSKBN1H70R0>
- [19] Boyd C. Sam Sam Ransomware: What You Need to Know. *Malwarebytes Labs*; 2018. Available from: <https://blog.malwarebytes.com/cybercrime/2018/05/samsam-ransomware-need-know/>
- [20] Hay Lily N. The Ransomware That Hobbled Atlanta Will Strike Again. *Wired*; 2018. p. 2018. Available from: <https://www.wired.com/story/atlanta-ransomware-samsam-will-strike-again/>
- [21] City Auditor's Office City of Atlanta. Compliance Audit: ISO/IEC 27001 ISMS Precertification Audit. 2018. Available from: [http://www.atlaudit.org/uploads/3/9/5/8/39584481/2017\\_iso-iec\\_27001\\_isms\\_precertification\\_audit\\_-\\_january\\_2018.pdf](http://www.atlaudit.org/uploads/3/9/5/8/39584481/2017_iso-iec_27001_isms_precertification_audit_-_january_2018.pdf)
- [22] Hatmaker T. The Damage from Atlanta's huge Cyberattack is Even Worse than the City First Thought. *TechCrunch*; 2018. Available from: <https://techcrunch.com/2018/06/06/atlanta-cyberattack-atlanta-information-management/>
- [23] Deere S. Atlanta's network almost recovered from cyber attack, cost still unknown. *The Atlanta Journal-Constitution*. 2018. Available from: [https://www.ajc.com/news/local/atlanta-network-almost-recovered-from-cyber-attack-cost-still-unknown/k6srGim85Q8dKwUFPbcDhN/?icmp=np\\_inform\\_variation-test](https://www.ajc.com/news/local/atlanta-network-almost-recovered-from-cyber-attack-cost-still-unknown/k6srGim85Q8dKwUFPbcDhN/?icmp=np_inform_variation-test)
- [24] Freed B. Atlanta Ransomware Attack was Worse than Originally Thought. *StateScoop*. 2018. Available from: <https://statescoop.com/atlanta-ransomware-attack-was-worse-than-originally-thought>
- [25] McMillian R. Corona Caltrans Sign Displays 'Vote Donald Trump' Message. *ABC 7*; 2015. p. 2015. Available from: <http://abc7.com/news/corona-caltrans-sign-hacked-with-pro-trump-message/1137513/>
- [26] Graham J. Cyberattack Cost OCTA \$660,000 to Fix, Held Servers for Ransom. *Orange County Register*. 2016. Available from: <https://www.ocregister.com/2016/08/05/cyberattack-cost-octa-660000-to-fix-held-servers-for-ransom/>
- [27] Jessica K. OCTA Takes Steps to Avoid Repeat of Cyber Attack. *Orange County Register*; 2017. Available from: <https://www.ocregister.com/2017/01/24/octa-takes-steps-to-avoid-repeat-of-cyber-attack/>
- [28] Li Z, Jin D, Hannon C, Shahidehpour M, Wang J. Assessing and mitigating cybersecurity risks of traffic light systems in smart cities. *IET Cyber-Physical Systems: Theory & Applications*. 2016;1(1):60-69

- [29] Cerrudo C. Hacking Washington DC Traffic Control Systems. IOActive Blog; 2014. Available from: [www.ioactive.com/2014/07/hacking-washington-dc-traffic-control.html](http://www.ioactive.com/2014/07/hacking-washington-dc-traffic-control.html)
- [30] Cerrudo C. An Emerging US (and World) Threat: Cities Wide Open to Cyber Attacks. IOActive White Paper; 2015. Available from: [www.ioactive.com/pdfs/IOActive-HackingCitiesPaper\\_CesarCerrudopdf](http://www.ioactive.com/pdfs/IOActive-HackingCitiesPaper_CesarCerrudopdf)
- [31] Wolski C. Lost Control of Traffic Control Systems. 360 Degree Cyber Security; 2018. Available from: [www.360cybersec.com/category/cyber360-blog/](http://www.360cybersec.com/category/cyber360-blog/)
- [32] Hughes C. 3 Tips to Reduce Cybersecurity Gaps. CSO, Cybersecurity Insights; 2017. Available from: [www.csoonline.com/Databreach](http://www.csoonline.com/Databreach)
- [33] Moskites T. The Most Critical Gap in Cybersecurity Today: Talent. CSO; 2016. Available from: [www.csoonline.com/Technology](http://www.csoonline.com/Technology)
- [34] Ghena B, Beyer W, Hillaker A, Pevarnek J, Halderman JA. Green lights forever: Analyzing the security of traffic infrastructure. WOOT. 2014;**14**:7-7
- [35] Li Z, Shahidehpour M. Deployment of cybersecurity for managing traffic efficiency and safety in smart cities. The Electricity Journal. 2017;**30**(4):52-61
- [36] Ghafouri A, Abbas W, Vorobeychik Y, Koutsoukos X. Vulnerability of fixed-time control of signalized intersections to cyber-tampering. In: Resilience Week (RWS). IEEE; 2016. pp. 130-135
- [37] Ivanova Y. Modelling the impact of cyber attacks on the traffic control centre of an urban automobile transport system by means of enhanced cybersecurity. In: MATEC Web of Conferences. Vol. 133. EDP Sciences; 2017. p. 07001
- [38] Chen QA, Yin Y, Feng Y, Mao ZM, Liu HX. Exposing Congestion Attack on Emerging Connected Vehicle based Traffic Signal Control. Network and Distributed Systems Security (NDSS) Symposium; San Diego, CA, USA. 2017
- [39] Zajac D. Principal Investigator on NCHRP 03-127. Cybersecurity of Traffic Management Systems, Project Effective Date; 2017. Available from: [www.systemoperations.transportation.org/wp-content/upload/](http://www.systemoperations.transportation.org/wp-content/upload/)
- [40] Ramon M, Zajac D. Cybersecurity Literature Review and Efforts Report, NCHRP Project 03-127. San Antonio, TX: Cybersecurity of Traffic Management Systems, Southwest Research Institute; 2018. Available from: [www.onlinepubs.trb.org/.../NCHR03-127\\_Cybersecurity\\_Literature\\_Review.pdf](http://www.onlinepubs.trb.org/.../NCHR03-127_Cybersecurity_Literature_Review.pdf)
- [41] National Institute of Standards and Technology. Framework for Improving Critical Infrastructure Cybersecurity. 2018. Available from: <https://nvlpubs.nist.gov/nistpubs/CSWP/NIST.CSWP.04162018.pdf>
- [42] US Department of Transportation. Federal Highway Administration, Manual on Uniform Traffic Control Devices, 2009 MUTCD with Revisions 1 and 2. 2012. Available from: [www.mutcd.fhwa.dot.gov/kno\\_2009r1r2.htm](http://www.mutcd.fhwa.dot.gov/kno_2009r1r2.htm)
- [43] Baldrige Cybersecurity Excellence Builder. Key Questions for Improving Your Organization's Cybersecurity Performance. 2016. Available from: [www.nist.gov/.../baldrige-cybersecurity-initiative](http://www.nist.gov/.../baldrige-cybersecurity-initiative)
- [44] California Department of Transportation. TEES Report. 2010. Available from: [www.dot.ca.gov/trafficcops/tech/tees](http://www.dot.ca.gov/trafficcops/tech/tees)

[45] Shueh J. Cybersecurity Reigns as Top Priority for City and County CIOs in 2017. Statescoop; 2017. Available from: [www.Statescoop.com/cybersecurity-reigns-as-top-priority-for-city-and](http://www.Statescoop.com/cybersecurity-reigns-as-top-priority-for-city-and)

[46] Palmer D. Ransomware: An Executive Guide to One of the Biggest Menaces on the Web. ZDNet; 2017. Available from: <https://www.zdnet.com/article/ransomware-an-executive-guide-to-one-of-the-biggest-menaces-on-the-web/>

[47] Bigelow P. Traffic lights could be next big cyber attack threat [w/ videos]. Autoblog. 2014;26. Available from: [www.autoblog.com/2014/11/26/traffic-lights-could-be-next](http://www.autoblog.com/2014/11/26/traffic-lights-could-be-next)

[48] Reilly J, Martin S, Payer M, Bayen A. On cybersecurity of freeway control systems: Analysis of coordinated ramp metering attacks. In: Transportation Research Board 94th Annual Meeting; Washington, DC. 2015. Available from: [www.trid.trb.org/view.aspx?id=1339121](http://www.trid.trb.org/view.aspx?id=1339121)



*Edited by Arif I. Sarwat, Asadullah Khalid  
and Ahmed Hasnain Jalal*

*Smart Mobility - Recent Advances, New Perspectives and Applications* explores the rapidly evolving world of connected and autonomous vehicles, providing a comprehensive look at the latest advancements and cutting-edge technologies driving this exciting industry forward. This book covers the most pressing topics in smart mobility, including sizing, sensing, simulations, safety, and cybersecurity applications, giving readers a deep understanding of the challenges and opportunities facing this emerging field. With perspectives from leading experts, the book provides insights into the future of mobility and the role that technology will play in shaping our transportation systems. Whether you are a student, engineer, or industry professional, this book offers a unique and valuable resource for those looking to stay ahead of the curve in the ever-evolving world of smart mobility and its growing impact on our daily lives.

Published in London, UK

© 2023 IntechOpen  
© sakkmasterke / iStock

**IntechOpen**

